CYCLIC DEFORMATION CHARACTERISTICS OF HIGH STRENGTH S690 AND S960 STEEL AND THEIR WELDED SECTIONS

YIBIN GUO

PhD

The Hong Kong Polytechnic University

2025

The Hong Kong Polytechnic University
Department of Civil and Environmental Engineering

Cyclic Deformation Characteristics of High Strength S690 and S960 Steel and Their Welded Sections

YIBIN GUO

A thesis submitted in partial fulfilment of the requirements
for the degree of Doctor of Philosophy

December 2024

CERTIFICATE OF ORIGINALITY

I hereby declare that this thesis is my own work and that, to the best of my knowledge and belief, it reproduces no material previously published or written, nor material that has been accepted for the award of any other degree or diploma, except where due acknowledgement has been made in the text.

_____ (Signed)

GUO Yibin (Name of student)

ABSTRACT

Owing to advances in metallurgical development in recent years, high strength S690 and S960 steel have been produced in an industrial scale in many parts of the world. These high strength steel are highly engineered steel products which strengths are readily achieved through carefully controlled heat treatments to achieve specific microstructures during steel production. However, many researchers consider that the microstructures of these high strength steel are readily affected during welding, resulting in significant reductions in various mechanical properties in the heat-affected zones of their welded sections. It should be noted that while such reductions are found in many tests reported in the literature, they may be successfully minimized or even eliminated if the welding processes have been properly controlled. It is highly desirable to examine and quantify such effects in high strength S690 and S960 steel plates and their welded sections under cyclic actions, in particular, low cycle high strain cyclic actions as those commonly found in earthquakes. This investigation provides both engineering data and scientific understanding on these high strength S690 and S960 steel and their welded sections to be adopted in seismic resistant structures.

This thesis presents a comprehensive examination into deformation characteristics of the high strength S690 and S960 steel under axial cyclic actions loads, and both experimental and numerical investigations have been conducted to provide scientific understanding and engineering data to assess their suitability in seismic resistant structures. It should be noted that the effects of welding onto the deformation characteristics of these S690 and S960 steel have also been studied systematically. Key activities and findings of the research are presented as follows:

Part I Experimental investigations

i) Deformation characteristics of the S355, the S690 and the S960 steel plates and their welded sections under monotonic actions were obtained from standard tensile tests on cylindrical coupons. These provide essential reference data on both strength and ductility of the steel.

ii) Cyclic deformation characteristics of the S355, the S690 and the S960 steel plates and their welded sections were also obtained, and funnel-shaped coupons were subjected to cyclic actions with 4 different target strains, i.e. ε_m = ±1.0%, ±2.5%, ±5.0%, ±7.5% and ±10.0%, and 2 loading frequency, f, i.e. f = 0.1 Hz and 1.0 Hz. It should be noted that 3 different heat input energy, i.e. q = 1.0, 1.5 and 2.0 kJ/mm, are adopted during welding.

iii) Deformation characteristics of a total of 6 T-joints between cold-formed circular hollow sections of S690 steel under in-plane cyclic bending actions were attained, and 2 different heat input energy, i.e. q = 1.0 and 2.0 kJ/mm, are adopted during welding of the T-joints. Detailed instrumentation was provided to measure both the applied load-lateral displacement curves and the applied load-strain curves at the chord members in the vicinity of the welded junctions during tests, and a comprehensive data analysis was performed.

Part II Numerical investigations

i) Advanced finite element models on cylindrical coupons of S355, S690 and S960 steel and their welded sections under monotonic actions have been established, and these models have been calibrated carefully against test data.

ii) Advanced finite element models have also been established to simulate deformation characteristics of funnel-shaped coupons of S355, S690 and S960 steel under cyclic actions of various target strains ε_m and loading frequencies f, and these models have been calibrated

successfully against test data.

iii) All these structural models are established with solid elements using the general finite element package **Abaqus**, and all structural analyses are performed to determine *structural responses* of these sections, i.e. deformations, and stresses and strains.

iv) Based on the modelling technique acquired from the two sets of models mentioned above, advanced finite element models on T-joints of S690 CFCHS under monotonic as well as cyclic actions of various target displacements have also been established, and these models have been calibrated against test data.

Key research findings are:

a) Axial cyclic actions in coupons of base plates and welded sections

According to the observed hysteretic curves of the coupons with various steel grades, it is found that both the numbers of cycles completed before fracture for the S690 and the S960 steel are about 70% of those of the S355 steel. However, the total energy dissipation of both the S690 and the S960 steel are found to be similar to those of the S355 steel. Hence, despite the number of cycles completed of the S690 and the S960 steel are smaller than those of the S355 steel, all of these steel possess the same amount of dissipation energy. In addition, similar results have also been obtained for all these welded sections. ***These contradicts to the common understanding on the high strength S690 and S960 steel held by many researchers***.

b) According to the measured deformation characteristics of the T-joints between cold-formed circular hollow sections of the S690 steel under cyclic in-plane bending, it is shown that ***these T-joints exhibit a high level of cyclic ductility with large dissipation energy. In general, the numbers of cycles completed before fracture of the T-joints are related***

inversely to the values of the target lateral displacements through a highly non-linear manner.

c) Simple and effective constitutive models for the S355, the S690 and the S960 steel and their welded sections under cyclic actions have been developed, and ***specific values of various parameters of the constitutive models are established after careful calibration against test data***. It is noteworthy that these proposed models are demonstrated to be capable of predicting both the hysteretic curves and the total strain energy dissipation of the S690 and the S960 steel coupons and their welded sections with a high level of accuracy.

d) ***The constitutive models developed for the coupons of the S690 and the S960 steel under cyclic actions are demonstrated to be able to predict successfully the cyclic deformation characteristics of the T-joints between circular hollow sections of the S690 steel.***

Consequently, it is demonstrated that the S690 and the S960 steel exhibit good cyclic deformation characteristics in both welded sections and T-joints under a wide range of cyclic actions with different magnitudes of target strains. Hence, these steel are considered to possess good cyclic deformation characteristics under repeated cyclic actions, and they are readily adopted for seismic resistant structures.

LIST OF PUBLICATIONS

Journal Papers

- **Guo, Y. B.**, Ho, H. C., Chung, K. F., & Elghazouli, A. Y. (2020). Cyclic deformation characteristics of S355 and S690 steels under different loading protocols. Engineering Structures, 221, 111093.
- Ho, H. C., Xiao, M, Hu, Y.F., **Guo, Y. B.**, Yam, C.H., Chung, K. F., & Elghazouli, A. Y. (2020). Determination of a full range constitutive model for high strength S690 steels. Journal of Constructional Steel Research.
- Ho, H. C., **Guo, Y. B.**, Xiao, M., Xiao, T. Y., Jin, H., Yam, M. C. H., Chung, K. F., & Elghazouli, A. Y. (2021). Structural response of high strength S690 welded sections under cyclic loading conditions. Journal of Constructional Steel Research, 182, 106696.

Conference Papers

- **Guo, Y. B.**, Xiao, M., Liu, X., Ho, H. C., & Chung, K. F. (2019). Hysteretic Behaviour of S355 and S690 Steels under Cyclic Tests with Constant and Varying Strain Amplitudes. The 12th Pacific Structural Steel Conference (PSSC2019). Tokyo, Japan.
- **Guo, Y. B.**, Ho, H. C., Xiao, M., Liu, X., & Chung, K. F. (2019). Structural Responses of High Strength S690 Welded Sections under Different Cyclic Actions. The 16th East Asia-Pacific Conference on Structural Engineering and Construction (EASEC-16). Brisbane, Australia.
- Ho H. C., Chung K. F., and **Guo Y. B.** (2019). Transformation rules on engineering stress strain curves of S690 funnel-shaped coupons. The 16th East Asia Pacific Conference on Structural Engineering & Construction (EASEC-16), 3 - 6 December 2019, Brisbane, Australia.
- **Guo, Y. B.**, Chung, K. F., & Ho, H. C. (2023). A Comparative Study on Hysteretic Characteristic of S355 and S690 Welded Sections under Cyclic Actions with Constant Magnitudes. The 13th Pacific Structural Steel Conference (PSSC2023). Chengdu, China.

ACKNOWLEDGEMENTS

I started my Ph.D. study in September 2017, and it took me over seven years to complete the journey. Looking back, what a long and dramatic seven years! There were periods of social movements, pandemics and lockdowns that prevented me from returning to my hometown for two years, suffering from depression, and the loss of my loved ones. It was as if all the hardships I would face in my life had been condensed into these seven years. I cannot remember how many tears I shed, how many times I wanted to quit my Ph.D. study, and there were even hard times when I lost hope of living… but here I am, finally presenting this dissertation with joy and tears.

If I could only thank one person, it would undoubtedly be my supervisor, Professor K. F. Chung. Not only did he guide me professionally and with dedication in my research, but he also cared a lot about me. Without his support and encouragement, I would not have been able to continue this journey. I would also like to thank my clinical psychologist, Ms. W. S. Liu, who taught me how to manage my emotions and love myself well. With her help, my depression has gradually improved.

Next, I would like to thank my parents, who have always respected and understood me, and have supported me financially and emotionally. I would also like to thank my grandmother. Although she passed away due to cancer three months ago, she always loved and encouraged me during her lifetime. Recently, she has often appeared in my dreams to cheer me up. Grandma, thank you so much, I love you! Special thanks also go to my beloved partner, Dr. R. Tani, whose calm and continuous love gave me the strength to persevere in the struggles.

I would also like to express my thanks to the technicians at CEE, Mr. M. C. Ng, Mr. K. L. Cheung, and the former technician at BRE, Mr. C. F. Wong, for their assistance with the experiments in the laboratories, as well as the financial support of the Research Committee and the Chinese National Engineering Research Centre for Steel Construction (Hong Kong Branch) of The Hong Kong Polytechnic University.

There are many more people to thank. Please allow me to include their names in the acknowledgements (in no particular order):

Ir. Dr. M. F. Hui,	Ir. Dr. H. C. Ho,	Ms. Catherine Ng,	Dr. X. Liu,
Dr. M. H. Shen,	Dr. K. Wang,	Dr. Y. F. Hu,	Dr. M. Xiao,
Dr. M. F. Zhu,	Dr. H. Jin,	Mr. W. Chen,	Ms. Q. Y. Zhao,
Ms. W. Feng,	Mr. Y. C. Wang,	Ms. T. Y. Xiao,	Dr. S. T. Mao,
Dr. P. C. Wu,	Dr. K. K. Das,	Dr. H. X. Zhang,	Mr. H. K. Lai,
Ms. Y. Kobayashi,	Mr. K. Kawamura,	Mr. T. Tanaka,	Mr. K. Ozawa,
Mr. H. Kanetake,	Mr. M. Yokotani,	Mr. M. Murotani,	Mr. S. Ono,
Mr. S. Abe,	Mr. N. Takahashi,	Mr. T. Nakamura,	Mr. T. Kasano,
Mr. T. Nishiho,	Mr. M. Suzuki,	Mr. T. Kurahachi,	Mr. T. Asano.

If I were to rely on my own strength alone, I would definitely not be able to complete my Ph.D. study. The reason why I have been able to come to this day, and even burst into tears of joy while writing at this moment, is because there are many kind and lovely people who have been with me for these seven years.

TABLE OF CONTENTS

LIST OF FIGURES

LIST OF TABLES

LIST OF SYMBOLS

f_u	Tensile strength of the steel
f_y	Yield strength of the steel
ε_L	Strain at failure
ε_u	Strain corresponding to f_u
ε_y	Strain corresponding to f_y
T_{max}	The maximum temperature
$T_{8/5}$	Cooling times from 800 ºC to 500 ºC
q	Heat input energy
ε_T	Target strain
f_L	Loading frequency
η	Efficiency of welding
U	Welding voltage
I	Welding current
v	Welding speed
ε_e	Engineering strain
ε_t	True strain
σ_e	Engineering stress
σ_t	True stress
A_0	Undeformed cross-sectional area
A_i	Measured instantaneous minimum cross-sectional area
P_i	Applied load corresponding to A_i
$\eta_{t,i}$	Tensile strength factor for each cycle
$\eta_{c,i}$	Compressive strength factor for each cycle
$f_{ut,i}$	Maximum tensile strength in each cycle
$f_{uc,i}$	Maximum compressive strength in each cycle
$f_{yt,1}$	Yield strength in the 1st cycle
n_c	No. of cycles completed
f_{y1}	Yield strength of the 1st cycle
L	Span of the chord member between pinned supports
L_0	Length of the chord member
d_o	Diameter of the chord member
d_1	Diameter of the brace member

t_o	Thickness of the chord member
t_l	Thickness of the brace member
P	Applied load
δ	Lateral displacement
E	Young's modulus
P_{max}	Peak load
P_{last}	Maximum load in the cycle before failure
α_k	Back stress
$\alpha_{k,1}$	Back stress at the reverse loading point
C_k	Initial kinematic hardening modulus
γ_k	Rate of decrease with plastic strain of kinematic hardening modulus
ε^{pl}	Equivalent plastic strain

CHAPTER 1 INTRODUCTION

1.1 Use of high strength steel in construction

High strength steel is commonly defined as steel materials with a nominal yield strength of 460 N/mm² or greater. These materials are typically referred as S460, S550, S690, or S960, with the symbol referring to the steel material, and the numeric denoting the yield strength. In recent years, high strength S690 and S960 steel has become increasingly available in numerous modern steel mills across the world, with these materials being produced in substantial quantities on a regular basis. In recent decades, the utilisation of high strength steel has seen a substantial increase in various applications, particularly in the construction of heavily loaded structural components of large machinery and lifting equipment. In comparison to normal strength S355 steel, which is commonly adopted in construction, these high strength S690 and S960 steel are widely considered efficient construction materials owing to their high strength-to-weight ratios. A broader utilisation of these S690 and S960 steel in construction would result in the reduction of member sizes and self-weights of structural components consequently leading to a substantial reduction in construction costs and time. Consequently, high strength steel is a highly attractive material for structural engineers when designing structures such as high-rise buildings and long-span bridges.

The S355 steel is typically regarded as possessing a relatively high level of ductility. This characteristic enables the structural components of various commonly adopted structural configurations to undergo large deformation at full plastic section resistances. Nevertheless, there is a pervasive concern regarding the ductility of higher strength steel, which is widely regarded as being considerably lower in comparison to the normal strength S355 steel. However, given the

lack of relevant design recommendations, it remains uncertain whether the direct adoption of these high strength S690 and S960 steel in such structures would result in behaviour similar to that observed with S355 steel. Consequently, it is necessary to quantify the ductility properties of the high strength S690 and S960 steel, in comparison with those of the S355 steel. A systematic investigation into mechanical properties of these high strength steel, in particular, their ability to sustain loading at large deformations up to fracture, i.e. ductility, is crucial to accept their applications in large scale steel structures and members in construction.

1.2 Ductility of high strength steel

There are fundamental yet crucial clauses regarding ductility requirements for structural steel in various codes and standards. In case of those S235 to S460 steel that are commonly used, the ductility requirements stipulated in EN 1993-1-1 (2005) are given as follows:

i) $f_u / f_y \geq 1.10$;

ii) $\varepsilon_L \geq 15\ \%$; and

iii) $\varepsilon_u \geq 15\ \varepsilon_y$

where

f_y and f_u are the yield and the tensile strengths of the steel;

ε_L is the strain at failure;

ε_u is the strain corresponding to f_u ; and

ε_y is the strain corresponding to f_y.

The ductility requirements for the high strength S690 steel under consideration in the present project are specified in EN 1993-1-12 (2007), and are given as follows:

i) $f_u / f_y \geq 1.05$;

ii) $\varepsilon_L \geq 10\ \%$; and

iii) $\varepsilon_u \geq 15\ \varepsilon_y$

In the latest version of EN 1993-1-1(2022) [S235 to S700] which is extended to cover the high strength S690 steel, the revised ductility requirements are given as follows:

i) $f_u / f_y \geq 1.10$ for plastic analysis;

≥ 1.05 for elastic analysis;

ii) $\varepsilon_L \geq 12\ \%$ for plastic analysis; and

$\geq 15\ \%$ for elastic analysis

In general terms, these requirements have been established on the basis of test results obtained from monotonic tensile tests on a large quantity of steel of various shapes and dimensions. It is widely considered that the high strength S690 steel behaves in a different manner to those S235 and S460 steel. This is due to the differing microstructures resulting from the different forms of heat treatment during manufacturing, i.e. different delivery conditions (CEN, 2004, 2022). It is important to note that the mechanical properties of these steel, as determined by monotonic tensile tests, are frequently found to be significantly different from those obtained from cyclic tests (Ho et al., 2018; Wang et al., 2017).

A general absence of rigorous experimental investigation has been observed in the field of seismic response of high strength steel and related materials within the practical ranges of seismic activity. Consequently, the adoption of high strength steel in seismic-resistant structures remains uncertain.

This represents an unexplored domain within the prevailing design standards and codes of practice. It can therefore be concluded that the necessity to conduct systematic comparative studies is imperative in order to generate new understandings and to formulate rational ductility requirements for high strength steel construction. Such an approach is fundamental in order to ensure the safe and effective utilisation of the materials in the construction of structures intended to resist seismic actions.

1.3 Objectives and scope of work

This project aims to investigate deformation characteristics of the high strength S690 and the S960 steel under monotonic as well as cyclic actions to provide scientific understandings and engineering data to establish whether the concern on reduced ductility in these S690 and S960 steel is justified. Hence, the following tasks are carried out:

i) to investigate the structural responses of specially-designed coupons of the S355, the S690 and the S960 steel in monotonic tensile tests,

ii) to also investigate in parallel the structural responses of these steel coupons in cyclic tests;

iii) to investigate the structural responses of T-joints between S690 cold-formed circular hollow sections under in-plane bending of monotonic and cyclic actions; and

iv) to establish advanced numerical models of both the specially-designed coupons and the T-joints between circular hollow sections of both steel under both monotonic and cyclic actions.

Through these experimental and numerical investigations, it is expected to develop a ductility requirement based on cyclic deformation characteristics for determination of whether the high strength S690 steel should be adopted in seismic resistant structures.

1.4 Outlines of chapters

The outline of each of the chapters are presented as follows:

Chapter 1 Introduction

An introduction of the project is presented together with the background of high strength steel on their ductility under monotonic and cyclic actions. The objectives of the project are clearly identified, and the scope of work and key activities are presented in a systematic manner.

Chapter 2 Literature review

A comprehensive review on the literature is presented, and details of the following areas are reported:

- deformation characteristics of high strength S690 and S960 steel under monotonic and cyclic actions;
- cyclic behaviour of welded sections and joints of high strength S690 and S960 steel; and
- advanced numerical modelling of high strength S690 and S960 steel under monotonic and cyclic actions, and simulation of the structural responses of high strength S690 and S960 steel connections.

Chapter 3 High strength steel and their welded sections under monotonic tests

This chapter presents an experimental investigation into deformation characteristics of the S355, the S690 and the S960 steel plates and their welded sections under monotonic actions which are obtained from standard tensile tests on cylindrical coupons. These provide essential reference data on both strength and ductility of the high strength steel under monotonic actions.

Chapter 4 High strength steel and their welded sections under cyclic tests

This chapter presents an experimental investigation into cyclic deformation characteristics of the S355, the S690 and the S960 steel plates and their welded sections. A detailed account of 154 cyclic tests on the funnel-shaped coupons of these steel together with their results is presented. An in-depth examination is conducted to investigate the effects of five different target strains and two different loading frequencies. For the range of loading protocols, strain amplitudes and frequencies that are under consideration, the hysteretic responses exhibited by the coupons of both steel are compared directly in the context of engineering stress-strain curves. This comparison is based on the nominal diameters of the materials. Furthermore, Microstructures of fractured coupons from the S355, S690 and S960 steel are examined. These provide essential engineering data on both strength and ductility of the S690 and the S960 steel under cyclic actions, and various parameters to quantify their deformation characteristics are proposed, and presented for comparison with those of the S355 steel.

Chapter 5 High strength steel T-joints under monotonic and cyclic in-plane bending

This chapter presents an experimental investigation into monotonic and cyclic deformation characteristics of T-joints of S690 cold-formed circular hollow sections. A detailed account of 2 monotonic tests and 6 cyclic tests on these T-joints with 2 different heat input energy during welding is presented together with their results. Effects of two target displacements onto the T-joints are examined in details. Microstructures of the fractured parts of the T-joints are also examined. These provide essential engineering data on both strength and ductility of the T-joints under cyclic actions. Various parameters to quantify their deformation characteristics are proposed,

and presented for comparison with those obtained from cyclic tests on specially designed coupons presented in Chapter 4.

Chapter 6 Simulation on high strength steel and their welded sections under cyclic tests

This chapter presents a numerical investigation into cyclic deformation characteristics of the S355, the S690 and the S960 steel plates and their welded sections. Effects of five different target strains are also examined in details. Predicted hysteretic responses of these coupons of the three steel are compared directly with those of the measured data presented in Chapter 4. Moreover, various parameters based on predicted and measured data to quantify their deformation characteristics are compared directly. Constitutive models for the S690 and the S960 steel are also proposed after a careful calibration against measured data.

Chapter 7 Simulation on high strength steel T-joints under cyclic tests

This chapter presents a numerical investigation into cyclic deformation characteristics of the S690 T-joints between cold-formed circular hollow sections. Effects of two different target displacements are also examined in details. It should be noted that the constitutive models of the high strength S690 steel proposed in Chapter 6 are adopted to predict the deformation characteristics of these S690 T-joints. Then, the predicted cyclic deformation characteristics of these T-joints are compared directly with those of the measured data presented in Chapter 5.

Chapter 8 Conclusions and future work

Key findings of the project are rationally presented, and cyclic deformation characteristics of the S690 and the S960 steel is thoroughly discussed according to the findings of the experimental and

the numerical investigations of the project. Based on both the conclusions and the limitations of the present study, future work is also recommended.

CHAPTER 2 LITERATURE REVIEW

This chapter presents a comprehensive review on the literature on the following topics which are directly related to the present study:

a) High strength steel, and effects of welding on their mechanical properties

b) Ductility, and demands in various codes

c) Experimental investigations

- Loading protocols with various target strains and frequencies
- Hysteretic behaviour and key test data

d) Numerical investigations

- Finite element modelling technique
- Simulations on hysteretic behaviour

Details of the review on various topics are presented in the following sections.

2.1 High strength steel, and effects of welding on their mechanical properties

In many modern steel mills around the world, high strength steel are produced with various heat-treatments (Easterling, 1992; Willms, 2009), namely, i) Quenching (Q) and Tempering (T) process for QT steel, and ii) Thermal (T) Mechanically-controlled (M) process for TM steel. These processes are carefully controlled to produce high strength steel with specific martensitic-ferritic microstructures which possess favourable mechanical properties. These high strength steel, commonly referred as i) S690-QT steel, and ii) S690-TM steel, when compared with those common strength S355 steel. It should be noted that these steel have different metallurgical responses under the effects of welding.

In the case of S690 steel, microstructure changes in the heat-affected-zones (HAZ) have been demonstrated to be initiated during the process of welding under a cycle of heating and cooling,

which involving heating to temperatures as high as 1,350°C and subsequent cooling to room temperature. As Easterling (1992) demonstrate, when the maximum temperature, T_{max}, at HAZ exceeds certain threshold values during the welding process, significant phase changes, re-crystallization and grain growth take place (see Figure 2.1). In subsequent phases of the cooling process, which occur within a time $t_{8/5}$ under practical air-cooling conditions following welding (see Figure 2.2), a range of constituents, such as martensite, bainite, ferrite and pearlite, are formed according to their specific cooling rates, ranging from 800°C to 500°C over a duration $t_{8/5}$. It is important to acknowledge the significance of microstructural changes in the HAZ of S690 welded sections, with the process being primarily dependent on welding procedures. This is in conjunction with various parameters, particularly the heat input energy, q (kJ/mm), during the welding process, the plate thicknesses, and the joint details. It has been established that the structural behaviour of the S690 welded sections is heavily dependent on the mechanical properties of the HAZ. It can therefore be deduced that the regulation of the welding procedures and parameters is of significant importance in order to minimise any deterioration in the strength and ductility of the S690 welded sections (Ho et al., 2020).

A number of previous investigations (Mayr, 2007; Ding et al., 2017; Azhari et al., 2018) were conducted in order to examine the microstructural changes in S690 welded sections. Concurrent studies have also been undertaken to investigate the correlation between the mechanical properties of various HAZ and those of S690 welded sections, utilising high-fidelity micro-mechanical models and meso-scale mechanical analyses (Śloderbach and Pajak, 2015; Tian et al., 2017). A significant proportion of these investigations involved the analysis of SEM images and volumetric fractions of the HAZ, in addition to their strengths and hardness, as a means of assessing their physical and mechanical properties. However, the focus remains limited on evaluating the ductility of these materials for structural applications subjected to

cyclic loading conditions. Consequently, there is a pressing need to undertake systematic structural evaluations to assess the response of S690 welded sections when subjected to substantial inelastic deformations under various cyclic loading conditions.

2.2 Ductility of high strength steel

As demonstrated in the recent experimental investigations of Wang et al. (2017), Ho et al. (2018), and Guo et al. (2020), the mechanical properties of common structural steel, including S235, S355, and high strength S690 steel, demonstrate significant variations under monotonic and cyclic actions.

Despite the fact that the reliability of welded steel sections of S355 has been thoroughly and rigorously examined, there remains a lack of information with regard to the strength and ductility characteristics of S690 welded sections when subjected to inelastic cyclic loading conditions. The adequacy of the ductility requirements stipulated in EN 1993-1-1 (CEN, 2014) for structures adopting S690 steel materials and subjected to cyclic seismic actions remains to be ascertained.

At present, there is an absence of precise specifications for the structural responses of the S690 steel and their welded sections under cyclic actions, as specified in structural design codes. Furthermore, there appears to be a lack of detailed guidance on the assessment of the structural behaviour of welded sections and joints employing high strength S690 steel under cyclic loadings. This has been noted in the literature, with CEN (2005, 2007) and AISC (2016) highlighting this particular gap in knowledge. The lack of systematic experimental assessments and technical guidance, therefore, hinders the effective application of high strength S690 steel in seismic-resistant structures across many regions worldwide.

2.3 Previous work on the cyclic response of high strength steel

A substantial corpus of experimental research has been published over the past four decades concerning the strength and ductility properties of structural steel and metal alloys when subjected to cyclic actions. These studies can be classified into two main categories:

a) For the vibration assessment in the serviceability limit state, high-cycle low-strain cyclic tests were commonly employed to investigate the long-term fatigue behaviour of welded sections in steel structures as well as various types of metal alloys in aircrafts and automobiles (Fournier et al., 2006; Khan et al., 2012; Chen et al., 2013). Typical numbers of cycles in such tests ranged from 0.5 to 50 million, while the stress levels were typically between 5 to 30% of the yield strengths of the steel or the metal alloys.

b) For structural elements exposed to seismic actions, two experimental methodologies were employed to investigate the response, i.e. simulated quasi-static cyclic tests and shaking table tests. For members or connections, it was deemed appropriate to implement a series of cyclic protocols, incorporating various low-cycle high-strain cyclic loadings (Nip et al., 2010; Zhou et al., 2015; Wang et al., 2015; Hu and Shi, 2018).

2.3.1 Common loading protocols for cyclic tests

In recent years, a number of studies have reported on cyclic tests conducted on coupons of various steel materials, specifically designed for the study. The objective of these tests was to examine the hysteretic characteristics of the materials under idealised, pre-defined displacement histories. The investigations conducted have employed various testing methods, reflecting the diverse applications and experimental constraints, with the objective of examining the hysteretic behaviour of structural steel materials. A number of these studies addressed issues of fatigue (Fournier et al., 2006; Khan et al., 2012; Li et al., 2013), with a focus on the fracture mechanisms and microstructures of steel materials at various temperatures.

By contrast, researchers involved in structural engineering applications (Nip et al., 2010; Chen et al., 2013; Zhou et al., 2015) investigated how steel materials behave structurally under varying loading protocols and strain amplitudes (Ho et al., 2016; Wang et al., 2017). This study aims to identify suitable testing methods for quantifying cyclic tests on steel materials for use in seismic design. To this end, three commonly adopted testing methods are compared:

a) *Recommendations for assessing behaviour of structural steel elements under cyclic loads (ECCS, 1986)*. It is important to note that the document defines of a loading protocol by establishing a conventional limit of elastic range, denoted F_y, and the corresponding deformation obtained from monotonic tests in both tension and compression actions, or sagging and hogging actions, denoted ε_y, as illustrated in Figure 2.3. Nevertheless, there is a lack of detail regarding the selection and implementation of the loading protocol, as well as the correlation between structural response to seismic actions and cyclic ductility under varying seismic levels;

b) *FEMA-461: Interim testing protocols for determining the seismic performance characteristics of structural and non-structural components (FEMA 461, 2007)*. This document has been considered by a number of researchers to be the definitive guidance document on the selection of loading protocols, with the basis of this selection being a stepwise loading protocol as illustrated in Figure 2.3. The document was selected for the cyclic tests that are described subsequently in this study;

c) *AISC 341: Seismic Provisions for Structural Steel Buildings (AISC, 2016)*. The present loading protocol has been developed with particular reference to the seismic design of steel and composite structures. It provides a loading protocol for cyclic tests (see Figure 2.3), and is considered to be primarily applicable for the qualification of beam-to-column connections. A comparison with the protocol outlined in FEMA reveals that the total

number of cycles is increased from 20 to 30 in order to achieve the same value of the target strain, whilst the step factor is decreased accordingly.

A number of experimental investigations have been conducted on the hysteretic behaviour exhibited by various types of carbon steel and stainless-steel materials, utilising a range of loading protocols. These protocols have included the following: (i) a cyclic ascending loading protocol, (ii) a cyclic alternate loading protocol, and (iii) a cyclic tensile loading protocol, with a maximum strain amplitude of ±2% (Chen et al., 2013; Zhou et al., 2015). It is imperative to establish a standardised testing method in order to define a suitable loading protocol, test specimens of suitable geometry, and establish an appropriate loading frequency. This is necessary for the characterisation of high strength S690 steel materials so that they can be qualified for use in seismic design.

2.3.2 Previous research on funnel-shaped coupons at CNERC

A preliminary experimental investigation into the tensile strength andductility properties of S690 steel plates (un-welded) was conducted at CNERC, the details of which can be found in the work of Ho et al. (2018). A total of 36 funnel-shaped coupons, with a diameter of 5.0 mm at mid-length, were tested in accordance with the following methodology:

a) The cyclic protocol with non-linearly increasing strains, as outlined in FEMA 461 (2007), was adopted for this purpose. This protocol involves the multiplication of strain magnitude by an amplification factor of 1.4 after every two cycles. It was deemed that the coupon had passed the test when it successfully reached the designated target strain at the 19^{th} and 20^{th} cycles.

b) The cyclic tests were performed on four target strains, i.e., ε_T of ±2.5%, ±5.0%, ±7.5% and ±10.0%, and for four loading frequencies, i.e., f_L of 0.1, 0.5, 1.0 and 2.0 Hz. The magnitude

of the target strain ε_T and the loading frequencies f_L were selected according to the typical seismic response observed in buildings and bridges.

Consequently, it can be concluded that S690 steel exhibits a high degree of ductility under such cyclic actions. It was imperative to assess the structural response of S690 steel under cyclic actions in comparison to that of S355 steel, given the long-established fact that S355 steel exhibit good ductility under monotonic tensile actions. An experimental investigation was conducted at the CNERC (Guo et al., 2020), in which 32 funnel-shaped coupons were tested under two different cyclic protocols, with combinations of four target strains and two loading frequencies. In addition to the cyclic protocol involving non-linear strain increases in accordance with the provisions of FEMA 461, as previously referenced, an alternative cyclic protocol employing constant strain levels throughout the duration of the test was also initiated. The following observation is made:

- For experiments carried out in accordance with the cyclic protocol of non-linearly increasing strain, a comparable structural response was observed for the two steel types, S355 and S690, under equivalent combinations of target strains and loading frequencies.
- For experiments conducted under the cyclic protocol of constant strains, the responses of S355 and S690 steel exhibited considerable variation according to the magnitude of the target strains. S690 steel demonstrated an inability to complete the same number of cycles as S355 steel when subjected to the same conditions. The specific parameters that resulted in this outcome included a target strain of ±2.5% and a loading frequency of 0.1 and 1.0 Hz. However, when the target strains were increased to ±5.0%, ±7.5% and ±10%, with loading frequency set at both 0.1 and 1.0 Hz, a significant decrease in the total number of cycles completed in the cyclic tests of both S355 and S690 steel was found, as would be expected. However, the findings of this study demonstrated the superiority of S690 steel,

with its ability to complete more cycles when subjected to the same conditions as S355 steel, and thus proving its superiority in terms of cyclic deformation characteristics when exposed to such significant target strains.

Consequently, these experiments provide an opportunity to examine the structural responses of the S690 high strength steel under the relevant cyclic actions of seismic loadings in structures. The experiments and their subsequent interpretation have provided valuable insights that will inform the selection of suitable loading protocols, target strains and loading frequencies for subsequent cyclic tests of the high-strength steel. Further investigation is recommended into the cyclic deformation characteristics of the S690 steel under varying loading protocols with more stringent demands. In addition, comparative studies with the S355 steel should be carried out so that differences in their cyclic responses can be quantified. It is necessary to extend the scope of the aforementioned evaluations to include S690 welded sections. This is of crucial importance for the purpose of conducting a comparative analysis of their response to various cyclic conditions, in conjunction with that of unwelded S690 steel. This is a prerequisite for the quantification of their strength and ductility. The present analysis will facilitate a comprehensive examination of the applicability of the aforementioned models in the context of seismic design.

2.3.3 Previous research on T-joints between circular hollow sections

Many researchers have previously examined the structural behaviour of joints between structural hollow sections over the past decades:

- In the study conducted by Wang and Chen (2007), the hysteretic response of T-joints subjected to cyclic loads in the S355 CHS configuration was investigated, offering valuable insights into the material behaviour under cyclic loading conditions. In the study, failure

modes were identified for T-joints under cyclic brace axial compression. These failure modes included i) weld fracture under tension and ii) chord plastification under compression. In the context of T-joints under cyclic brace in-plane bending, a range of failure modes have been identified, including punching shear, chord plastification and weld fracture.

- An experimental investigation was conducted on a total of twelve T-joints between high-strength CHS by Kim et al. (2012). The T-joints were tested under cyclic brace in-plane bending. Curved coupons were extracted from these sections, and their yield strengths were found to be 464 and 584 N/mm^2. The experimental findings demonstrated that all of the T-joints under scrutiny failed during the process of chord plastification when subjected to large in-plane brace moments. Furthermore, an analysis of ductility revealed that these T-joints exhibited a highly comparable ductility to that of T-joints between S355 CHS.
- Havula et al. (2018) conducted experimental investigations into the structural behaviour of T-joints in S420 to S700 structural hollow sections under monotonic brace in-plane bending. It has been demonstrated that these T-joints failed during the process of chord plastification, with strain hardening being extensively developed at the point of failure. Despite the prevalence of fracture in the HAZ upon excessively plastic deformation, it was observed that the rotational capacity of T-joints was consistently above the 3% deformation limit that is widely adopted (Yura et al., 1981; Wardenier et al., 2008; CEN, 2005).

2.3.4 Previous research on T-joints between circular hollow sections at CNERC

Hu et al. (2020, 2022) conducted experimental investigations into the structural behaviour of T-joints between cold-formed circular hollow sections of S690 steel under both monotonic and cyclic brace in-plane bending. It was found that for T-joints with small braces, failure occurred due to bending. In contrast, T-joints with larger braces exhibited punching shear failure in the

chords surrounding the welding collars. Moreover, although it was observed that fracture occurred at the HAZ in these T-joints following excessive plastic deformations, the rotational capacities of these T-joints were found to exceed the commonly adopted 3% deformation limit (Yura et al., 1981; Wardenier et al., 2008; CEN, 2005). The structural behaviour of these T-joints was demonstrated to be adequate in terms of resistance and ductility during large deformations.

2.4 Numerical investigations

In order to examine the cyclic deformation characteristics of the high strength steel and their welded sections, a number of relevant finite element investigations were reviewed. And key findings of these works are summarized as follows. It should be noted that Abaqus is a powerful finite element software for engineering simulations, and it is widely adopted in numerical analyses of steel members and structures, and more importantly, mechanical properties of welded joints and bolted connections of steel sections under monotonic and cyclic actions. Hence, Abaqus is adopted in the present study to simulate the cyclic behaviour of both the funnel-shaped coupons and the T-joints between cold-formed circular hollow sections of the S690 steel.

2.4.1 Simulation of welding

Welding simulation is an important topic of research at CNERC, and the effects of welding onto the mechanical properties of the high strength steel have been systematically investigated. These include i) welding-induced residual stresses, and ii) welding-induced microstructural changes, both in the high strength steel members. In general, as for the simulation of welding, a double ellipsoid heat source may be adopted to simulate a welding process. Liu et al. (2018) established various finite element models which replicate accurately the temperature history

and the residual stresses of the S690 welded sections. However, it should be noted that all the welded sections and the welded T-joints between cold-formed circular hollow sections in the present study were prepared with a proper control on the welding process, and hence, it is readily assumed that there is no reduction in the mechanical properties in both the welded sections and the T-joints. Hence, no welding simulation was performed in the numerical investigations of the present study.

2.4.2 Constitutive models for steel

The three main essential characteristics of a constitutive model for steel are, namely, i) yield criterion, ii) flow rule, and iii) hardening rule. A yield criterion specifies the initial yield surface of the material. The initial yield surface for a metallic material is specified by the yield criterion, and the von Mises criterion is widely adopted as the standard yield criterion for steel. The flow rule which defines the direction of plastic strain increment in steel is also based on the von Mises yield criterion. A hardening rule describes the subsequent yield surface that relies on the plastic loading history.

Three commonly adopted rules of hardening: isotropic hardening, kinematic hardening and combined hardening models, and these models are described as follows:

- Isotropic hardening mode - Figure 2.4a)

  Isotropic hardening rule refers to a process in which the strength of the material being examined is improved, or enhanced in one particular direction whilst the yield strength in another direction is also increasing at the same time. Hence, the shape of the yield surface does not change whilst the area of the surface undergoes an increase. This is to say that both the tensile strength and the compressive strength of the material being examined remain

equal over time if the initial values are known to be the same. The area of yield surface is described as follows:

$$\sigma^0 = \sigma|_0 + Q_\infty \left(1 - e^{-b\bar{\varepsilon}^{pl}}\right) \qquad \text{Equation 2.1}$$

where

$\sigma|_0$ is the yield surface at the beginning;

Q_∞ is the maximum change in the area of the yield surface; and

b is the changing rate.

- Kinematic hardening model - Figure 2.4b)

When steel is subjected to tensile forces, resulting in plastic deformation, subsequent application of tensile forces after unloading leads to an increase in the tensile yield strength to the unloading point. This phenomenon is known as strain hardening. In a similar manner, the application of compressive forces after unloading results in a reduction of the compression yield strength to a value that is lower than the value obtained during the previous compression loading. This phenomenon, in which the tensile strength increases and the compressive strength decreases after reaching strain hardening, is known as the Bauschinger effect. Consequently, the kinematic hardening rule may be adopted to simulate the Bauschinger effect and other similar situation.

The back stresses describe translation of the yield surface. There are two kinematic hardening rules in this model:

i) Linear hardening model

This model incorporated a linear back stress, α, which determine linear translation of the yield surface as follows:

$$\alpha = C\varepsilon^{pl} \qquad \text{Equation 2.2}$$

Where

C is the hardening parameter corresponding to the material; and

ε^{pl} is the plastic strain.

ii) Nonlinear hardening model – Figure 2.5

The nonlinear kinematic hardening rule facilitates the summation of multiple back stresses, thereby yielding an aggregate back stress. Consequently, each back stress is characterised by a distinct strain range, enabling the superimposed back stress to coincide with the actual back stress, as illustrated in Figure 2.3. In general, a triad of back stresses is sufficient to accommodate a wide range of practical scenarios. The derived formulation is expressed as follows:

$$\alpha = \sum_{K=1}^{n} \alpha_k = \sum_{k=1}^{n} \frac{c_k}{\gamma_k}\left(1 - e^{-\gamma_k \varepsilon^{pl}}\right) \qquad \text{Equation 2.3}$$

where

n is the number of back stresses;

c_k s is the kinematic hardening modulus; and

γ_k is the change of rate of back stresses.

- Combined hardening model - Figure 2.6

This hardening model consists of two parts, namely a part of the isotropic hardening rule which determines the area of the yield surface, and a part of the nonlinear kinematic hardening rule which determines the position of the yield surface, as shown in Figure 2.4. The yield surface can be obtained by eliminating the back stress from the yield stress in the low cycle high strain tests as follows:

$$\sigma_i^0 = \sigma_i^t - \alpha_i \qquad \text{Equation 2.4}$$

where

σ_i^0 is the equivalent stress; and

σ_i^{t} is the tensile yield stress.

The majority of classical constitutive models for steel with simple loading histories are based on a combination of isotropic hardening and kinematic hardening rules. While for those with complex loading histories, i.e. a cyclic loading within the plastic range, the constitutive model with mixed hardening rules is often found to be inadequate. Hence, a bounding surface model with two yield surfaces, also known as the two-surface plasticity model, was proposed by Dafalias and Popov (1975, 1976), and Krieg (1975) to describe the hysteretic behaviour of steel under cyclic actions within the plastic range. It should be noted that the plastic modulus varies continuously between the initial yield surface and the bounding surface which account for a nonlinear kinematic hardening rule.

The maximum plastic strain range was introduced as a significant parameter by Chaboche (1979), and modified by Ohno (1982), given that the plastic strain history on the hysteretic behaviour of steel. The cyclic plastic behaviour of steel is influenced by its plastic deformation history, i.e. an equivalent plastic strain, a plastic strain range, and a mean plastic strain (Chaboche, 1989 and 2008). In a recent study, these parameters were obtained from measured plastic deformation history, and they were examined explicitly. It should also be noted that constitutive models utilizing a number of sets of plastic parameters were proposed (Xie and Chen, 2021; He et al., 2022).

2.4.3 Previous numerical investigations on welded sections and T-joints

Wang et al. (2015) proposed a model to describe kinematic hardening in cyclic tests and verified its accuracy by comparing the results of numerical and experimental investigations. Chen et al. (2013) conducted a series of cyclic tests on steel plates with different yield strengths

up to 420 N/mm^2 under different loading protocols. In the hysteretic loops, it was shown that the effects of strain hardening increased with the increase of their plastic strain. A number of studies have also shown that strain hardening is common in cyclic testing of various steel. Furthermore, Xu et al. (2016) proposed a constitutive model to determine the hysteretic loops that showed both cyclic hardening and softening. The cyclic softening was caused by strain accumulation, which was reflected in the reduction of stresses during repeated cyclic loading and unloading. A new idea of a 'transformation zone' was also proposed to quantify such stress degradation due to an increase in back stresses and a reduction in yield stresses. The proposed method was shown to be capable of evaluating the hysteretic loops after cyclic softening.

2.4.4 Numerical simulations on T-joints between circular hollow sections at CNERC

A numerical modelling approach was integrated to develop advanced three-dimensional solid element finite element models of CFCHS (Hu et al., 2022). Following the establishment of precise definitions for the weld collars located at the brace/chord junctions of the T-joints between S690 CFCHS with varying diameters and thicknesses, these models were readily adopted for the purpose of sequentially performing a heat transfer analysis, a thermo-mechanical analysis and a structural analysis with compatible element types and meshes. As a result, the impact of welding-induced residual stresses at the junctions of welded braces and chords on the structural behaviour of these T-joints was readily ascertained. Consequently, the findings demonstrate that these advanced models possess the capability to systematically predict the deformation characteristics of the T-joint components in the S690 CFCHS subject to both monotonic and cyclic actions of brace in-plane bending, exhibiting a substantial degree of structural accuracy. The numerical simulations were executed using Abaqus. A combination of isotropic and kinematic constitutive models with differing back-stress parameters was adopted for models subject to cyclic actions, and this combination proved successful.

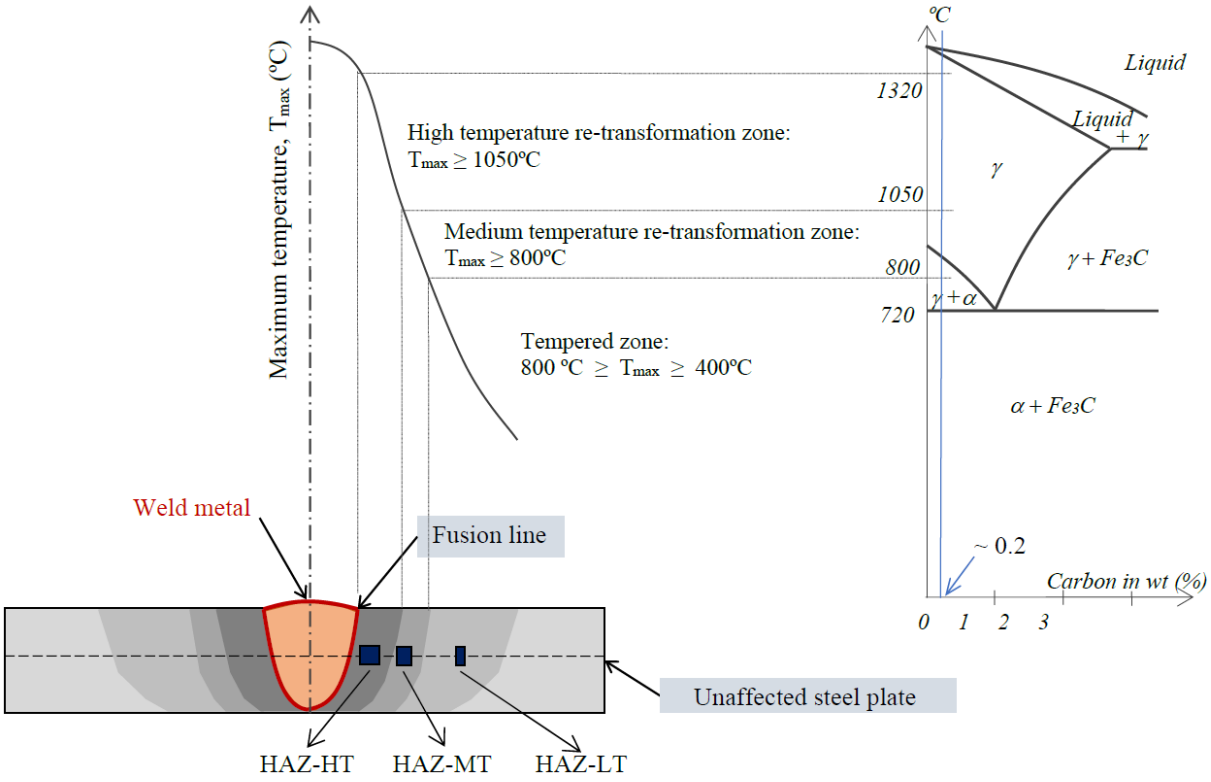

Figure 2.1 Phase change of steel under welding

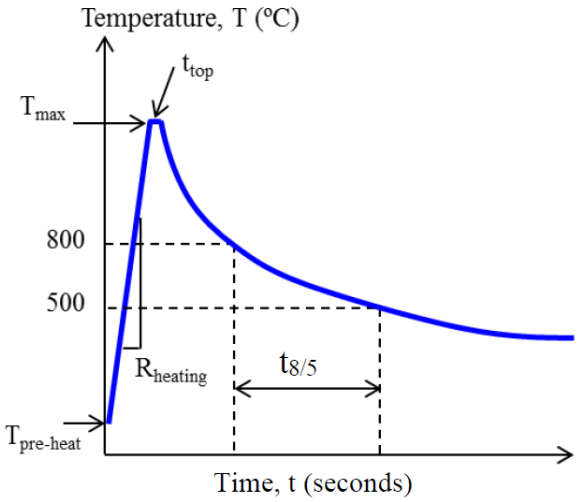

Figure 2.2 $t_{8/5}$ of steel

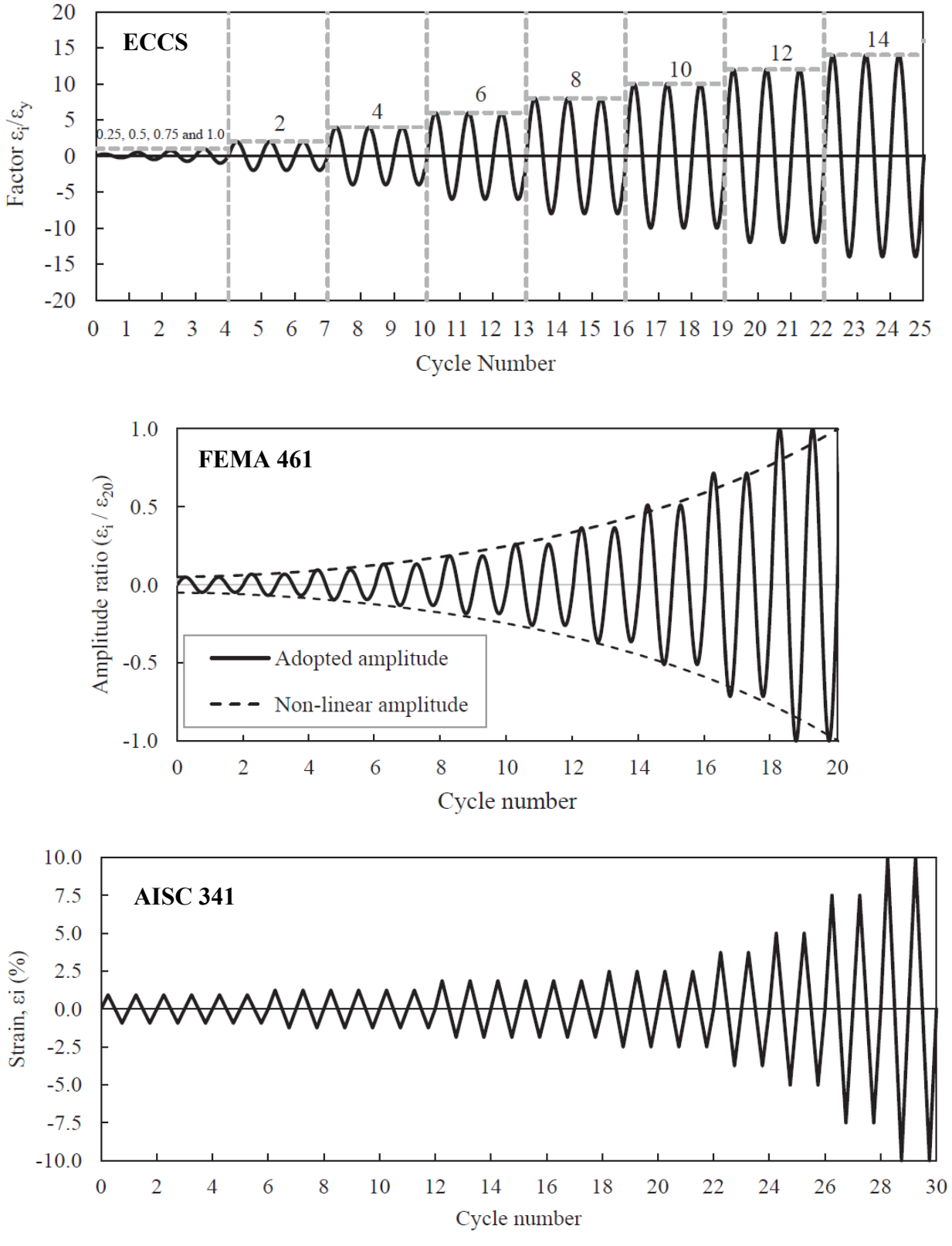

Figure 2.3 Various loading protocols

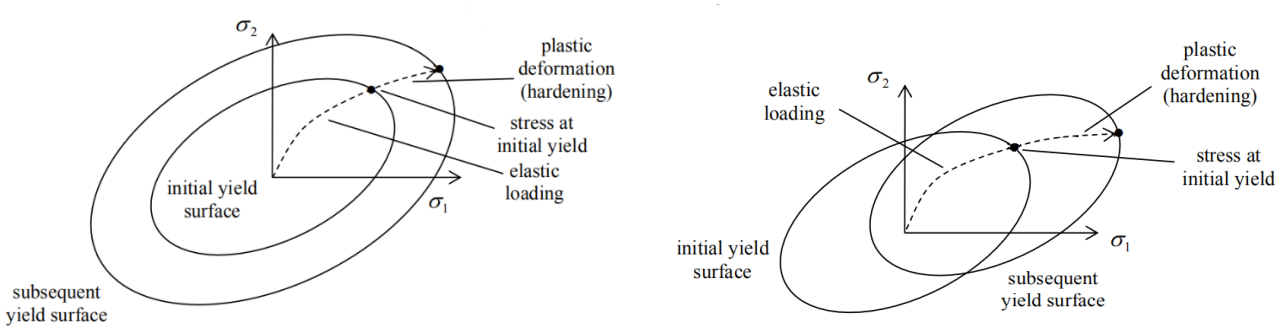

a) Isotropic hardening b) Kinematic hardening

Figure 2.4 Yield surface change

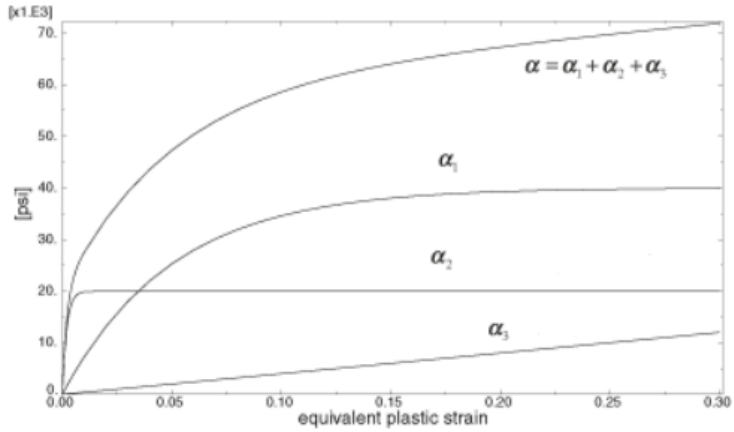

Figure 2.5 Nonlinear kinematic hardening model with three back stresses

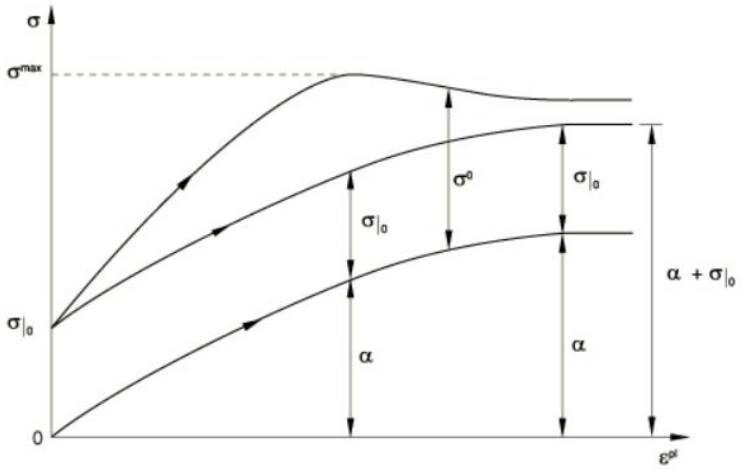

Figure 2.6 Combined hardening model

CHAPTER 3 HIGH STRENGTH STEEL AND THEIR WELDED SECTIONS UNDER MONOTONIC TESTS

3.1 Introduction

This chapter presents material properties of various materials which are examined and reported in subsequent chapters. In this project, various steel materials were manufactured into coupon specimens with specific shapes and T-joints for different types of experimental investigations. The results of these experiments were adopted into corresponding complementary numerical simulations for verification and parametric studies.

In this chapter, standard tensile tests on various steel materials were conducted to investigate the mechanical properties of these materials. For S355 steel, coupons of the base metal and their welded sections with three values of heat input energy (i.e., 1.0 kJ/mm, 1.5 kJ/mm, and 2.0 kJ/mm) were tested and compared. For S690 steel, steel materials from two different manufacturers (i.e., Nangang and Shougang) were tested for comparison, and coupons of the base metal and their welded sections with three values of heat input energy (i.e., 1.0 kJ/mm, 1.5 kJ/mm, and 2.0 kJ/mm) were tested. For S960 steel, coupons of the base metal and their welded sections with three values of heat input energy (i.e., 1.0 kJ/mm, 1.5 kJ/mm, and 2.0 kJ/mm) were tested for comparison.

In addition, monotonic tensile tests were conducted on funnel-shaped coupons manufactured from the S355 base metal, the S690 base metal, and their welded sections to investigate differences in the mechanical properties when compared with those of standard cylindrical-shaped coupons.

3.2 Testing method

3.2.1 Preparation work before tests

A) Delivery condition

The chemical compositions and typical carbon equivalent value (CEV) of each steel are listed in Table 3.1. It should be noted that all steel plates from the same test programme are from the same batch, and they all satisfy the upper limit requirements of the chemical compositions and CEV given in EN 10025-6:2019+A1:2022 (CEN, 2022).

B) Details of welding

The steel plates of various steels were welded together in pairs by multi-pass gas metal arc welding (GMAW). In this project, effects on welding were examined through a systematic comparison on the mechanical properties of the coupons of these welded sections with different values of heat input energy. Therefore, parameters including voltage, current and welding speed were preset, and strictly controlled during the welding process in order to achieve specified heat input energy in the welded sections. The linear heat input energy is calculated as follows:

$$q = \eta \cdot U \cdot I / v \qquad \text{Equation 3.1}$$

where

q is the linear heat input energy (kJ/mm);

η is the efficiency of welding, normally taken 0.80 ~ 0.90 for GMAW;

U is the welding voltage (V);

I is the welding current (A); and

v is the welding speed (mm/s).

There are three types of weld joints, i.e. i) a square shape, ii) a trapezoidal shape, and iii) a single-V shape. The use of the square shape and the trapezoidal shape allows the heat-affected

zones to penetrate the entire critical cross-sections of the coupons while the use of the single-V shape allows the heat affected zones to be located in the middle of the gauge length of the coupons. Details of multi-pass GMAW and these three types of weld joints are illustrated in Figure 3.1.

C) Inspection of weld joints

After welding, ultrasonic testing was carried out on the welded sections to check for any defect. This is one of the most commonly used non-destructive testing (NDT) methods. Defective areas of the welded sections were identified so that they should not be used for preparation of coupons. The procedure of ultrasonic testing is illustrated in Figure 3.2.

D) Specimen machining

Welded sections were then cut into strips for preparation of coupons through machining. All machining was performed with a computer numerical control (CNC) machine. It ensures that all the vertical sides of the square and the trapezoidal welds were precisely positioned at the mid-length of the gauges of the coupons. The manufacturing details are illustrated in Figure 3.3. Both the shapes and the dimensions of these coupons are designed in accordance with EN 6892-1:2019 (CEN, 2019). The dimensions of the coupons are shown in Figure 3.4.

3.2.2 Testing procedures of monotonic tensile test

The monotonic tensile tests were conducted on a servo hydraulic fatigue testing system Instron 8803. Displacement-controlled mode was chosen for these monotonic tensile tests due to a steady control of straining rates.

In each test, an extensometer was mounted onto the coupon to measure its elongations in order

to control the straining rates. A slow straining rate of 0.05% per minute was adopted before yielding to acquire a stable elastic range of the test. After yielding, the straining rate was increased to 0.3% per minute, and then to 0.5% per minute after necking of the coupon till the end of the test. It should be noted that these straining rates satisfy the requirements stipulated in EN 6892-1:2019. Specification of the extensometer is listed in Table 3.2.

A high resolution camera was set still in front of the testing system, and photos were taken at 30-second intervals throughout each test. The whole test setup is shown in Figure 3.5, and the test programme of all these monotonic tensile tests are summarized in Table 3.3.

3.2.3 Data processing after monotonic tensile test

A) Cylindrical-shaped coupons

Engineering stresses are calculated with the measured applied forces based on the measured diameters of the undeformed coupons while engineering strains are calculated with the measured elongations based on the measured gauge lengths of the undeformed coupons.

Before necking, the elongations of the coupons measured by the extensometer is assumed to take place evenly. Hence, both the true stresses and the true strains can be calculated by the integral method (Bridgman, 1952; Ling, 1996). The relationships between the engineering stress and strain, and the true stress and strain are given as follows:

$$\varepsilon_t = \ln (1+\varepsilon_e) \qquad \text{Equation 3.2}$$

$$\sigma_t = \sigma_e (1+\varepsilon_e) \qquad \text{Equation 3.3}$$

where

ε_e is the engineering strain;

ε_t is the true strain;

σ_e is the engineering stress; and

σ_t is the true stress.

However, Equation 3.2 and 3.3 are not applicable after necking takes place in the coupon because the diameter at the critical cross-section of the necking region is progressively reduced, and thus, the corresponding plastic deformation is no longer uniform. As shown in those photos taken every 30 seconds throughout the test, the diameters of instantaneous minimum cross-sections can be measured by counting its pixels appeared in the photos. At the onset of necking, the true stress and the true strain can be calculated as follows:

$$\varepsilon_t = \ln (A_0 / A_i) \qquad \text{Equation 3.4}$$

$$\sigma_t = P_i / A_i \qquad \text{Equation 3.5}$$

where

A_0 is the undeformed cross-sectional area;

A_i is the measured instantaneous minimum cross-sectional area; and

P_i is the applied load corresponding to A_i.

A comparison between the engineering stress-strain curve and the true stress-strain curve is plotted in Figure 3.6.

B) Funnel-shaped coupons

It should be noted that in this chapter, only the engineering mechanical properties of the funnel-shaped coupons are compared with those of the cylindrical-shaped coupons. Similar to the cylindrical-shaped coupons, both the engineering stress and strain of the funnel-shaped coupons can be obtained easily. However, due to complexity of the internal stress state, the true strain cannot be obtained with Equation 3.4. The true stress-strain curves of these funnel-shaped coupons can be obtained and justified using finite element simulations in Abaqus (2020).

3.3 Experimental results of monotonic tensile tests

Key mechanical properties of these steels including the Young's modulus E, the 0.2% proof strength f_y, the tensile strength f_u, the engineering strain at fracture ε_L, and the tensile to yield strength ratio f_u / f_y are summarized in Table 3.4.

The engineering stress-strain curves of various steel materials are plotted in Figure 3.7.

Typical deformations at fracture of both the cylindrical-shaped and the funnel-shaped coupons are shown in Figure 3.8, and these are considered to be typical cup and cone failure with good ductility at large deformations.

3.4 Conclusions

A total of 33 monotonic tensile tests were completed successfully on coupons of various steel plates and their welded sections. It is shown that:

All S355 coupons are able to achieve the elongation over 20% at fracture, which is considerably greater than the required value of 15% as stipulated in EN 1993-1-1:2005+A1:2014 (CEN, 2014). It is also found that the S355 welded sections with q = 1.0 kJ/mm and 1.5 kJ/mm show nearly no reduction in f_y and f_u, when compared to those of the base plates, and only a small reduction of 5% with q = 2.0 kJ/mm. This indicates that welding with small heat input energy does not significantly affect both the strength and the ductility of the S355 steel.

For those S690 coupons manufactured from the 16 mm thick steel plate, they satisfy the requirement of the elongation at fracture, ε_L, at 10% as stipulated in EN 1993-1-12:2007 (CEN, 2007). However, welding has a noticeable effect on their mechanical properties. The strength

reduction becomes more pronounced as the heat input energy increases. The funnel-shaped coupons show better strength and ductility than the cylindrical-shaped coupons.

For those S690 coupons cut from the 50 mm thick steel plate, they satisfy the requirement of the elongation at fracture, ε_L, as stipulated in EN 1993-1-12:2007. It is worth noting that they have better ductility, but larger strength reduction after welding, when compared to those of the 16 mm thick S690 steel plates.

For those S960 coupons, though their elongation at fracture, ε_L, satisfy the requirement stipulated in EN 1993-1-12:2007, significant reduction in the yield strengths in their welded sections are found, and some of them are less than the nominal value. One possible reason for this is the use of the undermatch welding wires.

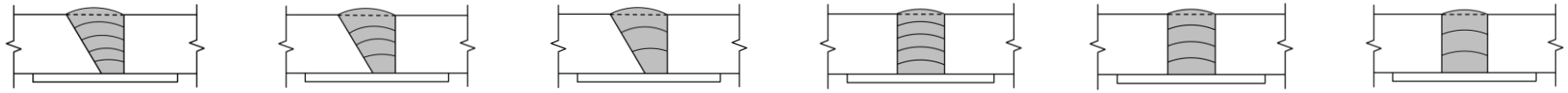

Trapezoidal weld joint with 5 passes @1.0 kJ/mm

Trapezoidal weld joint with 4 passes @1.5 kJ/mm

Trapezoidal weld joint with 3 passes @2.0 kJ/mm

Square weld joint with 5 passes @1.0 kJ/mm

Square weld joint with 4 passes @1.5 kJ/mm

Square welding joint with 3 passes @1.0 kJ/mm

S355 welded sections with t = 16 mm

S690 welded sections with t = 16 mm

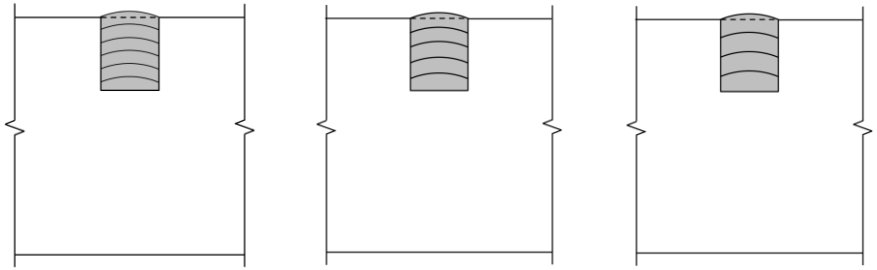

Square weld joint with 6 passes @1.0 kJ/mm

Square weld joint with 5 passes @1.5 kJ/mm

Square weld joint with 4 passes @2.0 kJ/mm

S690 welded sections with t = 50 mm

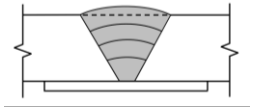

Single-V weld joint with 4 passes @1.0, 1.5 & 2.0 kJ/mm

S960 welded sections with t = 15 mm

Figure 3.1 Details of multi-pass GMAW and weld joints

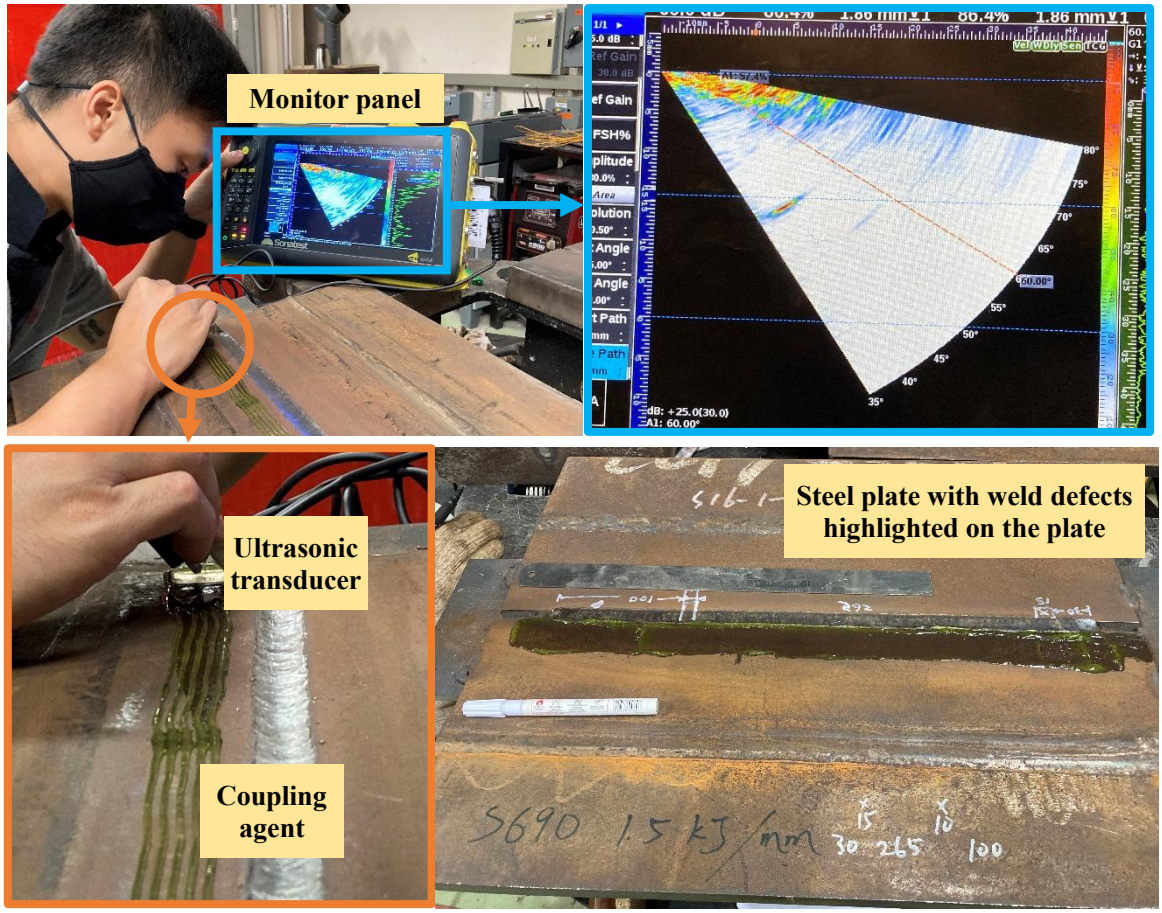

Figure 3.2 Procedure of ultrasonic testing

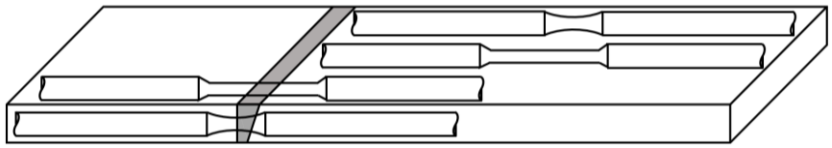

S355 welded sections with t = 16 mm

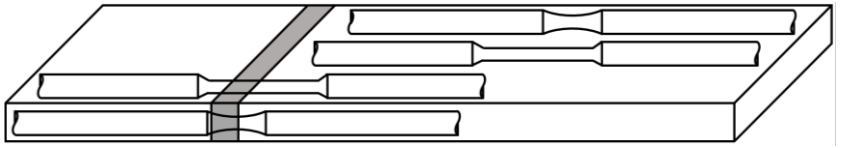

S690 welded sections with t = 16 mm

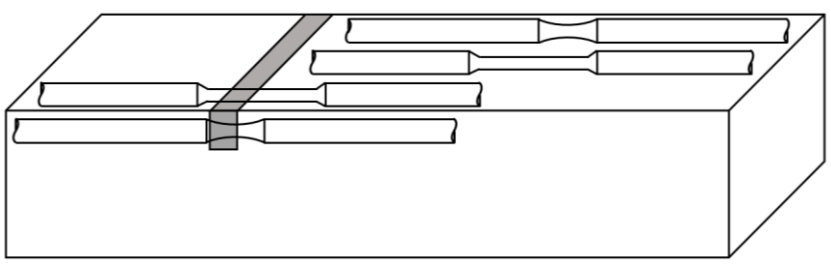

S690 welded sections with t = 50 mm

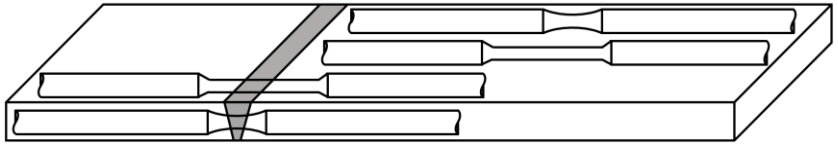

S960 welded sections with t = 15 mm

Figure 3.3 Manufacturing details of coupon specimens

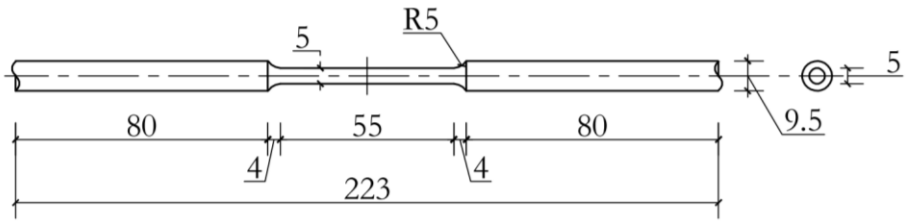

a) Cylindrical-shaped coupon of base metal

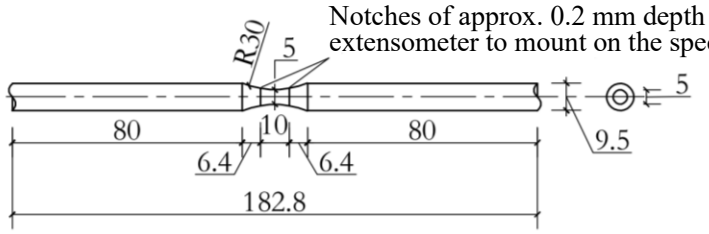

b) Funnel-shaped coupon of base metal

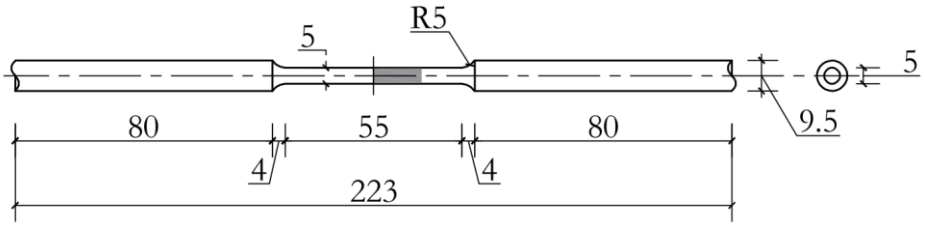

c) Cylindrical-shaped coupon of welded sections

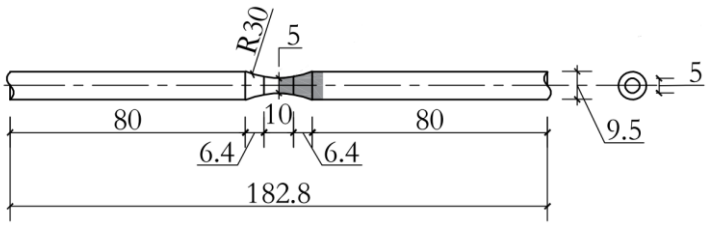

d) Funnel-shaped coupon of welded sections

Figure 3.4 Dimensions of coupons

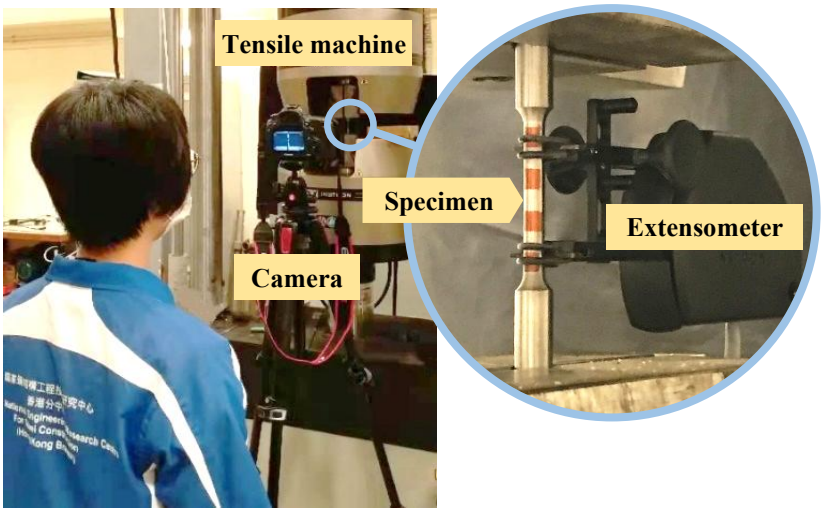

Figure 3.5 Test setup of monotonic tensile test

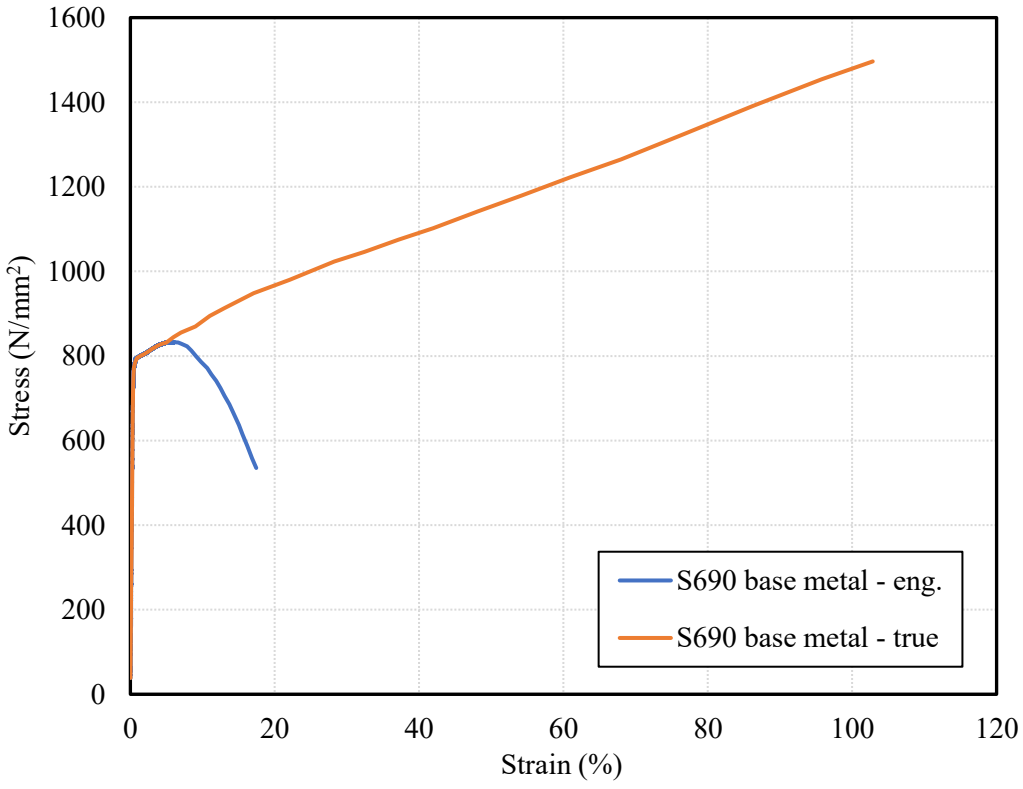

Figure 3.6 Comparison between engineering stress-strain and true stress-strain

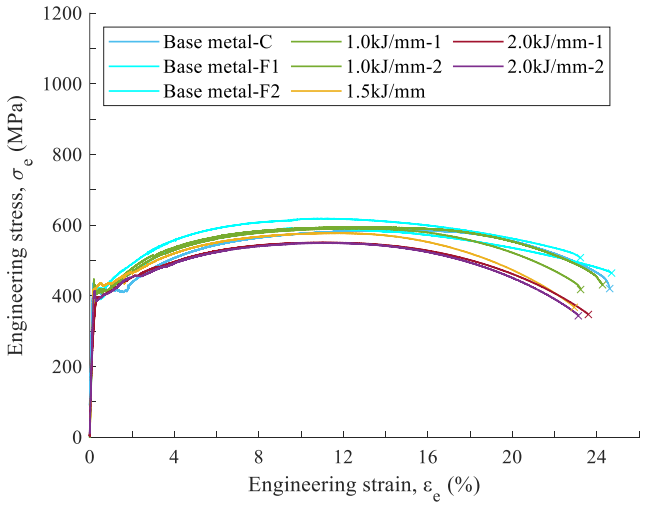

a) S355

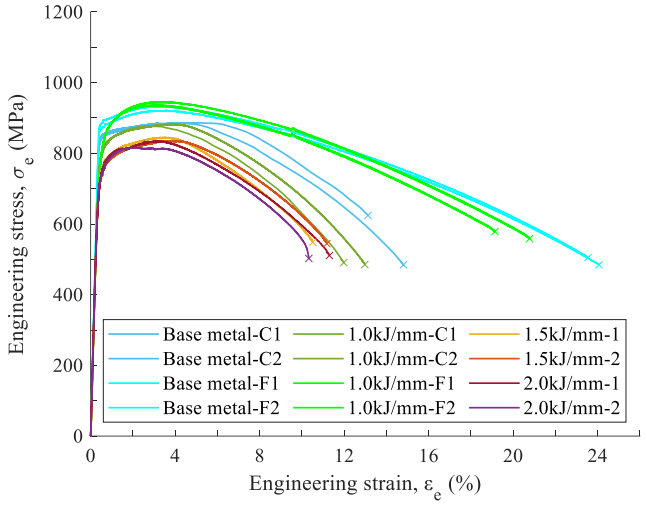

b) S690 (Nangang)

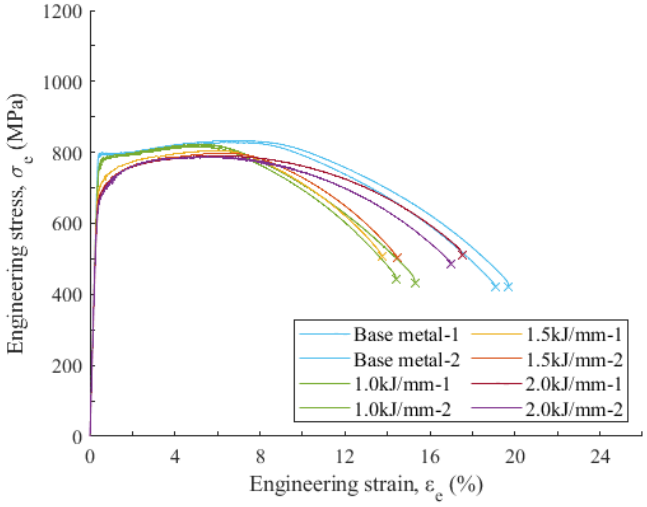

c) S690 (Shougang)

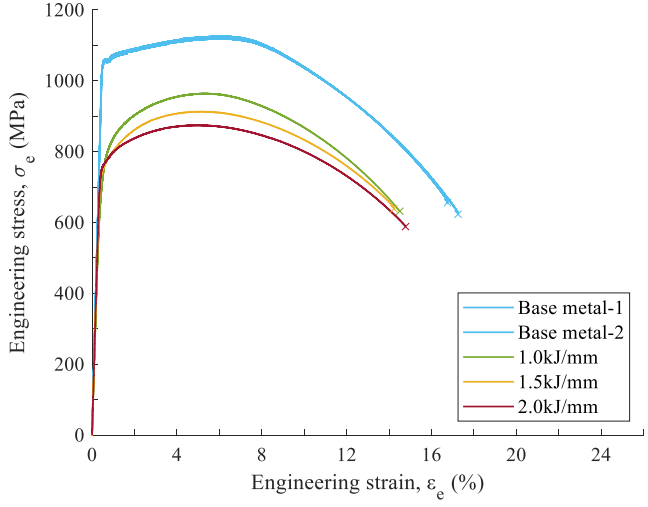

d) S960

Figure 3.7 Engineering stress-strain curves

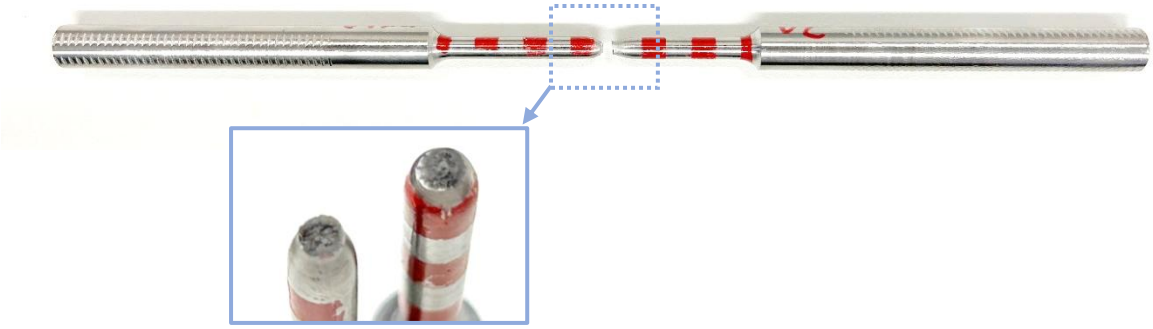

a) Typical deformation of a cylindrical-shaped coupon at fracture

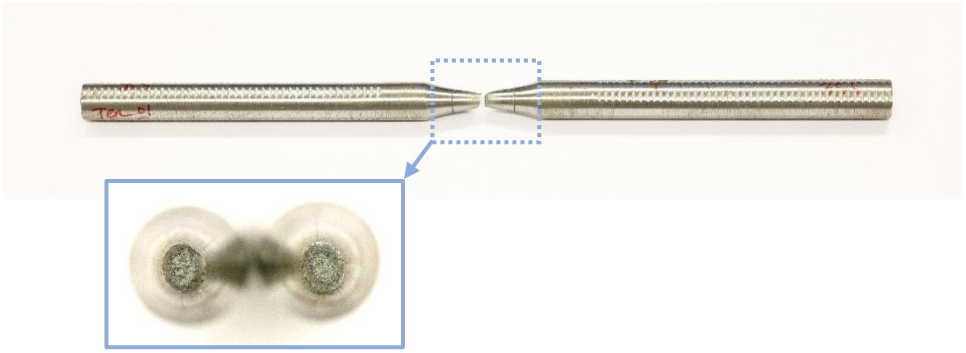

b) Typical deformation of a funnel-shaped coupon at fracture

Figure 3.8 Failed coupons after monotonic tensile tests

Table 3.1 Chemical compositions and CEV of various steel plates

Steel plate	Chemical composition (wt %)														
	C	**Si**	**Mn**	**P**	**S**	**B**	**Cr**	**Cu**	**Mo**	**Nb**	**Ni**	**Al**	**Ti**	**V**	**CEV**
S355 16 mm plate	0.154	0.3	1.15	0.019	0.006	-	0.35	0.01	0.002	0.014	0.01	0.043	0.023	0.001	0.42
S690 16 mm plate	0.13	0.25	1.38	0.010	0.001	-	0.28	0.47	0.24	-	0.04	-	-	-	0.50
S690 50 mm plate	0.076	0.08	1.23	0.011	0.0025	0.0016	0.306	0.186	0.41	0.013	0.905	-	0.017	0.046	0.47
S960 15 mm plate	0.17	0.25	1.03	0.01	0.002	0.0015	0.43	0.01	0.579	-	-	-	-	-	0.55

Table 3.2 Specification of the extensometer

Coupon type	Gauge length (mm)	Travel range (mm)	Strain range (%)
C	25.00	0 ~ +12.50	0 ~ +50
F	10.00	-1.00 ~ +1.00	-10 ~ +10

Notes:
"C" denotes a cylindrical-shaped coupon; "F" denotes a funnel-shaped coupon, and
"+" denotes tension; "-" denotes compression.

Table 3.3 Test programme of monotonic tensile tests

Steel grade	Thickness of steel plates (mm)	Heat input energy q (kJ/mm)	Nos of test
S355	16	-	1 C + 2 F
		1.0	2 C
		1.5	1 C
		2.0	2 C
S690 (Nangang)	16	-	2 C + 2 F
		1.0	2 C + 2 F
		1.5	2 C
		2.0	2 C
S690 (Shougang)	50	-	2 C
		1.0	2 C
		1.5	2 C
		2.0	2 C
S960	15	-	2 C
		1.0	1 C
		1.5	1 C
		2.0	1 C

Notes: “C” denotes a cylindrical-shaped coupon, and “F” denotes a funnel-shaped coupon.

Table 3.4 Mechanical properties of various steel materials

a) S355

Coupons	Coupon type	Heat input energy q (kJ/mm)	E (kN/mm^2)	f_y (N/mm^2)	f_u (N/mm^2)	ε_L (%)	f_u/f_y
S355-0.0-C1	C	-	223	414	586	24.6	1.42
S355-0.0-F1	F	-	216	391	592	24.7	1.51
S355-0.0-F1	F	-	223	422	619	23.2	1.47
S355-1.0-1	C	1.0	218	414	595	24.3	1.44
S355-1.0-2	C	1.0	227	409	591	23.2	1.45
S355-1.5-1	C	1.5	218	429	578	22.9	1.35
S355-2.0-1	C	2.0	201	395	552	23.6	1.40
S355-2.0-2	C	2.0	227	388	550	23.1	1.42

Notes: Plate thickness = 16 mm, and “C” denotes a cylindrical-shaped coupon; “F” denotes a funnel-shaped coupon.

b) S690 (Nangang)

Coupons	Coupon type	Heat input energy q (kJ/mm)	E (kN/mm^2)	f_y (N/mm^2)	f_u (N/mm^2)	ε_L (%)	f_u/f_y
S690-0.0-1C	C	-	230	853	885	14.8	1.04
S690-0.0-2C	C	-	228	849	886	13.1	1.04
S690-0.0-1F	F	-	232	873	922	24.1	1.06
S690-0.0-2F	F	-	226	895	933	23.5	1.04
S690-1.0-1C	C	1.0	217	805	882	13.0	1.10
S690-1.0-2C	C	1.0	217	813	876	12.0	1.08
S690-1.0-1F	F	1.0	208	831	936	19.1	1.13
S690-1.0-2F	F	1.0	214	825	946	20.8	1.15
S690-1.5-1	C	1.5	214	761	845	10.5	1.11
S690-1.5-2	C	1.5	215	744	836	11.2	1.12
S690-2.0-1	C	2.0	214	753	834	11.3	1.11
S690-2.0-2	C	2.0	215	744	816	10.3	1.10

Notes: Plate thickness = 16 mm, and “C” denotes a cylindrical-shaped coupon; “F” denotes a funnel-shaped coupon.

c) S690 (Shougang)

Coupons	Coupon type	Heat input energy q (kJ/mm)	E (kN/mm^2)	f_y (N/mm^2)	f_u (N/mm^2)	ε_L (%)	f_u/f_y
S690-0.0-1	C	-	206	793	829	19.1	1.05
S690-0.0-2	C	-	215	800	834	19.7	1.04
S690-1.0-1	C	1.0	209	775	817	14.4	1.05
S690-1.0-2	C	1.0	213	781	823	15.3	1.05
S690-1.5-1	C	1.5	202	716	806	13.8	1.13
S690-1.5-2	C	1.5	201	690	798	14.5	1.16
S690-2.0-1	C	2.0	208	686	792	17.5	1.15
S690-2.0-2	C	2.0	203	676	789	17.0	1.17

Notes: Plate thickness = 50 mm, and "C" denotes a cylindrical-shaped coupon.

d) S960

Coupons	Coupon type	Heat input energy q (kJ/mm)	E (kN/mm^2)	f_y (N/mm^2)	f_u (N/mm^2)	ε_L (%)	f_u/f_y
S960-0.0-1	C	-	225	1061	1126	16.8	1.06
S960-0.0-2	C	-	228	1053	1120	17.3	1.06
S960-1.0	C	1.0	196	764	964	14.5	1.26
S960-1.5	C	1.5	204	760	913	14.2	1.20
S960-2.0	C	2.0	208	764	875	14.8	1.14

Notes: Plate thickness = 15 mm, and "C" denotes a cylindrical-shaped coupon.

CHAPTER 4 HIGH STRENGTH STEEL AND THEIR WELDED SECTIONS UNDER CYCLIC TESTS

4.1 Introduction

Welding is widely used in steel structures, especially in their connections and joints. However, welding has been found to have a detrimental effect on the mechanical properties of the high strength steel. Therefore, it is necessary to examine and evaluate the performance of these high strength steel plates and their welded sections under large cyclic actions

It should be noted that Chapter 3 presents the mechanical properties, in particular the ductility, of these high strength steels under the requirements of current codes and standards. However, these requirements are limited to the results of monotonic tensile tests. There is a lack of understanding and engineering data on hysteretic properties of these high strength steel plates and their welded sections.

In order to carry out a systematic and comprehensive experimental investigation into the hysteretic properties of these high strength steel plates and their welded sections, a total of 154 cyclic tests were conducted on the funnel-shaped coupons of S355, S690, and S960 base metals, and their welded sections with different values of heat input energy. Ductility and energy dissipation capacity are carefully examined and compared among these steels. Various criteria to evaluate their hysteretic properties under large cyclic actions at the material level are proposed based on the results obtained from these cyclic tests.

4.2 Limitations of current codes and standards

To ensure that steel structures are safe and effective, various ductility requirements are specified in current codes and standards. These requirements are mainly for strengths and elongations at the material level (BD, 2023; CEN, 2007, 2014, 2022; SAMR and SAC, 2018), and for inter-

storey drifts and energy dissipation capacities at the structural level (BD, 2023; CEN, 2013; MOHURD and AQSIQ 2016, 2017). However, these requirements are primarily based on monotonic tensile test results, and many research works have shown that the high strength steel behave differently under cyclic actions (Ho et al., 2018; Wang et al., 2017).

Many current codes and standards include fatigue design for structural members, and yet, these design rules are limited to low strain/high cycle fatigue (HCF) with small deformations, but large numbers of cycles to failure (BD, 2023; CEN, 2005; MOHURD and AQSIQ, 2016, 2017). These design rules are not adequate for high strain/low cycle fatigue (LCF) analyses, which have large deformations and small numbers of cycles to failure. There is also a lack of technical guidance on the energy dissipation capacities at the material level based on the cyclic test results, and this is often considered to be an important criterion for quantifying ductility in seismic design. As welding is often used in steel structures as well as their connections and joints which are critical energy dissipation zones, and these connections and joints are prone to fail with brittle fracture at their heat affected zones under large cyclic actions. Thus, the energy dissipation capacities of these welded sections are also crucial.

4.2.1 Strengths and elongations at failure

Many codes and standards have detailed requirements for the strength and elongation at failure of various steel materials, from normal grade steel to high strength steel with the nominal yield strengths up to 700 N/mm^2 (BD, 2023; CEN, 2007, 2014, 2022; SAMR and SAC, 2018).

4.2.2 Inter-storey drifts

Limits on inter-storey drifts are required by most codes and standards (BD, 2023; CEN, 2013; MOHURD and AQSIQ 2016, 2017). It should be noted that two limit states are proposed,

namely i) elastic state, or serviceability limit state and ii) elasto-plastic state, or ultimate limit state under the rare earthquake. In the China Standard for Design of Steel Structures GB 50017-2017 (MOHURD and AQSIQ, 2017), the inter-storey drifts regarding the two limit states are called i) elastic storey drift, and ii) elasto-plastic storey drift.

4.2.3 Design for fatigue

There is extensive technical guidance on fatigue design in many codes and standards, ranging from members to connections (BD, 2023; CEN, 2005; MOHURD and AQSIQ, 2016, 2017). However, these design rules are limited to the HCF, where structures are under elastic deformations, whereas those for LCF are under elasto-plastic deformations. Furthermore, the methods for evaluation of a HCF test, i.e. S-N curves and Miner's summation, are not suitable for a LCF test. It is necessary to propose technical guidance for the design of LCF and complementary methods for evaluation of LCF tests.

4.2.4 Energy dissipation capacities

The energy dissipation capacity of a structure is always critical in seismic design. Therefore, many codes and standards provide various design rules to ensure that both the members and the whole structures have good energy dissipation capacities (CEN, 2013; MOHURD and AQSIQ, 2016). It should be noted that in EN 1998-1:2004+A1:2013 (CEN, 2013), a behaviour factor, q, is introduced to reduce design forces in a structure obtained from linear analysis. It is an approximation of the force ratio, taking into account the energy dissipation capacity of the structure according to its ductility. The purpose of using the behaviour factor is to achieve a balance between the design resistance and the design force so that its non-linear response is to be exploited. As the behaviour factor is based on the ductility of the whole structure or system, it is difficult to compare directly the energy dissipation capacities of the members at the material

level. Therefore, there is a strong need to propose a new set of criteria to evaluate the energy dissipation capacities of steel members as well as their connections and joints at the material level.

4.3 Testing method

4.3.1 Design of coupon and test setup

Based on previous research work for structural responses of steel structures under seismic actions, for a steel plate with a thickness of 6 to 16 mm, the heat input energy q at 1.0 kJ/mm has little effects on the mechanical properties while q at 2.0 kJ/mm causes some significant reductions in both strength and ductility. In order to investigate the hysteretic properties of various steel and the adverse effects of welding on their heat affected zones, a systematic and comprehensive test programme of cyclic tests on coupons of S355, S690, and S960 base metal and their welded sections with heat input energy of i) 1.0 kJ/mm, ii) 1.5 kJ/mm, and iii) 2.0 kJ/mm was carried out. For the preparation work before tests including i) the delivery condition of steel plates, ii) the welding process, iii) the inspection of the weld joints, and iv) the machining of the specimens, refer to Chapter 3.2.1.

The funnel-shaped coupons are specifically designed for cyclic tests, and they are deemed appropriate for strain amplitudes ranging from 5-10%. The gauge lengths of these coupons may exhibit buckling when subjected to significant axial shortenings. In the coupons of S355 and S690 welded sections, the mid-lengths of the coupons are the heat affected zones, and hence the critical cross sections of these coupons are the heat affected zones. It should be noted that matching electrodes for S960 are somehow not easily available. Therefore, undermatching electrodes are used in practice. For those coupons of S960 welded sections, the single-V weld joints are located at the mid-length of the coupons, as shown in Figure 3.3. This means that the

critical cross sections are weld metals rather than the heat affected zones, and their test results reflect the hysteretic behaviour of the entire welded sections rather than that of the heat affected zones.

The setup of the cyclic tests is the same as that of the monotonic tensile tests, except that only a dynamic extensometer with a 10 mm gauge length was used. A high resolution digital camera was used to record videos throughout the tests to monitor the deformation of the coupons under large cyclic actions. Refer to Table 3.2 for technical specification of the dynamic extensometer.

4.3.2 Loading method

A) Loading protocol

All loading protocols for cyclic tests are broadly classified into two types, i.e. i) constant amplitudes, and ii) varying amplitudes. The loading protocols with constant amplitudes refer to application of constant stress or strain amplitudes in a cyclic test, whereas the loading protocols with varying amplitudes involves applications of various combinations of different stress and strain amplitudes. The most commonly used loading protocols with varying amplitudes are: i) Protocol I in FEMA 461 (FEMA, 2007) and ii) ECCS (ECCS, 1986).

The loading protocols given in FEMA 461 and ECCS are very similar to each other. Both of them start with a very low amplitude which are repeated for one or several cycles, and then the amplitudes are increased in a repeated manner till failure of the test specimen. It is worth noting that both FEMA 461 and ECCS present the loading protocol which may cause various types of damage in structures. Hence, the use of the loading protocol with gradually increasing amplitudes is applicable to those structures which undergo small deformations more often than large deformations that lead directly to failure. In addition, the accumulative effect of completed

cycles with small amplitudes will influence the assessment of the energy dissipation capacities of those structures to which large cyclic actions are present solely.

Previous research (Guo et al., 2020; Ho et al., 2018) found that all S690 coupons were able to complete at least 19 cycles in cyclic tests using the FEMA 461 loading protocol with target stain up to 10%. However, as these tests are incompatible to evaluate the performance of all these coupons at specific cyclic actions, and also difficult to compare them with each other. In order to investigate the hysteretic behaviour and cyclic performance of various steel, and to directly compare and evaluate their energy dissipation capacities under large cyclic actions, the loading protocol of constant strain amplitudes is adopted in this project. Typical loading protocol of constant strain amplitude is illustrated in Figure 4.1.

B) Target strain amplitude

Since the purpose of this study is to investigate the hysteretic properties of various steel under LCF, the target strain amplitude should be set within a practical range under seismic actions. The minimum target strain amplitude should be greater than the strain at the yield strength of the steel, which is approximately 0.3% to 0.4%, but close to the strain at their tensile strengths. Therefore, ±1.0% is selected as the minimum strain amplitude for the cyclic tests. In an analysis of a tubular steel column after a major earthquake in Japan, it was found that the maximum strain is about 10% under compression, with local buckling at the bottom of the column (JSCE, 2000). Therefore, ±10.0% is adopted as the maximum strain amplitude for the cyclic tests. Target strains at ±2.5%, ±5.0%, and ±7.5% are set between ±1.0% and ±10.0%, so that their hysteretic behaviour can be evaluated and compared over a wide range of target strain amplitudes.

C) Loading frequency

Typical dominant frequencies in seismic actions in South China range from 0.1 to 2.0 Hz, and previous research work show that both 0.1 and 1.0 Hz are sufficient. Therefore, two loading frequencies, i.e. i) 0.1 Hz, and ii) 1.0 Hz, are adopted in the cyclic tests to examine the influence of loading frequencies. The use of the displacement-controlled mode allows the straining rate to be steadily controlled.

4.3.3 Test programme of cyclic tests

A total of 154 cyclic tests on the coupons of S355, S690, and S960 base metal and their welded sections with different values of heat input energy, i.e. i) 1.0 kJ/mm, ii) 1.5 kJ/mm, and iii) 2.0 kJ/mm were carried out. Constant amplitudes with target strains at i) ±1.0 %, ii) ±2.5 %, iii) ±5.0 %, iv) ±7.5 %, and v) ±10.0 % under loading frequencies at i) 0.1 Hz and ii) 1.0 Hz are adopted for all these tests. Table 4.1 summarizes the test programme as described above. It should be noted that due to some defects in the welded S960 steel plates, the strain amplitudes for S960 welded sections vary only from ±2.5 % to ±10.0 %, and no coupons of these welded sections were tested under a strain amplitude at ±1.0 %.

4.4 Experimental investigation into cyclic tests on coupons of various steel

4.4.1 Determination on the number of completed cycles

Each test was manually stopped when the maximum tensile force fell under 1.0 kN. However, the numbers of the completed cycles at this point should not be taken as the test results of these cyclic tests, because both the maximum tensile and the maximum compressive forces are significantly different in each test. Therefore, a general criterion is proposed to determine the test results of these cyclic tests. Two strength factors, η_t and η_c are proposed to calculate reductions in the maximum tensile and the maximum compressive strengths in each cycle (Ho

et al., 2021). The equations are modified and shown as follows:

$$\eta_{t,i} = f_{ut,i} / f_{yt,1} \quad \text{Equation 4.1}$$

$$\eta_{c,i} = f_{uc,i} / f_{yt,1} \quad \text{Equation 4.2}$$

where

$\eta_{t,i}$ is the tensile strength factor for each cycle;

$\eta_{c,i}$ is the compressive strength factor for each cycle;

$f_{ut,i}$ is the maximum tensile strength in each cycle (kN/mm^2);

$f_{uc,i}$ is the maximum compressive strength in each cycle (kN/mm^2);

$f_{yt,1}$ is the yield strength in the 1st cycle (kN/mm^2).

The yield strengths of the 1st cycle are extracted from each test and summarised in Table 4.2. The strength factors η_t and η_c against the cycle number of each cyclic test are plotted in Figure 4.2 to 4.9. It is shown that both η_t and η_c decrease dramatically after falling below 0.8, which means that both the maximum tensile strength and the maximum compressive strength in each cycle begin to decrease rapidly. Therefore, 0.8 is taken as the threshold below which the coupon is considered to have failed, and the cycles completed at this point are taken as the number of cycles completed, n_c, of the test. The numbers of cycles completed for each test are summarised in Table 4.3.

4.4.2 Experimental observations of the cyclic tests

All 154 cyclic tests were completed successfully. The engineering stress-strain curves of all these tests are plotted in Figure 4.10 to 4.29. It should be noted that the curves in red demonstrate the completed cycles, n_c, of the tests before the force ratio is decreased to 0.8, while the curves in black are the cycles after the coupons are considered to have failed till the end of the tests. Typical failed coupons and their fractured surfaces are shown in Fig. 4.30.

They are found to be very different from those of the monotonic tensile tests illustrated in the Chapter 3. Observations on the cyclic test results are as follows:

A) S355 steels and their welded sections – Table 4.3 a) Figure 4.10 to 4.14

In the cyclic tests at target strains of ±1.0 %, ±2.5 %, and ±5.0 %, there are apparent reductions in the numbers of n_c for the S355 welded sections compared to those of the base metal. However, in the cyclic tests at target strains of ±7.5 % and ±10.0 %, there is no evidence of significant reductions in the numbers of n_c for the S355 welded sections compared to those of the base metal. This indicates that welding has little effect on the S355 steels.

Both the S355 base metal and its welded sections show small deteriorations in strength before failure. Moreover, the coupons were able to maintain a slow rate of strength degradation even after n_c at a target strain of ±1.0 %. However, for the cyclic tests at target strains of ±2.5 %, ±5.0 %, ±7.5 %, and ±10.0 %, the deterioration was significant after n_c, and the coupons fractured completely within one or a few cycles.

It is also found that a loading frequency has little effect on the test results. The numbers of n_c in the cyclic tests with a loading frequency of 0.1 Hz are very close to those with a loading frequency of 1.0 Hz. The shapes of the engineering stress-strain curves and the tendency of strength deterioration are also comparable.

B) S690 (Nangang) steels and their welded sections – Table 4.3 b) Figure 4.15 to 4.19

It is found that in the cyclic tests at a target strain of ±1.0 %, there are only small reductions in the numbers of n_c for the S690 (Nangang) welded sections when compared to those of the base metal. However, the reductions become obvious as the strain amplitudes increase. This means

that welding has a detrimental effect on the S690 (Nangang) steels, especially when their welded sections undergo large deformations.

The S690 (Nangang) base metal and its welded sections show slightly more pronounced deteriorations in strength than the S355 steels. In the cyclic tests at a target strain of ±1.0 %, the coupons were able to maintain a slow rate of strength degradation even after n_c, whereas those at target strains of ±2.5 %, ±5.0 %, ±7.5 %, and ±10.0 %, and they fractured completely within one or a few cycles after n_c.

Similar to that of S355 steels, the loading frequency has little effect on the test results of S690 (Nangang) steels. Both the shapes of the engineering stress-strain curves and the tendency of strength deterioration are comparable for the tests with a loading frequency of 0.1 Hz and 1.0 Hz.

C) S690 (Shougang) steels and their welded sections – Table 4.3 c) Figure 4.20 to 4.24

The test results of the S690 (Shougang) steels are very similar to those of the S690 (Nangang) steels. In the cyclic tests at a target strain of ±1.0 %, the S690 (Shougang) welded sections exhibit only minor decreases in the numbers of n_c compared to the base metal. While these reductions are more pronounced in those cyclic tests at target strains of ±2.5 %, ±5.0 %, ±7.5 %, and ±10.0 %. This is also consistent with the findings for S690 (Nangang) steels, where welding has an adverse effect on the S690 steels, and this effect becomes significant when the welded sections are subjected to large cyclic actions.

Overall, the S690 (Shougang) base metal and its welded sections exhibit slightly greater deteriorations in strength when compared to the S355 steels. In those cyclic tests with their

strain amplitude at ±1.0 %, the coupons display a gradual decrease in strength even after n_c, while for those subjected to strain amplitudes of ±2.5 %, ±5.0 %, ±7.5 %, and ±10.0 %, the coupons exhibit complete fracture within one or a few cycles after n_c.

It is found that the loading frequency has little effect on the test results of S690 (Shougang) steels, as both the shapes of the engineering stress-strain curves and the strength deterioration tendency are comparable for the two loading frequencies.

D) S960 steels and their welded sections – Table 4.3 d) Figure 4.25 to 4.29

In the cyclic tests with target strains of ±1.0 %, ±5.0 %, ±7.5 %, and ±10.0 %, the numbers of n_c for the S960 base metal are similar to those of the S690 steels. This means that the ductility of S960 base metal is comparable to that of the S690 steels. However, when comparing the number of n_c for S960 welded sections with those of the S960 base metal, significant reductions are found in all the cyclic tests with target strains of ±2.5 %, ±5.0 %, ±7.5 %, and ±10.0 %. This is similar to the test results for the S690 steels where welding affects the performance of the welded sections as they are subjected to large deformations.

Similar to the S690 steels, the S960 base metal and its welded sections show a slightly more pronounced deterioration in strength than the S355 steels. In the cyclic tests with a target strain of ±1.0%, the coupons show a gradual deterioration in strength up to the end of the tests, whereas the coupons subjected to strain amplitudes of ±2.5 %, ±5.0 %, ±7.5 % and ±10.0 % fracture within one or a few cycles after n_c.

Since both the shapes of the engineering stress-strain curves and the strength deterioration tendency are comparable for different loading frequencies, the loading frequency does not

affect the test results of the S960 steels.

4.4.3 Strain energy dissipation

In order to quantify and evaluate the energy dissipation performance of these base metals and their welded sections under cyclic actions, the total strain energy dissipation of each coupon is obtained from the engineering stress-strain curves of these cyclic tests. For ease of comparison, the hysteretic energy dissipation density, i.e. the energy dissipated per unit volume of steel, of each coupon at specific target strain amplitudes is also obtained.

It should be noted that the strain energy dissipation of each cycle is the area enclosed by the engineering stress-strain curve of the corresponding cycle. The total strain energy dissipation is therefore obtained by summing up the areas of all cycles in a cyclic test. The total strain energy dissipation of each test is summarised in Table 4.4, and they are plotted against different target strain amplitudes in Figure 4.31 to 4.35 for direct comparison. It is found that:

A) Target strain ε_T of ±1.0 %

At a target strain of ±1.0 %, the S355 base metal has larger energy dissipation capacities than those of the S690 and the S960 base metals, while the S355 welded sections and the S690 welded sections are comparable in the energy dissipation performance.

B) Target strain ε_T of ±2.5 %

At a target strain of ±2.5 %, the S355 base metal exhibits superior energy dissipation capacities, when compared to the S690 and the S960 base metals. The S355 and the S960 welded sections perform larger energy dissipation capacities than the S690 welded sections. It is evident that the energy dissipation capacities of these S355, S690 and S960 steels have been reduced

significantly by the welding process.

C) Target strain ε_T of ±5.0 %

At a target strain of ±5.0 %, the S690 and the S960 base metals show similar energy dissipation performance compared to the S355 base metal. However, all the welded sections have fairly good energy dissipation capabilities despite welding has a detrimental effect on their performance. Overall, this effect is less pronounced in the S355 welded sections than in the S690 and the S960 welded sections.

D) Target strain ε_T of ±7.5 %

At a target strain of ±7.5 %, the 690 and the S960 base metals have larger energy dissipation capacities than the S355 base metal, except for the S690 (Nangang and Shougang) base metals in the cyclic tests with a loading frequency of 0.1 Hz, which are only slightly lower than the S355 base metal. Surprisingly, the S355 welded sections perform as well as their base metal in terms of the energy dissipation. In addition, the S690 and the S960 welded sections also show excellent energy dissipation capacities, and the reduction in these capacities due to the welding process is less than that in the cyclic tests at target strains of ±2.5 % and ±5.0 %.

E) Target strain ε_T of ±10.0 %

At a target strain of ±10.0 %, the 690 and the S960 base metals have overall better energy dissipation capacities than the S355 base metal, despite in the cyclic test with a loading frequency of 0.1 Hz, the S690 (Shougang) base metal has lower energy dissipation capacities due to the completion of only 1 cycle. The S355 welded sections have excellent energy dissipation capacities as their base metal. It can be seen that welding may have little effect on the energy dissipation capacities for the S355 steels under very large cyclic loadings. However,

for the S690 and the S960 welded sections, the reductions in the energy dissipated are significant, but they still have good energy dissipation capacities under very large cyclic loadings.

4.5 Conclusions

This chapter presents a comprehensive experimental investigation of the hysteretic properties of various steel materials. Various requirements in current codes and practices regarding i) strength, ii) ductility, and iii) energy dissipation capacity, are discussed extensively, and their limitations in quantifying ductility in seismic design at the material level are explained.

In order to investigate the hysteretic properties of various steel materials and the adverse effects of welding on heat affected zones, a total of 154 cyclic tests were successfully completed on the funnel-shaped coupons of the S355, S690 (Nangang), S690 (Shougang), and S960 base metals and their welded sections with different values of heat input energy, i.e. i) 1.0 kJ/mm, ii) 1.5 kJ/mm, and iii) 2.0 kJ/mm. Constant amplitudes with target strains at i) ±1.0 %, ii) ±2.5 %, iii) ±5.0 %, iv) ±7.5 %, and v) ±10.0 % and loading frequencies at i) 0.1 Hz and ii) 1.0 Hz are adopted for the cyclic tests. The hysteretic properties are discussed in terms of i) number of cycles completed, ii) strength deterioration, and iii) total strain energy dissipation. It is found that:

All the coupons were able to perform steady deterioration in strength in the cyclic tests at a target strain of ±1.0 % and ±2.5 %. However, the coupons fractured completely within one or a few cycles after n_c as the target strains increase. It is found that the loading frequency has no effect on the test results. The typical fractured surfaces of the coupons after the cyclic tests are very different from those of the monotonic tensile tests.

Welding may have little effect on the energy dissipation capacity of the S355 steels under very large cyclic loadings (i.e. ±7.5 % and ±10.0 %), but it has an adverse effect on the hysteretic properties of the S355 steels in the cyclic tests at target strains of ±1.0 %, ±2.5 %, and ±5.0 %, resulting a reduction in the number of cycles completed. For both S690 (Nangang & Shougang) and S960 steels, reductions in both the number of completed cycles and the energy dissipation capacities are found in their welded sections. Despite the significant detrimental effect of welding on the S690 and the S960 steels, they still have good energy dissipation capacities in the cyclic tests at target strains of ±5.0 %, ±7.5 %, and ±10.0 %.

Welding techniques are now widely used in construction projects, particularly in the beam-to-column connections which are critical energy dissipation zones, and these connections are prone to fail with brittle fracture at the heat affected zones under large cyclic loadings. The quality of the welding therefore plays an important role in the overall seismic performance of the structure. In addition to the urgent need to propose a new set of criteria to evaluate the energy dissipation capacity of welded sections at the material level, it is equally important to regulate welding techniques and improve welding quality.

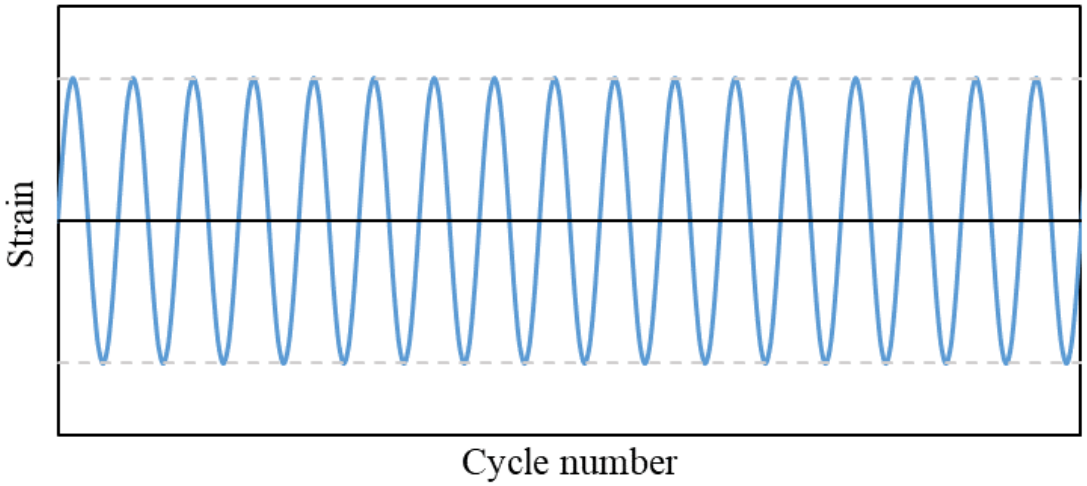

Figure 4.1 Loading protocol of constant strain amplitude

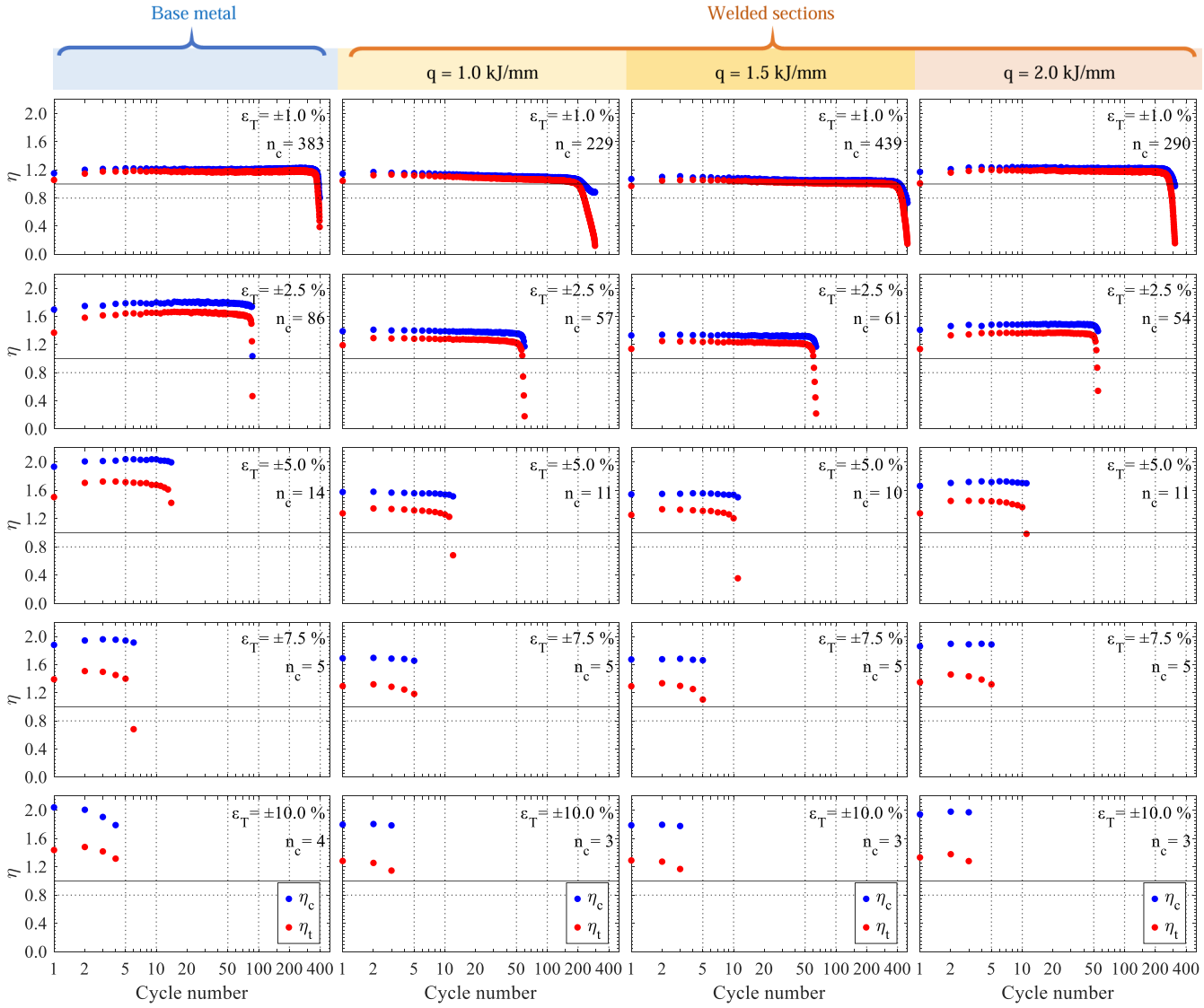

Figure 4.2 η_t and η_c of the cyclic tests on S355 with f = 0.1 Hz

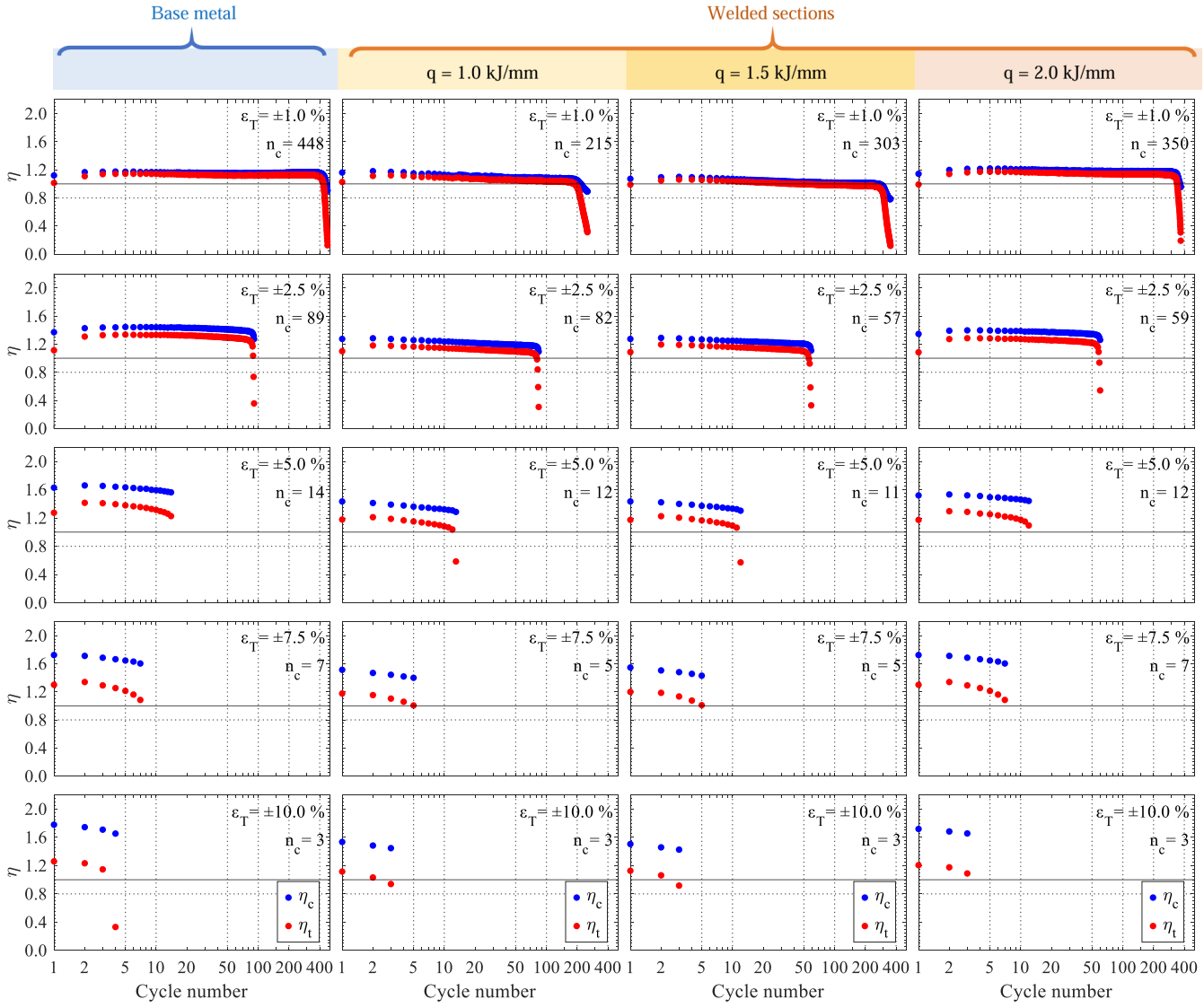

Figure 4.3 η_t and η_c of the cyclic tests on S355 with f = 1.0 Hz

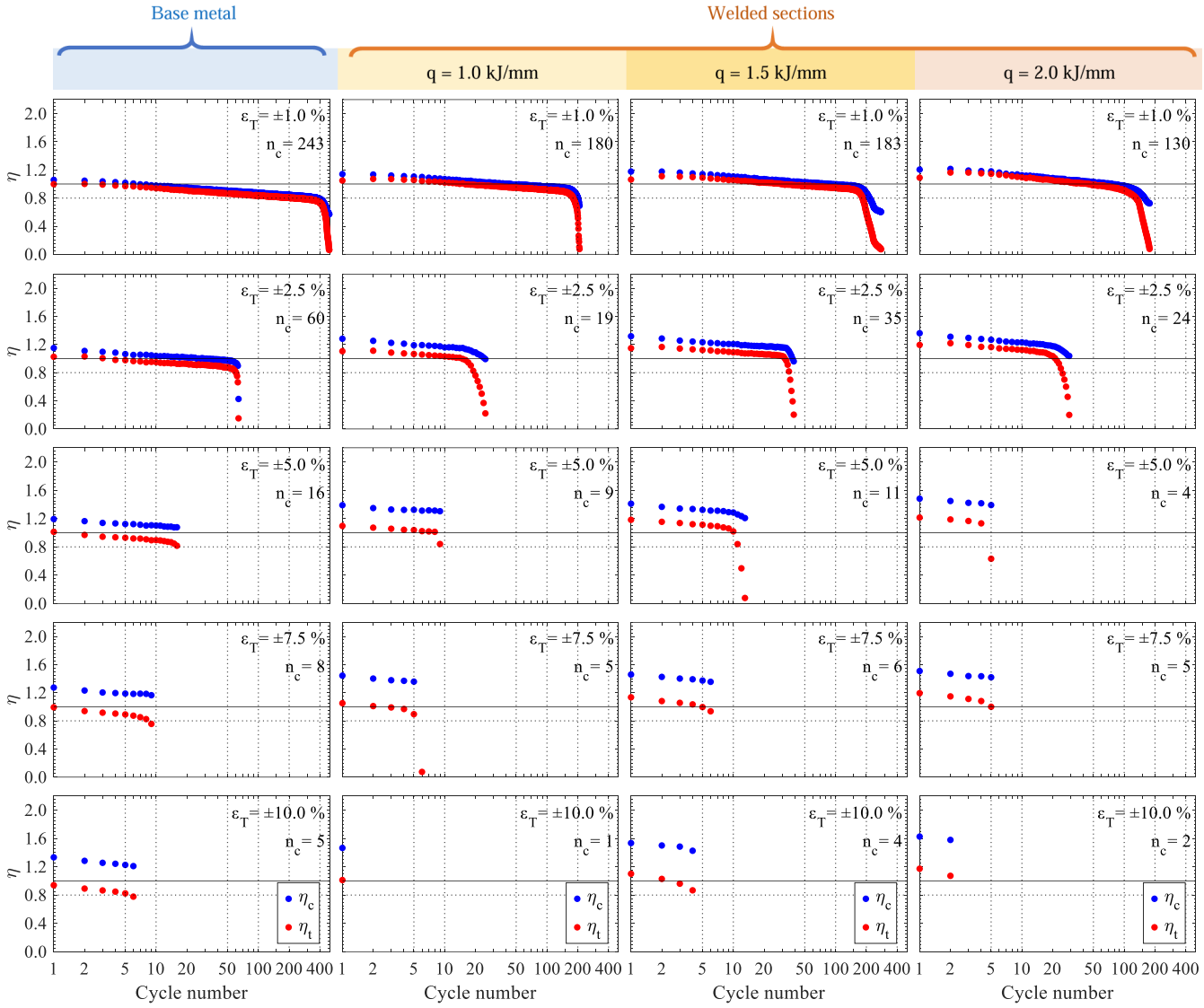

Figure 4.4 η_t and η_c of the cyclic tests on S690 (Nangang) with f = 0.1 Hz

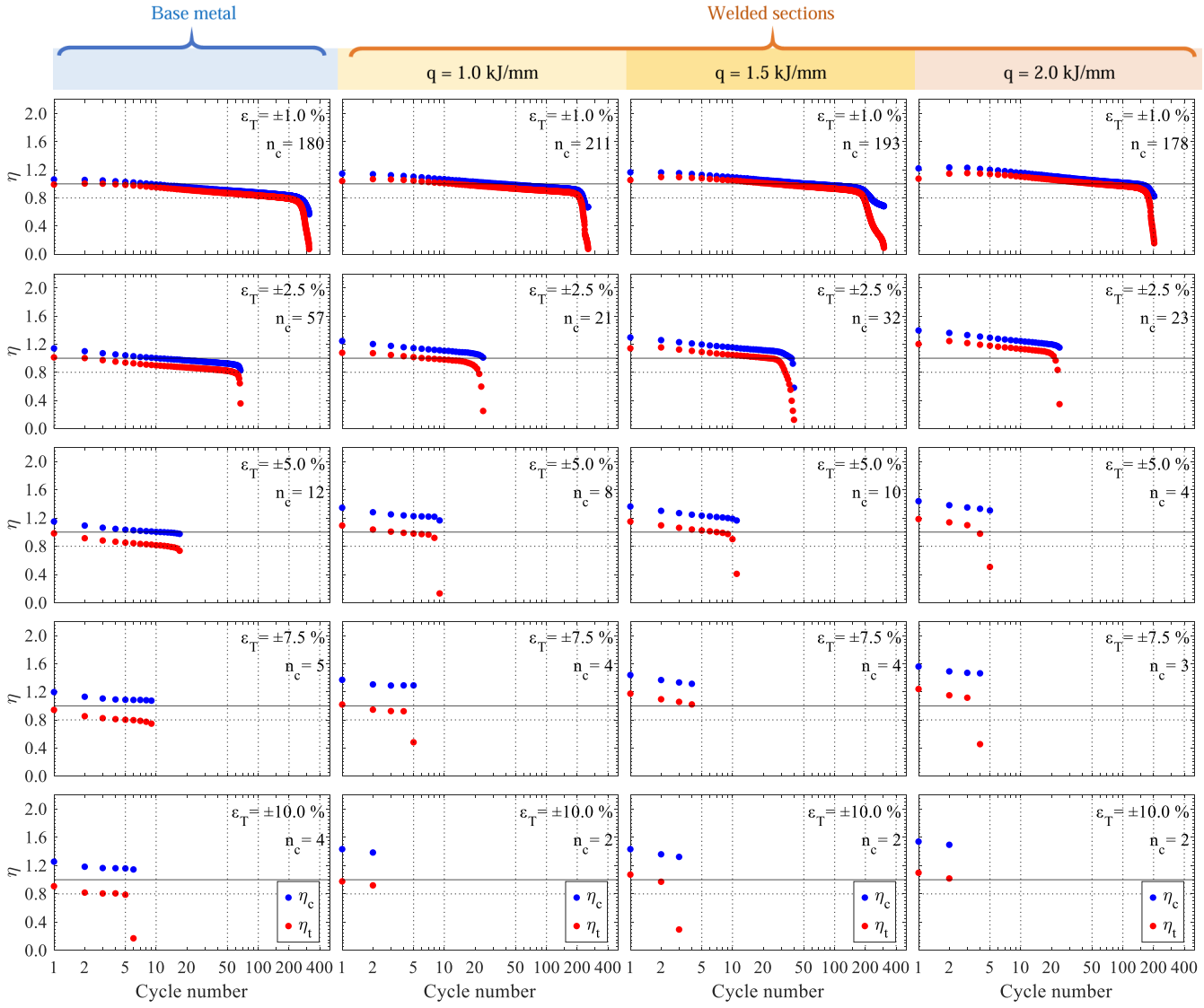

Figure 4.5 η_t and η_c of the cyclic tests on S690 (Nangang) with f = 1.0 Hz

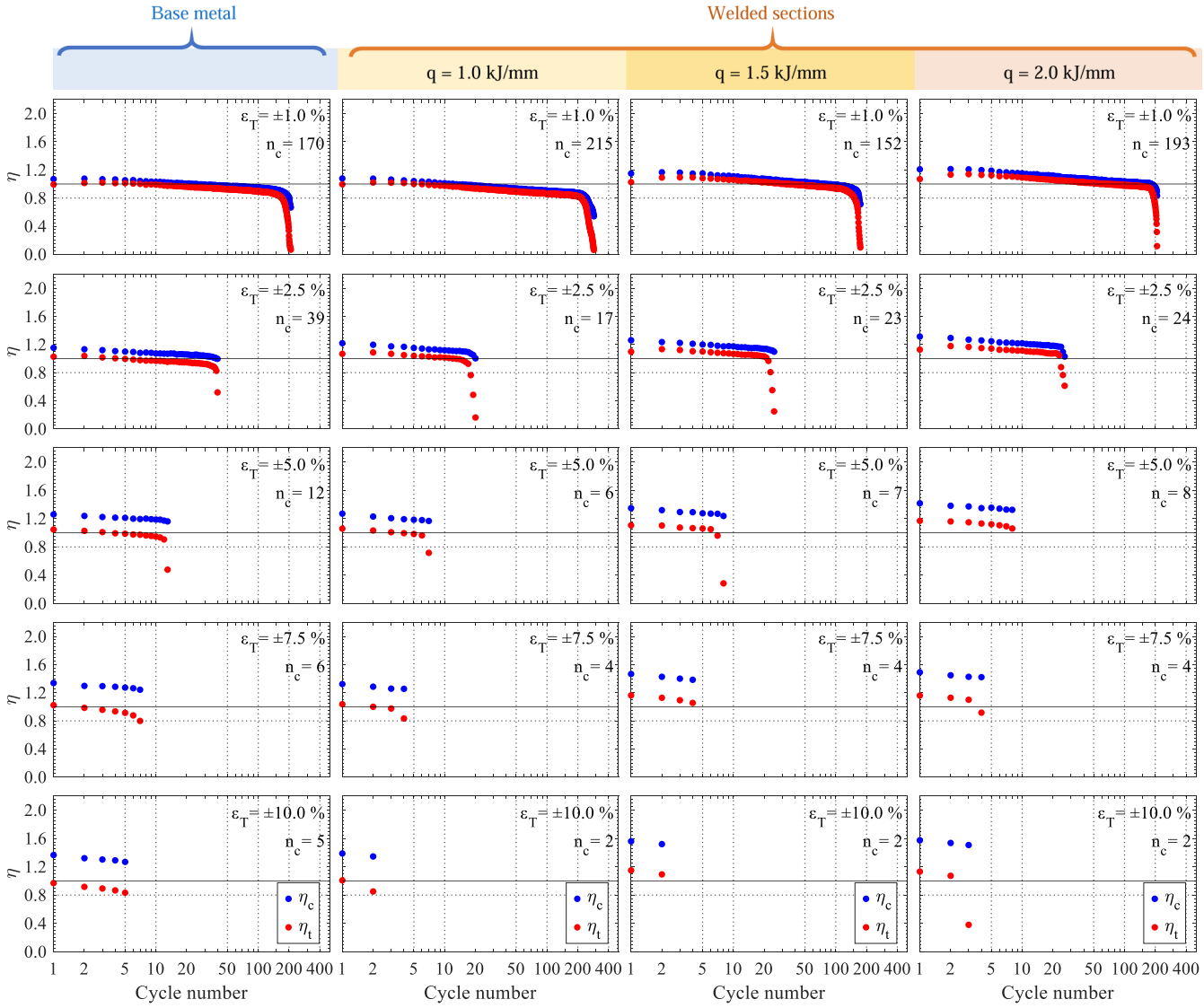

Figure 4.6 η_t and η_c of the cyclic tests on S690 (Shougang) with f = 0.1 Hz

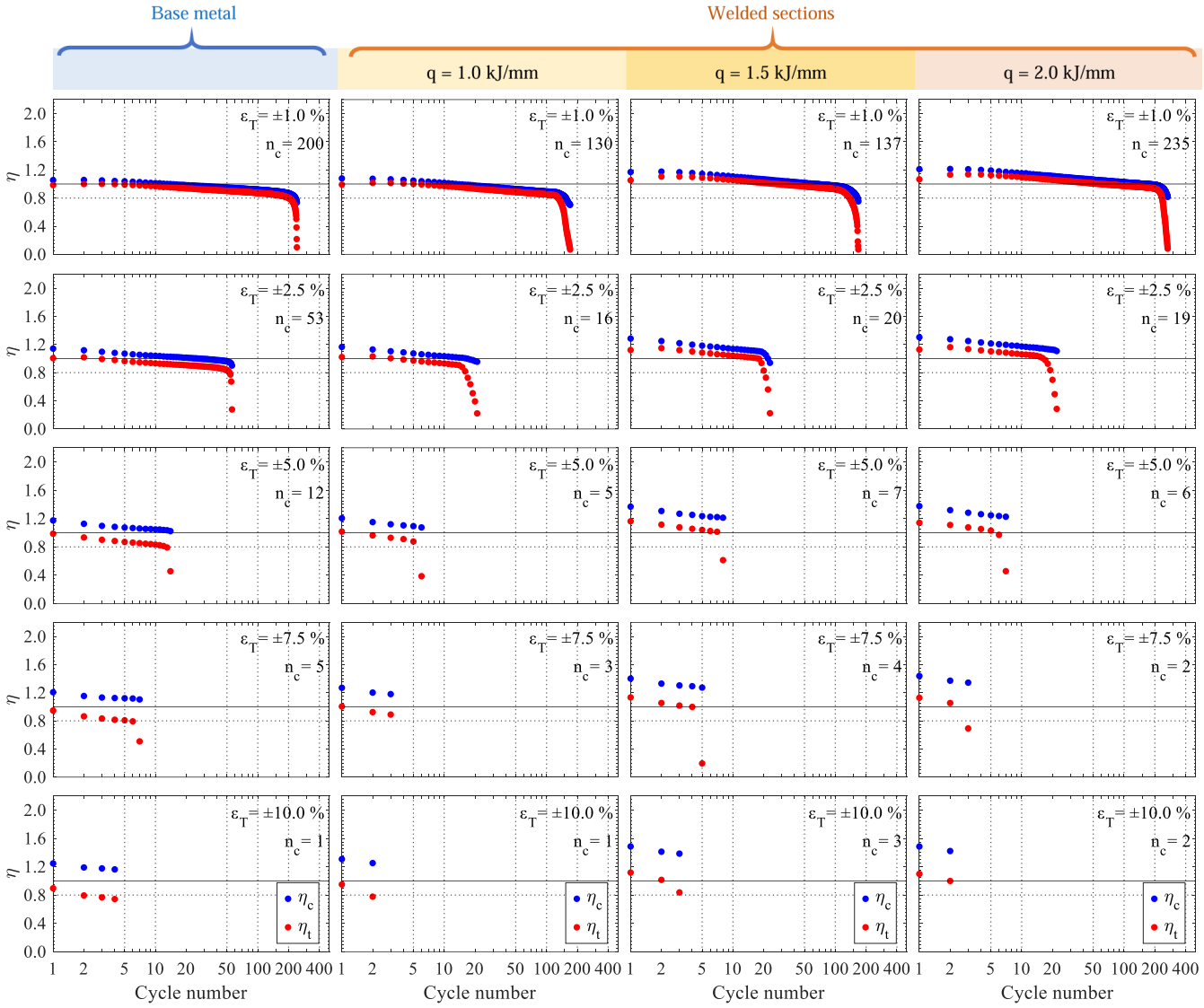

Figure 4.7 η_t and η_c of the cyclic tests on S690 (Shougang) with f = 1.0 Hz

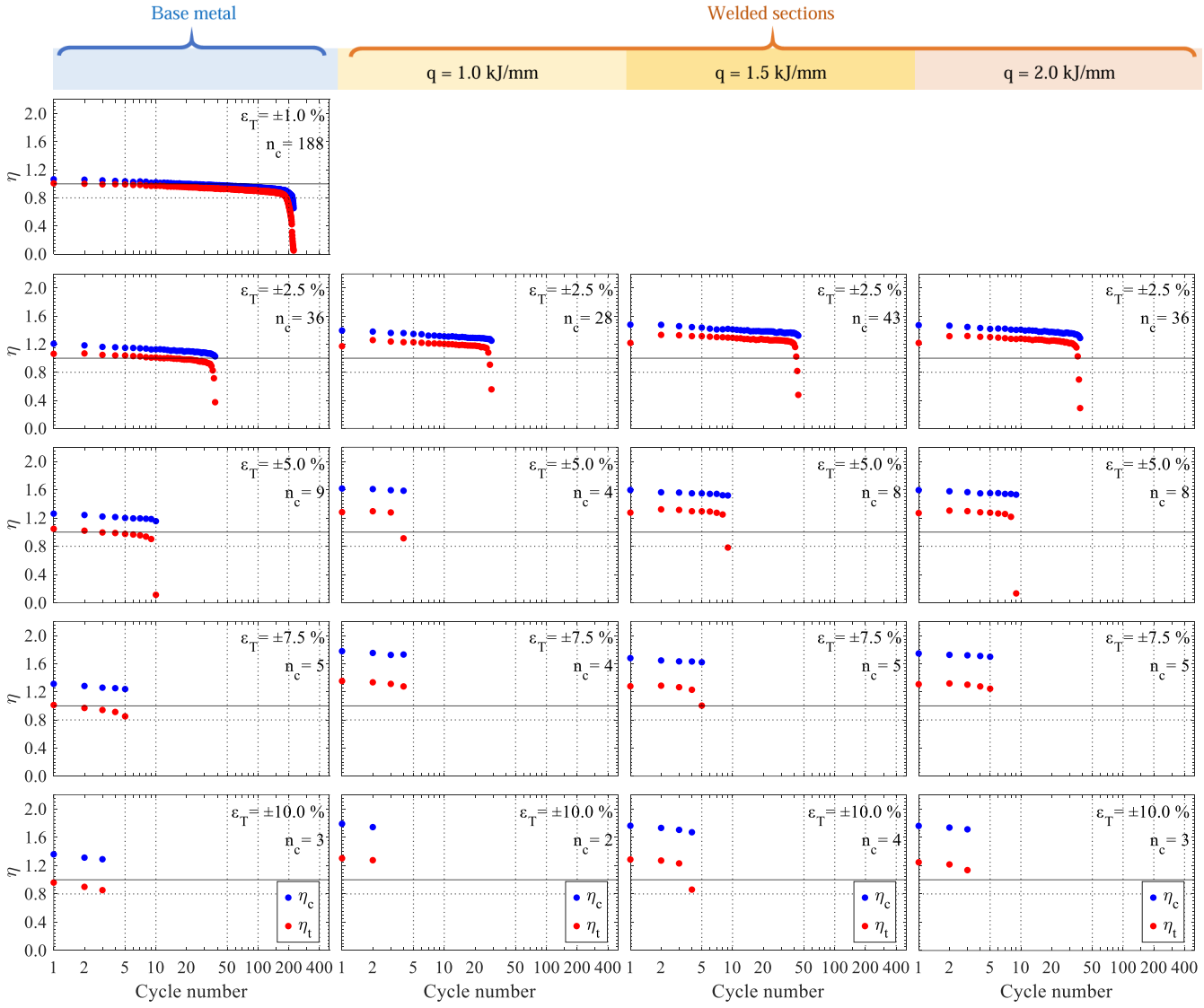

Figure 4.8 η_t and η_c of the cyclic tests on S960 with f = 0.1 Hz

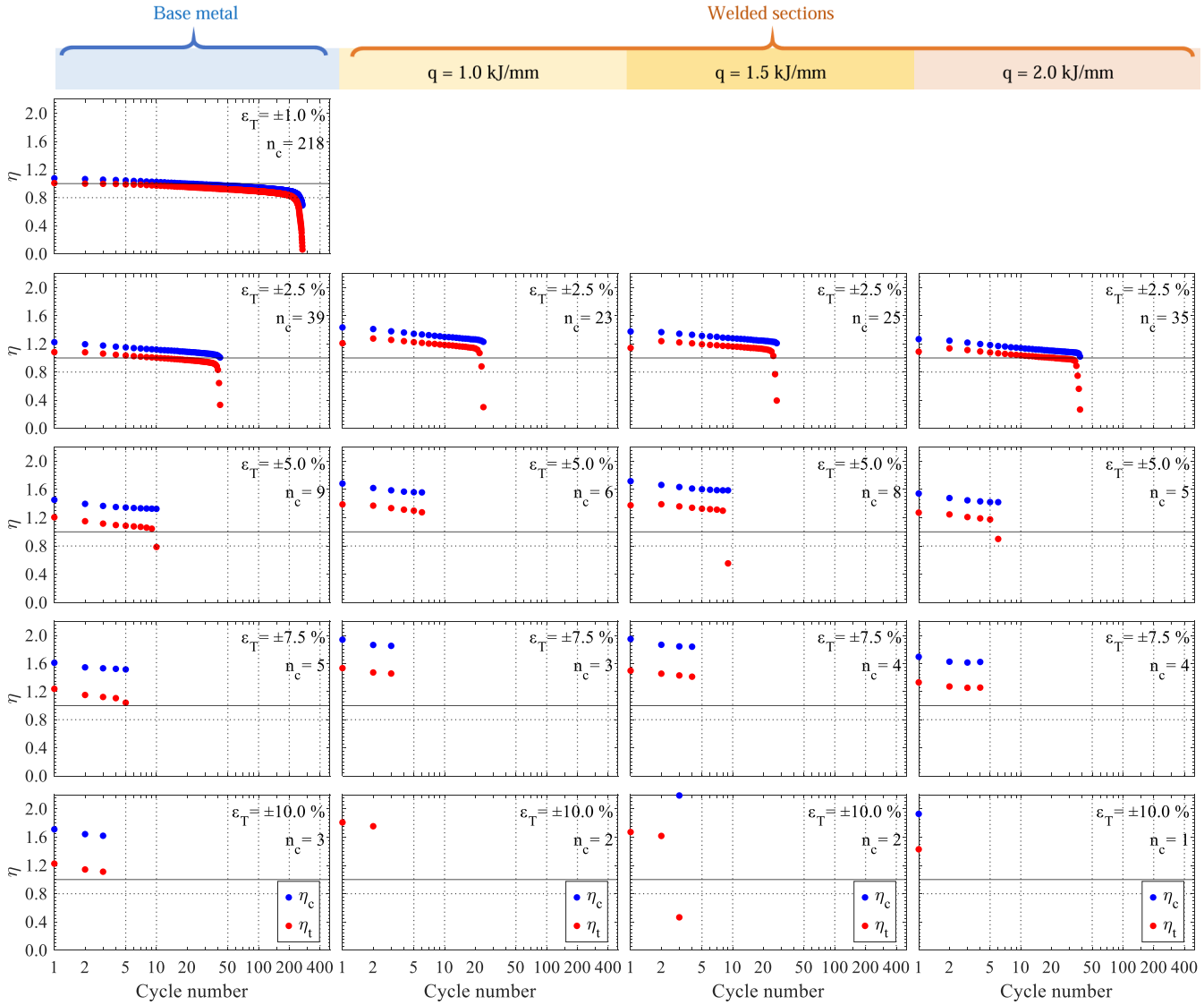

Figure 4.9 η_t and η_c of the cyclic tests on S960 with f = 1.0 Hz

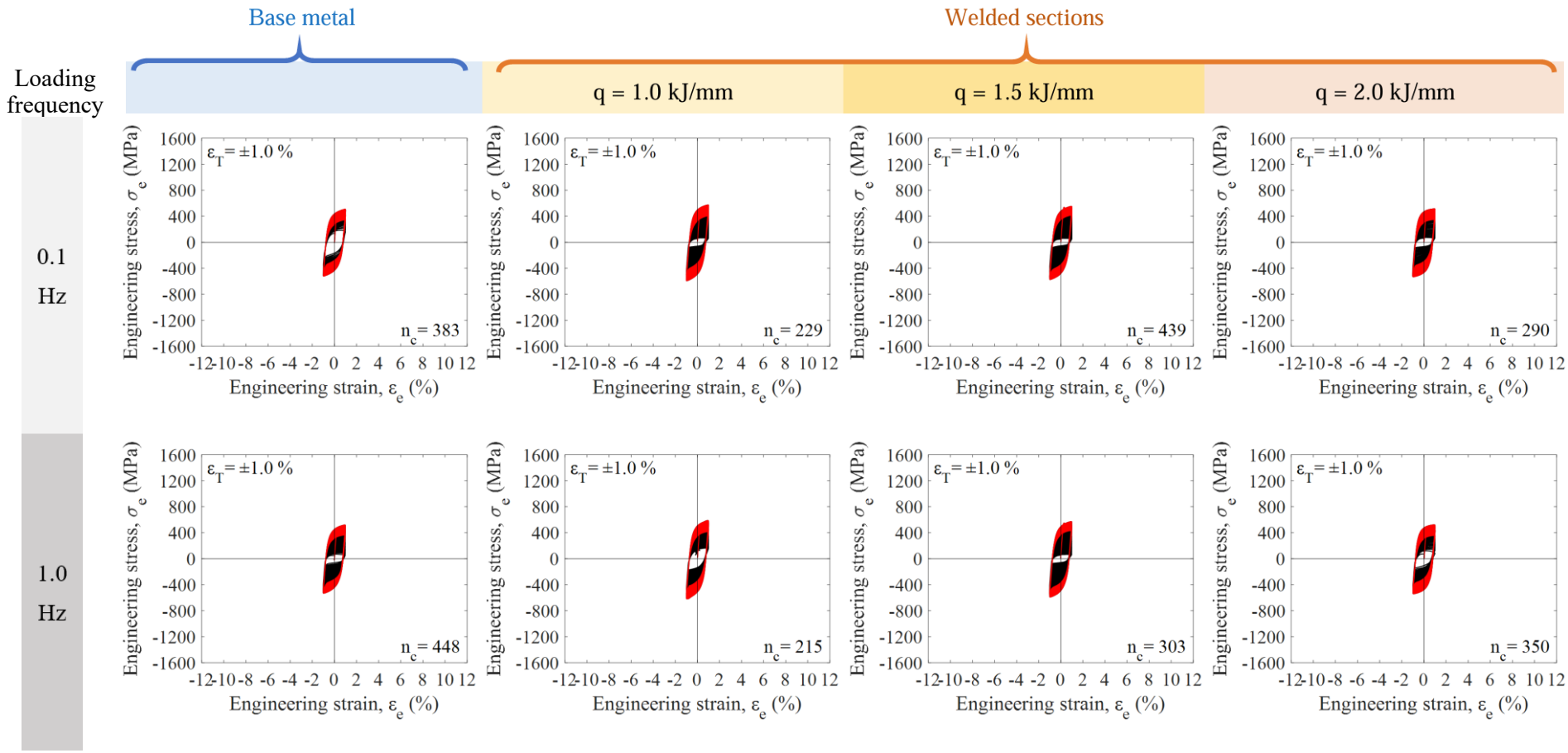

Figure 4.10 Engineering stress-strain curves of the cyclic tests on S355 at $\varepsilon_T = \pm 1.0$ %

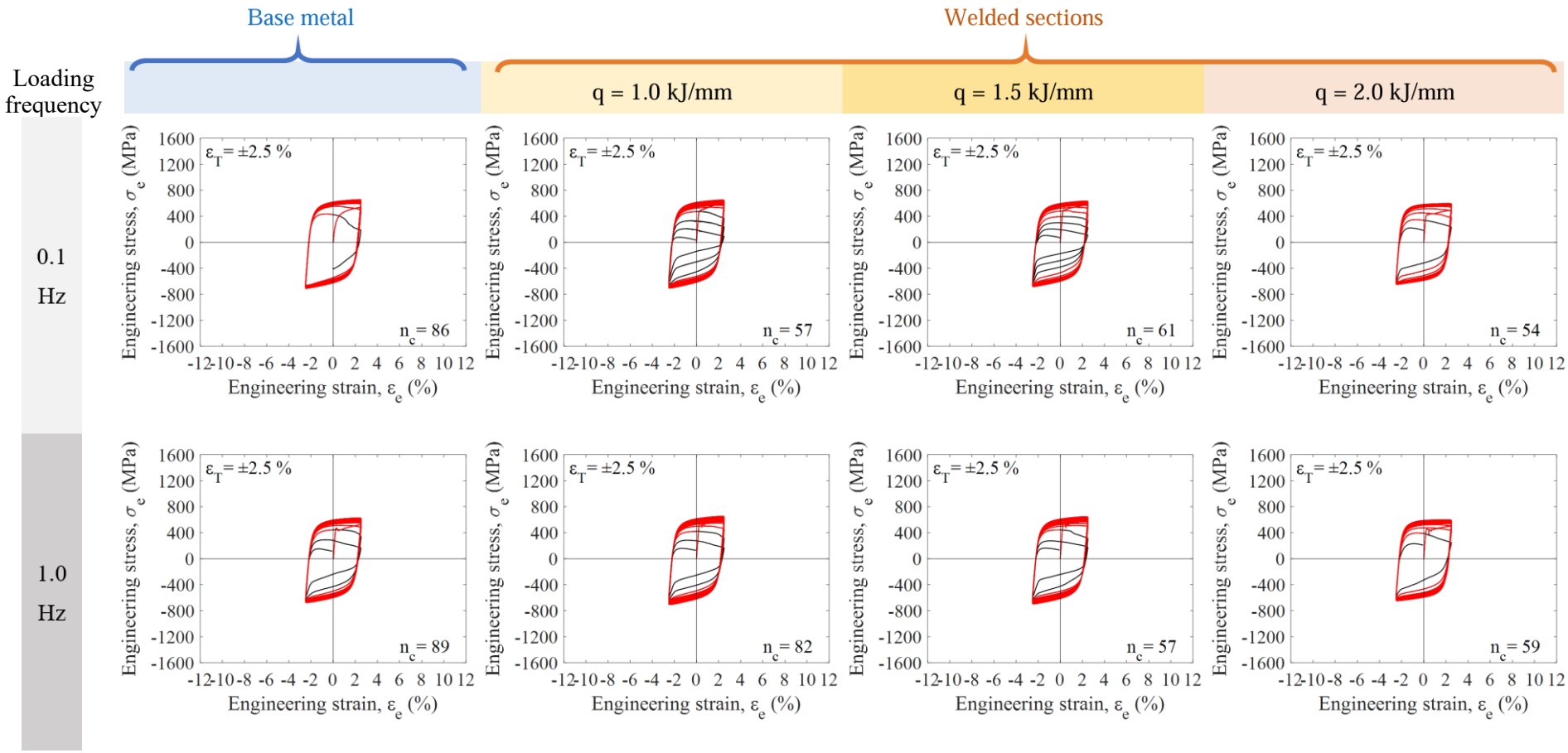

Figure 4.11 Engineering stress-strain curves of the cyclic tests on S355 at $\varepsilon_T = \pm 2.5$ %

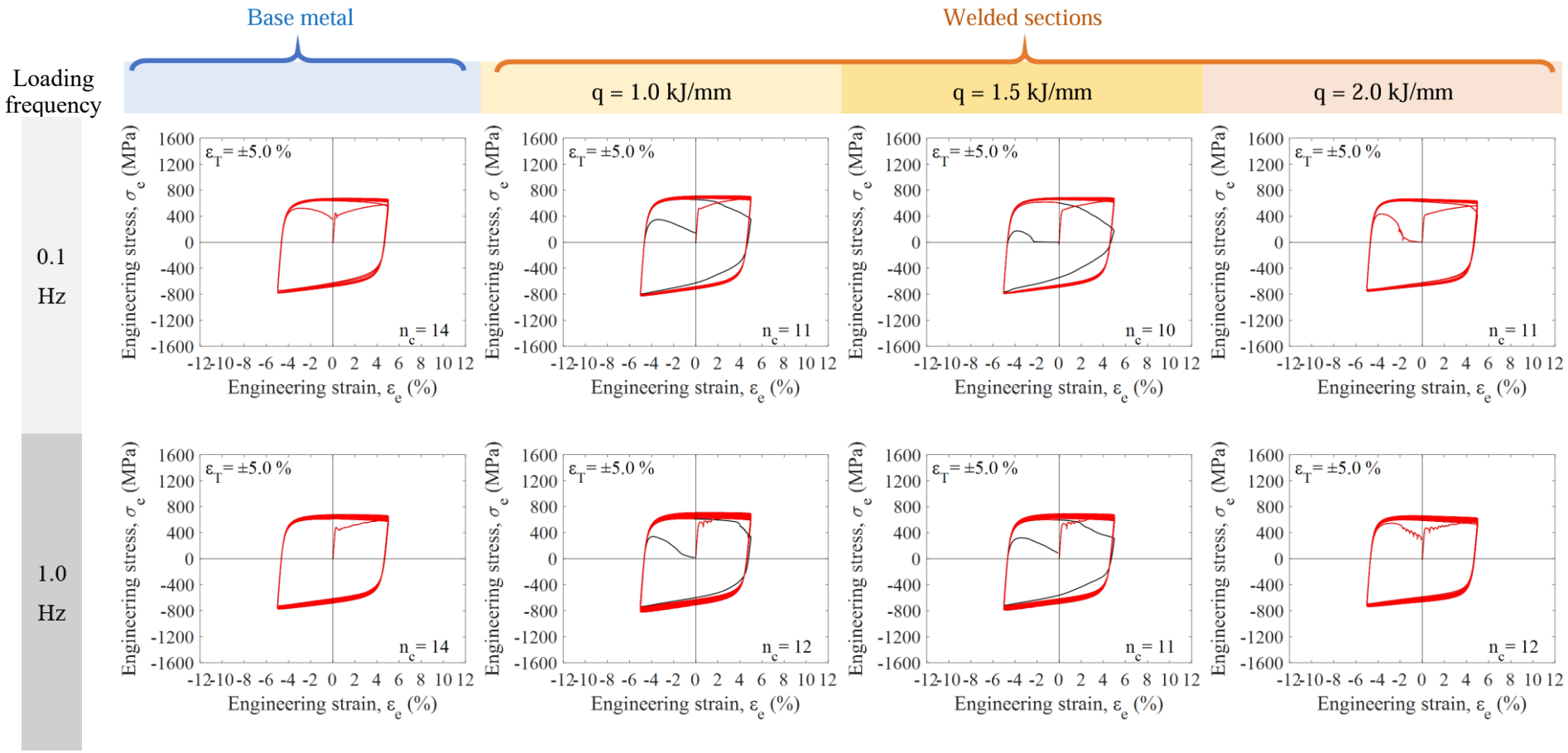

Figure 4.12 Engineering stress-strain curves of the cyclic tests on S355 at $\varepsilon_T = \pm 5.0$ %

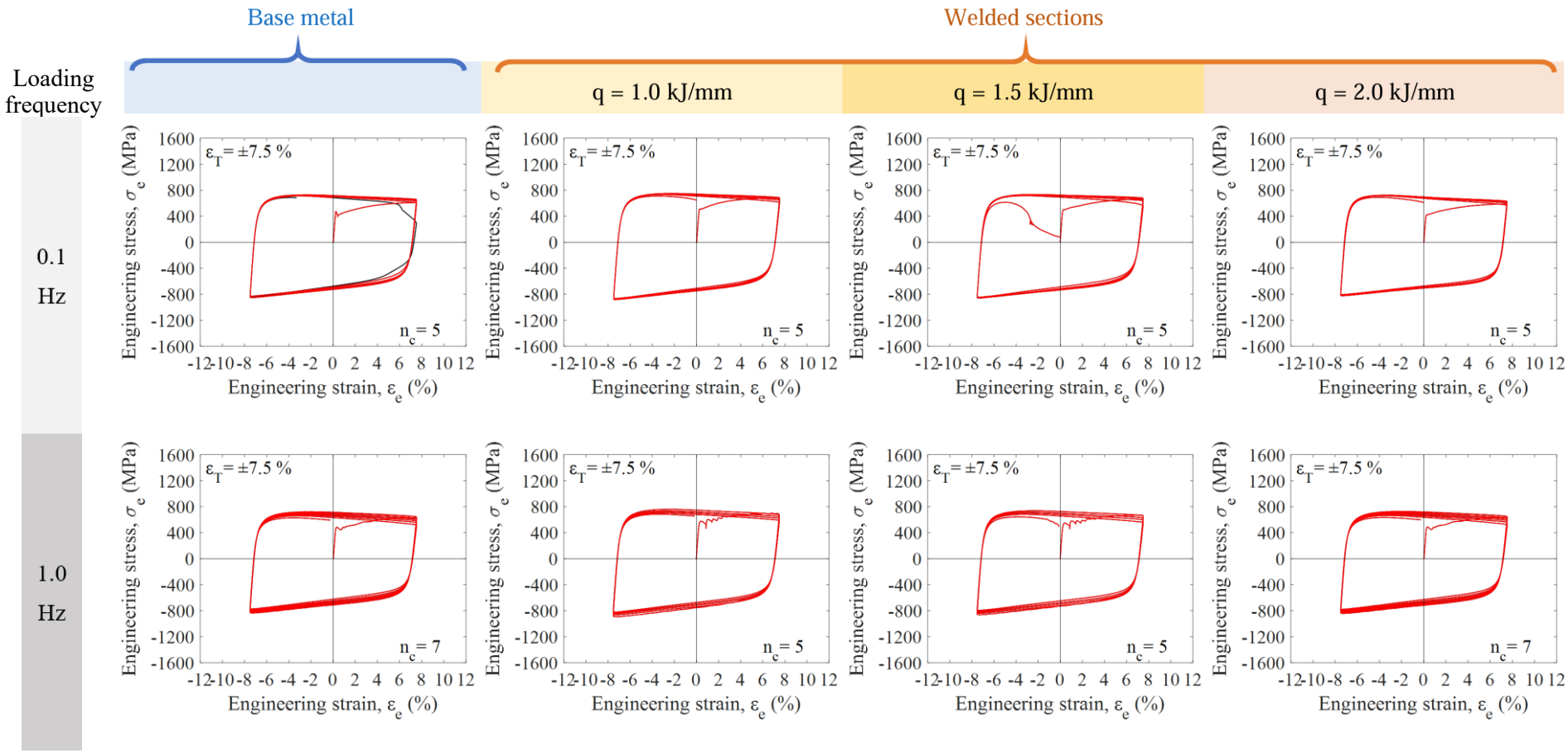

Figure 4.13 Engineering stress-strain curves of the cyclic tests on S355 at $\varepsilon_T = \pm 7.5$ %

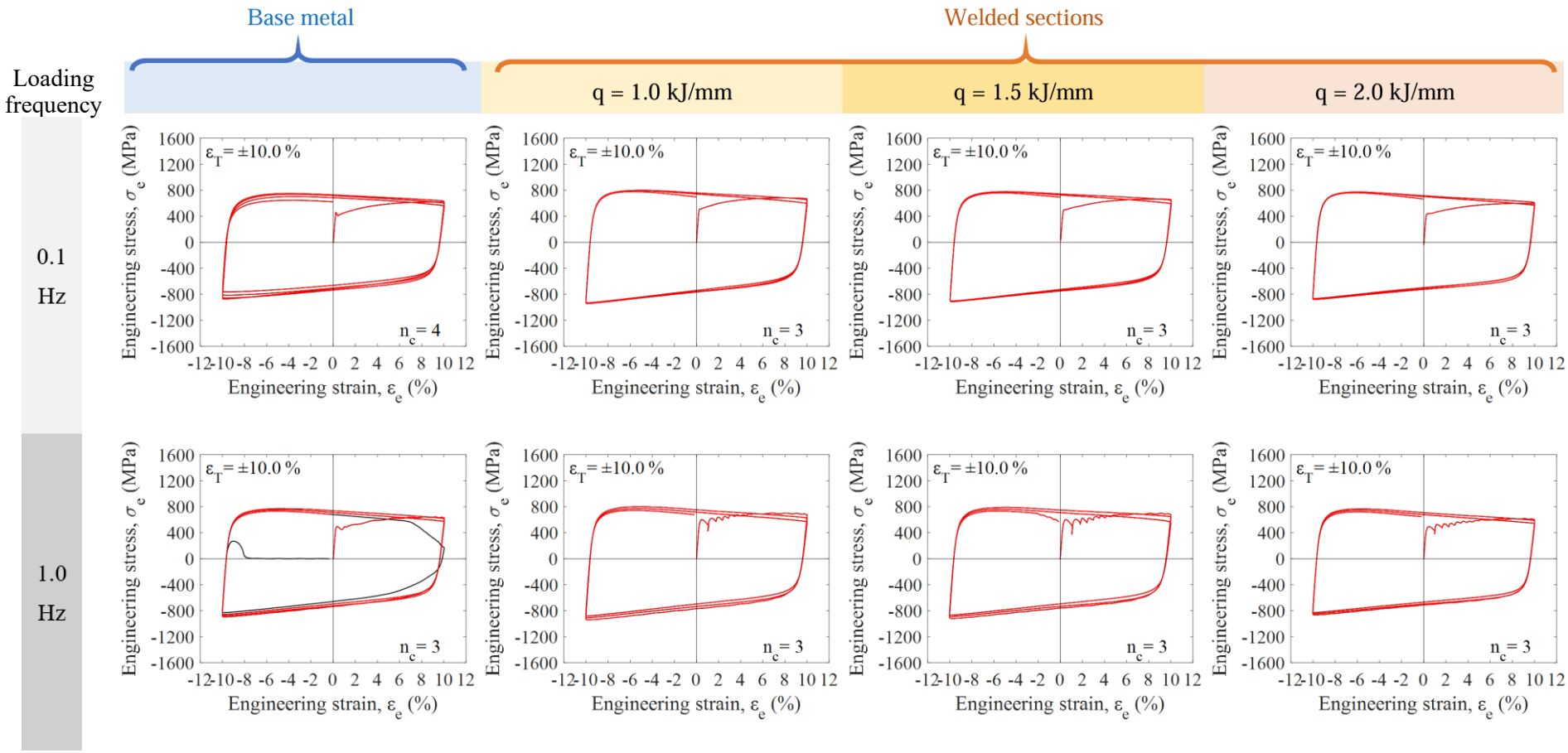

Figure 4.14 Engineering stress-strain curves of the cyclic tests on S355 at $\varepsilon_T = \pm 10.0$ %

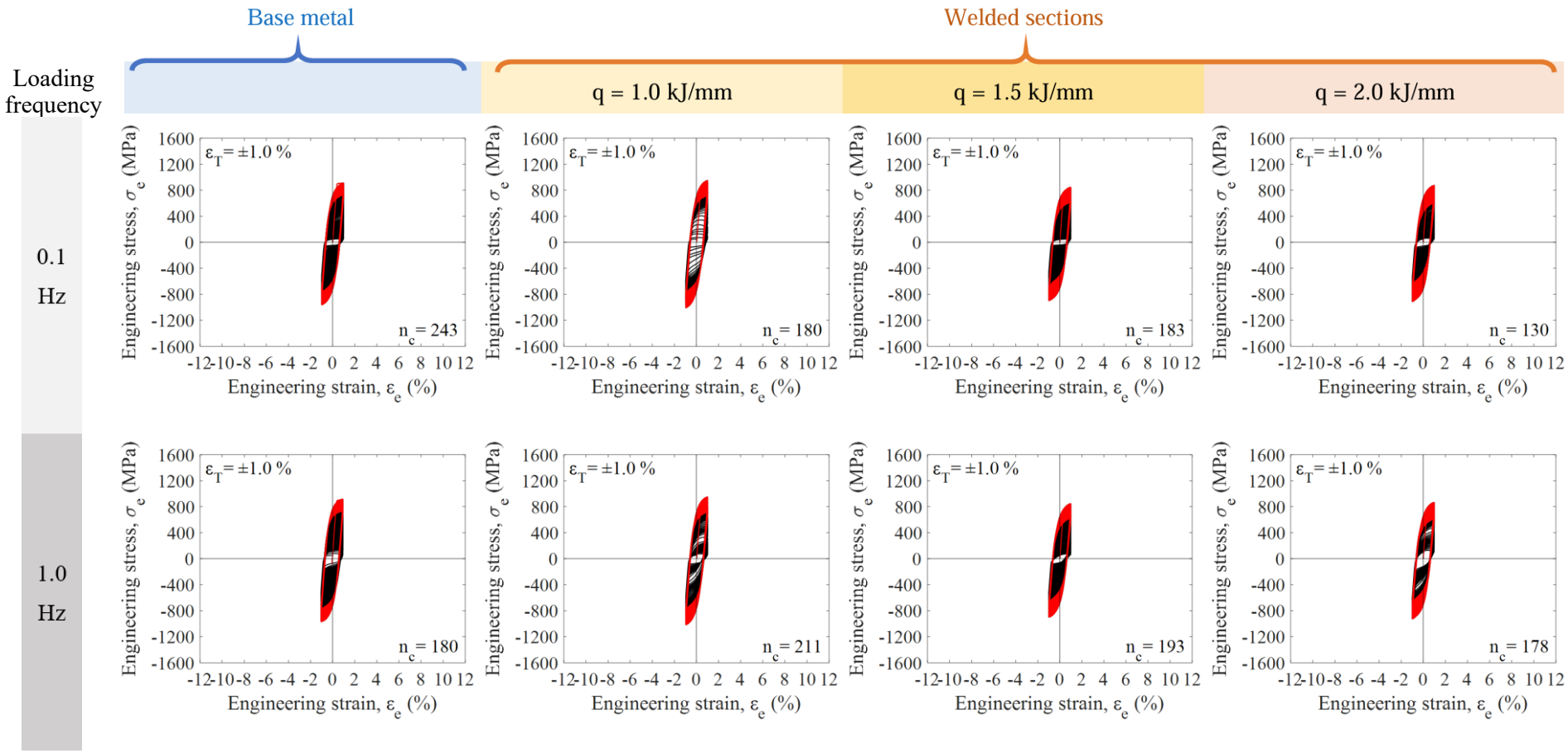

Figure 4.15 Engineering stress-strain curves of the cyclic tests on S690 (Nangang) at $\varepsilon_T = \pm 1.0$ %

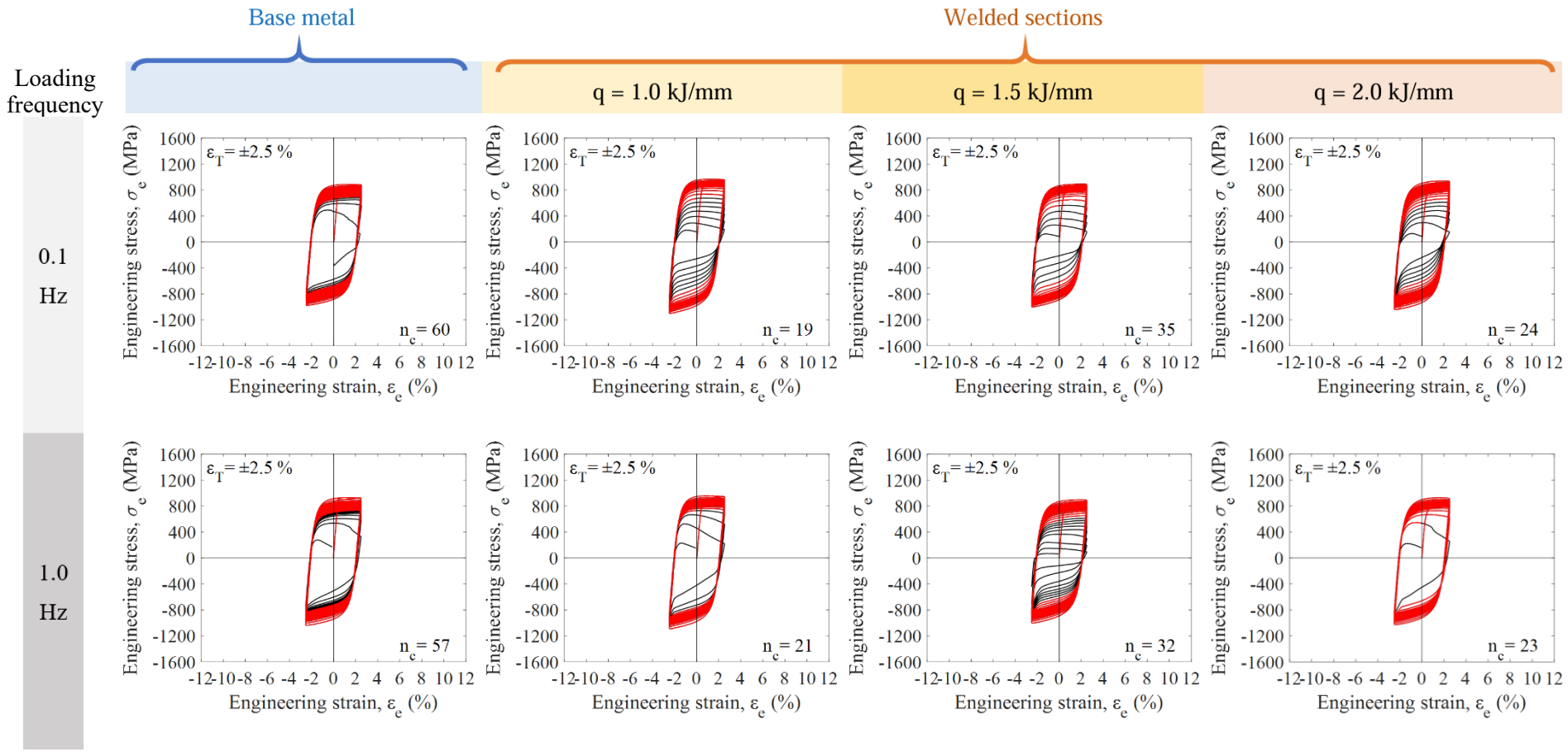

Figure 4.16 Engineering stress-strain curves of the cyclic tests on S690 (Nangang) at $\varepsilon_T = \pm 2.5$ %

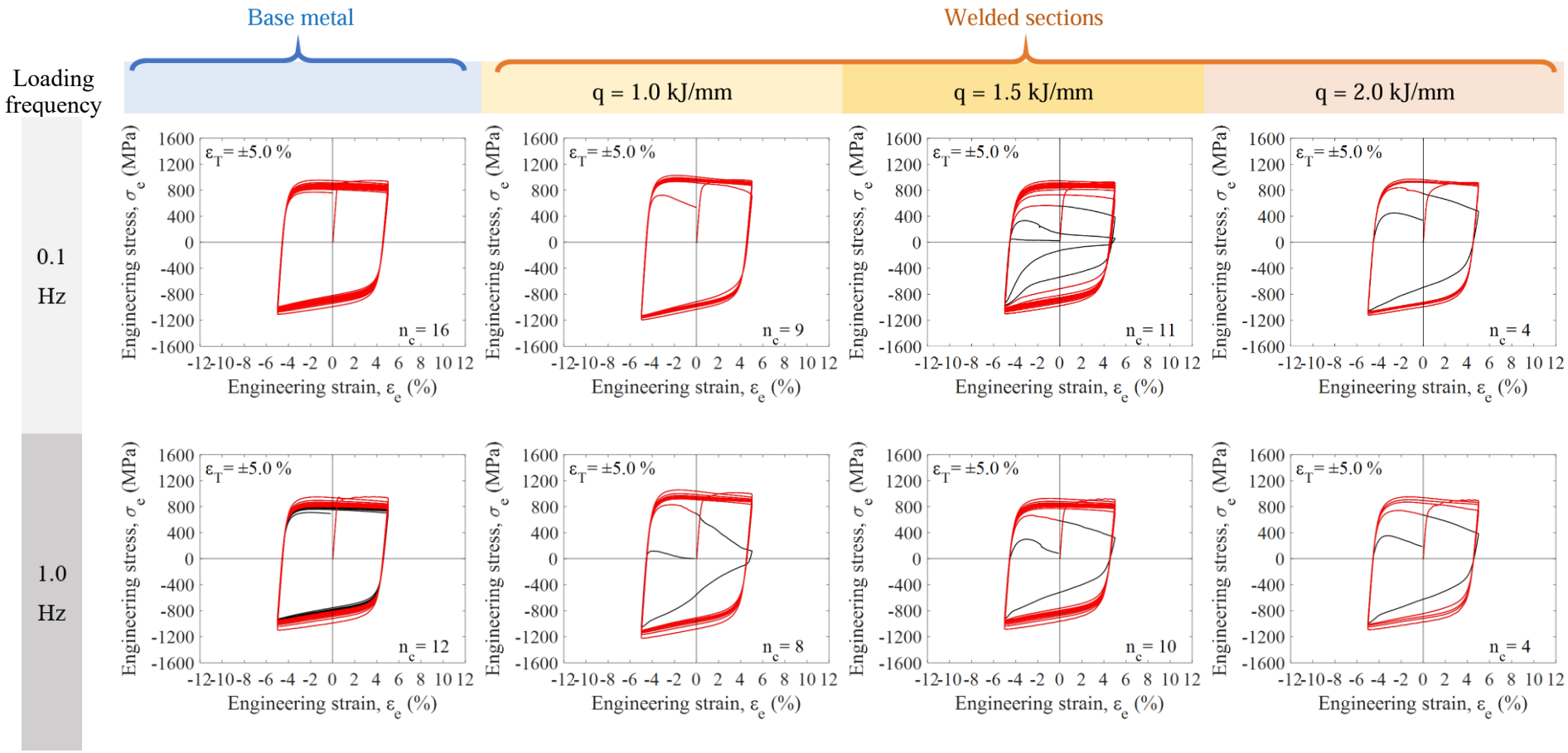

Figure 4.17 Engineering stress-strain curves of the cyclic tests on S690 (Nangang) at $\varepsilon_T = \pm 5.0$ %

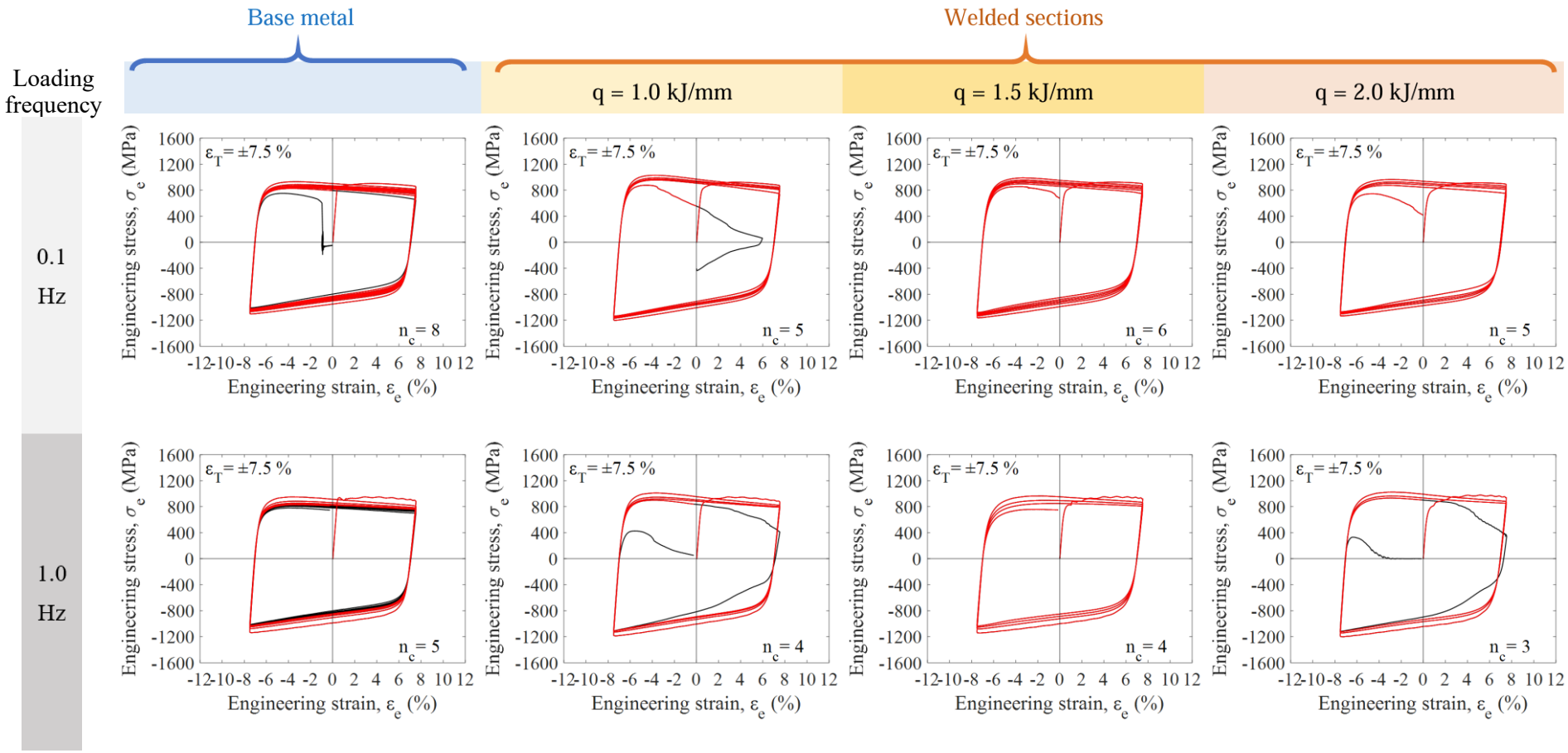

Figure 4.18 Engineering stress-strain curves of the cyclic tests on S690 (Nangang) at ε_T = ±7.5 %

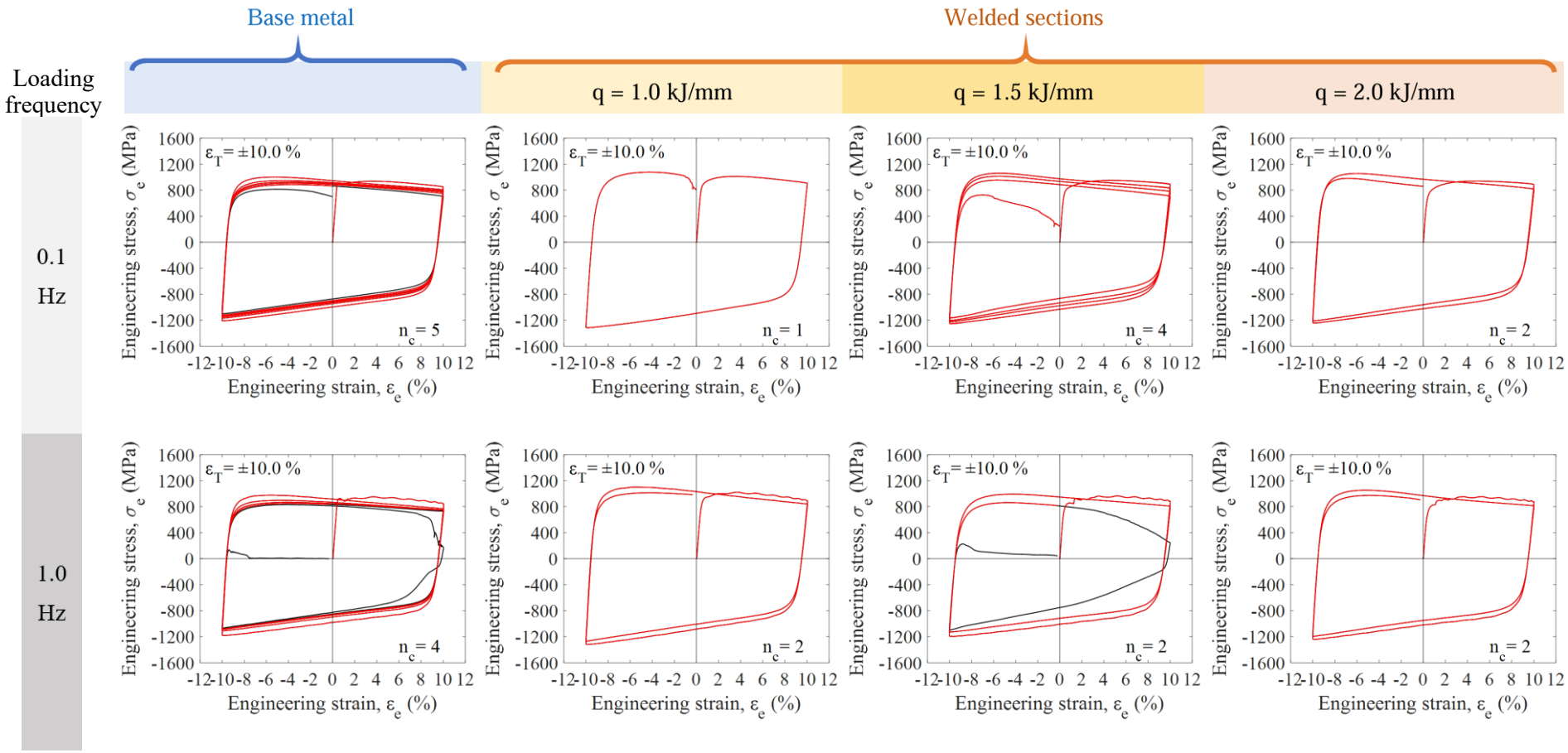

Figure 4.19 Engineering stress-strain curves of the cyclic tests on S690 (Nangang) at $\varepsilon_T = \pm 10.0$ %

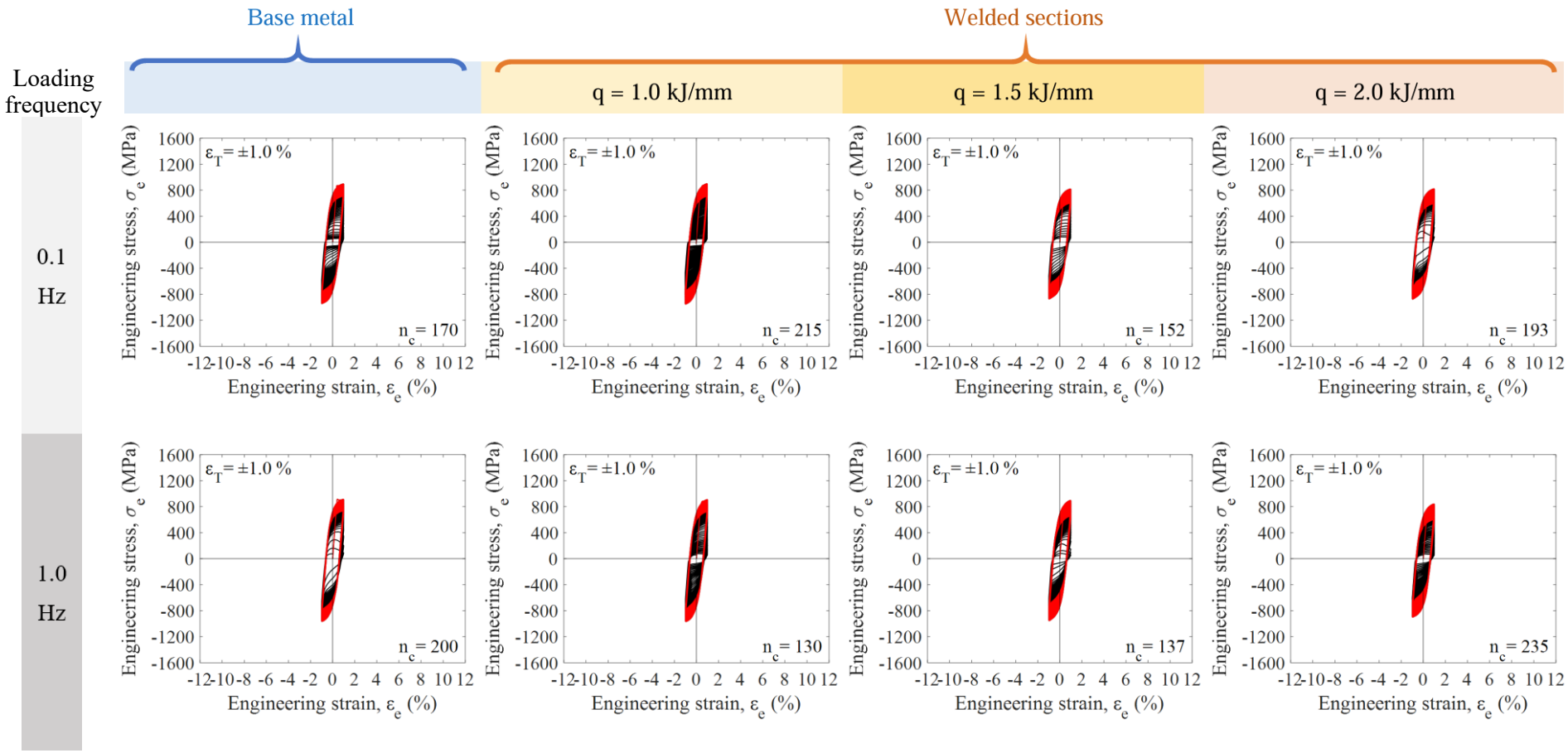

Figure 4.20 Engineering stress-strain curves of the cyclic tests on S690 (Shougang) at $\varepsilon_T = \pm 1.0$ %

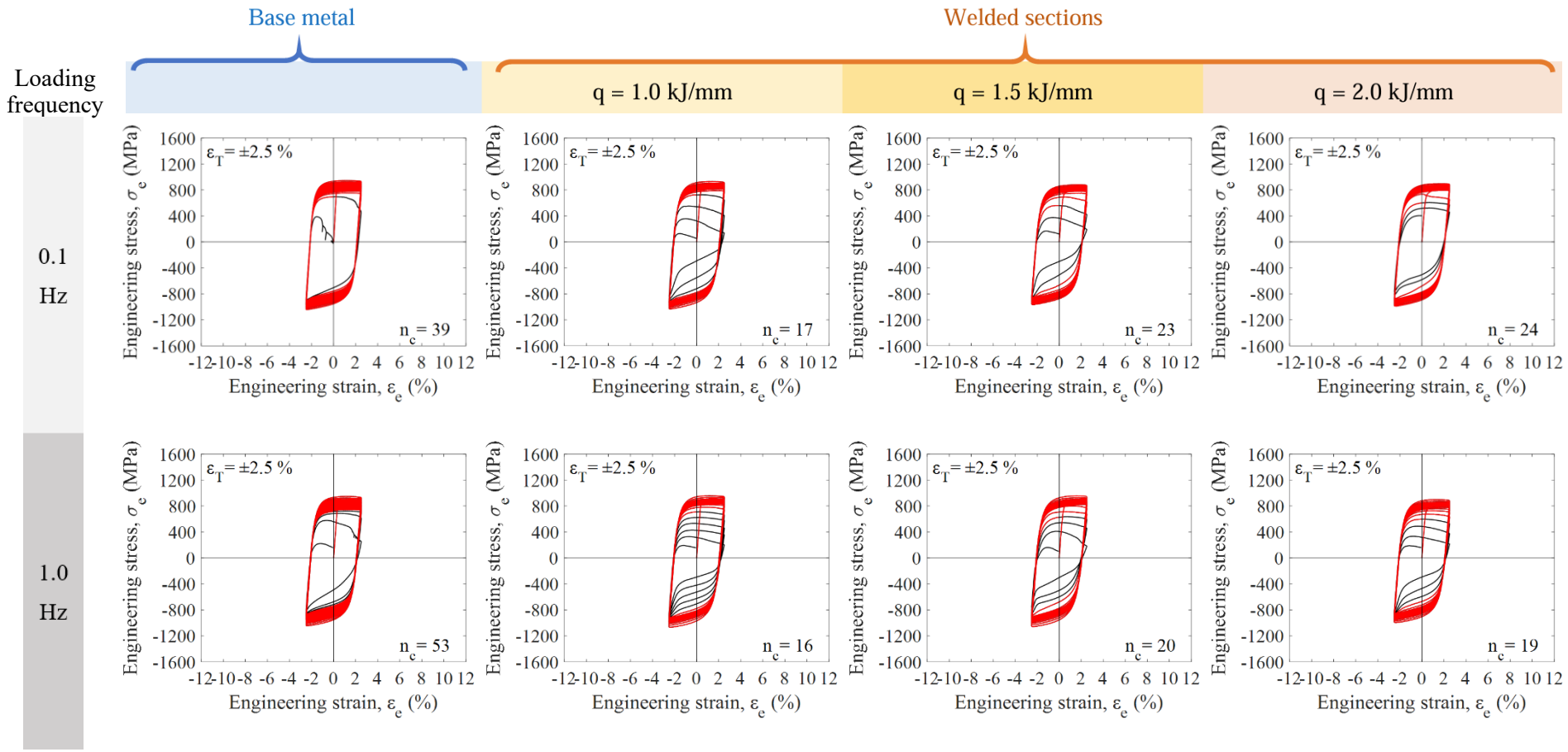

Figure 4.21 Engineering stress-strain curves of the cyclic tests on S690 (Shougang) at $\varepsilon_T = \pm 2.5$ %

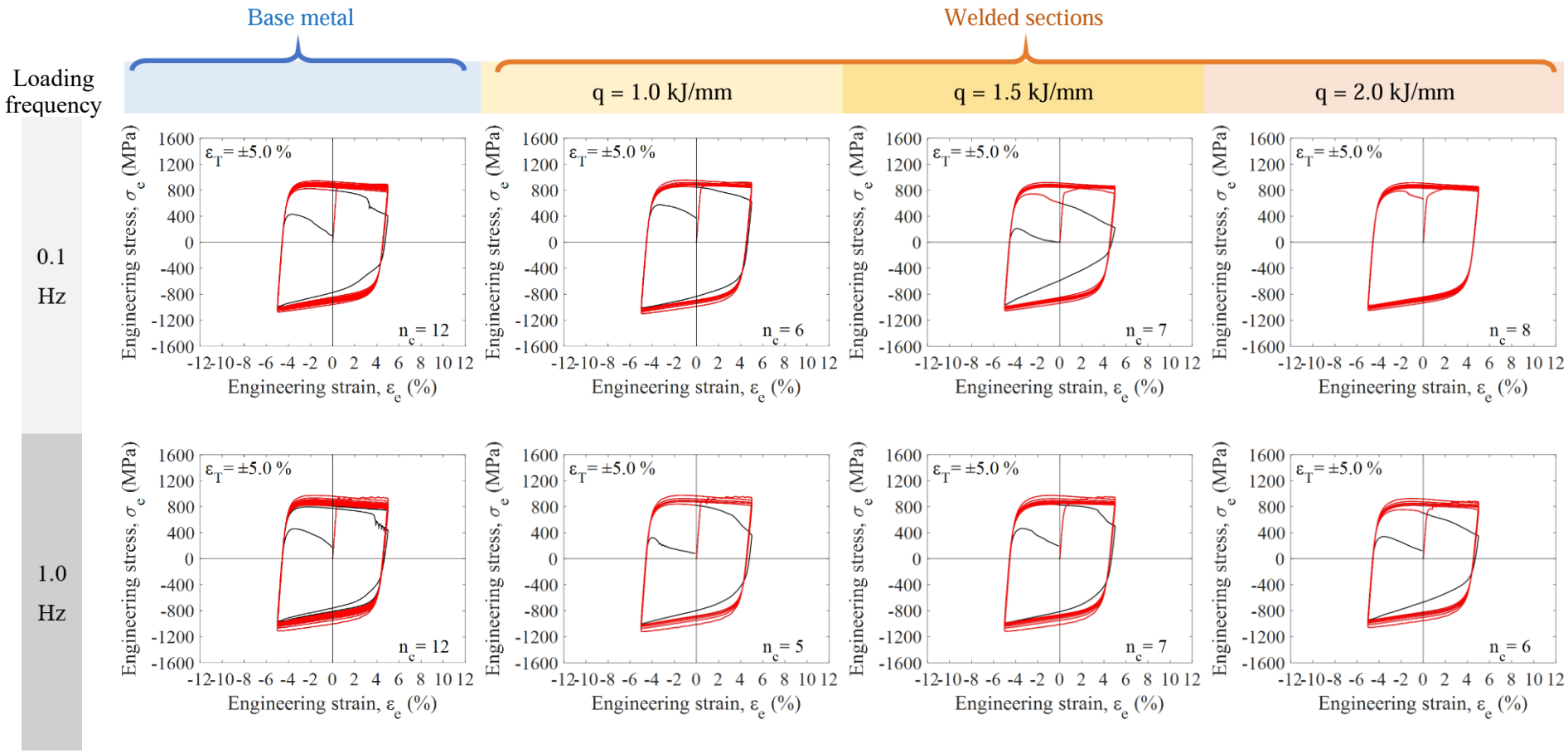

Figure 4.22 Engineering stress-strain curves of the cyclic tests on S690 (Shougang) at $\varepsilon_T = \pm 5.0$ %

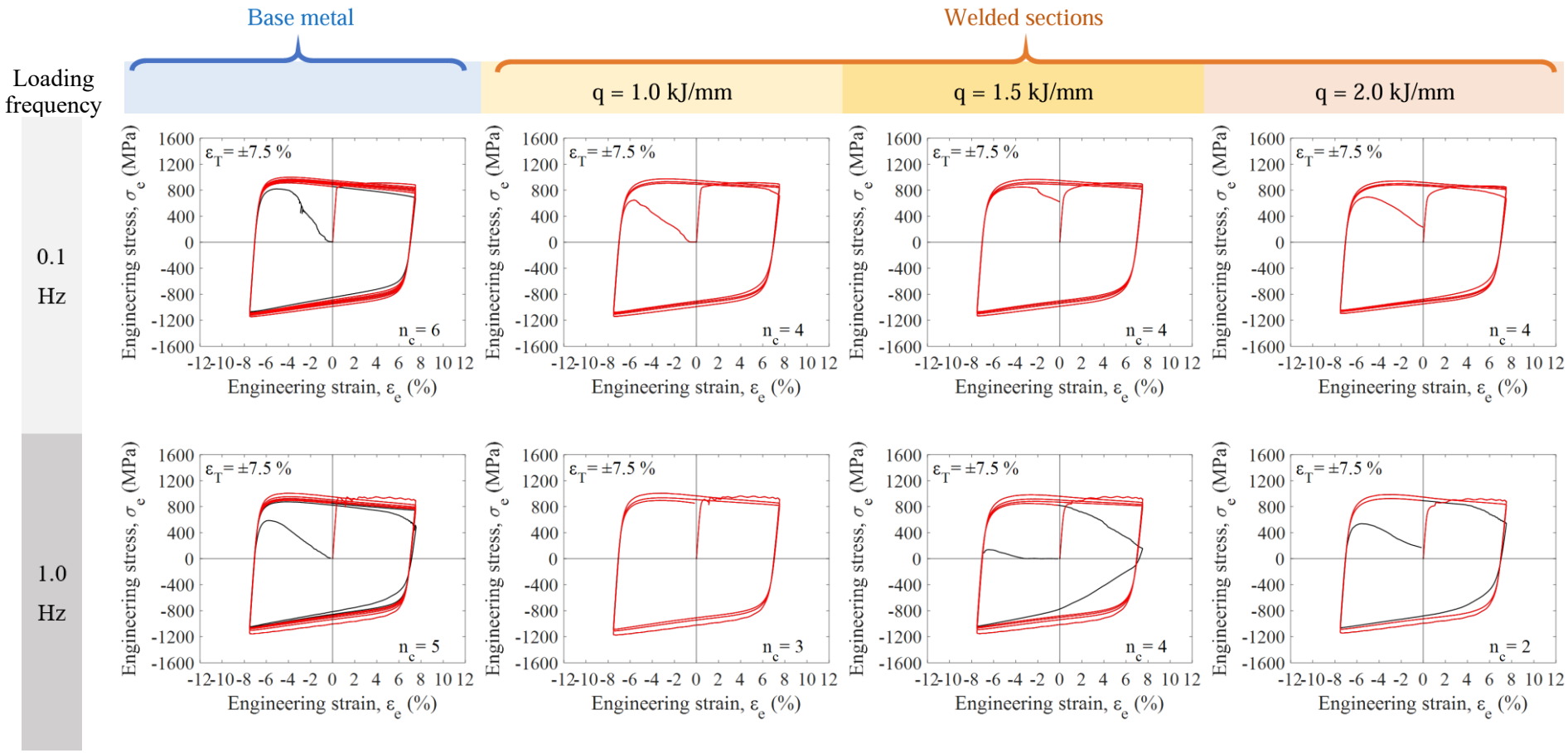

Figure 4.23 Engineering stress-strain curves of the cyclic tests on S690 (Shougang) at $\varepsilon_T = \pm 7.5$ %

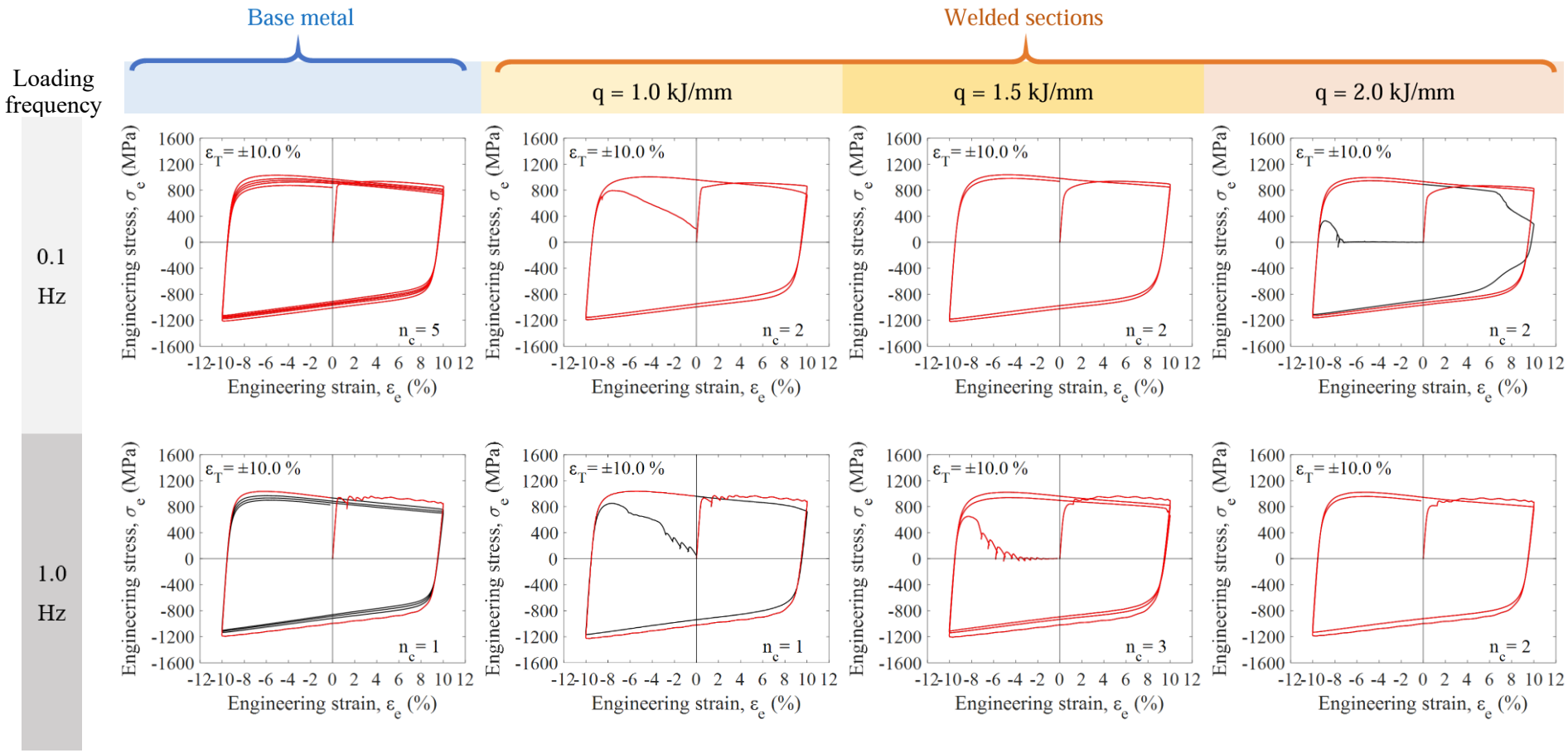

Figure 4.24 Engineering stress-strain curves of the cyclic tests on S690 (Shougang) at $\varepsilon_T = \pm 10.0$ %

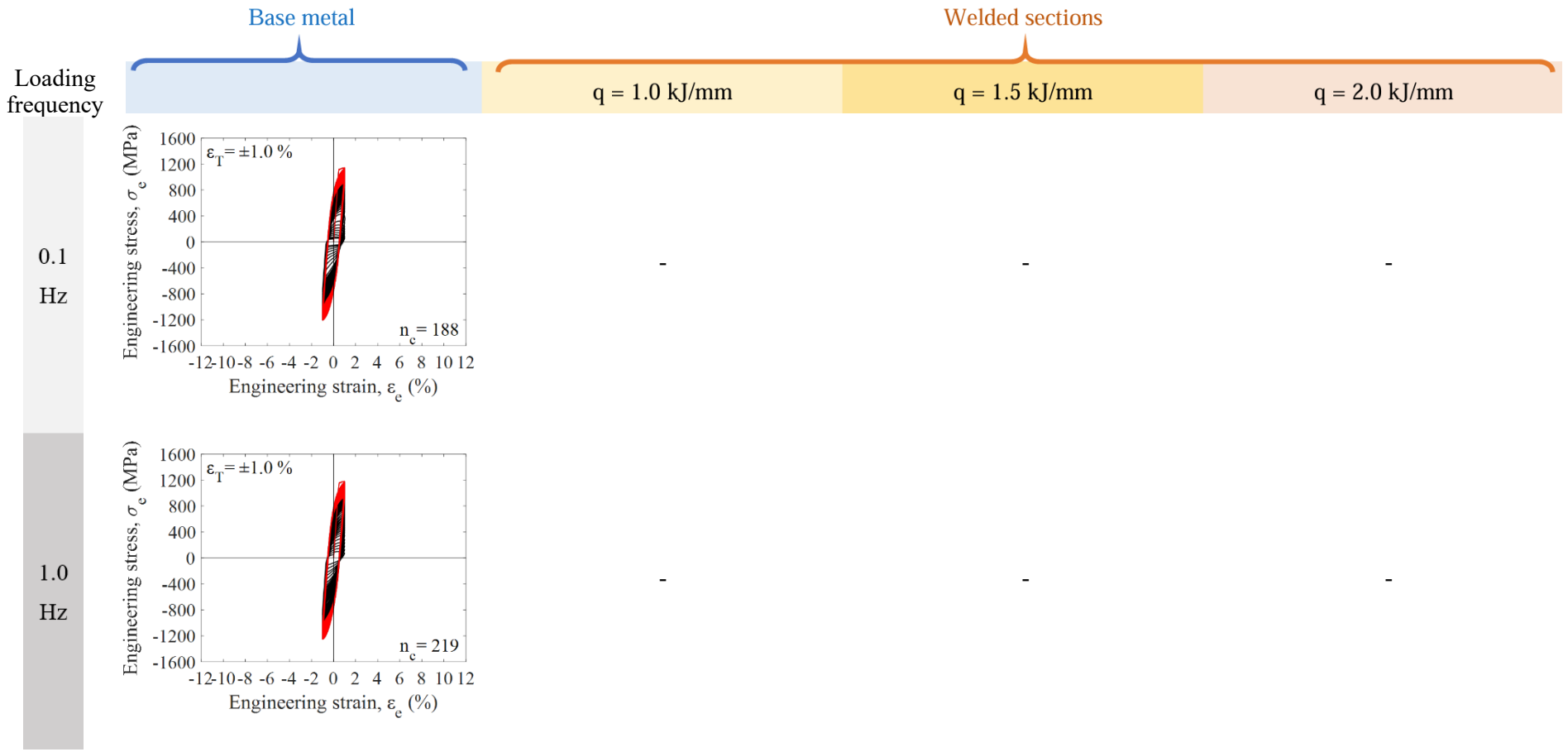

Figure 4.25 Engineering stress-strain curves of the cyclic tests on S960 at ε_T = ±1.0 %

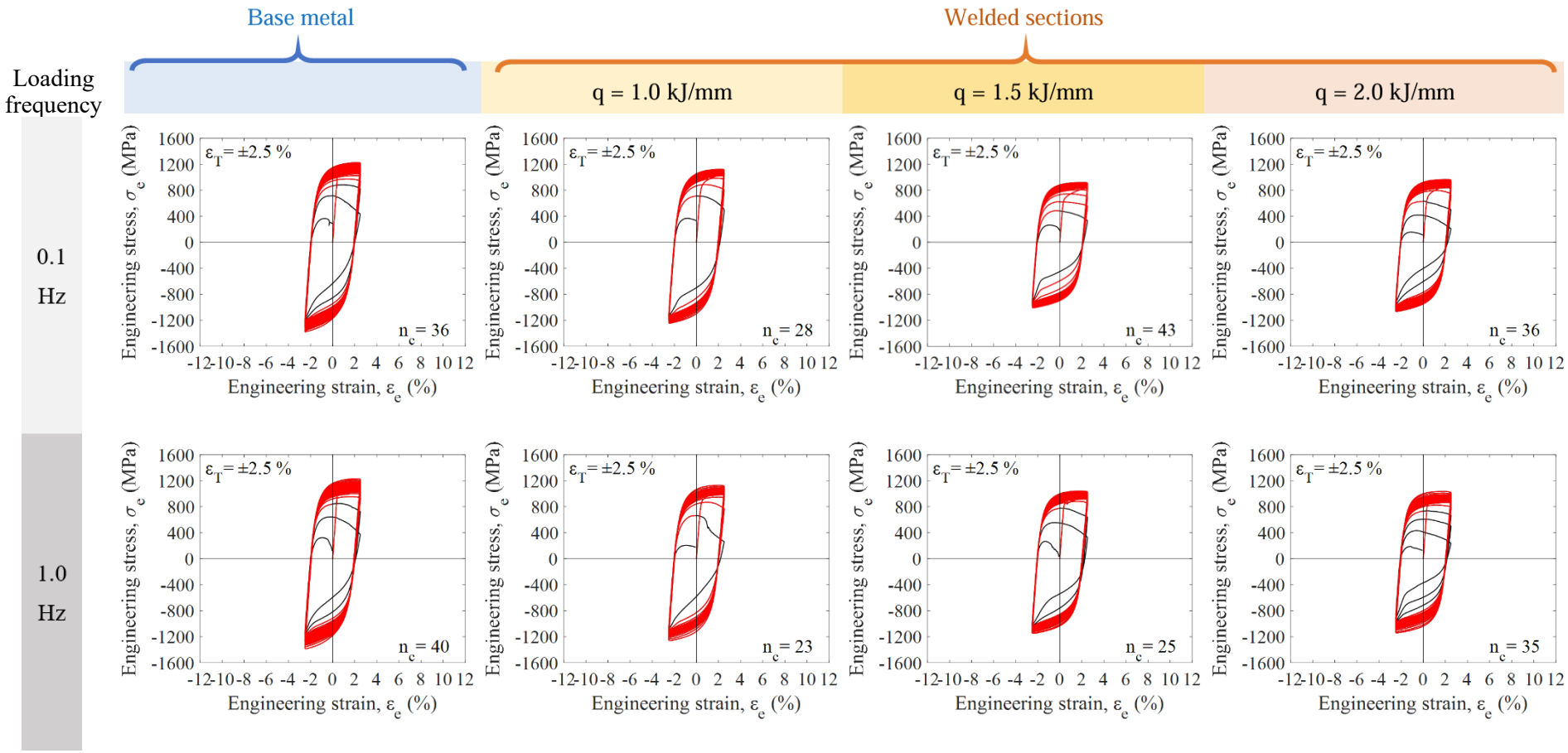

Figure 4.26 Engineering stress-strain curves of the cyclic tests on S960 at $\varepsilon_T = \pm 2.5$ %

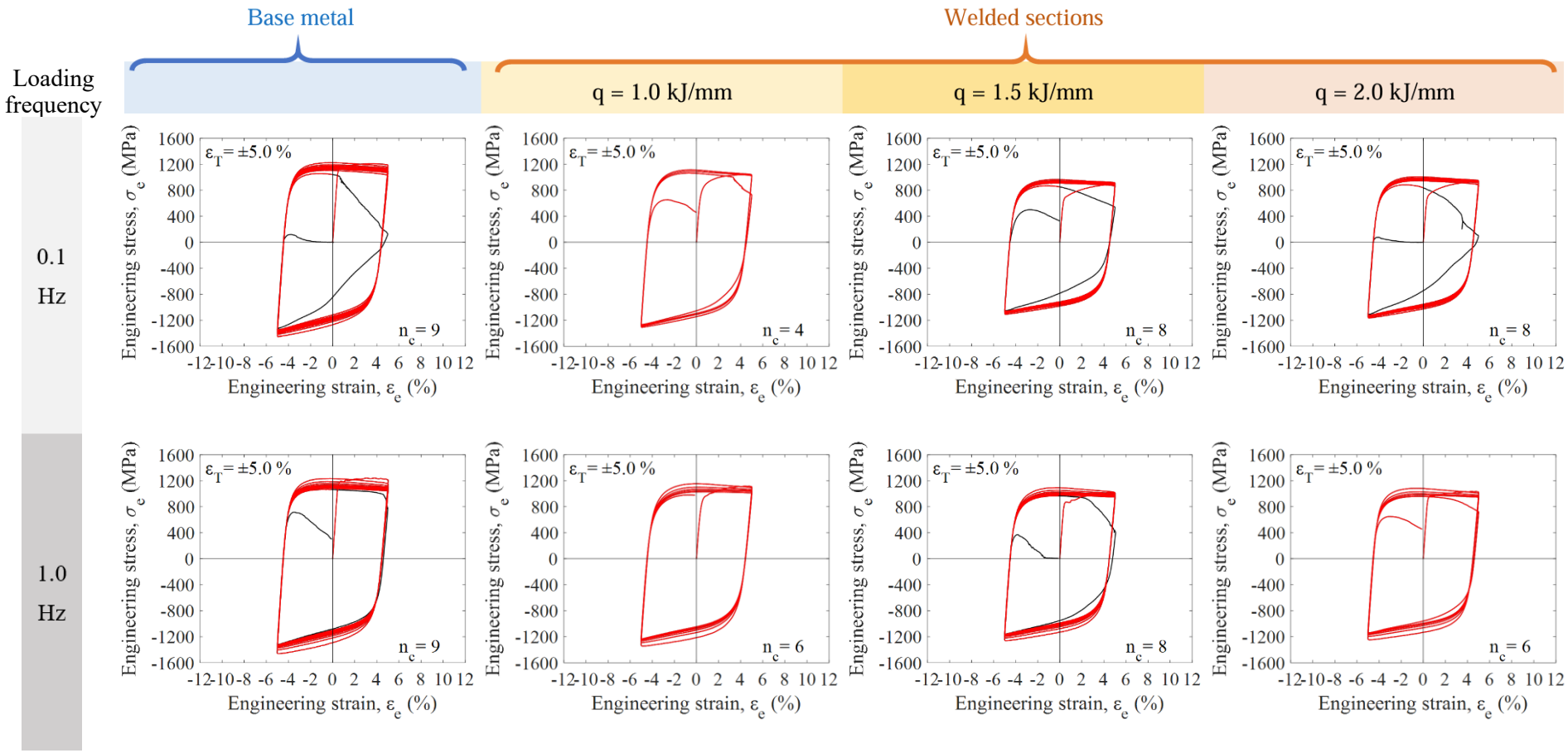

Figure 4.27 Engineering stress-strain curves of the cyclic tests on S960 at $\varepsilon_T = \pm 5.0$ %

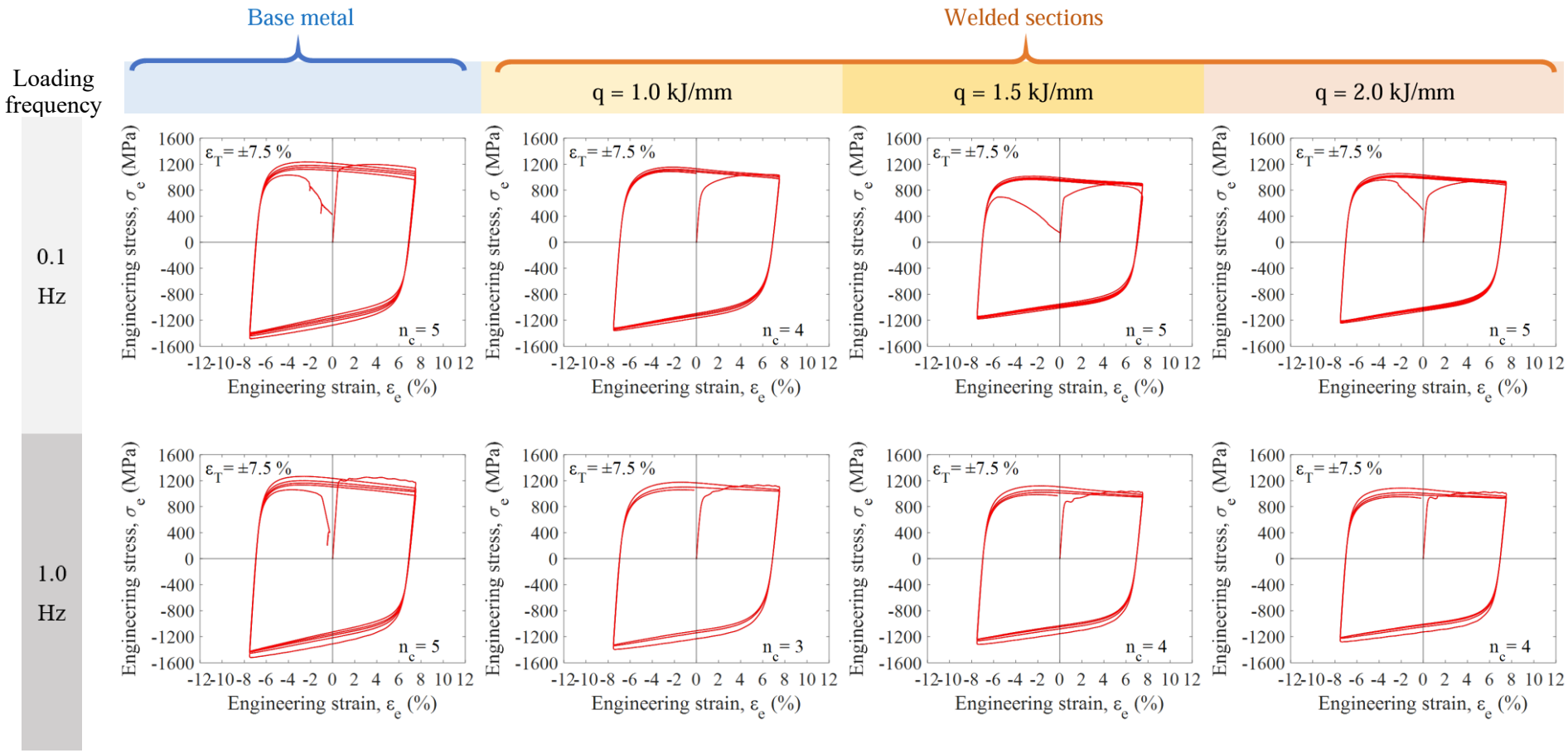

Figure 4.28 Engineering stress-strain curves of the cyclic tests on S960 at $\varepsilon_T = \pm 7.5$ %

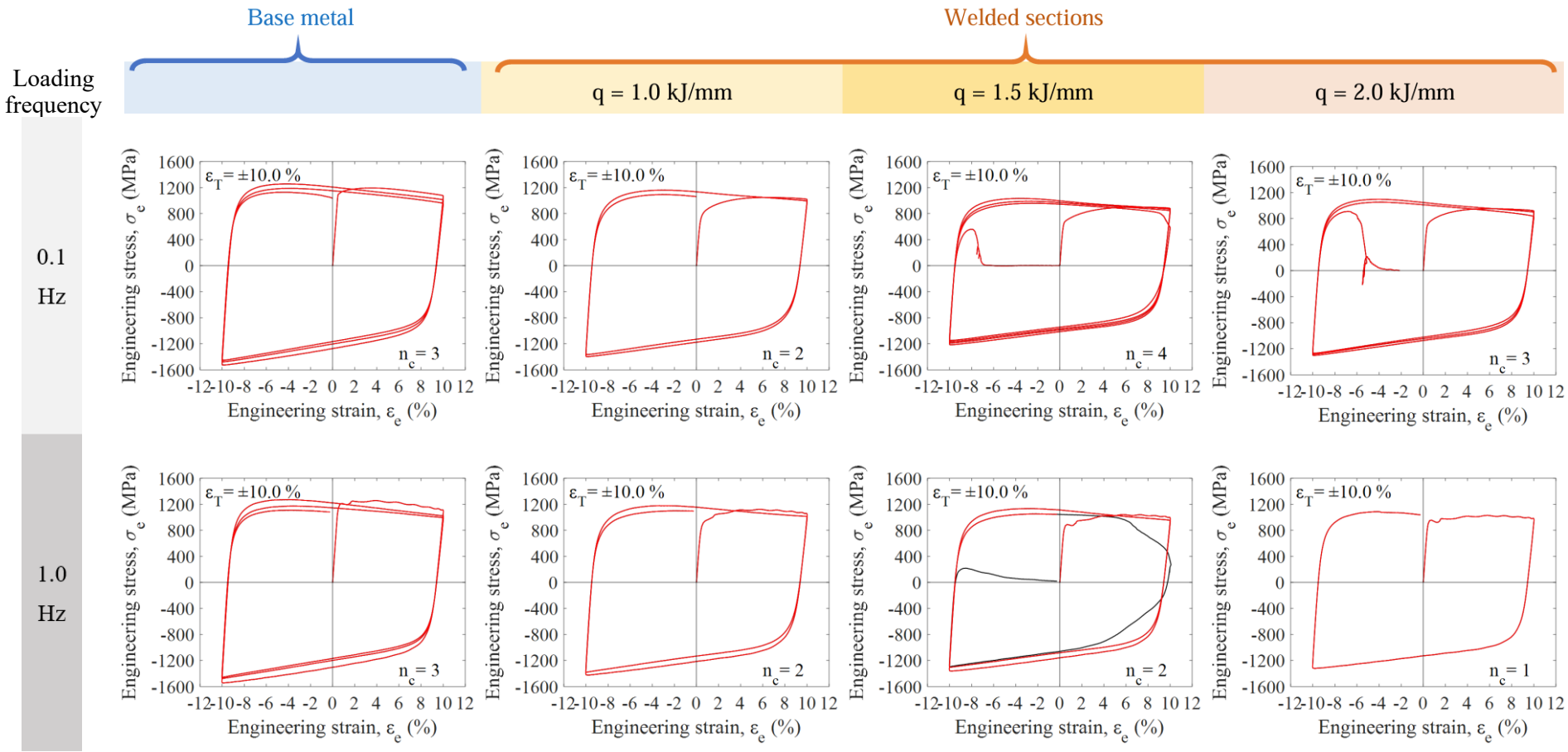

Figure 4.29 Engineering stress-strain curves of the cyclic tests on S960 at $\varepsilon_T = \pm 10.0$ %

S355 base metal

S355 welded section

S690 base metal

S690 welded section

S960 base metal

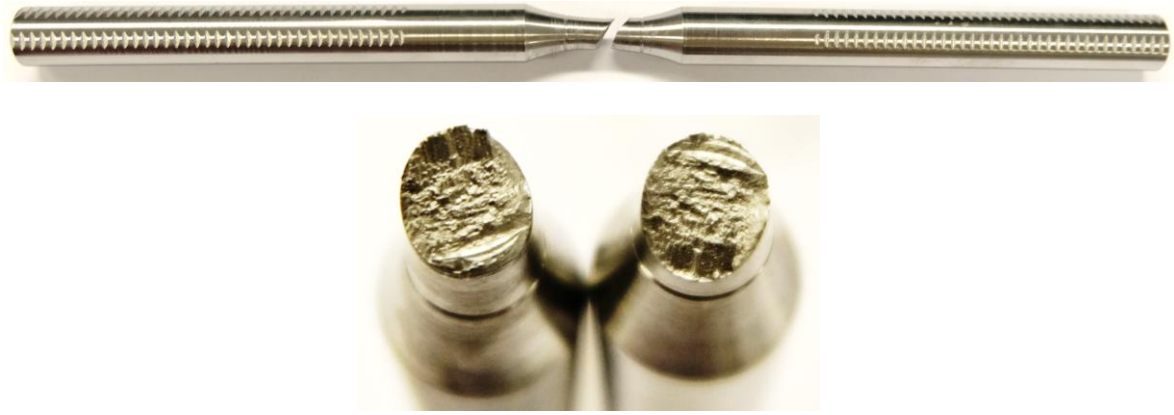

S960 welded section

Figure 4.30 Typical failed coupons and their fractured surfaces after cyclic tests

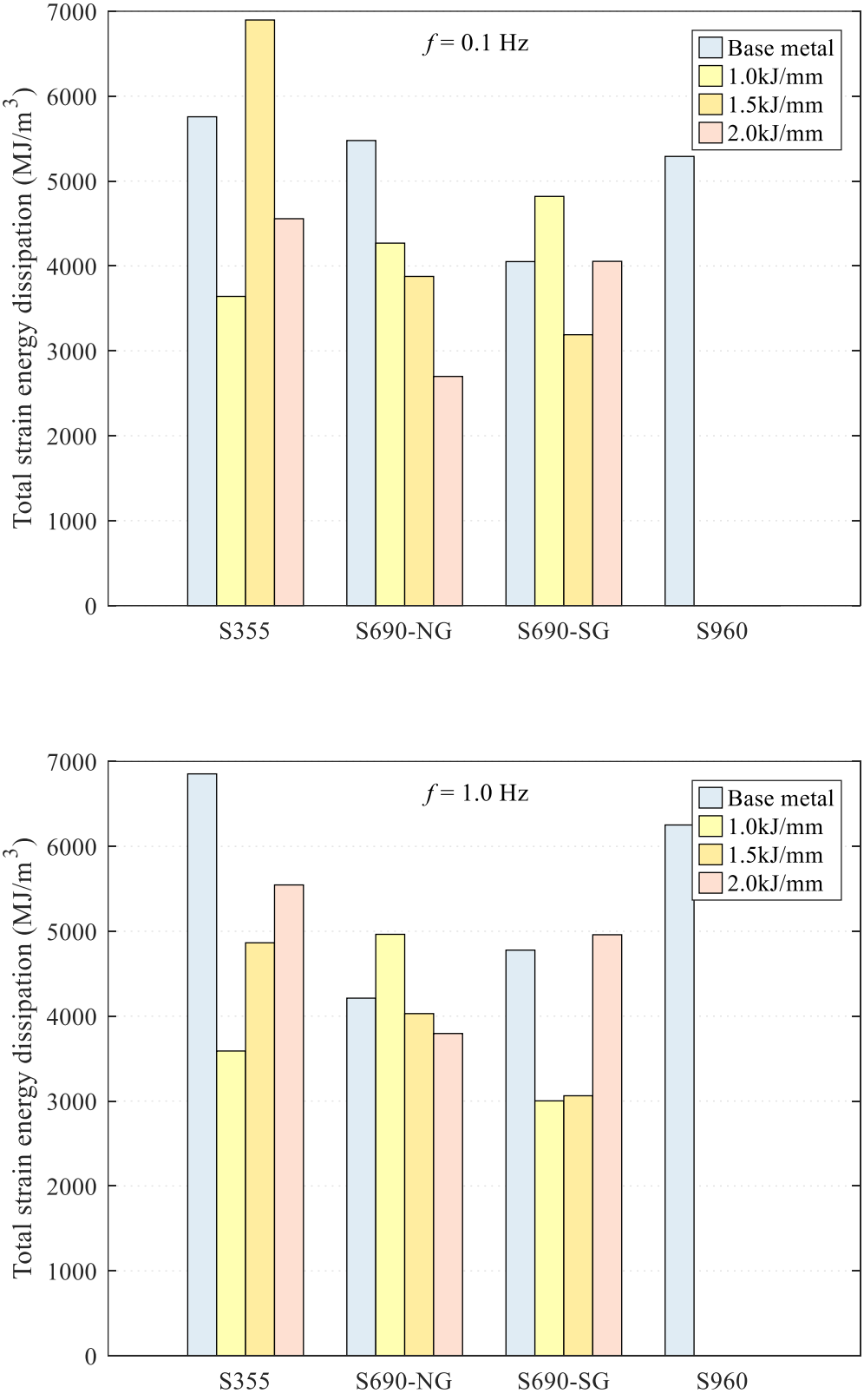

Figure 4.31 Total strain energy dissipation of the cyclic tests at $\varepsilon_T = \pm 1.0$ %

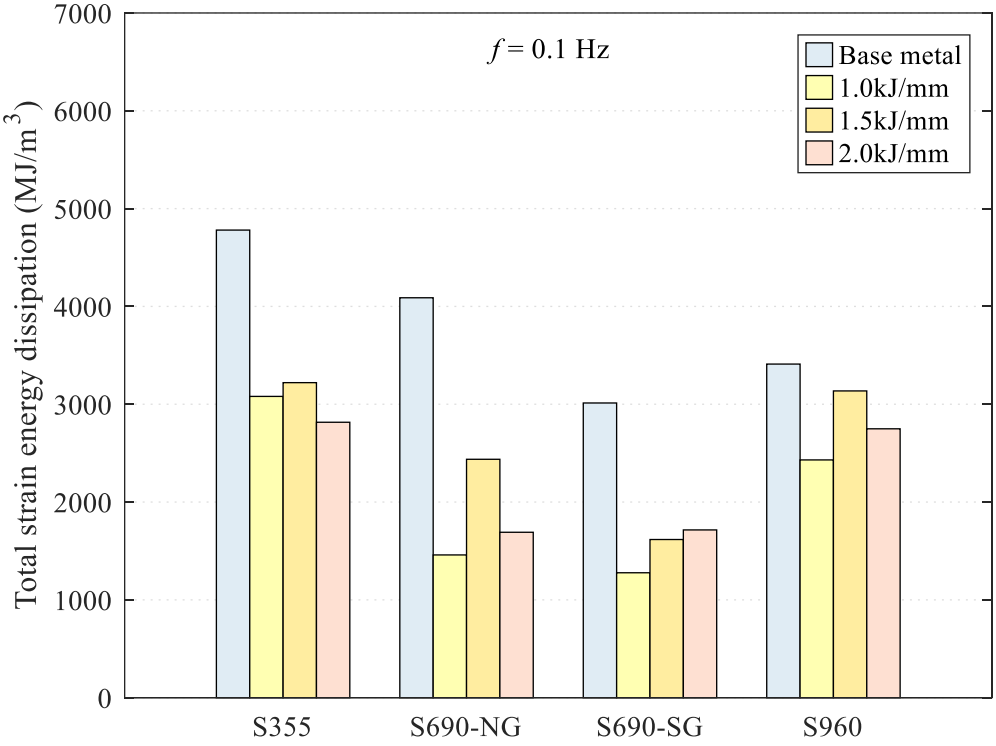

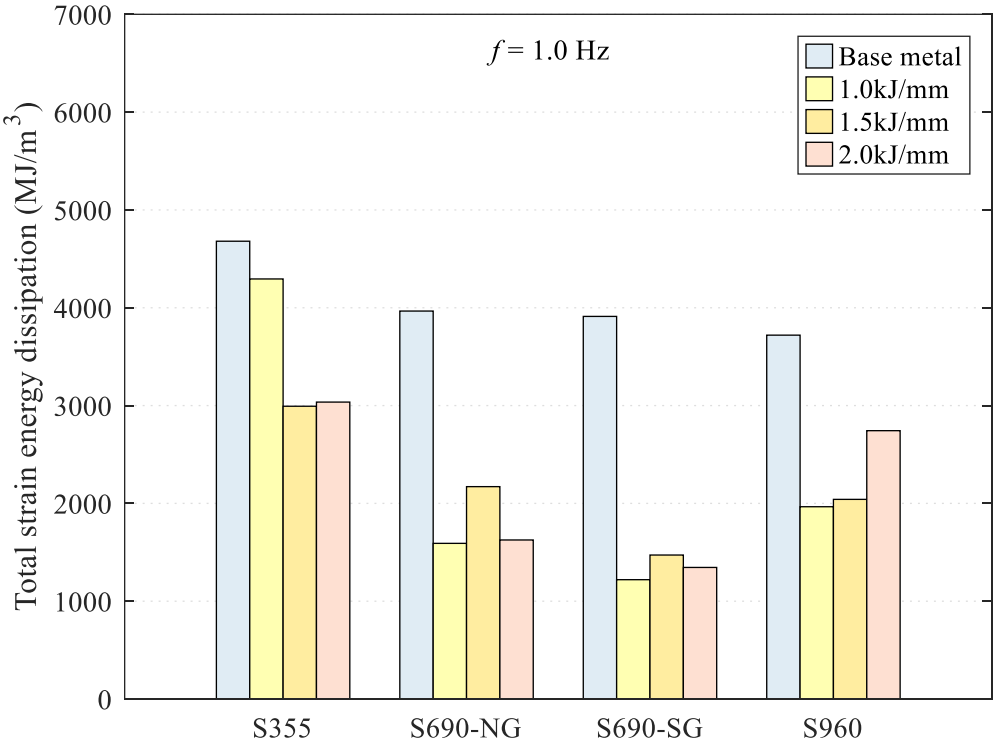

Figure 4.32 Total strain energy dissipation of the cyclic tests at $\varepsilon_T = \pm 2.5$ %

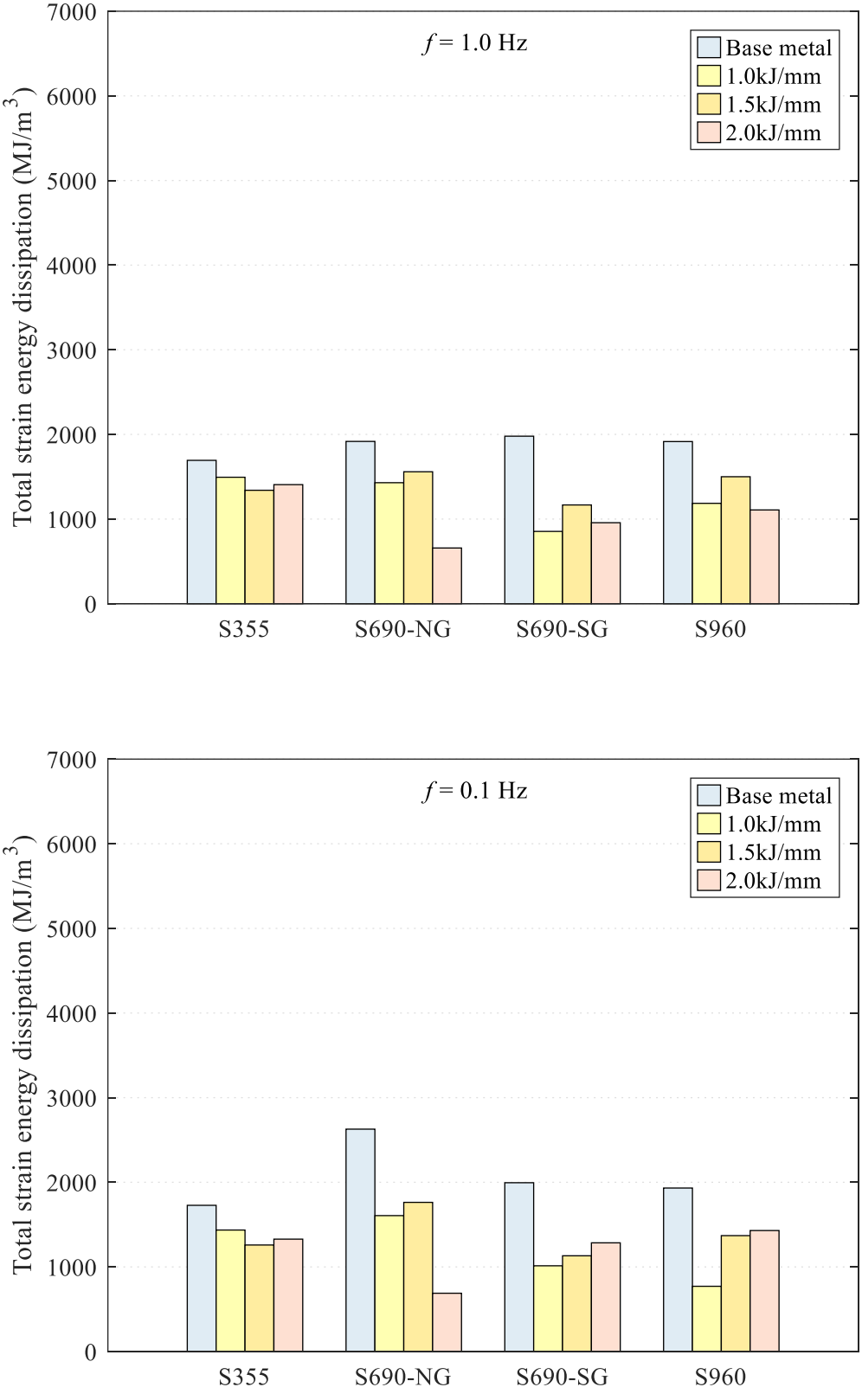

Figure 4.33 Total strain energy dissipation of the cyclic tests at $\varepsilon_T = \pm 5.0$ %

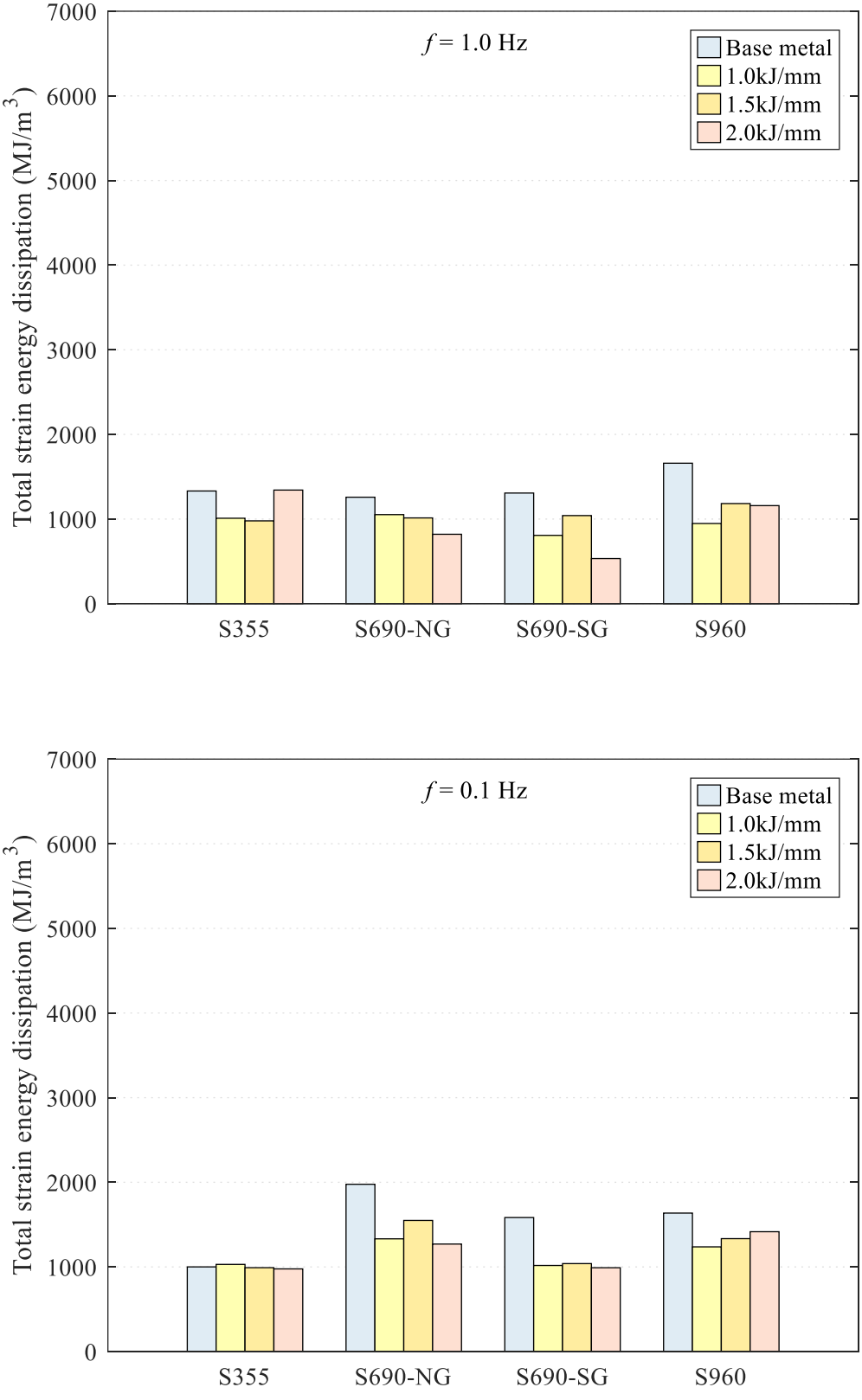

Figure 4.34 Total strain energy dissipation of the cyclic tests at $\varepsilon_T = \pm 7.5$ %

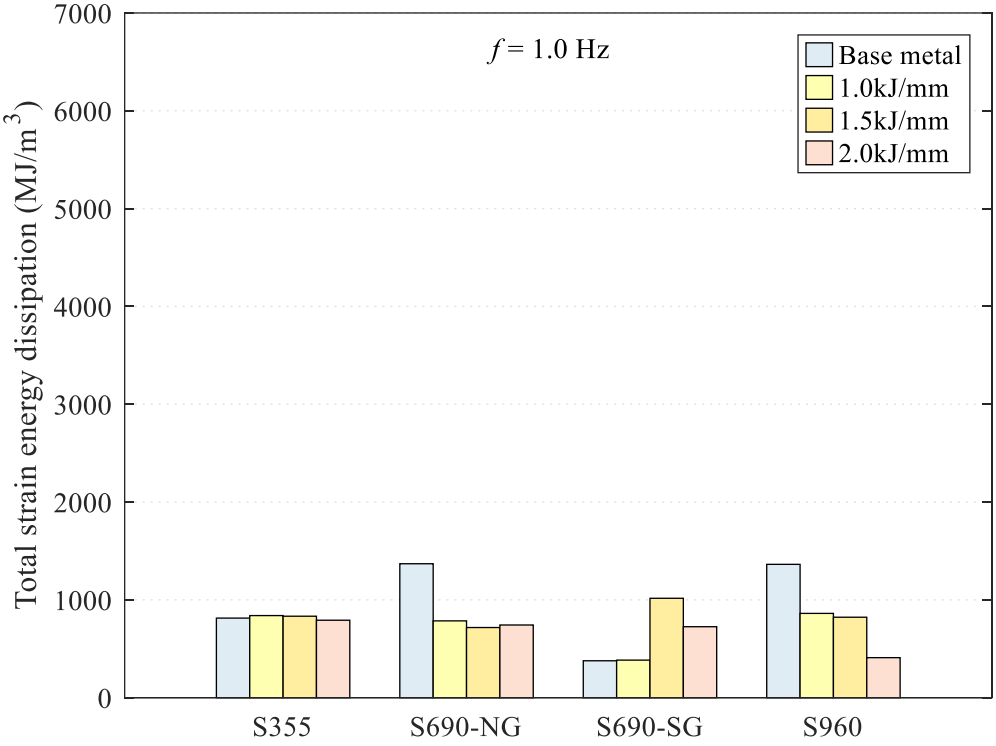

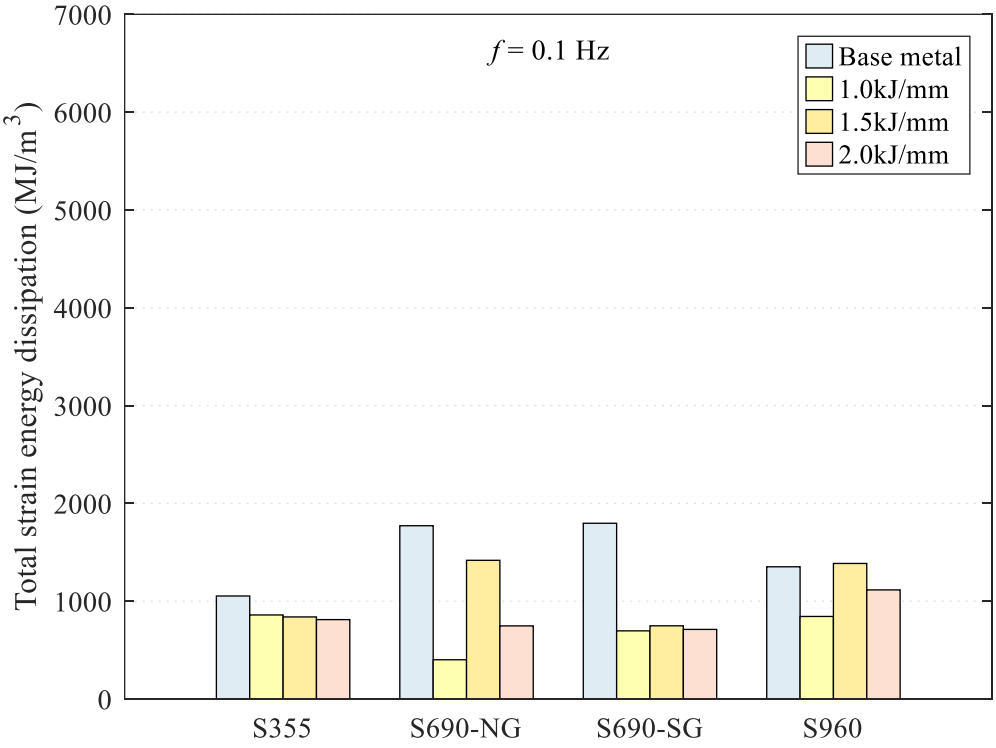

Figure 4.35 Total strain energy dissipation of the cyclic tests at $\varepsilon_T = \pm 10.0$ %

Table 4.1 Test programme of cyclic tests on funnel-shaped coupons

a) S355, S690 (Nangang) and S690 (Shougang)

Loading frequency f (Hz)	Nos of test for each steel plate and corresponding welded sections																			
	$\varepsilon_T = \pm 1.0$ %				$\varepsilon_T = \pm 2.5$ %				$\varepsilon_T = \pm 5.0$ %				$\varepsilon_T = \pm 7.5$ %				$\varepsilon_T = \pm 10.0$ %			
	Base metal	Welded sections			Base metal	Welded sections			Base metal	Welded sections			Base metal	Welded sections			Base metal	Welded sections		
		$q_{1.0}$	$q_{1.5}$	$q_{2.0}$		$q_{1.0}$	$q_{1.5}$	$q_{2.0}$		$q_{1.0}$	$q_{1.5}$	$q_{2.0}$		$q_{1.0}$	$q_{1.5}$	$q_{2.0}$		$q_{1.0}$	$q_{1.5}$	$q_{2.0}$
0.1	1	1	1	1	1	1	1	1	1	1	1	1	1	1	1	1	1	1	1	1
1.0	1	1	1	1	1	1	1	1	1	1	1	1	1	1	1	1	1	1	1	1

Notes: "$q_{1.0}$" denotes q = 1.0 kJ/mm, "$q_{1.5}$" denotes q = 1.5 kJ/mm, and "$q_{2.0}$" denotes q = 2.0 kJ/mm.

b) S960

Loading frequency f (Hz)	Nos of test for each steel plate and corresponding welded sections																			
	$\varepsilon_T = \pm 1.0$ %				$\varepsilon_T = \pm 2.5$ %				$\varepsilon_T = \pm 5.0$ %				$\varepsilon_T = \pm 7.5$ %				$\varepsilon_T = \pm 10.0$ %			
	Base metal	Welded sections			Base metal	Welded sections			Base metal	Welded sections			Base metal	Welded sections			Base metal	Welded sections		
		$q_{1.0}$	$q_{1.5}$	$q_{2.0}$		$q_{1.0}$	$q_{1.5}$	$q_{2.0}$		$q_{1.0}$	$q_{1.5}$	$q_{2.0}$		$q_{1.0}$	$q_{1.5}$	$q_{2.0}$		$q_{1.0}$	$q_{1.5}$	$q_{2.0}$
0.1	1	-	-	-	1	1	1	1	1	1	1	1	1	1	1	1	1	1	1	1
1.0	1	-	-	-	1	1	1	1	1	1	1	1	1	1	1	1	1	1	1	1

Notes: "$q_{1.0}$" denotes q = 1.0 kJ/mm, "$q_{1.5}$" denotes q = 1.5 kJ/mm, and "$q_{2.0}$" denotes q = 2.0 kJ/mm.

Table 4.2 Summary of f_y of the 1st cycle

a) S355

Loading frequency *f* (Hz)	Yield strength of the 1st cycle, f_{y1} (N/mm^2)																			
	ε_T = ±1.0 %				ε_T = ±2.5 %				ε_T = ±5.0 %				ε_T = ±7.5 %				ε_T = ±10.0 %			
	Base metal	Welded sections			Base metal	Welded sections			Base metal	Welded sections			Base metal	Welded sections			Base metal	Welded sections		
		$q_{1.0}$	$q_{1.5}$	$q_{2.0}$		$q_{1.0}$	$q_{1.5}$	$q_{2.0}$		$q_{1.0}$	$q_{1.5}$	$q_{2.0}$		$q_{1.0}$	$q_{1.5}$	$q_{2.0}$		$q_{1.0}$	$q_{1.5}$	$q_{2.0}$
0.1	420	500	512	421	388	493	498	425	377	515	499	428	429	511	501	425	419	513	500	437
1.0	444	513	528	433	459	539	528	452	456	561	539	471	473	575	545	477	492	597	596	491

Notes: "$q_{1.0}$" denotes q = 1.0 kJ/mm, "$q_{1.5}$" denotes q = 1.5 kJ/mm, and "$q_{2.0}$" denotes q = 2.0 kJ/mm.

b) S690 (Nangang)

Loading frequency *f* (Hz)	Yield strength of the 1st cycle, f_{y1} (N/mm^2)																			
	ε_T = ±1.0 %				ε_T = ±2.5 %				ε_T = ±5.0 %				ε_T = ±7.5 %				ε_T = ±10.0 %			
	Base metal	Welded sections			Base metal	Welded sections			Base metal	Welded sections			Base metal	Welded sections			Base metal	Welded sections		
		$q_{1.0}$	$q_{1.5}$	$q_{2.0}$		$q_{1.0}$	$q_{1.5}$	$q_{2.0}$		$q_{1.0}$	$q_{1.5}$	$q_{2.0}$		$q_{1.0}$	$q_{1.5}$	$q_{2.0}$		$q_{1.0}$	$q_{1.5}$	$q_{2.0}$
0.1	904	877	756	747	844	852	751	757	911	851	771	744	857	822	784	741	896	886	802	752
1.0	902	878	765	742	899	864	760	724	940	897	782	745	936	853	778	753	924	905	817	791

Notes: "$q_{1.0}$" denotes q = 1.0 kJ/mm, "$q_{1.5}$" denotes q = 1.5 kJ/mm, and "$q_{2.0}$" denotes q = 2.0 kJ/mm.

c) S690 (Shougang)

Loading frequency f (Hz)	Yield strength of the 1st cycle, f_{y1} (N/mm^2)																			
	ε_T = ±1.0 %				ε_T = ±2.5 %				ε_T = ±5.0 %				ε_T = ±7.5 %				ε_T = ±10.0 %			
	Base metal	Welded sections			Base metal	Welded sections			Base metal	Welded sections			Base metal	Welded sections			Base metal	Welded sections		
		$q_{1.0}$	$q_{1.5}$	$q_{2.0}$		$q_{1.0}$	$q_{1.5}$	$q_{2.0}$		$q_{1.0}$	$q_{1.5}$	$q_{2.0}$		$q_{1.0}$	$q_{1.5}$	$q_{2.0}$		$q_{1.0}$	$q_{1.5}$	$q_{2.0}$
0.1	873	875	741	714	890	832	756	743	839	856	768	723	846	848	759	724	875	844	766	724
1.0	903	886	802	731	902	901	809	751	932	915	801	755	939	907	805	778	939	920	795	784

Notes: "$q_{1.0}$" denotes q = 1.0 kJ/mm, "$q_{1.5}$" denotes q = 1.5 kJ/mm, and "$q_{2.0}$" denotes q = 2.0 kJ/mm.

d) S960

Loading frequency f (Hz)	Yield strength of the 1st cycle, f_{y1} (N/mm^2)																			
	ε_T = ±1.0 %				ε_T = ±2.5 %				ε_T = ±5.0 %				ε_T = ±7.5 %				ε_T = ±10.0 %			
	Base metal	Welded sections			Base metal	Welded sections			Base metal	Welded sections			Base metal	Welded sections			Base metal	Welded sections		
		$q_{1.0}$	$q_{1.5}$	$q_{2.0}$		$q_{1.0}$	$q_{1.5}$	$q_{2.0}$		$q_{1.0}$	$q_{1.5}$	$q_{2.0}$		$q_{1.0}$	$q_{1.5}$	$q_{2.0}$		$q_{1.0}$	$q_{1.5}$	$q_{2.0}$
0.1	1,128	-	-	-	1,140	893	686	727	1,135	817	693	731	1,117	778	698	716	1,119	790	683	736
1.0	1,167	-	-	-	1,170	911	849	926	1,183	926	871	956	1,199	927	880	943	1,207	886	880	953

Notes: "$q_{1.0}$" denotes q = 1.0 kJ/mm, "$q_{1.5}$" denotes q = 1.5 kJ/mm, and "$q_{2.0}$" denotes q = 2.0 kJ/mm.

Table 4.3 Summary of number of completed cycles

a) S355

Loading frequency f (Hz)	No. of cycles completed, n_c																			
	$\varepsilon_T = \pm 1.0$ %				$\varepsilon_T = \pm 2.5$ %				$\varepsilon_T = \pm 5.0$ %				$\varepsilon_T = \pm 7.5$ %				$\varepsilon_T = \pm 10.0$ %			
	Base metal	Welded sections			Base metal	Welded sections			Base metal	Welded sections			Base metal	Welded sections			Base metal	Welded sections		
		$q_{1.0}$	$q_{1.5}$	$q_{2.0}$		$q_{1.0}$	$q_{1.5}$	$q_{2.0}$		$q_{1.0}$	$q_{1.5}$	$q_{2.0}$		$q_{1.0}$	$q_{1.5}$	$q_{2.0}$		$q_{1.0}$	$q_{1.5}$	$q_{2.0}$
0.1	383	229	439	290	86	57	61	54	14	11	10	11	5	5	5	5	4	3	3	3
1.0	448	215	303	350	89	82	57	59	14	12	11	12	7	5	5	7	3	3	3	3

Notes: "$q_{1.0}$" denotes q = 1.0 kJ/mm, "$q_{1.5}$" denotes q = 1.5 kJ/mm, and "$q_{2.0}$" denotes q = 2.0 kJ/mm.

b) S690 (Nangang)

Loading frequency f (Hz)	No. of cycles completed, n_c																			
	$\varepsilon_T = \pm 1.0$ %				$\varepsilon_T = \pm 2.5$ %				$\varepsilon_T = \pm 5.0$ %				$\varepsilon_T = \pm 7.5$ %				$\varepsilon_T = \pm 10.0$ %			
	Base metal	Welded sections			Base metal	Welded sections			Base metal	Welded sections			Base metal	Welded sections			Base metal	Welded sections		
		$q_{1.0}$	$q_{1.5}$	$q_{2.0}$		$q_{1.0}$	$q_{1.5}$	$q_{2.0}$		$q_{1.0}$	$q_{1.5}$	$q_{2.0}$		$q_{1.0}$	$q_{1.5}$	$q_{2.0}$		$q_{1.0}$	$q_{1.5}$	$q_{2.0}$
0.1	243	180	183	130	60	19	35	24	16	9	11	4	8	5	6	5	5	1	4	2
1.0	180	211	193	178	57	21	32	23	12	8	10	4	5	4	4	3	4	2	2	2

Notes: "$q_{1.0}$" denotes q = 1.0 kJ/mm, "$q_{1.5}$" denotes q = 1.5 kJ/mm, and "$q_{2.0}$" denotes q = 2.0 kJ/mm.

c) S690 (Shougang)

Loading frequency *f* (Hz)	No. of cycles completed, n_c																		
	$\varepsilon_T = \pm 1.0$ %				$\varepsilon_T = \pm 2.5$ %				$\varepsilon_T = \pm 5.0$ %				$\varepsilon_T = \pm 7.5$ %				$\varepsilon_T = \pm 10.0$ %			
	Base metal	Welded sections			Base metal	Welded sections			Base metal	Welded sections			Base metal	Welded sections			Base metal	Welded sections		
		$q_{1.0}$	$q_{1.5}$	$q_{2.0}$		$q_{1.0}$	$q_{1.5}$	$q_{2.0}$		$q_{1.0}$	$q_{1.5}$	$q_{2.0}$		$q_{1.0}$	$q_{1.5}$	$q_{2.0}$		$q_{1.0}$	$q_{1.5}$	$q_{2.0}$
0.1	170	215	152	193	39	17	23	24	12	6	7	8	6	4	4	4	5	2	2	2
1.0	200	130	137	235	53	16	20	19	12	5	7	6	5	3	4	2	1	1	3	2

Notes: "$q_{1.0}$" denotes q = 1.0 kJ/mm, "$q_{1.5}$" denotes q = 1.5 kJ/mm, and "$q_{2.0}$" denotes q = 2.0 kJ/mm.

d) S960

Loading frequency *f* (Hz)	No. of cycles completed, n_c																		
	$\varepsilon_T = \pm 1.0$ %				$\varepsilon_T = \pm 2.5$ %				$\varepsilon_T = \pm 5.0$ %				$\varepsilon_T = \pm 7.5$ %				$\varepsilon_T = \pm 10.0$ %			
	Base metal	Welded sections			Base metal	Welded sections			Base metal	Welded sections			Base metal	Welded sections			Base metal	Welded sections		
		$q_{1.0}$	$q_{1.5}$	$q_{2.0}$		$q_{1.0}$	$q_{1.5}$	$q_{2.0}$		$q_{1.0}$	$q_{1.5}$	$q_{2.0}$		$q_{1.0}$	$q_{1.5}$	$q_{2.0}$		$q_{1.0}$	$q_{1.5}$	$q_{2.0}$
0.1	188	-	-	-	36	28	43	36	9	4	8	8	5	4	5	5	3	2	4	3
1.0	218	-	-	-	39	23	25	35	9	6	8	5	5	3	4	4	3	2	2	1

Notes: "$q_{1.0}$" denotes q = 1.0 kJ/mm, "$q_{1.5}$" denotes q = 1.5 kJ/mm, and "$q_{2.0}$" denotes q = 2.0 kJ/mm.

Table 4.4 Summary of total strain energy dissipation of S355, S690, and S960 steels

a) S355

Loading frequency *f* (Hz)	Total strain energy dissipation, *MJ/mm³*																			
	$\varepsilon_T = \pm 1.0$ %				$\varepsilon_T = \pm 2.5$ %				$\varepsilon_T = \pm 5.0$ %				$\varepsilon_T = \pm 7.5$ %				$\varepsilon_T = \pm 10.0$ %			
	Base metal	Welded sections			Base metal	Welded sections			Base metal	Welded sections			Base metal	Welded sections			Base metal	Welded sections		
		$q_{1.0}$	$q_{1.5}$	$q_{2.0}$		$q_{1.0}$	$q_{1.5}$	$q_{2.0}$		$q_{1.0}$	$q_{1.5}$	$q_{2.0}$		$q_{1.0}$	$q_{1.5}$	$q_{2.0}$		$q_{1.0}$	$q_{1.5}$	$q_{2.0}$
0.1	5,757	3,641	6,897	4,556	4,781	3,080	3,221	2,816	1,728	1,436	1,259	1,328	1,000	1,030	991	977	1,053	859	839	812
1.0	6,854	3,589	4,864	5,546	4,680	4,294	2,993	3,036	1,694	1,494	1,340	1,407	1,331	1,009	979	1,342	814	839	833	792

Notes: "$q_{1.0}$" denotes q = 1.0 kJ/mm, "$q_{1.5}$" denotes q = 1.5 kJ/mm, and "$q_{2.0}$" denotes q = 2.0 kJ/mm.

b) S690 (Nangang)

Loading frequency *f* (Hz)	Total strain energy dissipation, *MJ/mm³*																			
	$\varepsilon_T = \pm 1.0$ %				$\varepsilon_T = \pm 2.5$ %				$\varepsilon_T = \pm 5.0$ %				$\varepsilon_T = \pm 7.5$ %				$\varepsilon_T = \pm 10.0$ %			
	Base metal	Welded sections			Base metal	Welded sections			Base metal	Welded sections			Base metal	Welded sections			Base metal	Welded sections		
		$q_{1.0}$	$q_{1.5}$	$q_{2.0}$		$q_{1.0}$	$q_{1.5}$	$q_{2.0}$		$q_{1.0}$	$q_{1.5}$	$q_{2.0}$		$q_{1.0}$	$q_{1.5}$	$q_{2.0}$		$q_{1.0}$	$q_{1.5}$	$q_{2.0}$
0.1	4,617	4,269	3,877	2,699	4,089	1,459	2,437	1,691	2,628	1,606	1,763	689	1,977	1,332	1,549	1,270	1,772	401	1,418	748
1.0	4,167	4,964	4,030	3,796	3,966	1,591	2,171	1,626	1,917	1,429	1,559	658	1,258	1,052	1,013	820	1,369	785	717	743

Notes: "$q_{1.0}$" denotes q = 1.0 kJ/mm, "$q_{1.5}$" denotes q = 1.5 kJ/mm, and "$q_{2.0}$" denotes q = 2.0 kJ/mm.

c) S690 (Shougang)

Loading frequency *f* (Hz)	Total strain energy dissipation, *MJ/mm³*																			
	$\varepsilon_T = \pm 1.0$ %				$\varepsilon_T = \pm 2.5$ %				$\varepsilon_T = \pm 5.0$ %				$\varepsilon_T = \pm 7.5$ %				$\varepsilon_T = \pm 10.0$ %			
	Base metal	Welded sections			Base metal	Welded sections			Base metal	Welded sections			Base metal	Welded sections			Base metal	Welded sections		
		$q_{1.0}$	$q_{1.5}$	$q_{2.0}$		$q_{1.0}$	$q_{1.5}$	$q_{2.0}$		$q_{1.0}$	$q_{1.5}$	$q_{2.0}$		$q_{1.0}$	$q_{1.5}$	$q_{2.0}$		$q_{1.0}$	$q_{1.5}$	$q_{2.0}$
0.1	4,051	4,819	3,190	4,054	3,013	1,277	1,617	1,715	1,995	1,014	1,132	1,285	1,583	1,017	1,039	990	1,797	697	749	712
1.0	4,778	3,002	3,062	4,959	3,912	1,220	1,472	1,345	1,979	854	1,167	957	1,307	807	1,041	533	377	384	1,016	725

Notes: "$q_{1.0}$" denotes q = 1.0 kJ/mm, "$q_{1.5}$" denotes q = 1.5 kJ/mm, and "$q_{2.0}$" denotes q = 2.0 kJ/mm.

d) S960

Loading frequency *f* (Hz)	Total strain energy dissipation, *MJ/mm³*																			
	$\varepsilon_T = \pm 1.0$ %				$\varepsilon_T = \pm 2.5$ %				$\varepsilon_T = \pm 5.0$ %				$\varepsilon_T = \pm 7.5$ %				$\varepsilon_T = \pm 10.0$ %			
	Base metal	Welded sections			Base metal	Welded sections			Base metal	Welded sections			Base metal	Welded sections			Base metal	Welded sections		
		$q_{1.0}$	$q_{1.5}$	$q_{2.0}$		$q_{1.0}$	$q_{1.5}$	$q_{2.0}$		$q_{1.0}$	$q_{1.5}$	$q_{2.0}$		$q_{1.0}$	$q_{1.5}$	$q_{2.0}$		$q_{1.0}$	$q_{1.5}$	$q_{2.0}$
0.1	5,290	-	-	-	3,411	2,431	3,136	2,749	1,932	771	1,370	1,430	1,636	1,237	1,334	1,416	1,352	844	1,386	1,116
1.0	6,226	-	-	-	3,639	1,966	2,041	2,744	1,915	1,186	1,500	946	1,660	947	1,183	1,158	1,363	862	823	409

Notes: "$q_{1.0}$" denotes q = 1.0 kJ/mm, "$q_{1.5}$" denotes q = 1.5 kJ/mm, and "$q_{2.0}$" denotes q = 2.0 kJ/mm.

CHAPTER 5 T-JOINTS BETWEEN HIGH STRENGTH S690 STEEL CIRCULAR HOLLOW SECTIONS

5.1 Introduction

This chapter presents a systematic experimental investigation into the structural behaviour of T-joints between cold-formed circular hollow sections of S690 steel under cyclic actions. A brief description on fabrication process of the cold-formed circular hollow sections and their T-joints is provided.

In order to provide specific reference data on structural behaviour of these T-joints under in-plane bending, a total of 4 monotonic tests on T-joints are carried out, and their deformation characteristics are analysed to provide data for subsequent tests. Then, a total of 6 cyclic tests on these T-joints are carried out, and their deformation characteristics are analysed to provide engineering data to appraise their cyclic responses. These include the applied load-lateral displacement curves of the T-joints together with their corresponding applied load-strain curves. A series of close-up views on the welded junctions of these T-joints are also provided to examine crack initiation and growth during the tests.

All the monotonic and the cyclic tests provide measured data for calibration of subsequent finite element modelling presented in Chapter 7.

5.2 Fabrication process of cold-formed circular hollow sections

The S690 steel plates adopted in the present investigation are 6.0 and 10.0 mm thick, and they are manufactured to EN 10025-6:2019+A1:2022 (CEN, 2022) which requirements on mechanical properties are presented in Table 5.1a). Standard tensile tests on these steel plates are conducted, and key test results are also summarized in Table 5.1a) for easy comparison.

The welding electrode ER110S-G (with a diameter of 1.2 mm) to AWS A5.28 (2005) is employed. The mechanical properties of the welding electrode are presented in Table 5.1b) for easy comparison.

It should be noted that all the CFCHS are fabricated in a qualified steelwork fabricator with highly experienced welders, and the manufacturing process of both the cold-formed circular hollow sections and their T-joints are described as follows:

- As demonstrated in Figure 5.1a), illustrations of steel plates of varying thicknesses and dimensions are provided. The material is then cut into narrow strips using plasma cutting. The edges of these plates are locally bent using a press-braking machine, after which they are transversely bent using a three-roller bending machine, positioned at various points along the length of the plates to form circular sections with specific diameters.
- Cold-bent tubes with tack welds are shown in Figure 5.1b).
- Longitudinal welding is carried out by a qualified welder utilising the gas metal arc welding (GMAW) method as demonstrated in Figure 5.1c). This is performed in accordance with standard welding practices.
- In order to prepare welding of the junctions between the brace and the chord members, the ends of the brace members are profile-cut, as shown in Figure 5.1d), to allow for direct welding with the chord members.
- Figure 5.1e) illustrates the joint assembly of the brace/chord junctions after alignment and provision of temporary attachments.
- Figure 5.1f) illustrates typical welding process of the brace/chord junctions of the T-joints.

Figure 5.2 illustrates details of various welding equipment and materials employed in the fabricator. Close-up views of various welding details of parts of these T-joints between CFCHS

are shown in Figure 5.3. Figure 5.4 illustrates the geometry of a T-joint with various cross-sectional dimensions and geometrical parameters α, β, 2γ and τ. These geometrical parameters are defined as follows:

$$\alpha = 2 L_0 / d_0 \quad \text{Equation 5.1}$$

$$\beta = d_1 / d_0 \quad \text{Equation 5.2}$$

$$2\gamma = d_0 / t_0 \quad \text{Equation 5.3}$$

$$\tau = t_1 / t_0 \quad \text{Equation 5.4}$$

where

L is the span of the chord member between pinned supports;

L_0 is the length of the chord member;

d_o and d_1 are the diameters of the chord and the brace members respectively; and

t_o and t_1 are the thicknesses of the chord and the brace members respectively.

5.3 Experimental investigation into S690 T-joints under monotonic actions

A total of 4 monotonic tests on T-joints with two different sets of dimensions are tested to provide reference data for subsequent tests of these T-joints under cyclic actions. Details of the monotonic tests are presented as follows.

5.3.1 Objectives and test programme

In order to provide reference data for selection of various parameters for subsequent cyclic tests on T-joints, a total of 4 monotonic tests on T-joints with the following sets of dimensions are conducted:

a) CHS 250 x 10 S690 are employed to be the chord members of all the 4 T-joints, and
b) CHS 150 x 6 S690 are employed to be the brace members of 2 T-joints while CHS 200 x 10 S690 are employed to be the brace members of the other 2 T-joints

Table 5.2 summarizes the test programme. It should be noted that the lateral load is applied at a distance which is equal to 760 mm from the top surface of the chord member.

5.3.2 Test set-up, instrumentation, and loading procedures

Figure 5.5a) illustrates the test set-up for the T-joints under monotonic actions. It should be noted that the test specimen is pin-supported at both ends onto a strong floor. A lateral load is applied to the brace member of the test specimen through a pinned attachment with an actuator in a displacement control mode. Figure 5.5b) illustrates details of the instrumentation adopted in the test, and both the applied load P, and the lateral displacement δ are measured continuously and recorded with a computer data logger throughout the test. It should be noted that the load is applied gradually at a rate about 0.5 to 1.0 mm per minute, and the test is terminated when there is a sudden failure in the test specimen or an excessive deformation at 100 mm. Table 5.3 summarizes details of the instrumentation.

5.3.3 Test results and data analysis

All the tests have been conducted successfully, and Table 5.4 summarizes key results of all the tests. The measured applied load-lateral displacement (P-δ) curves of all the T-joints are plotted onto the same graph in Figure 5.6a) for a direct comparison. It is shown that

a) the measured curves for Tests MT1a and MT1b as well as those for Tests MT2a and MT2b follow each other very closely throughout the entire deformation ranges, and
b) all the T-joints exhibit a high degree of ductility until a sudden failure of the T-joints take place, i.e. a failure mode of punching shear, as shown in Figure 5.6b).

After data analysis on the measured applied load-strain (P-ε) curves, the values of the applied

loads and the displacements at specific values of ε at 0.5%, 2.5% and 5.0% are plotted in Figure 5.6a) for cyclic tests described in Section 5.4.

5.4 Experimental investigation into S690 T-joints under cyclic actions

5.4.1 Objectives and test programme

In order to examine the cyclic responses of T-joints with various sets of geometrical parameters under different target strains, a total of 6 cyclic tests on T-joints with the following sets of dimensions are conducted:

a) CHS 250 x 10 S690 are employed to be the chord members of all the 6 T-joints, and
b) CHS 150 x 6 S690 are employed to be the brace members of 2 T-joints while CHS 200 x 10 S690 are employed to be the brace members of the other 4 T-joints.

Table 5.5 summarizes the test programme. It should be noted that these T-joints are welded under two different heat energy input q, i.e. q = 1.0 and 2.0 kJ/mm. Therefore, Joints CT1 and CT2 have the same member configuration with two different heat energy input q. Similarly, Joints CT3 to CT6 have the same member configuration under two different heat energy input.

5.4.2 Test setup, instrumentation and loading procedures

The loading protocol for the T-joints under cyclic actions is plotted in Figure 5.7, and the target displacement is designed to be constant in every cycle, and controlled through an actuator in a displacement control mode. Figure 5.8 illustrates both the test set-up and the instrumentation for the T-joints under cyclic actions. It should be noted that the test specimen is pin-supported at both ends onto a strong floor. A total of 8 displacement transducers, i.e. LVDT1 to LVDT8, were employed to measure both the vertical and the horizontal displacements of specific locations of the T-joints. Four strain gauges, i.e. SG1 to SG4, were mounted onto specific

locations in the vicinities of the welded junctions of the T-joints. Table 5.3 summarizes details of the instrumentation.

According to the test results of the monotonic tests on T-joints presented in Section 5.3, it should be noted that

- for Joints MT1a and MT1b, when the principal strains in the vicinity of the welded junctions reach 0.5% and 2.5%, the corresponding lateral displacements at the top of the brace members δ are found to be 19.0 and 38.0 mm respectively; and
- for Joints MT2a and MT2b, when the principal strains in the vicinity of the welded junctions reach 2.5% and 5.0%, the corresponding lateral displacements at the top of the brace members δ are found to be 20.3 and 30.3 mm respectively.

These lateral displacements δ are adopted as the target displacements of cyclic tests on these T-joints under displacement control. All these loading details are presented in Table 5.6.

In each cyclic test, preloading is carried out and a preload of 30% of the target applied load is adopted. Then, the applied load P, and both the lateral displacement δ^+ and δ^- (which are the displacements along the positive and the negative x-axis respectively) are measured continuously and recorded with a computer data logger throughout the test. It should be noted that the load is applied gradually at a rate about 10 mm per minute. The test is terminated when there is a sudden failure in the test specimen.

5.4.3 Test results and data analysis

All the tests have been conducted successfully except Joint CT2, and Table 5.7 summarizes key results of all the tests. Various load-displacement curves and load-strain curves of the tests

are presented in the following section with photos on crack initiation and growth in the vicinity of the welded junctions. It is shown that these T-joints exhibit a high level of cyclic ductility with large dissipation energy.

In order to illustrate various plots of the deformation characteristics of these T-joints under cyclic actions, an example is taken on Joint CT1, and Figure 5.9 plots the following:

- Figure 5.9a) plots the applied load-lateral displacement (P-δ) curve of Joint CT1, and a bi-linear relationship is shown. It should be noted that there is a significant degradation in resistance when the applied load is applied along the negative x-axis while no degradation in resistance when the applied load is applied along the positive x-axis.
- Figure 5.9b) plots the strain variation (P-4ε) curves measured at four locations along the chord member in the vicinity of the welded junction, namely SG1 to SG4, and hence, different characteristics are apparent.
- For improved clarity, Figure 5.9c) plots each of these strain variations in four separate graphs for easy comparison. It is apparent that there is a significant degradation in the slope of the (P-ε) curve of SG1, and this indicates a gradual reduction in stiffness. Minor or even no reduction in stiffness is found in SG2 to SG4.

For easy of comparison, the test results of all the T-joints are organized and compared as follows for direct presentation.

a) Deformation characteristics of Joints CT1 and CT2

The applied load-lateral displacement (P-δ) curve and the strain variation curve (P-4ε) measured at four locations along the chord member for Joint CT1 are plotted in Figure5.10a) & b). As the target displacement is 19.0 mm, the number of cycles completed for Joint CT1 is 388. Similarly, the (P-δ) curve and the (P-4ε) for Joint CT2 are plotted in

Figure 5.10c) & d). Owing to the large target displacement at 38.0 mm, only one cycle is completed before fracture at the welded junction.

Figure 5.11 illustrates the development of cracks in the vicinity of the welded junction of Joint CT1 at various cycles. It is evident that at cycle 310, crack initiation is identified near the crown at the left hand side of the welded junction while no crack is found near the crown at its right hand side. An obvious crack is found at cycle 380.

Similarly, Figure 5.12 illustrates the development of cracks in the vicinity of the welded junction of Joint CT2 at various cycles. It is evident that after cycle 1, crack initiation is identified near the crown at the right hand side of the welded junction while no crack is found near the crown at its left hand side. An obvious crack is found at cycle 2.

b) Deformation characteristics of Joints CT3 and CT4

The applied load-lateral displacement (P-δ) curve and the strain variation curve (P-4ε) measured at four locations along the chord member for Joint CT3 are plotted in Figure 5.13a) & b). As the target displacement is 20.3 mm, the number of cycle completed for Joint CT3 is 237. Similarly, the (P-δ) curve and the (P-4ε) for Joint CT4 are plotted in Figure 5.13c) & d). Owing to the large target displacement at 30.3 mm, only 18 cycles are completed before fracture at the welded junction.

Figure 5.14 illustrates the development of cracks in the vicinity of the welded junction of Joint CT3 at various cycles. It is evident that at cycle 9, crack initiation is identified near the crown at both the left and the right hand sides of the welded junction. An obvious crack is found at cycle 259.

Similarly, Figure 5.15 illustrates the development of cracks in the vicinity of the welded junction of Joint CT4 at various cycles. It is evident that after cycle 5, crack initiation is identified near the crown at both the left and the right hand sides of the welded junction. An obvious crack is found at cycle 21.

c) Deformation characteristics of Joints CT5 and CT6

The applied load-lateral displacement (P-δ) curve and the strain variation curve (P-4ε) measured at four locations along the chord member for Joint CT5 are plotted in Figure 5.16a) & b). As the target displacement is 20.3 mm, the number of cycle completed for Joint CT3 is 207. Similarly, the (P-δ) curve and the (P-4ε) for Joint CT6 are plotted in Figure 5.16c) & d). Owing to the large target displacement at 30.3 mm, only 26 cycles are completed before fracture at the welded junction.

Figure 5.17 illustrates the development of cracks in the vicinity of the welded junction of Joint CT5 at various cycles. It is evident that at cycle 30, crack initiation is identified near the crown at the left hand side of the welded junction. An obvious crack is found at cycle 225.

Similarly, Figure 5.18 illustrates the development of cracks in the vicinity of the welded junction of Joint CT6 at various cycles. It is evident that after cycle 2, crack initiation is identified near the crown at both the left and the right hand sides of the welded junction. An obvious crack is found at cycle 30.

d) Typical fracture in T-joints after tests

Fractured parts of two selected T-joints, namely, Joints CT3 and CT5, are cut from their welded junctions, and they are shown in Figure 5.19 after etching. Through thickness fracture in all these welded junctions is evident, and this corresponds to complete failure of the T-joints.

e) Strength degradation during tests

- Joints CT1 and CT2

Figure 5.20 plot the strength degradation of Joints CT1 and CT2 during the cyclic tests. For Joint CT 1, it is shown in the plot of the maximum lateral displacements against various cycles, the values of the displacements are maintained at a high level of consistency. The corresponding maximum applied load along the negative x-axis exhibits a gradual reduction while that along the positive x-axis is shown to remain fairly constant. For Joint CT2, little information is provided as there is only 1 cycle completed.

- Joints CT3 and CT4

Figure 5.21 plot the strength degradation of Joints CT3 and CT4 during the cyclic tests. For Joint CT3, it is shown in the plot of the maximum lateral displacements against various cycles, the values of the displacements along the positive and the negative x-axis are maintained at a high level of consistency. The corresponding maximum applied loads along both the positive and the negative x-axis exhibit a gradual reduction. Similar characteristics for Joint CT4 are also evident. As the target displacement for Joint CT4 is 30.3 mm, i.e. about 50% larger than that for Joint CT3, the number of cycles completed before fracture is decreased from 237 to 18, i.e. 13.2 to 1 or 0.076.

- Joints CT5 and CT6

Figure 5.22 plot the strength degradation of Joints CT5 and CT6 during the cyclic tests. For Joint CT5, it is shown in the plot of the maximum lateral displacements against various cycles, the values of the displacements along the positive and the negative x-axis are maintained at a high level of consistency. The corresponding maximum applied loads along the negative x-axis exhibit a significant reduction while that along the positive x-axis remains to be fairly constant. Similar characteristics for Joint CT6 are also evident. As the target displacement for Joint CT6 is 30.3 mm, i.e. about 50% larger than that for Joint CT5, the number of cycles completed before fracture is decreased from 207 to 26, i.e. 7.96 to 1 or 0.126.

As a whole, the values of heat input energy adopted during welding of the welded junctions between the brace and the chord members of these T-joints are considered to have only minor effects on the numbers of cycles completed before fracture.

5.5 Conclusions

A systematic experimental investigation into the structural behaviour of the T-joints between cold-formed circular hollow sections of S690 steel under cyclic actions is presented. A total of 4 monotonic tests and then a total of 6 cyclic tests on these T-joints are carried out, and their deformation characteristics are analysed to provide data for calibration of subsequent finite element modelling presented in Chapter 7.

It should be noted that:

a) Both the applied load-lateral displacement (P-δ) curve and the strain variation curve (P-4ε) measured at four locations along the chord member for each of the T-joins under cyclic actions provide important deformation characteristics, and detailed analyses on these data

are conducted. It is shown that these T-joints exhibit a high level of cyclic ductility with large dissipation energy.

b) In general, the numbers of cycles completed before fracture of the T-joints are related inversely to the values of the target lateral displacements through a highly non-linear manner.

c) As the target displacement for Joint CT4 is 30.3 mm, i.e. about 50% larger than that for Joint CT3, the number of cycles completed before fracture is decreased from 237 to 18, i.e. 13.2 to 1 or 0.076. Similarly, as the target displacement for Joint CT6 is 30.3 mm, i.e. about 50% larger than that for Joint CT5, the number of cycles completed before fracture is decreased from 207 to 26, i.e. 7.96 to 1 or 0.126.

d) The values of heat input energy adopted during welding of the welded junctions between the brace and the chord members of these T-joints are considered to have only minor effects on the numbers of cycles completed before fracture.

a) S690 steel plates

b) Cold-bent steel tubes with tack welds

c) Welding of steel tubes

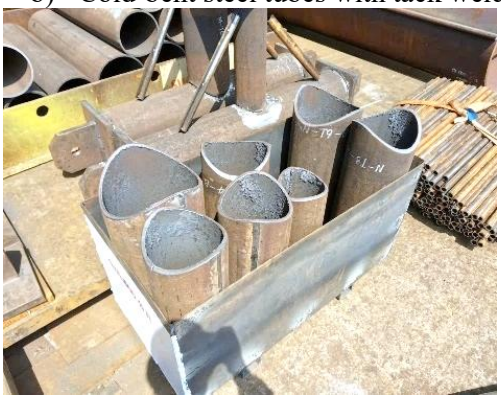

d) Profile-cutting

e) Joint assembling

f) Welding of brace/chord junction

Figure 5.1 Manufacturing process of T-joints

a) I = 169 A & U=19.8 V

b) Electrode: Bohler GM110

c) Shield gas: 20% Ar + 80% CO_2

Figure 5.2 Welding equipment and materials

a) Chord end plates

b) Brace/chord junctions

c) Welded T-joints

Figure 5.3 Welded connections of T-joints

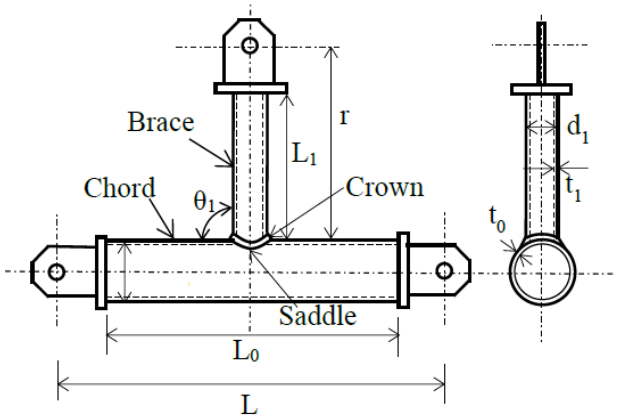

α	$= 2L_0/d_0$
β	$= d_1/d_0$
2γ	$= d_0/t_0$
τ	$= t_1/t_0$
L	= 1500 mm
L_0	= 1200 mm
L_1	= 600 mm
r	= 760 mm

Figure 5.4 Configuration of S690 T-joints

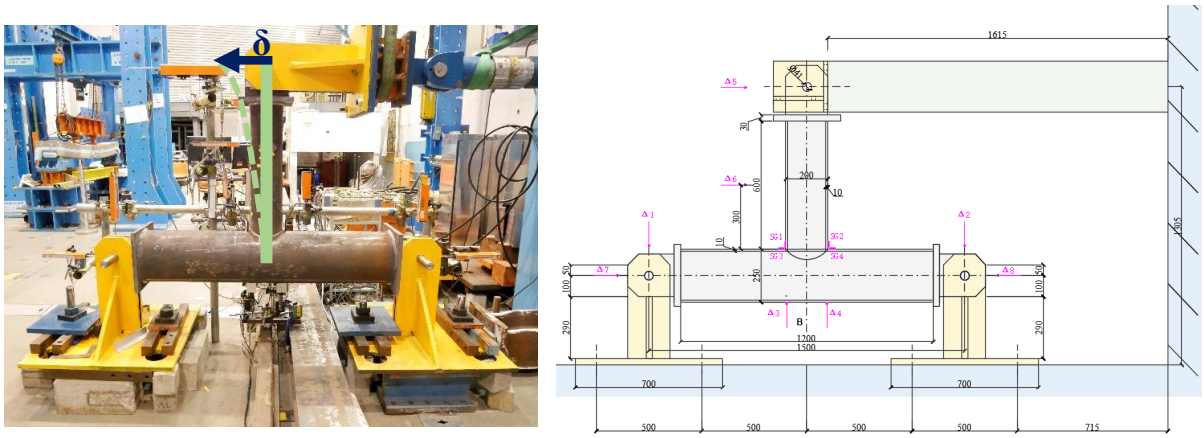

a) Test setup of monotonic actions b) Test instrumentation

Figure 5.5 Test setup for monotonic tests

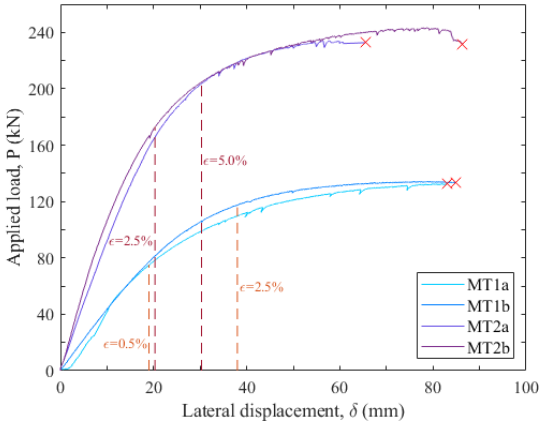

Failure mode: punching shear

Joints MT1a MT1b	Lateral displacement, δ (mm)	
	ε = 0.5%	ε = 2.5%
	19.0	38.0

Joints MT2a MT2b	Lateral displacement, δ (mm)	
	ε = 2.5%	ε = 5.0%
	20.3	30.3

Figure 5.6 Applied load-displacement curves of T-joints under monotonic tests

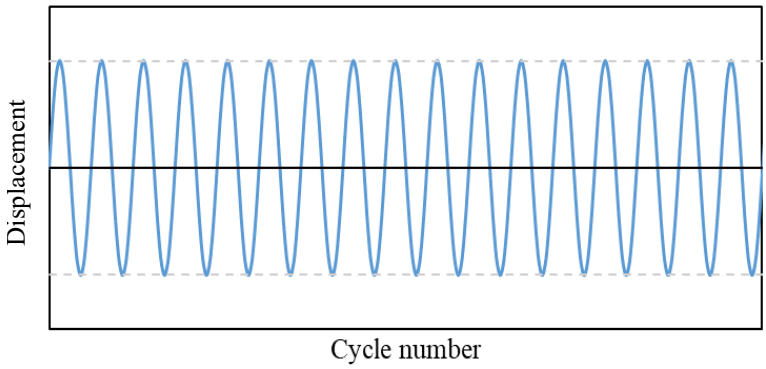

Figure 5.7 Loading protocol of cyclic actions

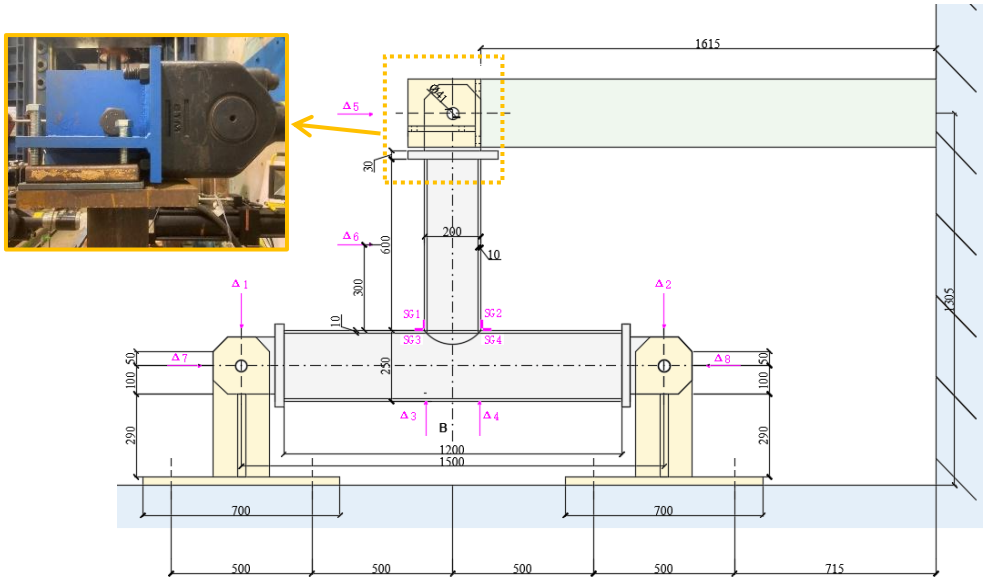

a) Test setup and instrumentation

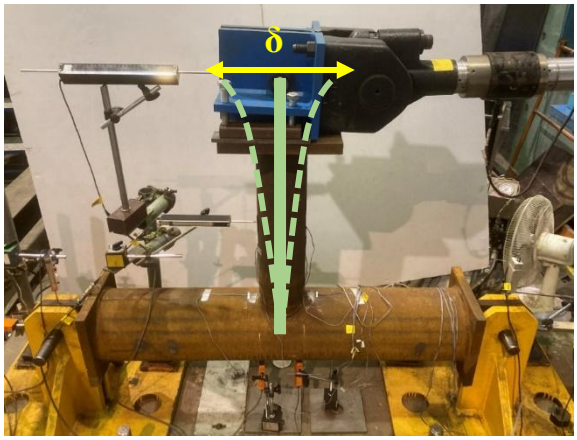

b) Overview of typical T-joint under testing

Figure 5.8 Testing of T-joints under cyclic actions

Target displacement δ (mm) = 19.1 for Joint CT1

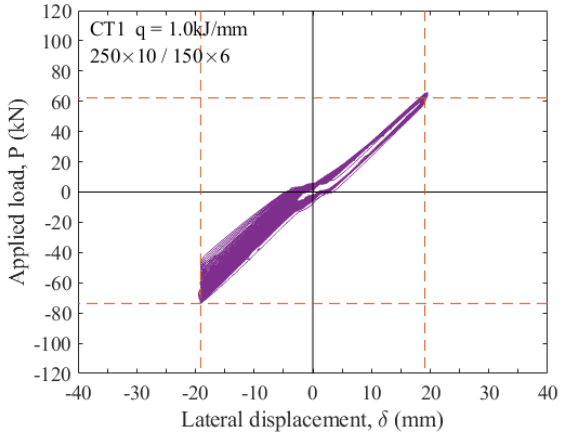

a) Applied load-lateral displacement (P-δ) curve

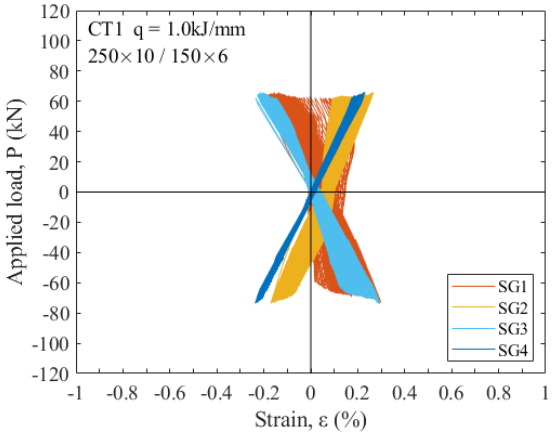

b) Applied load-strain (P-4ε) curves

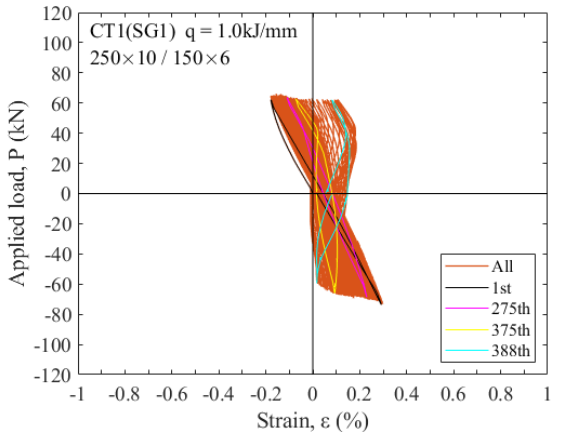

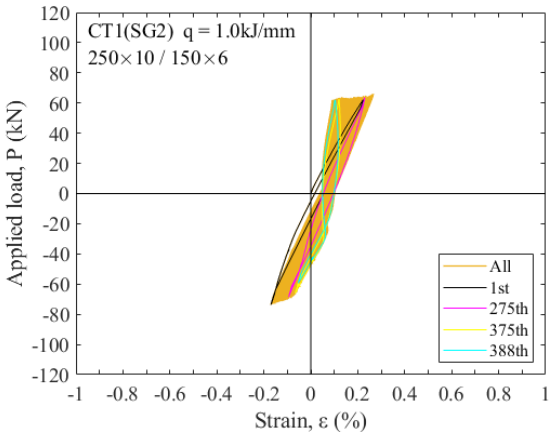

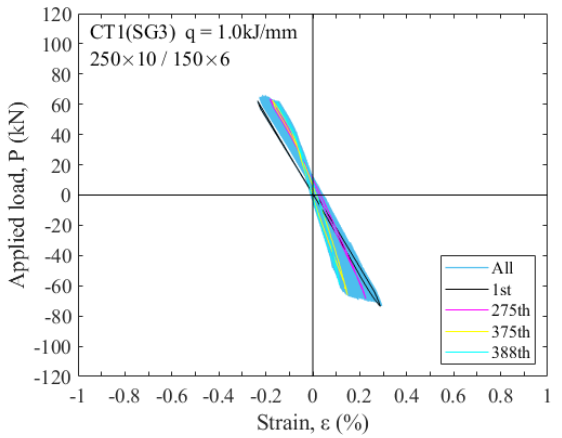

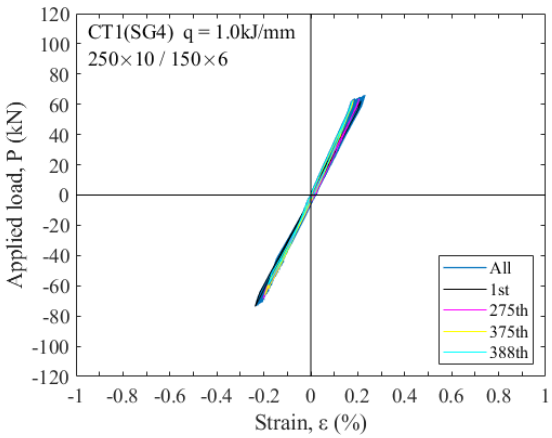

c) Applied load-strain (P-ε) curves at various locations

Figure 5.9 Measured data of Joint CT1: Load-displacement curves and load-strain curves

Target displacement δ (mm) = 19.1 for Joint CT1

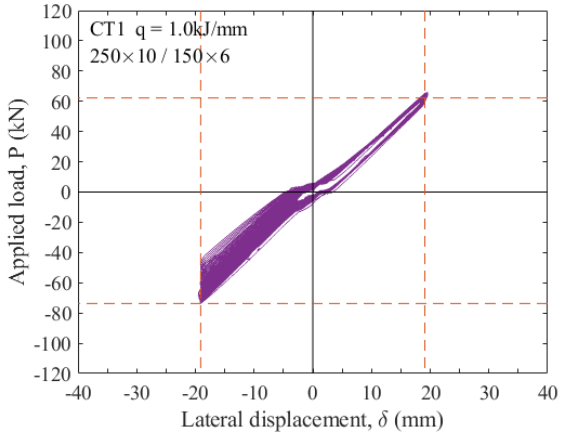

a) Applied load-lateral displacement (P-δ) curve Joint CT1

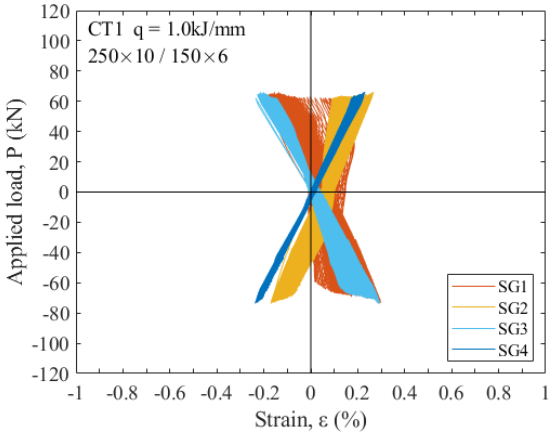

b) Applied load-strain (P-4ε) curves Joint CT1

Target displacement δ (mm) = 38.1 for Joint CT2

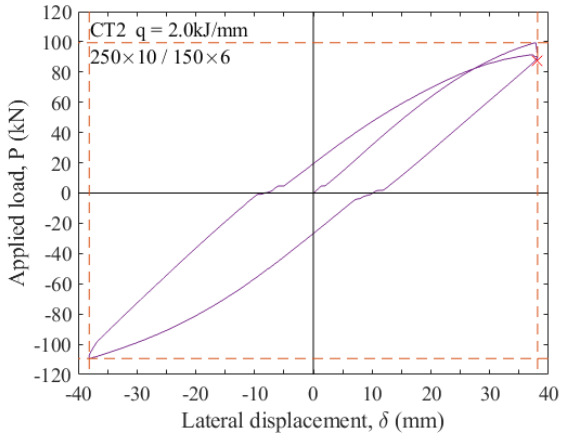

c) Applied load-lateral displacement (P-δ) curve Joint CT2

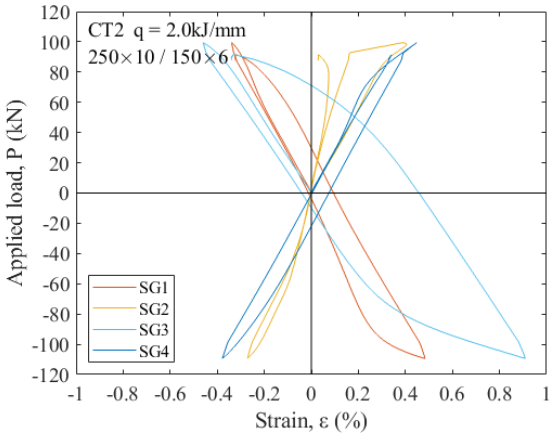

d) Applied load-strain (P-4ε) curves Joint CT2

Figure 5.10 Load-displacement and load-strain curves of Joints CT1 and CT2

No crack at cycle 0 (before test)

No crack at cycle 80

Crack initiation at cycle 310

No crack at cycle 310

Obvious crack growth at cycle 325

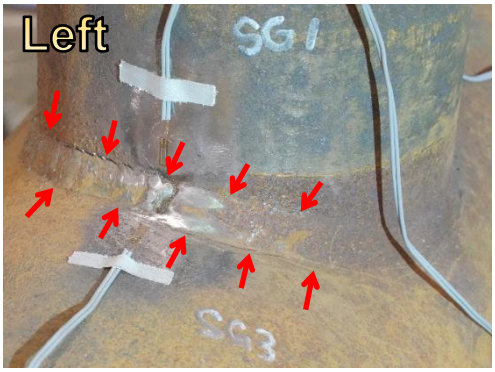

Obvious crack growth at cycle 380

Figure 5.11 Crack initiation and growth in Joint CT1

No crack at cycle 0 (before test)

No crack at cycle 1

Crack initiation at cycle 1

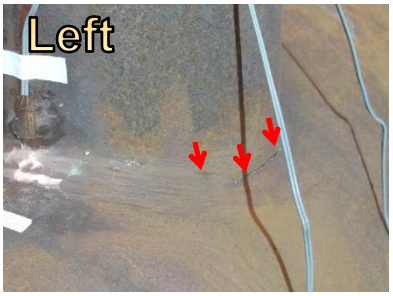

Crack growth at cycle 2

Crack growth at cycle 2

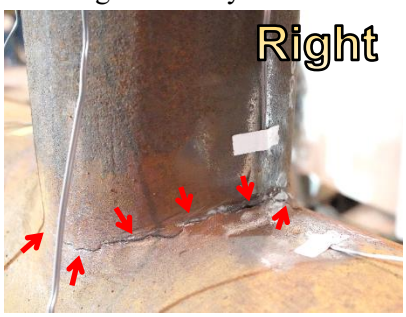

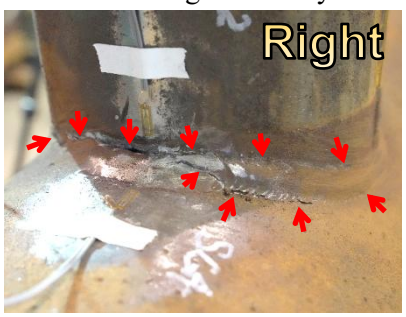

Crack growth at cycle 2

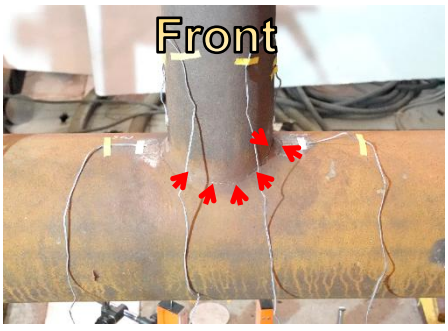

Crack growth at cycle 2

Figure 5.12 Crack initiation and growth in Joint CT2

Target displacement δ (mm) = 20.3 for Joint CT3

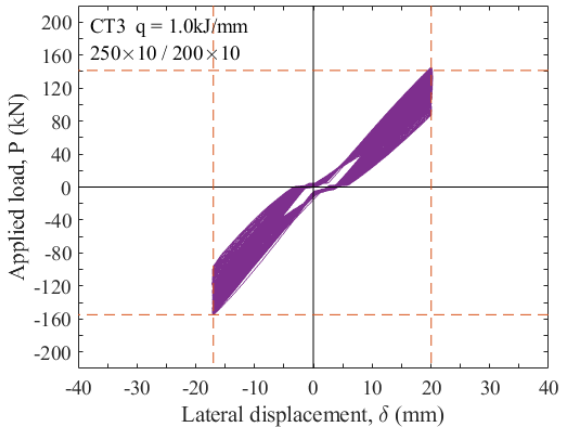

a) Applied load-lateral displacement (P-δ) curve Joint CT3

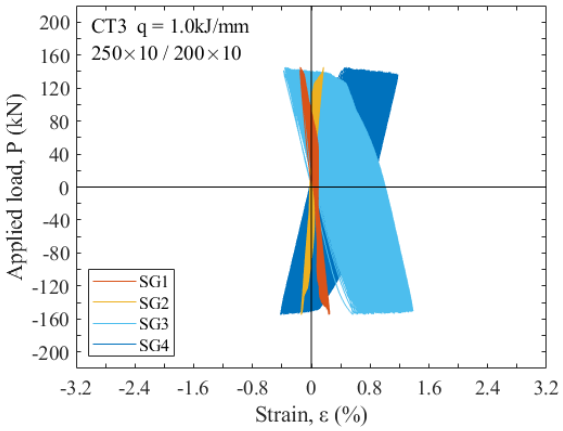

b) Applied load-strain (P-4ε) curves Joint CT3

Target displacement δ (mm) = 30.3 for Joint CT4

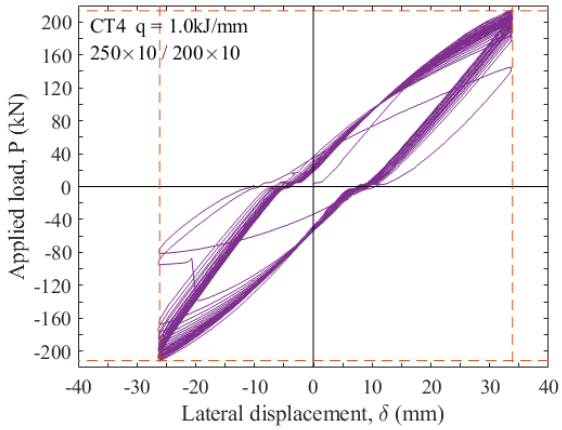

c) Applied load-lateral displacement (P-δ) curve Joint CT4

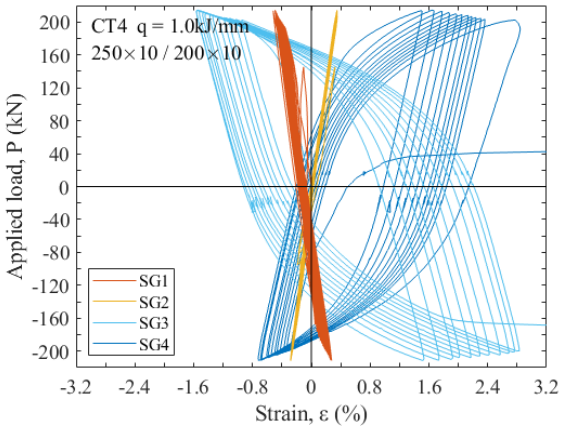

d) Applied load-strain (P-4ε) curves Joint CT4

Fig. 5.13 Load-displacement and load-strain curves of Joints CT3 and CT4

No crack at cycle 0 (before test)

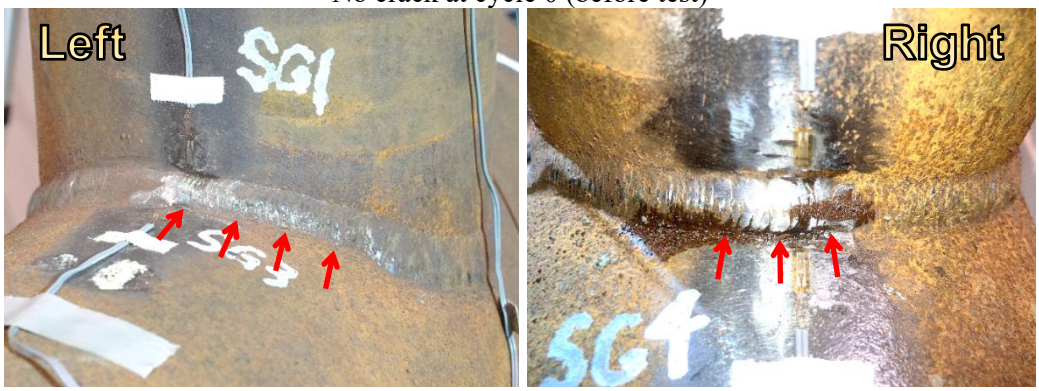

Crack initiation on both sides at cycle 9

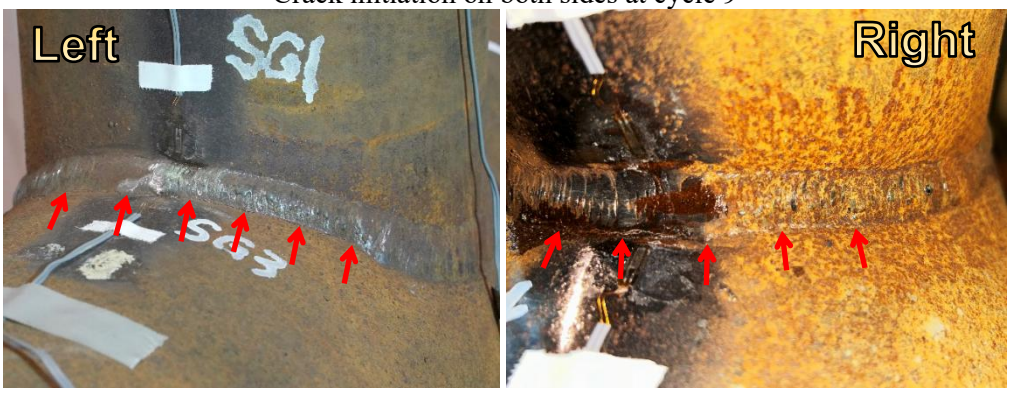

Cracks on both sides at cycle 200

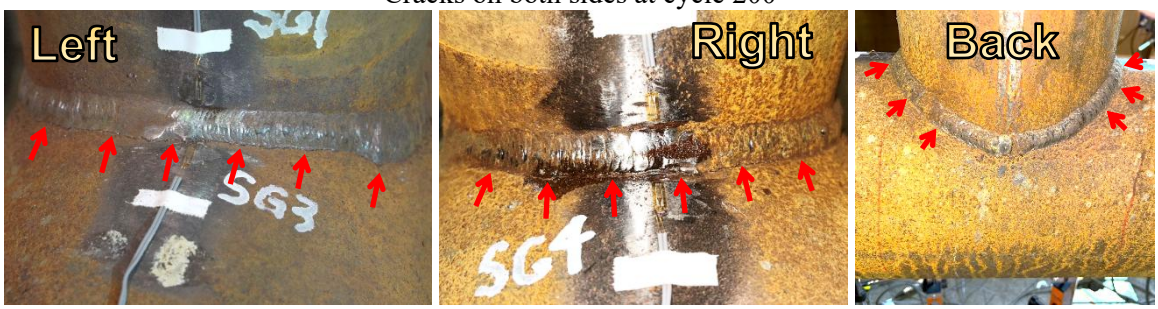

Obvious cracks on both sides at cycle 259

Figure 5.14 Crack initiation and growth in Joint CT3

No crack at cycle 0 (before test)

Crack initiation on both sides at cycle 5

Crack growth at cycle 13

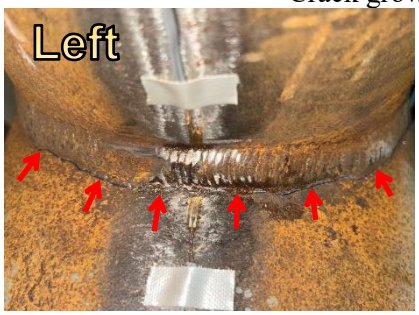

Crack growth at cycle 19

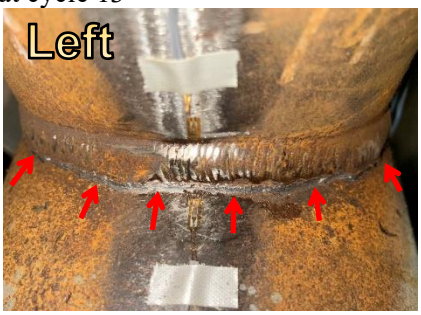

Crack growth at cycle 21

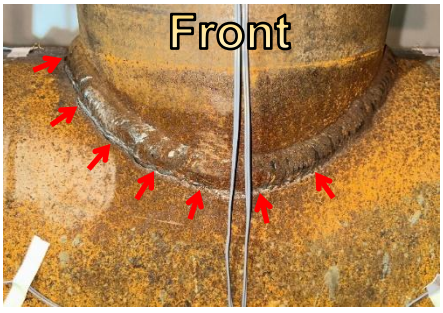

Crack growth at cycle 21

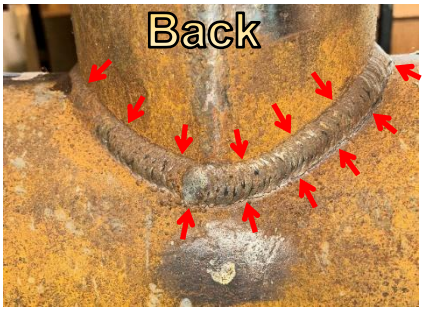

Crack growth at cycle 21

Figure 5.15 Crack initiation and growth in Joint CT4

Target displacement δ (mm) = 20.3 for Joint CT5

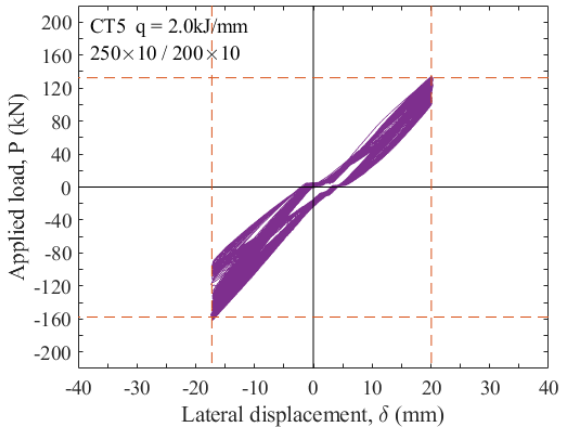

a) Applied load-lateral displacement (P-δ) curve Joint CT5

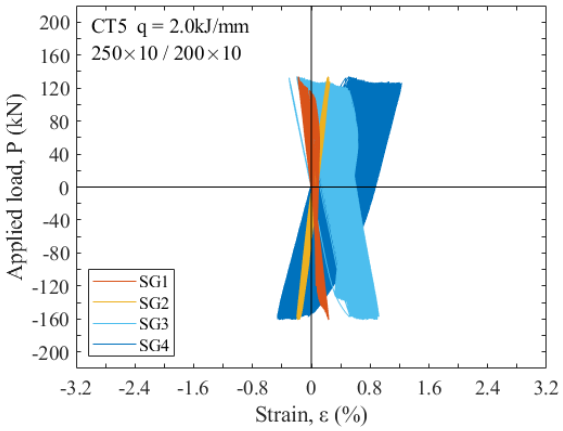

b) Applied load-strain (P-4ε) curves Joint CT5

Target displacement δ (mm) = 30.3 for Joint CT6

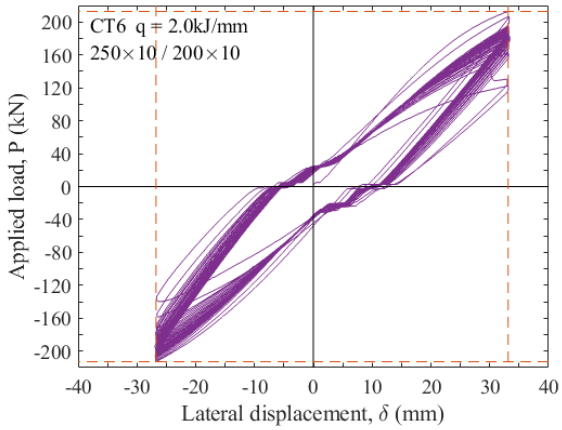

c) Applied load-lateral displacement (P-δ) curve Joint CT6

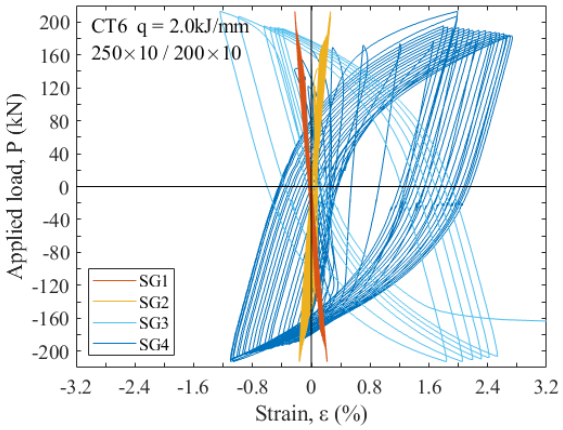

d) Applied load-strain (P-4ε) curves Joint CT6

Figure 5.16 Load-displacement and load-strain curves of Joints CT5 and CT6

No crack on both sides at cycle 0 (before test)

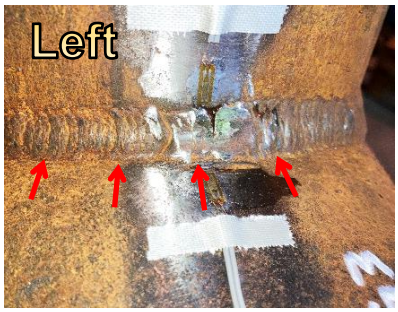

Crack initiation at cycle 30

Crack growth at cycle 55

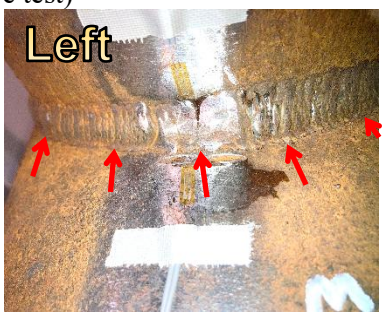

Crack growth at cycle 113

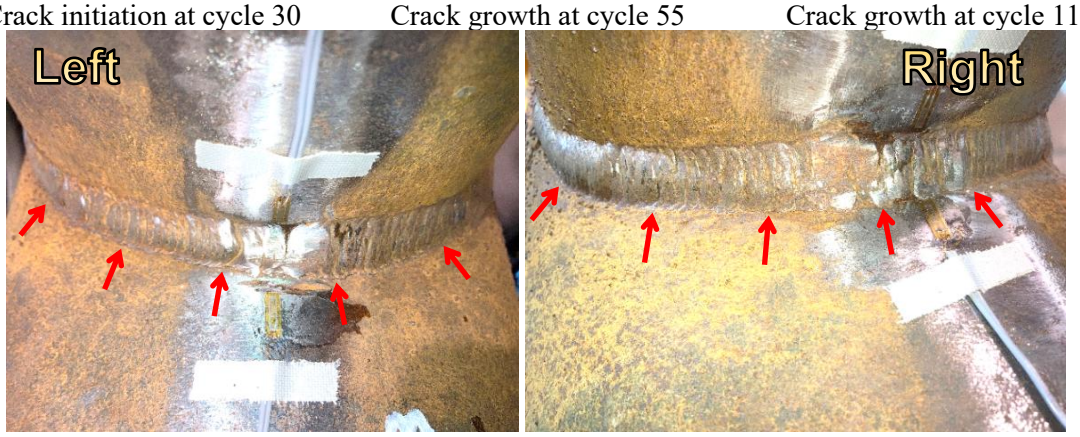

Crack growth at cycle 165

Crack growth at cycle 225

Figure 5.17 Crack initiation and growth in Joint CT5

No crack on both sides at cycle 0 (before test)

Crack initiation at cycle 2

Crack growth at cycle 11

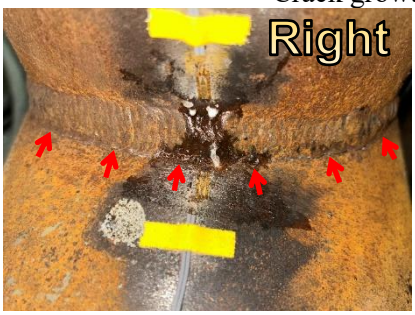

Crack growth at cycle 23

Crack growth at cycle 25

Crack growth at cycle 30

Figure 5.18 Crack initiation and growth in Joint CT6

Joint CT3: Fractured part L

Joint CT3: Fractured part R

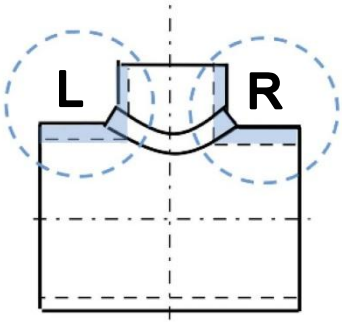

Joint CT5: Fractured part L

Joint CT5: Fractured part R

Figure 5.19 Fractured parts of T-joints (after etching)

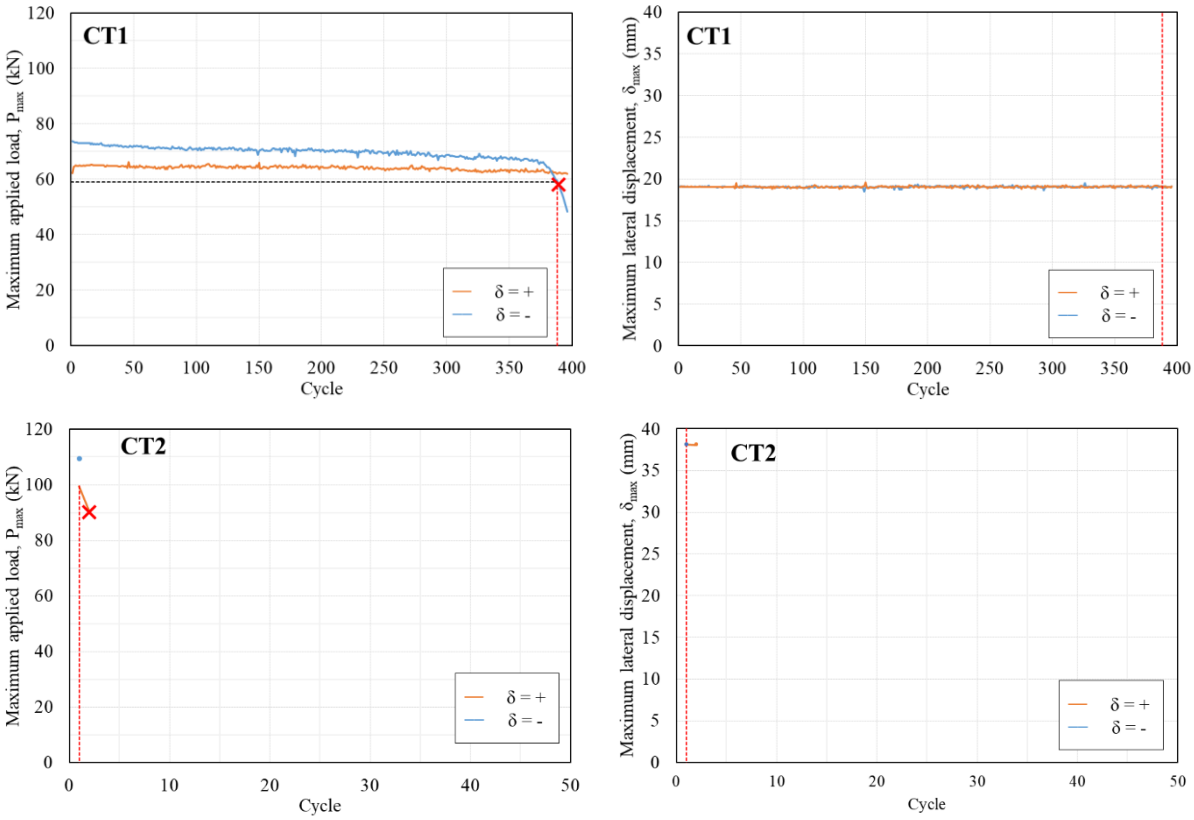

Figure 5.20 Strength degradation of Joints CT1 and CT2

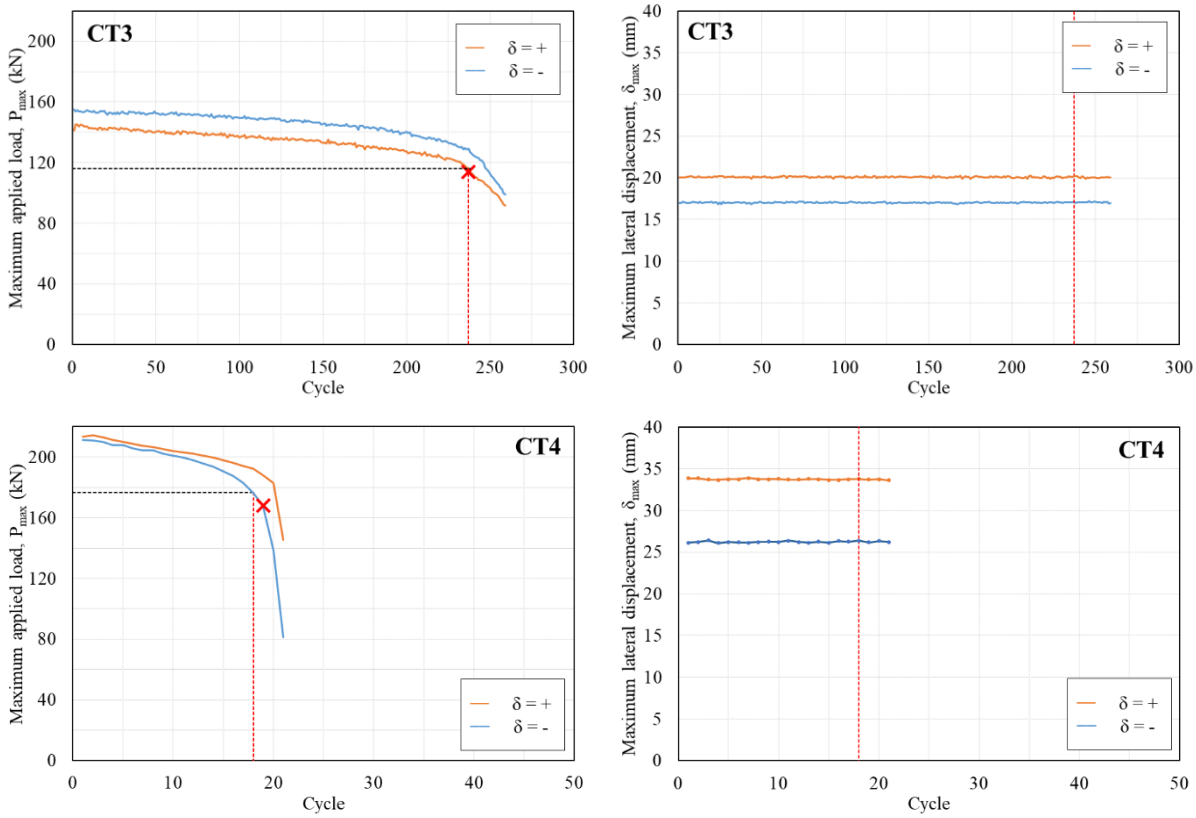

Figure 5.21 Strength degradation of Joints CT3 to CT4

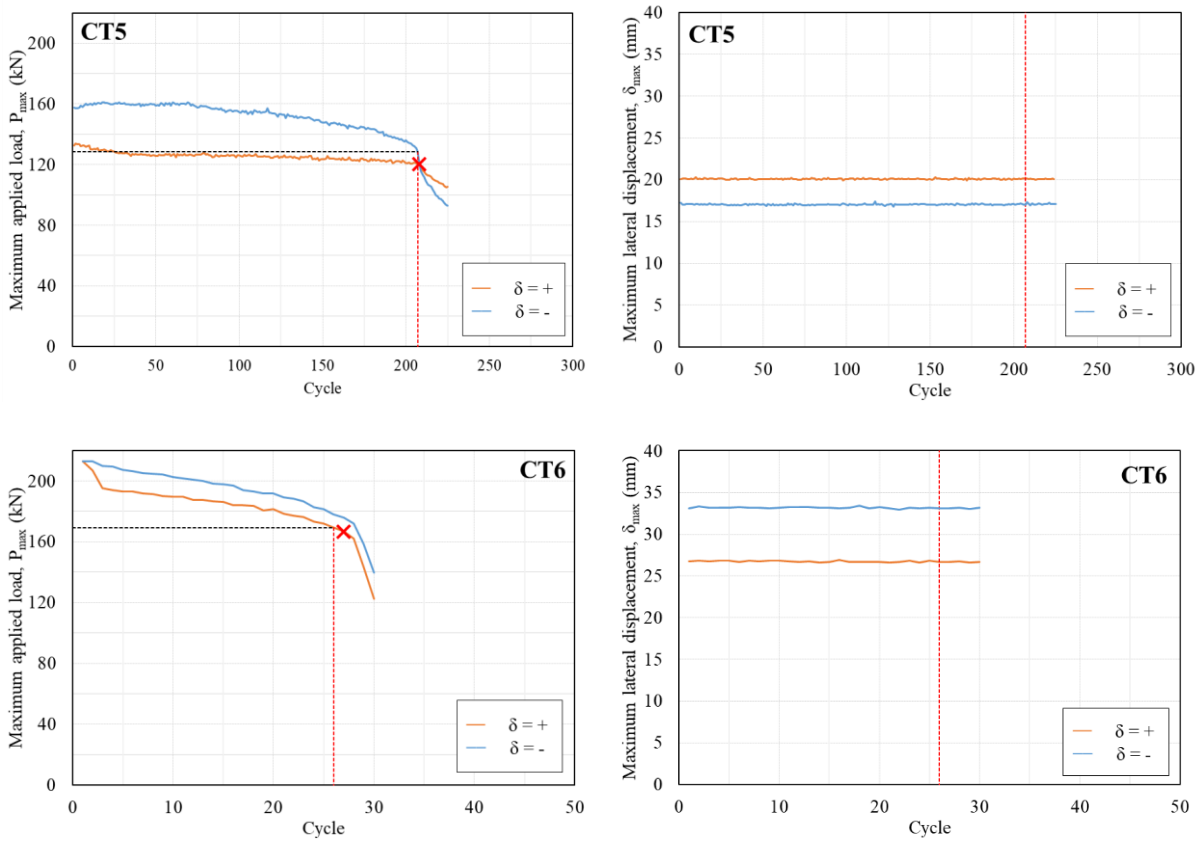

Figure 5.22 Strength degradation of Joints CT5 to CT6

Table 5.1 Mechanical properties of S690 steel plates and electrodes

a) Steel plates

Steel plate	Plate thickness, t (mm)	Young's modulus, E (kN/mm^2)	Yield strength, f_u (N/mm^2)	Tensile strength, f_y (N/mm^2)	f_u/f_y
EN 10025-6	≤ 16	210	690	770	1.05
T06	6	202	747	811	1.08
T10	10	201	766	828	1.08

b) Electrodes

Standard	Electrodes	Diameter, d (mm)	Yield strength, f_u (N/mm^2)	Tensile strength, f_y (N/mm^2)	Elongation, ε (%)
AWS A5.28	ER110S-G	1.2	720	880	15

Table 5.2 Configuration of S690 T-joint for monotonic tests

Test specimen	Heat energy input (kJ/mm)	Prediction of failure mode	Chord member $d_0 \times t_0$	Section class of the chord	Brace member $d_1 \times t_1$	Section class of the brace	α	β	2γ	τ	Design yield strength f_y (N/mm^2)
MT1a	1.2~1.5	BF	250×10	Class 3	150×6	Class 3	9.6	0.60	25.0	0.6	690
MT1b	1.2~1.5	BF	250×10	Class 3	150×6	Class 3	9.6	0.60	25.0	0.6	690
MT2a	1.2~1.5	CP-S	250×10	Class 3	200×10	Class 2	9.6	0.80	25.0	1.0	690
MT2b	1.2~1.5	CP-S	250×10	Class 3	200×10	Class 2	9.6	0.80	25.0	1.0	690

Table 5.3 Instrumentation of S690 T-joint cyclic tests

Channel no.	Channel
1	Actuator force
2	Actuator displacement
3 ~ 8	LVDT3 ~ LVDT8
9	LVDT1
10	LVDT2
11 ~ 14	SG1 ~ SG4

Table 5.4 Summary of measured test results (monotonic actions)

Test	Failure mode	Peak load P_{max} (kN)	Lateral displacement δ at P_{max} (mm)	Inter-storey drift $\delta / 760$ (rad)
MT1a	BF	132.7	83.0	0.109
MT1b	BF	134.2	84.8	0.112
MT2a	CP-S	234.2	65.5	0.086
MT2b	CP-S	243.3	86.3	0.114

Table 5.5 Configuration of S690 T-joint for cyclic tests

Test specimen	Heat energy input (kJ/mm)	Prediction of failure mode	Chord member $d_0 \times t_0$	Section class of the chord	Brace member $d_1 \times t_1$	Section class of the brace	α	β	2γ	τ	Design yield strength f_y (N/mm^2)
CT1	1.0	BF	250×10	Class 3	150×6	Class 3	9.6	0.60	25.0	0.6	690
CT2	2.0	BF	250×10	Class 3	150×6	Class 3	9.6	0.60	25.0	0.6	690
CT3	1.0	CP-S	250×10	Class 3	200×10	Class 2	9.6	0.80	25.0	1.0	690
CT4	1.0	CP-S	250×10	Class 3	200×10	Class 2	9.6	0.80	25.0	1.0	690
CT5	2.0	CP-S	250×10	Class 3	200×10	Class 2	9.6	0.80	25.0	1.0	690
CT6	2.0	CP-S	250×10	Class 3	200×10	Class 2	9.6	0.80	25.0	1.0	690

Table 5.6 Loading details of S690 T-joint cyclic tests

Test	Heat energy input q (kJ/mm)	Target load (kN)	Target displacement δ (mm)	Inter-storey drift $\delta / 760$ (rad)	Predicted maximum principal strain FEM (%)	Loading rate (mm/min)
CT1	1.0	70	19.0	0.025	~ 0.5	10.0
CT2	2.0	120	38.0	0.050	~ 2.5	10.0
CT3	1.0	190	20.3	0.027	~ 2.5	10.0
CT4	1.0	212	30.3	0.040	~ 5.0	10.0
CT5	2.0	190	20.3	0.027	~ 2.5	10.0
CT6	2.0	212	30.3	0.040	~ 5.0	10.0

Table 5.7 Summary of measured test results of T-joints under cyclic actions

Test	Failure mode	Target lateral displacement (mm)		Peak load among all cycles P_{max} (kN)		Maximum load in the cycle before failure P_{last} (kN)		Lateral displacement δ at P_{max} (mm)		Inter-storey drift $\delta/760$ (rad)		Maximum measured strain (%)	No. of cycle completed	Total energy dissipation (J)	Testing time (hr)
		δ^+	δ^-	δ^+	δ^-	δ^+	δ^-	δ^+	δ^-	δ^+	δ^-				
CT1	BF	19.0	19.0	66.1	73.7	62.1	59.5	19.1	19.1	0.025	0.025	0.30	388	11,326	79
CT2	WF	38.0	38.0	99.4	109.5	99.4	109.5	38.1	38.1	0.050	0.050	0.91	1	84	1
CT3	CP-S	20.3	20.3	145.2	154.9	116.3	129.0	20.0	17.2	0.026	0.023	1.38	237	13,607	52
CT4	CP-S	30.3	30.3	214.5	211.5	192.5	176.6	33.9	26.1	0.045	0.034	-	18	2,253	7
CT5	CP-S	20.3	20.3	134.0	161.1	120.1	128.7	20.0	17.0	0.026	0.022	1.23	207	11,721	50
CT6	CP-S	30.3	30.3	212.8	212.8	169.3	178.0	26.8	33.1	0.035	0.044	-	26	3,296	9

Notes:
δ^+ denotes a displacement moving along the positive x axis, and
δ^- denotes a displacement moving along the negative x axis.

CHAPTER 6 SIMULATION ON HIGH STRENGTH STEEL AND THEIR WELDED SECTIONS UNDER CYCLIC TESTS

6.1 Introduction

Over the last few decades, many researchers have proposed a number of constitutive models for different steel materials with a wide range of steel grades, i.e. from normal grade steel to high strength steel. The basis of many of these models is the combined isotropic and kinematic hardening model which was initially proposed by Armstrong and Frederick (1966), and later modified by Chaboche (1986, 1989). It should be noted that these constitutive models had been continually improved to provide high precision in simulating hysteretic curves. However, extensive prior experiments were often required to provide data for determination of numerous parameters according to specific materials and shapes of test specimens. Consequently, implementing improved or even new models in structural members is extremely challenging.

The purpose of this chapter is to present a number of simplified constitutive models for S355, S690 and S960 steel and their welded sections under cyclic loadings. These models are directly adopted in simulation of T-joint tests presented in the following chapter. It is noteworthy that the simulated energy dissipations on various steel and their welded sections are compared with those obtained from the cyclic coupon tests demonstrated in Chapter 4. It is demonstrated that there are only minor discrepancies between the measured and the predicted data, and hence, the simplified constitutive model is demonstrated to be highly acceptable for simulation of cyclic tests of these steel and their welded sections.

6.2 Limitations of application of existing constitutive models for steel

It should be noted that the latest constitutive models for steel subjected to cyclic loadings that are mentioned in Chapter 2 have attained a high degree of precision. However, these models

require an explicit acquisition of numerous parameters obtained from experimental data. As a result, a considerable number of prior experiments are necessary to calibrate and optimize these sets of parameters. The hysteretic behaviour of steel materials is influenced by their plastic deformation history, which is determined by both material properties and geometrical dimensions of the test specimens. Therefore, each set of these parameters applies exclusively to specific materials with specific shapes and sizes. Since there is no standardized geometry for test specimens nor quantitative criteria for experimental results in cyclic testing, there may be significant variations in experimental results as well as calibrations of constitutive model parameters among different studies. Moreover, an extensive and complicated calibration on these model parameters makes it difficult to apply current high precision constitutive models quickly and efficiently to structural members or even to a whole building.

The energy dissipation capacity of materials and structural members subjected to large cyclic actions is crucial in seismic design. Instead of repeating laborious experiments and calculations to obtain a precise simulation of the hysteresis loop, a simplified approach may be employed to achieve a satisfactorily accurate simulation of energy dissipation. The simplified constitutive models can greatly simplify calculation processes, and shorten calculation time, making it quick and easy to apply to structural members.

6.3 Proposed constitutive models for various steel under cyclic loadings

6.3.1 Establishment of simplified constitutive models

Simplified constitutive models for various steel under cyclic loadings according to the test programme presented in Chapter 4 are proposed in this chapter. Table 6.1 presents the test programme, and hence, the numbers of the proposed finite element models. All these models (FEM) are established with Abaqus (2020).

In order to allow an efficient modelling on the cycle tests, a structural model with only parts of the test coupons, as shown in Figure 6.1a), is established, and solid elements C3D8R are adopted in the model. The material properties such as Young's modulus, yield strength, and true stress-strain characteristics of the S355, the S690, and the S960 steel derived from test data reported in Chapters 3 and 4 are adopted into the structural model.

The boundary conditions of the structural model are identified in accordance with the actual situation in the tests. As illustrated in Figure 6.1b), all six degrees of freedom at the top surface of the model are fixed, i.e., $U_x = U_y = U_z = 0$ and $R_x = R_y = R_z = 0$. At the bottom surface, a reference point is defined which is positioned at the vertical centroid line of the model 0.05 mm away from the bottom surface. The bottom surface is fully coupled with this reference point. It should be noted that the boundary conditions of the reference point are set as follows: $U_x = U_z = 0$ and $R_x = R_y = R_z = 0$ while U_y is the axial deformation, i.e. an axial elongation or shortening to be imposed during structural analysis. These boundary conditions are also expected to prevent any sudden buckling of the model even under significant shortenings.

In general, a non-regular mesh is adopted in the model, and the element sizes ranging from 0.1 to 0.5 mm are distributed throughout the model using a 'dense in the middle and sparser on both sides' approach to achieve accurate numerical predictions at large deformations, for example, after coupon necking. Typical mesh configuration of the structural model is illustrated in Figure 6.1c), and the total number of elements is 35,068.

A displacement in the y-direction is applied directly onto the reference point of the structural model, rather than onto its bottom surface, in order to prevent any buckling of the model, which

is not the desired failure mode in the present investigation. The amplitude of such a displacement is set to a sinusoidal wave which is identical to that of the experiments.

6.3.2 Modification of simplified constitutive models

A) Before the 1st reverse loading

It is observed that the material properties, i.e. Young's Modulus E, and yield strength f_y , and shapes of the load-deformation curves are slightly different before and after the 1st reverse loading, as shown in Figure 6.2.

In general, before the 1st reverse loading in the 1st cycle, the material properties are similar to those obtained in the monotonic tests. However, after the 1st reverse loading, a plastic behaviour on loading history (loading and unloading) has modified the material properties. It is possible to edit the user-defined yield criteria and hardening rules using subroutine UMAT or UHARD in Abaqus. However, these require tedious and complex parameter modifications for each specific material, and shapes and sizes of the test coupons, and therefore, this cannot be easily applied in practice to a large number of different models with different materials.

In order to simplify the process of modelling, it is recommended to adopt the constitutive model obtained from monotonic actions for the 1st loading, but before the 1st reverse loading as there are often large discrepancies between the simulated and the measured curves. In this present study, only cyclic tests of S355 steel and their welded sections adopt the two-stage model. For cyclic tests of S690 and S960 steel and their welded sections, the differences between the simulated and the measured curves for the 1st loading as well as the 1st reverse loading as this only gives a negligible effect on subsequent calculation of the total strain energy dissipation.

B) Calibration of kinematic hardening parameters

It should be noted that normal strength steel has little isotropic hardening while high strength steel has both isotropic and kinematic hardening. Hence, calibration of kinematic hardening parameters for S355 steel and both isotropic and kinematic hardening parameters for S690 and S960 steel are crucial for the proposed simplified constitutive model. The following model is based on Lemaitre and Chaboche (1990).

Stress and strain data are obtained from a stabilized cycle of the cyclic tests on the S355 base metal. The nonlinear kinematic hardening rule is defined as follows:

$$\alpha_k = \frac{C_k}{\gamma_k}\left(1 - e^{-\gamma_k \varepsilon^{pl}}\right) + \alpha_{k,1} e^{-\gamma_k \varepsilon^{pl}} \qquad \text{Equation 6.1}$$

where

α_k is the back stress, the number of back stresses is taken as 3 in this study, i.e. k = 1, 2 and 3;

$\alpha_{k,1}$ is the back stress at the reverse loading point, and it is assumed to be α_1 in this study;

C_k is the initial kinematic hardening modulus;

γ_k is the rate of decrease with plastic strain of kinematic hardening modulus; and

ε^{pl} is the equivalent plastic strain.

The kinematic hardening parameters, i.e. C_1, C_2, C_3, γ_1, γ_2 and γ_3, are calibrated and optimized using the software MATLAB (2021). It is found that when the kinematic hardening parameters for both the S690 and the S960 steel are calibrated using the same methodology, the simulated curves differ significantly from the measured curves, particularly at each yield turning point, as shown in Figure 6.3. However, it is observed that the yield turning points of the measured curves are similar for all the S355, the S690, and the S960 steel. Therefore, an attempt is made to apply the same set of kinematic hardening parameters as for the S355 steel to both the S690 and S960 the steel, and it is shown that the yield turning points of the simulated curves coincide

with the measured curves successfully.

Another discrepancy between the simulated and the measured curves of both the S690 and the S960 steel is the hardening part of the curves after yielding. For a kinematic hardening model with three back stresses, each of the back stresses covers a different strain range with the linear hardening law α_3 playing a significant role at large strains, as shown in Figure 6.4. Therefore, the value of $\frac{C_3}{\gamma_3}$, which stands for the slope of α_3, can be modified by solely increasing or reducing the value of C_3 or γ_3 according to the characteristics of the hardening part of the curves after yielding. The values of the kinematic hardening parameters adopted in this study are summarised in Table 6.2. It should be noted that:

- the same set of kinematic hardening parameters has been used for both the S355 and the S690 steel and their welded sections; and
- for S960 steel, the same set of kinematic hardening parameters of those of the S355 and the S690 steel has been used, except that C3 is taken as 5.5.

In general, a good comparison between the simulated and the measured curves of all these steel is attained in all loading cycles of various target strains. Despite there are some discrepancies near the maximum strains in a few curves of the S690 steel, this is only a negligible effect on the total strain energy dissipation.

As for the isotropic hardening part of the curves of both the S690 and the S960 steel, the measured curves show that the equivalent stress defining the size of the yield surface does not increase monotonically with the number of completed cycles. It reaches a maximum in the 2nd cycle, and then, decreases with each subsequent cycle which cannot be precisely described by a simple exponential law. Hence, a piecewise function defined in Abaqus subroutine UHARD is then required. However, this discrepancy is demonstrated to have a negligible effect on the

subsequent calculation of the total strain energy dissipation. Therefore, for simplicity of calculation and modelling, the isotropic hardening parameters are calibrated within Abaqus by directly inputting tabular data of equivalent stresses obtained from the cyclic tests.

C) Base metal vs welded sections

According to the test results presented in Chapter 3, the differences in elongation between the base metal and the welded sections of different steel are typically small when the strains are not greater than 10%. These changes have often a negligible effect on the total strain energy dissipation of the cyclic tests while the number of cycles completed has a major impact on the total strain energy dissipation. Thus, the same constitutive model can be used for modelling both the base metal and the welded sections in cyclic tests with a target strain of up to 10%, and only the number of cycles completed can be adjusted against the actual conditions of the experiments reported in Chapter 4. This has significantly simplified the process of modelling and also reduced the time of calculation.

6.4 Numerical analyses and validation of finite element models

6.4.1 Simulated hysteretic curves and deformed shapes

The simulated stress and strain data are extracted from the FEM models in Abaqus. The simulated hysteretic curves of the S355, the S690 (Nanjing and Shougang), and the S960 base metal and their welded sections under cyclic loadings are plotted together with the measured hysteretic curves for direct comparison in Figure 6.5 to 6.16. Typical deformed shapes of the structural are depicted in Figure 6.17.

A) S355 steel and their welded sections – Figure 6.5 to 6.7

Since a two-stage model including both monotonic actions before the 1st reverse loading and

cyclic actions afterwards are adopted, simulated hysteretic curves coincide with the measured curves closely at the target strains of ±1.0 %, ±5.0 %, ±7.5 %, and ±10.0 %. For the target strain of ±2.5 %, strength deterioration is challenging to be simulated adequately when the number of cycles completed is greater than 80. However, when the number of cycles completed is less than 80, a good accuracy is readily achieved.

B) S690 (NJ and SG) steel and their welded sections – Figure 6.8 to 6.13

The proposed simplified constitutive models are shown to be able to predict the hysteretic curves precisely, with an exception of slight discrepancies between the simulated and the measured curves before the 1st loading reverse. At large target strains of ±5.0 %, ±7.5 %, and ±10.0 %, both the strength hardening and the deterioration in tension are found to be difficult to fit accurately after the first few cycles. These can be modestly improved by adjusting the value of $\frac{C_3}{\gamma_3}$.

C) S960 steel and their welded sections – Figure 6.14 to 6.16

The simulated hysteretic curves are shown to compare generally well with the measured curves despite there are discrepancies before the 1st reverse loading. At large target strains of ±10.0 %, both the strength hardening and the deterioration in tension are found to be difficult to fit accurately after the 3rd cycle.

6.4.2 Simulated total strain energy dissipation

The total strain energy dissipation of all structural models is summarized in Table 6.3. The percentage errors between the simulated and the measured total strain energy dissipation are highlighted in blue under the simulated values.

As indicated in the table, the proposed simplified constitutive models demonstrate an accurate prediction of the total strain energy dissipation. Only 3 out of 77 models have a percentage error greater than 5% (highlighted in blue and underlined in the table). Despite a challenge in the simulation of the strength deterioration with a large number of cycles completed, the effects of discrepancies between the simulated and the measured curves before the 1st reverse loading, and the material properties between the base metal and their welded sections are minor and negligible in the calculation of the total strain energy dissipation. The results provide substantial evidence that the proposed simplified constitutive models are both effective and accurate, and thus, they are readily applied to structural members.

6.5 Conclusions

Simple and effective constitutive models for the S355, the S690 and the S960 steel and their welded sections under cyclic loadings are proposed in this chapter. It is noteworthy that without extensive and complex procedures for calibration of various parameters, these simplified models are demonstrated to be capable of predicting both the hysteretic curves and the total strain energy dissipation with adequate accuracy.

Despite difficulty in simulating the strength deterioration of the base plates and their welded sections with a large number of cycles completed, the impact of discrepancies between the simulated and the measured curves before the 1st loading reverse, as well as the differences in the material properties between the base metal and their welded sections, is found to be typically minor and negligible in the calculation of the total strain energy dissipation.

It is demonstrated in this study that the proposed simplified constitutive models are effective in simulating cyclic tests, and they are generally applicable to a wide range of steel materials, including normal strength and high strength steel, and also their welded sections. This enables

a straightforward and efficient process of constitutive modelling and its application to structural members.

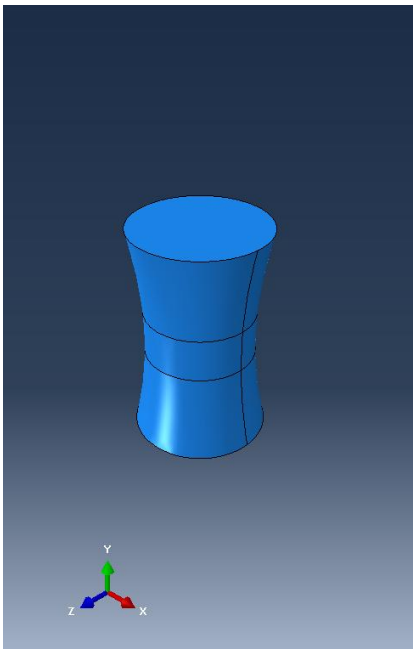

a) Geometry of FEM

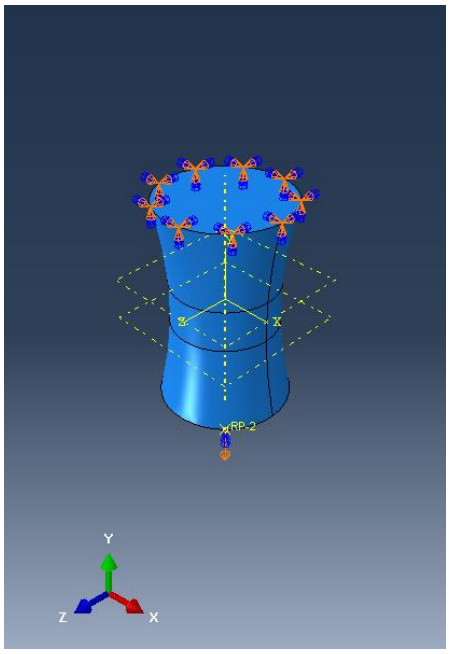

b) Boundary conditions

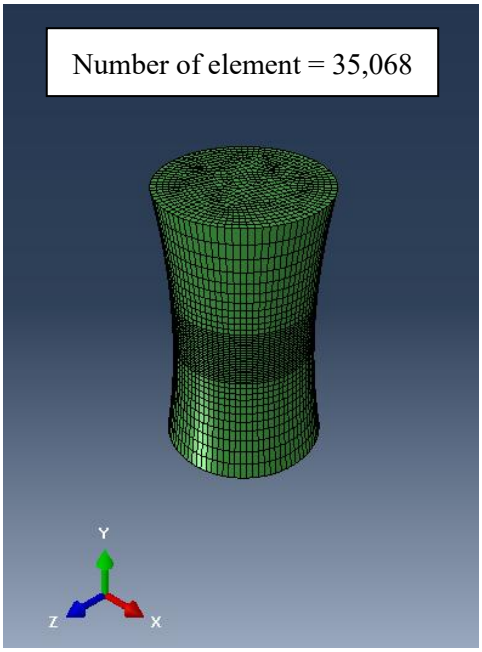

c) Typical mesh

Figure 6.1 FEM models of funnel-shaped coupon in Abaqus

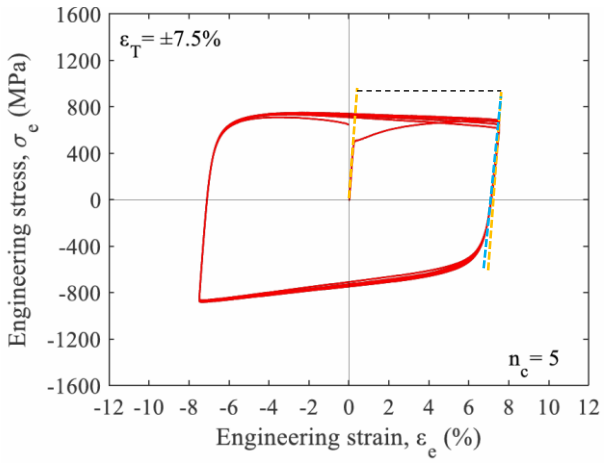

Figure 6.2 Change in Young's Modulus of a typical cyclic test

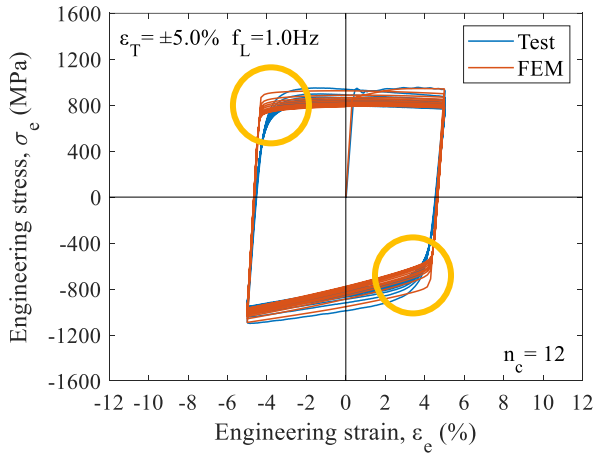

Figure 6.3 Difference at yield turning point between simulated and measured curves for high strength steel

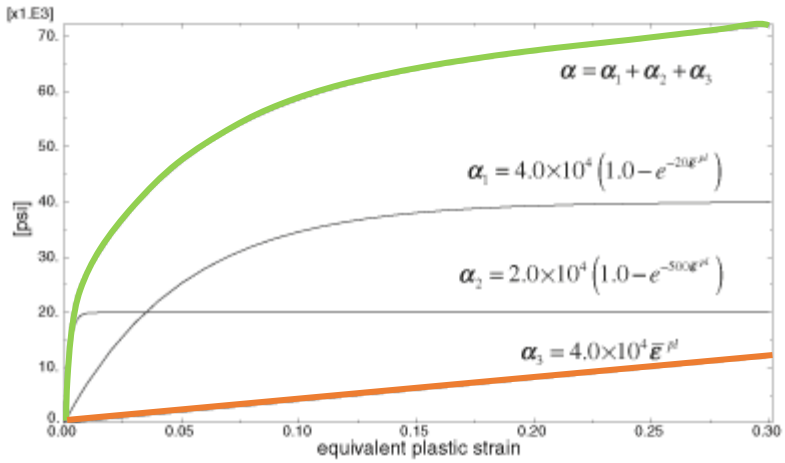

Figure 6.4 Three back stresses for kinematic hardening model

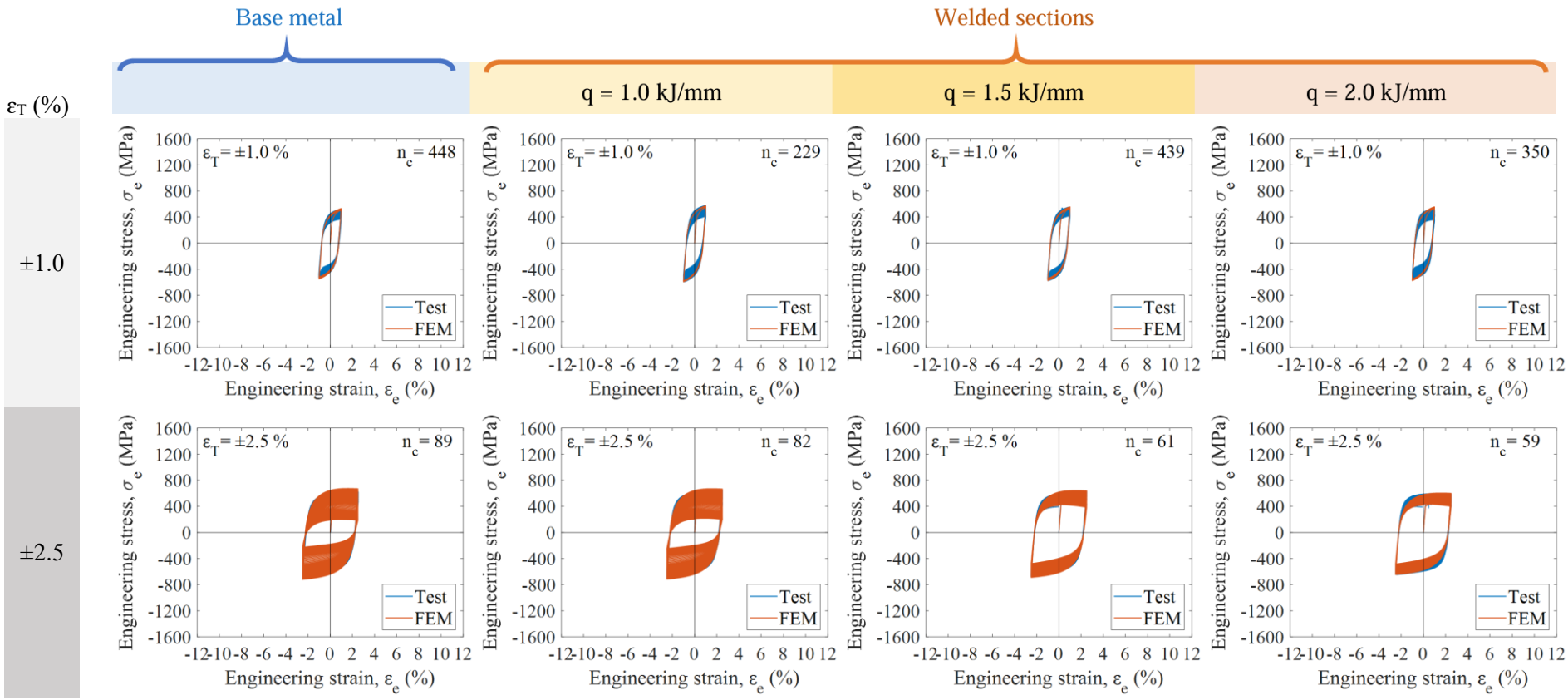

Figure 6.5 Engineering stress-strain curves of the cyclic tests on S355 at ε_T = ±1.0 % and ±2.5 % (FEM vs Test)

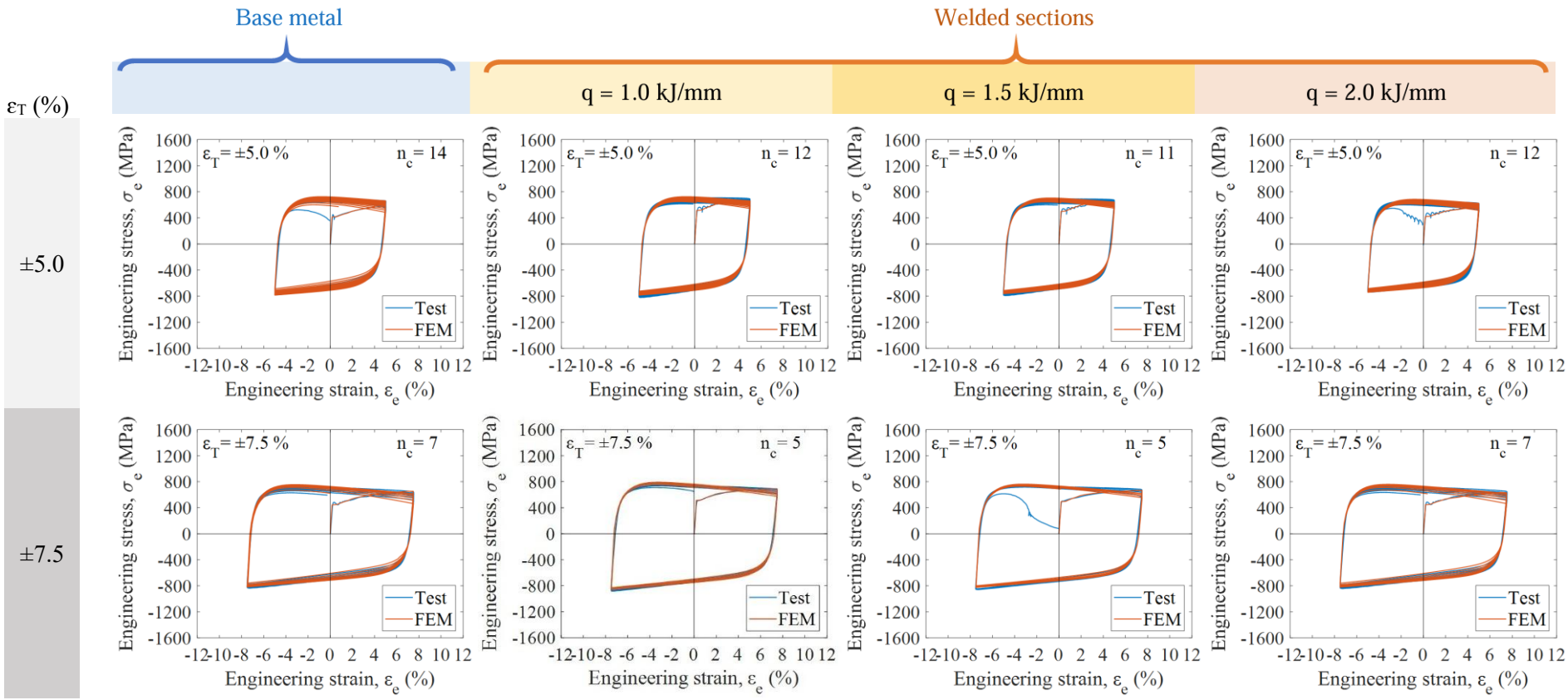

Figure 6.6 Engineering stress-strain curves of the cyclic tests on S355 at ε_T = ±5.0 % and ±7.5 % (FEM vs Test)

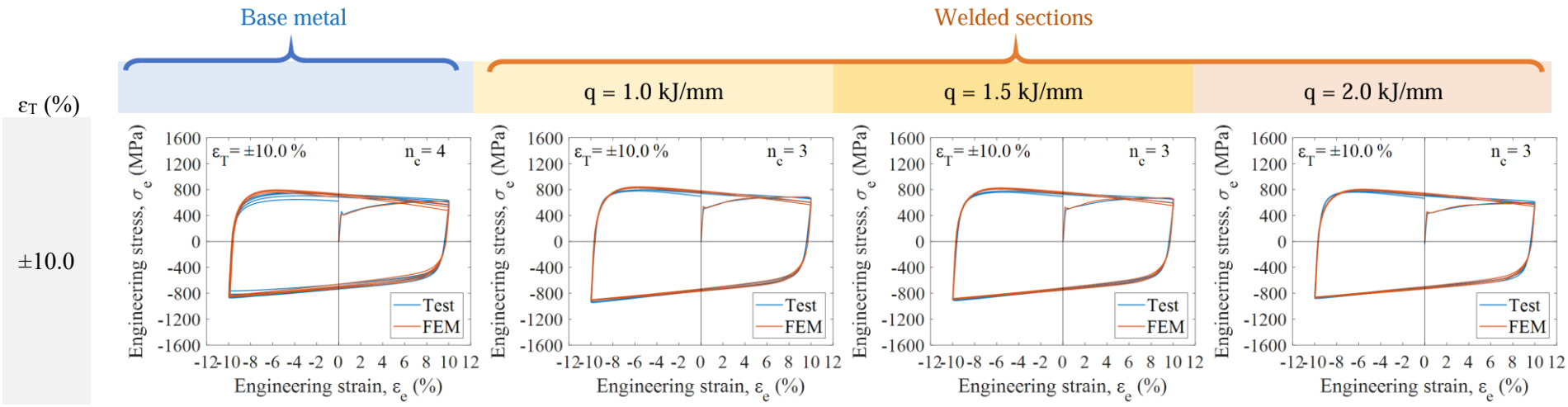

Figure 6.7 Engineering stress-strain curves of the cyclic tests on S355 at $\varepsilon_T = \pm 10.0$ % (FEM vs Test)

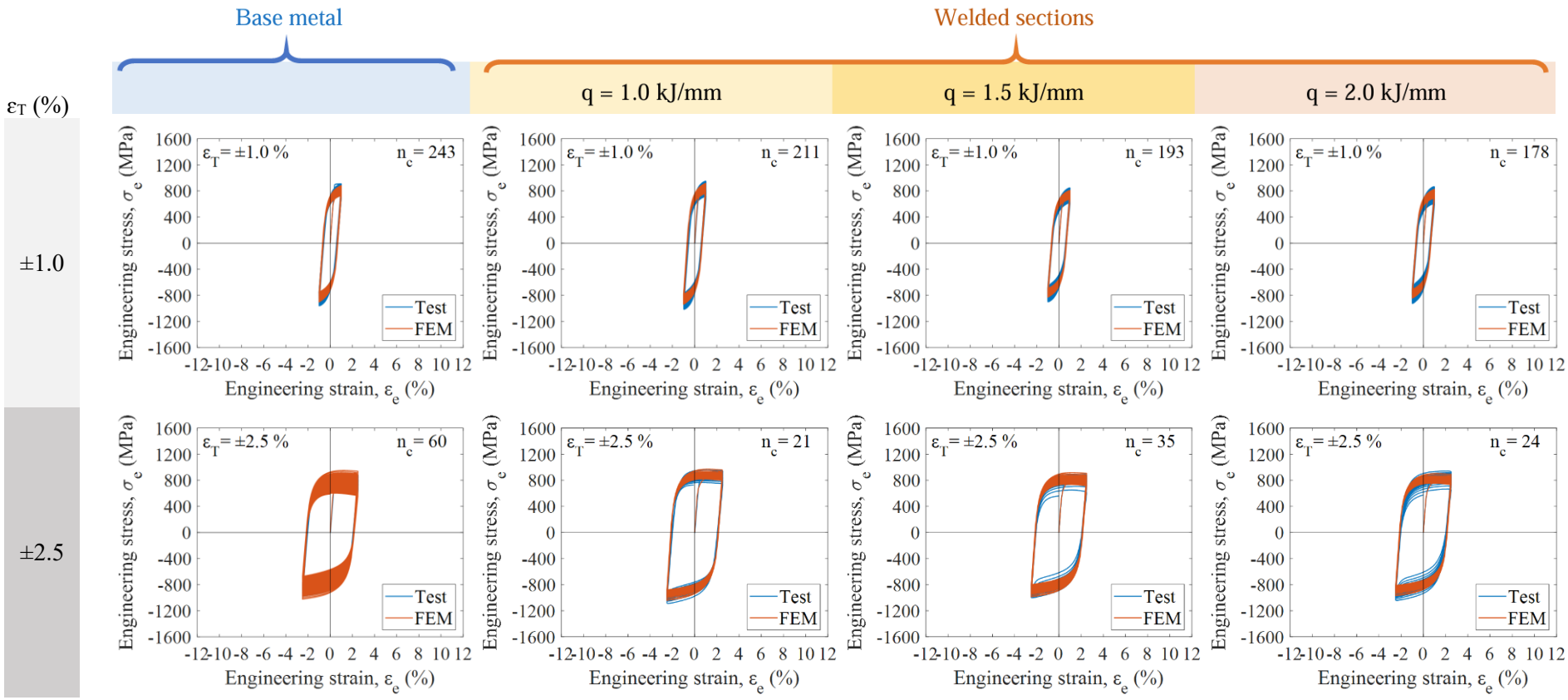

Figure 6.8 Engineering stress-strain curves of the cyclic tests on NJS690 at ε_T = ±1.0 % and ±2.5 % (FEM vs Test)

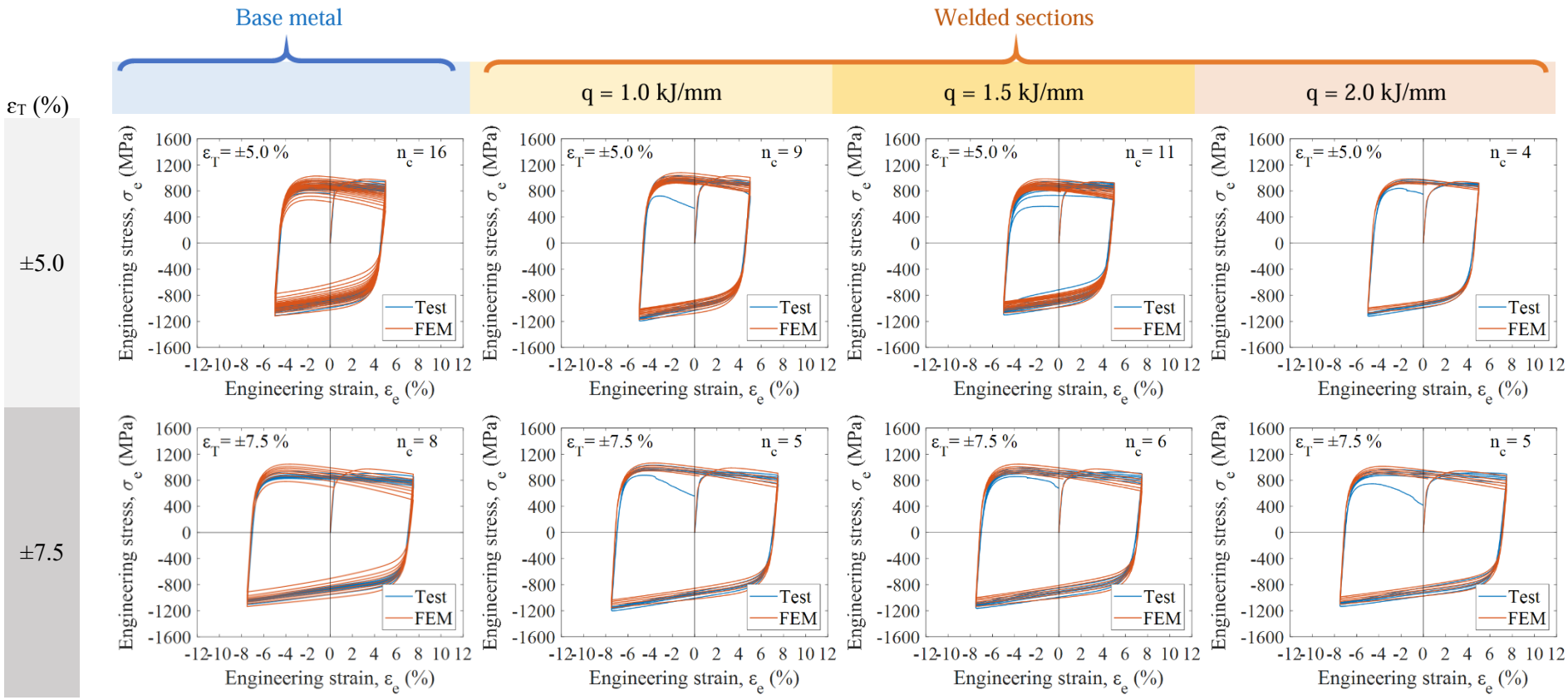

Figure 6.9 Engineering stress-strain curves of the cyclic tests on NJS690 at ε_T = ±5.0 % and ±7.5 % (FEM vs Test)

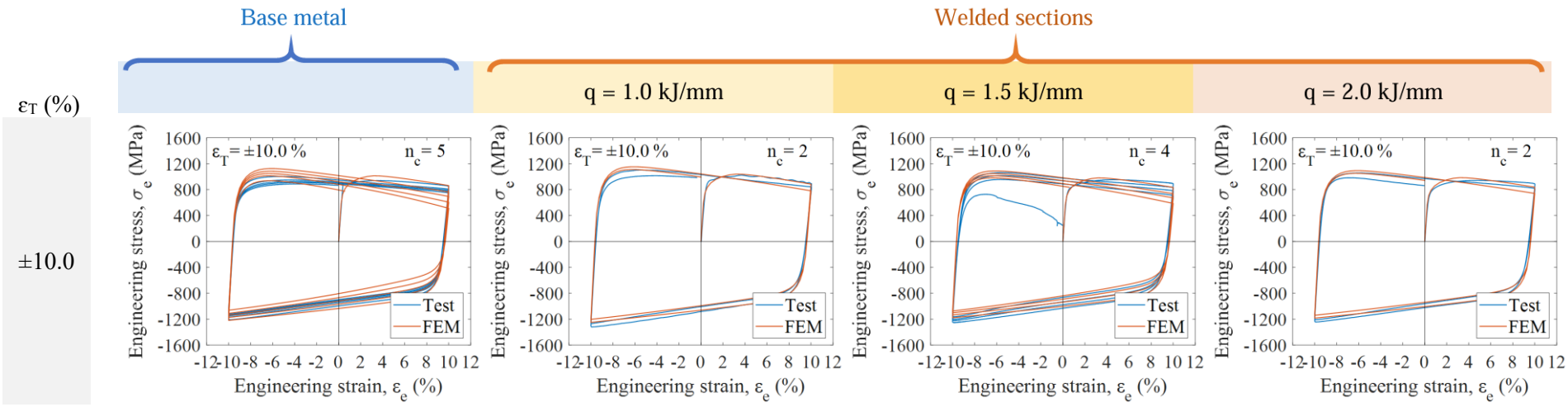

Figure 6.10 Engineering stress-strain curves of the cyclic tests on NJS690 at ε_T = ±10.0 % (FEM vs Test)

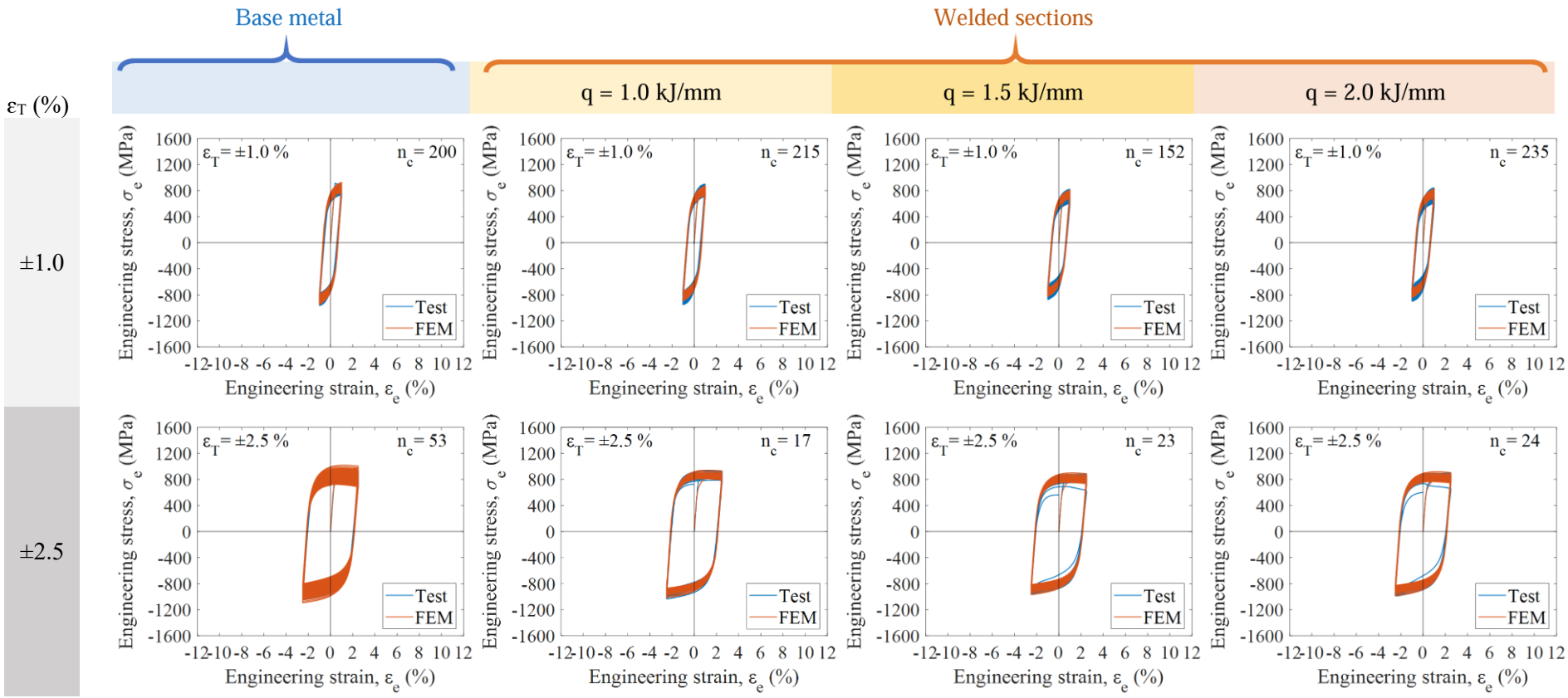

Figure 6.11 Engineering stress-strain curves of the cyclic tests on SGS690 at ε_T = ±1.0 % and ±2.5 % (FEM vs Test)

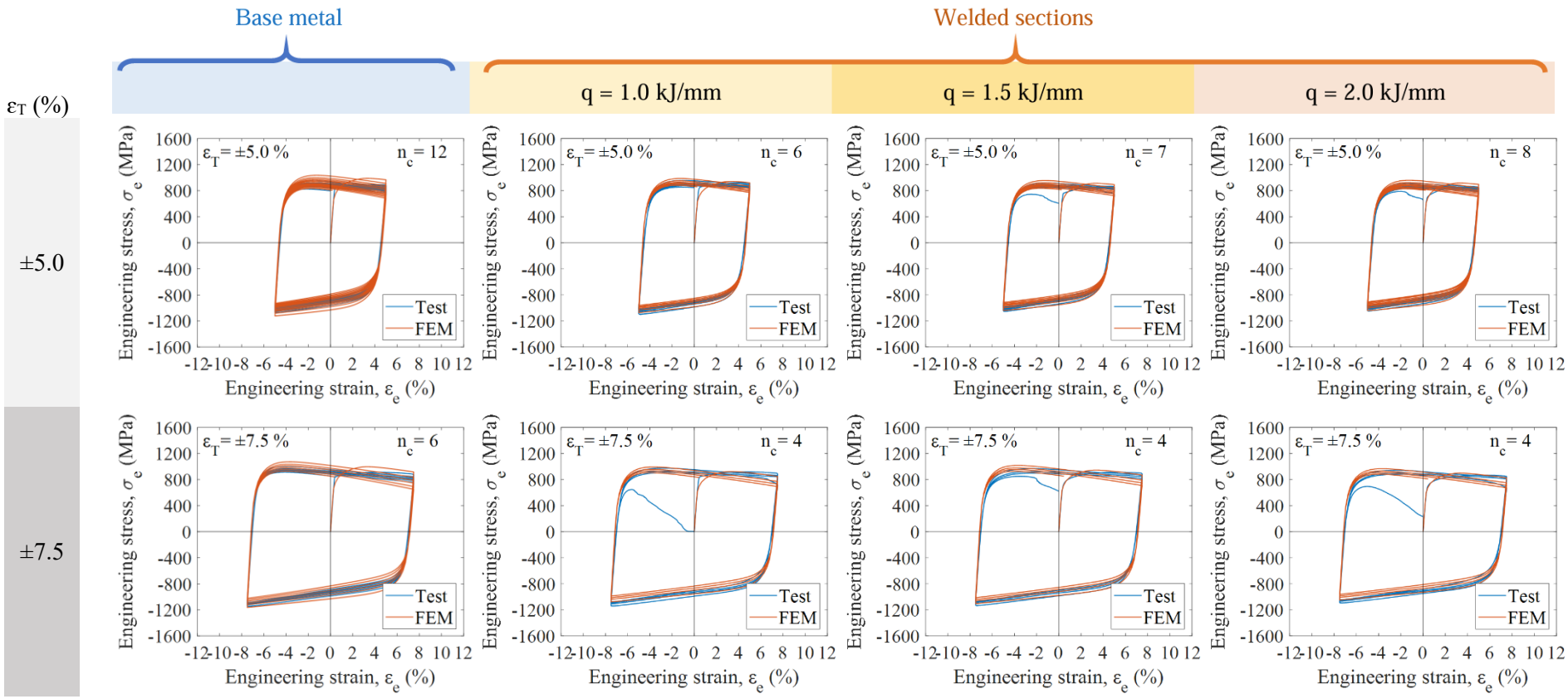

Figure 6.12 Engineering stress-strain curves of the cyclic tests on SGS690 at ε_T = ±5.0 % and ±7.5 % (FEM vs Test)

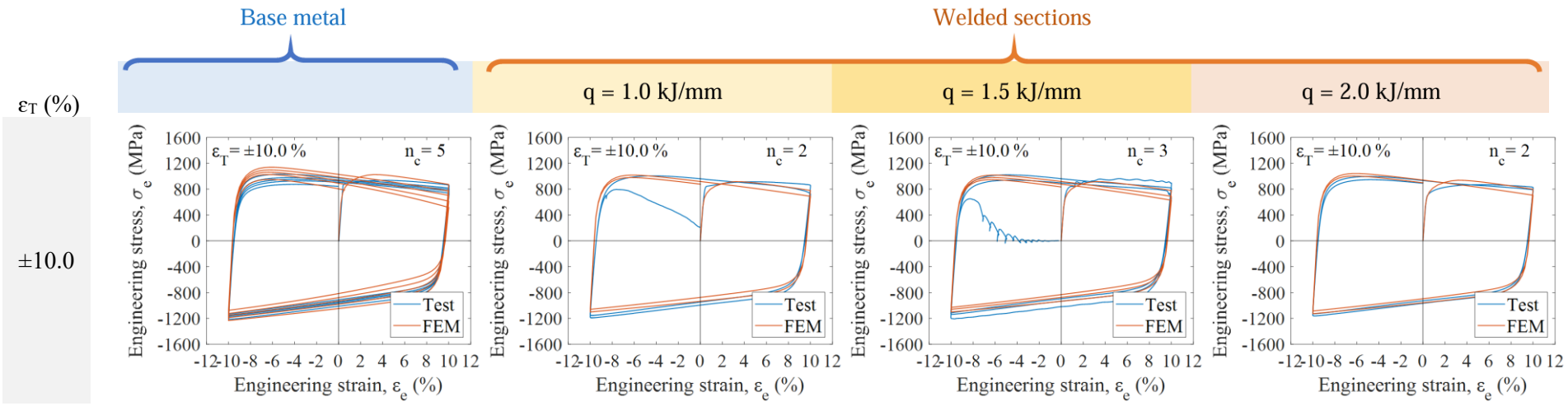

Figure 6.13 Engineering stress-strain curves of the cyclic tests on SGS690 at ε_T = ±10.0 % (FEM vs Test)

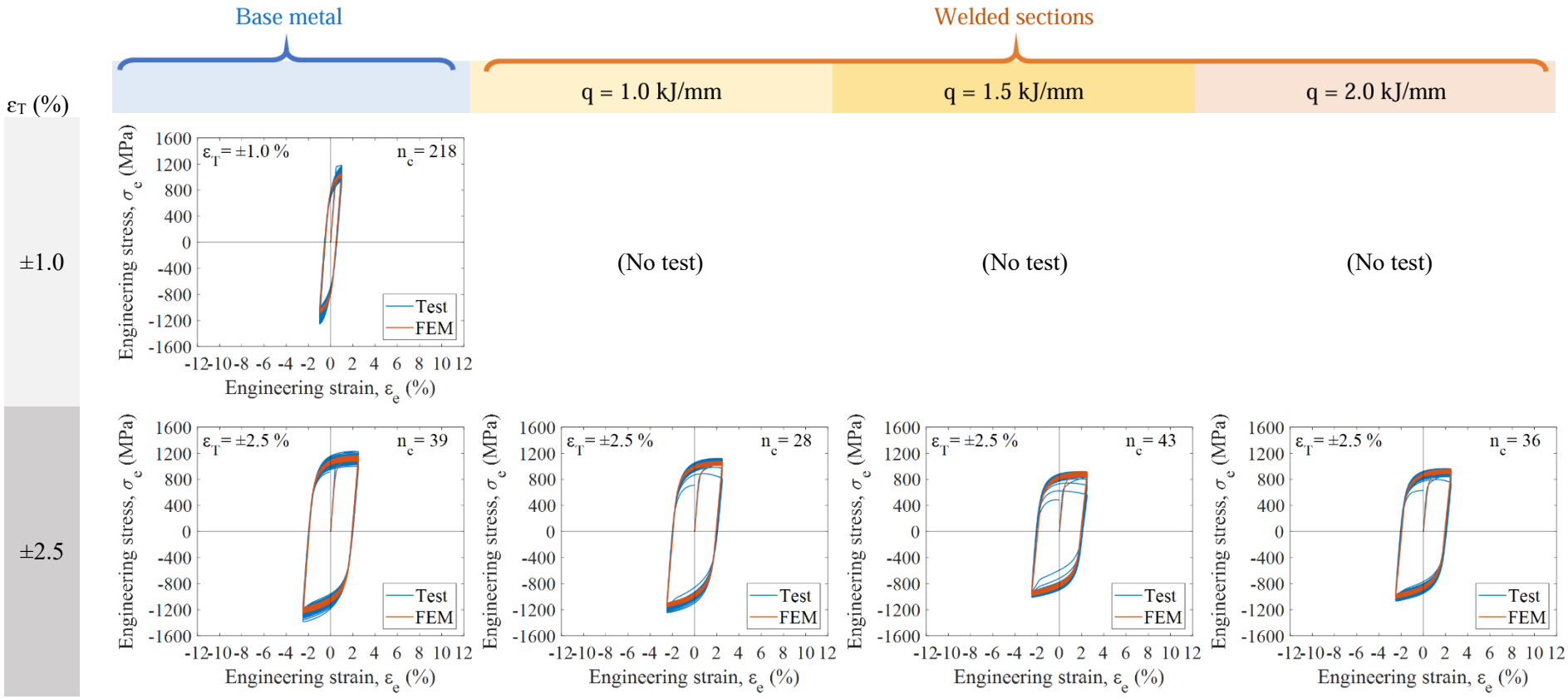

Figure 6.14 Engineering stress-strain curves of the cyclic tests on S960 at ε_T = ±1.0 % and ±2.5 % (FEM vs Test)

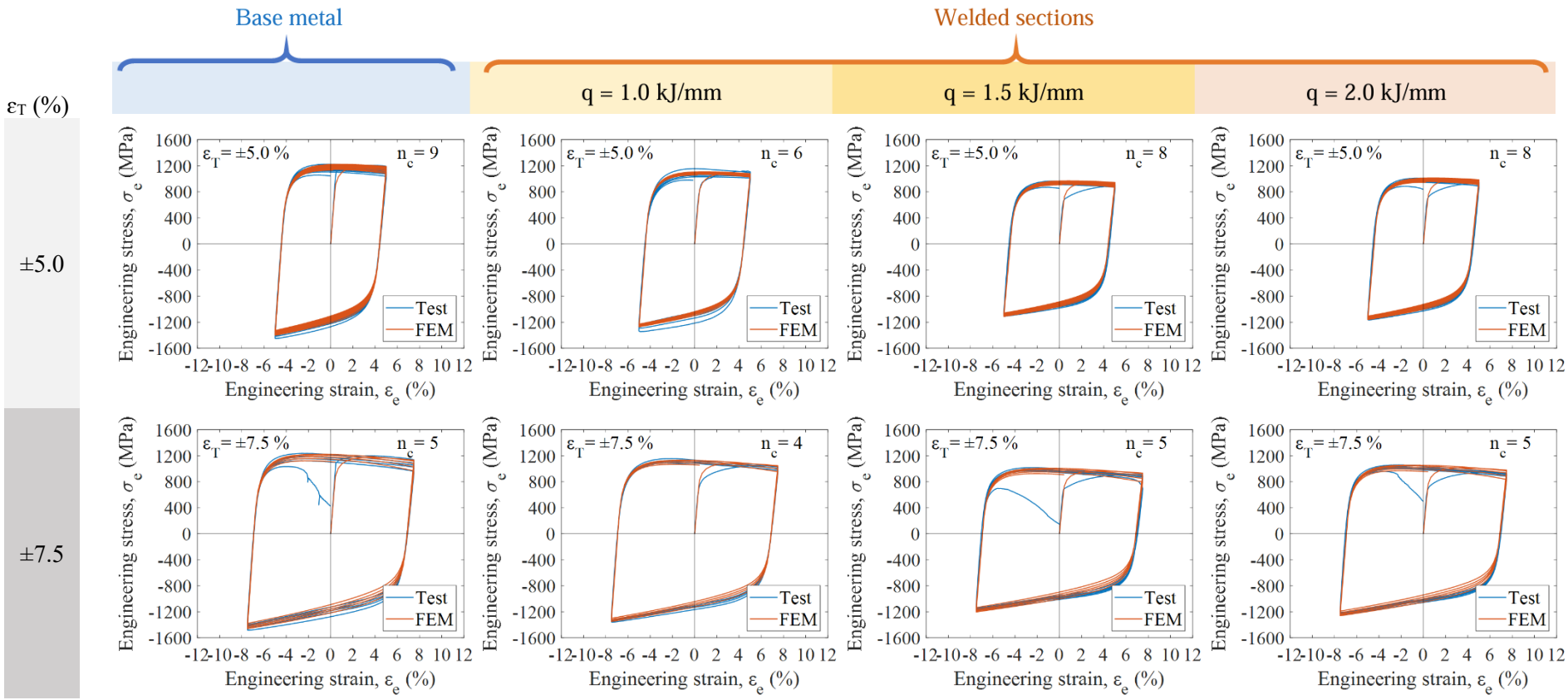

Figure 6.15 Engineering stress-strain curves of the cyclic tests on S960 at ε_T = ±5.0 % and ±7.5 % (FEM vs Test)

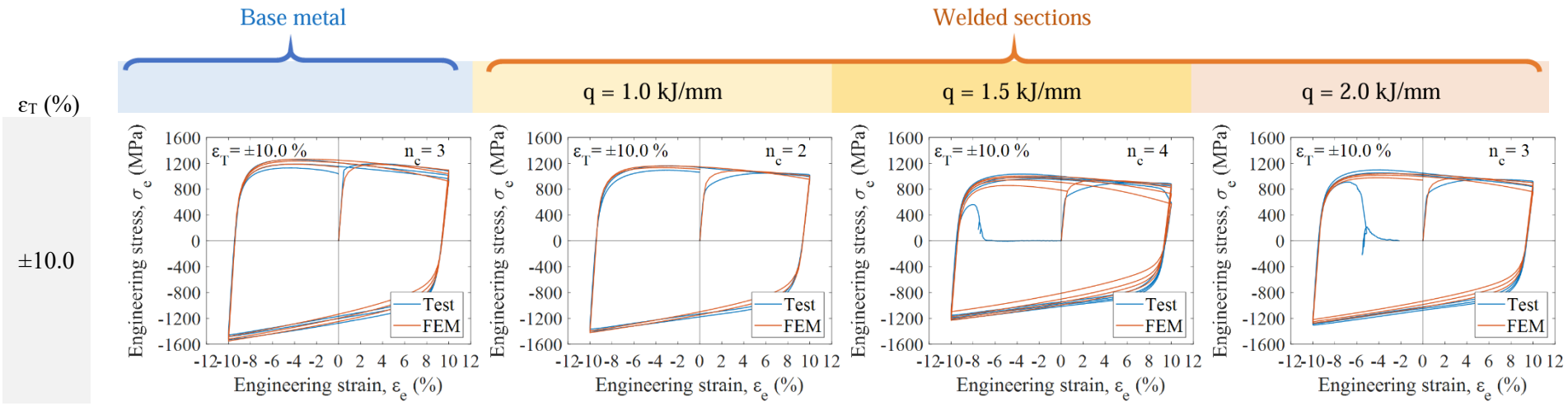

Figure 6.16 Engineering stress-strain curves of the cyclic tests on S960 at $\varepsilon_T = \pm 10.0$ % (FEM vs Test)

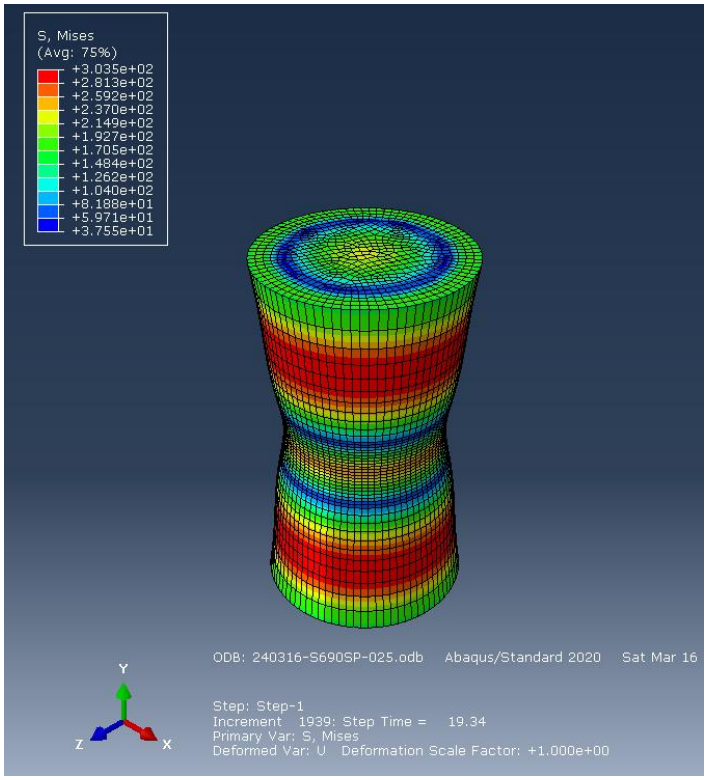

a) Under tension

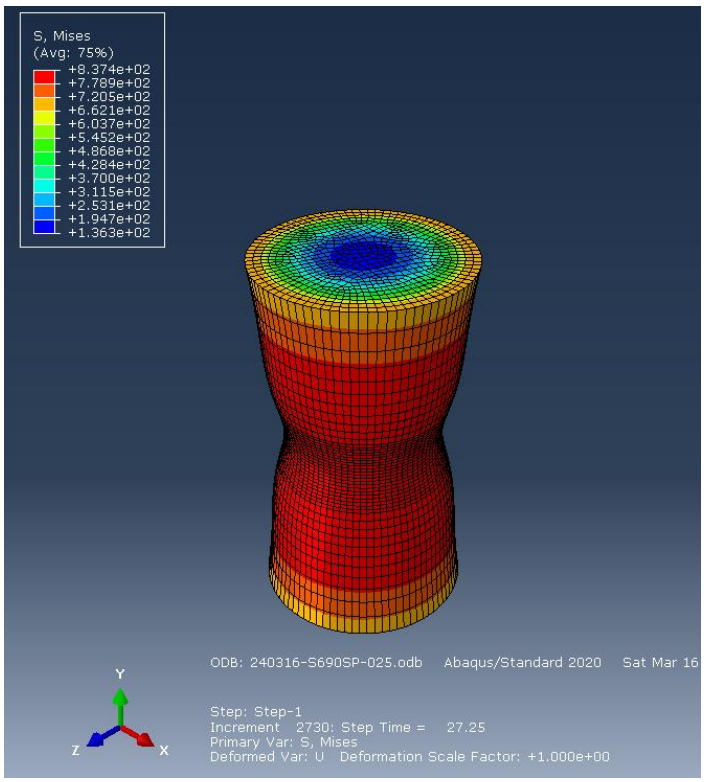

b) Under compression

Figure 6.17 Deformed shapes of FEMs of typical funnel-shaped coupon under cyclic actions

Table 6.1 Finite element models of cyclic tests

S355, S690 (Nangang and Shougang) and S960 steel

Steel grade	Nos of FEM for each steel plate and corresponding welded sections																		
	$\varepsilon_T = \pm 1.0$ %				$\varepsilon_T = \pm 2.5$ %				$\varepsilon_T = \pm 5.0$ %				$\varepsilon_T = \pm 7.5$ %				$\varepsilon_T = \pm 10.0$ %			
	Base metal	Welded sections			Base metal	Welded sections			Base metal	Welded sections			Base metal	Welded sections			Base metal	Welded sections		
		$q_{1.0}$	$q_{1.5}$	$q_{2.0}$		$q_{1.0}$	$q_{1.5}$	$q_{2.0}$		$q_{1.0}$	$q_{1.5}$	$q_{2.0}$		$q_{1.0}$	$q_{1.5}$	$q_{2.0}$		$q_{1.0}$	$q_{1.5}$	$q_{2.0}$
S355	1	1	1	1	1	1	1	1	1	1	1	1	1	1	1	1	1	1	1	1
S690NJ	1	1	1	1	1	1	1	1	1	1	1	1	1	1	1	1	1	1	1	1
S690SG	1	1	1	1	1	1	1	1	1	1	1	1	1	1	1	1	1	1	1	1
S960	1	-	-	-	1	1	1	1	1	1	1	1	1	1	1	1	1	1	1	1

Notes:
"$q_{1.0}$" denotes q = 1.0 kJ/mm, "$q_{1.5}$" denotes q = 1.5 kJ/mm, and "$q_{2.0}$" denotes q = 2.0 kJ/mm, and
"1" denotes 1 model for each material.

Table 6.2 Kinematic hardening parameters of various steel materials

C_1	C_2	C_3	γ_1	γ_2	γ_3
45,980	12,880	1,048	382	67.3	545.9 for S355 and S690 steel
					5.5 for S960 steel

Note: The parameters are applicable to both base metal and welded sections.

Table 6.3 Summary of total strain energy dissipation of FEMs of cyclic tests and percentage errors between simulated and measured values

Steel grade	Total strain energy dissipation, MJ/mm^3 Percentage error (%) between simulated and measured total strain energy dissipation																		
	$\varepsilon_T = \pm 1.0$ %				$\varepsilon_T = \pm 2.5$ %				$\varepsilon_T = \pm 5.0$ %				$\varepsilon_T = \pm 7.5$ %				$\varepsilon_T = \pm 10.0$ %			
	Base metal	Welded sections			Base metal	Welded sections			Base metal	Welded sections			Base metal	Welded sections			Base metal	Welded sections		
		$q_{1.0}$	$q_{1.5}$	$q_{2.0}$		$q_{1.0}$	$q_{1.5}$	$q_{2.0}$		$q_{1.0}$	$q_{1.5}$	$q_{2.0}$		$q_{1.0}$	$q_{1.5}$	$q_{2.0}$		$q_{1.0}$	$q_{1.5}$	$q_{2.0}$
S355	6,830	3,812	7,011	5,617	3,881	3,739	3,107	2,806	1,715	1,497	1,342	1,410	1,335	1,028	991	1,347	1,053	839	841	813
	0.35	4.68	1.64	1.29	17.07	12.94	3.52	7.58	0.73	0.18	0.15	0.21	0.28	0.13	0.03	0.32	0.03	0.06	0.18	0.16
NJS690	5,473	4,970	4,030	3,799	4,041	1,598	2,434	1,688	2,505	1,608	1,762	690	1,970	1,335	1,547	1,272	1,775	789	1,419	748
	0.08	0.13	0.00	0.09	1.16	0.42	0.13	0.18	4.68	0.10	0.05	0.13	0.33	0.23	0.16	0.14	0.19	0.48	0.06	0.04
SGS690	4,778	4,826	3,192	4,963	3,917	1,276	1,615	1,715	1,998	1,012	1,131	1,284	1,585	1,017	1,041	989	1,797	696	1,017	712
	0.00	0.14	0.06	0.08	0.13	0.12	0.11	0.02	0.16	0.16	0.05	0.05	0.10	0.04	0.19	0.12	0.01	0.19	0.10	0.09
S960	6,227	-	-	-	3,634	2,437	3,134	2,753	1,932	1,185	1,369	1,430	1,636	1,227	1,348	1,414	1,353	845	1,387	1,114
	0.01	-	-	-	0.13	0.25	0.05	0.15	0.01	0.04	0.07	0.00	0.02	0.79	1.04	0.17	0.11	0.08	0.04	0.14

Notes:
"$q_{1.0}$" denotes q = 1.0 kJ/mm, "$q_{1.5}$" denotes q = 1.5 kJ/mm, and "$q_{2.0}$" denotes q = 2.0 kJ/mm, and
Percentage error (%) = $\frac{|\text{Simulated value} - \text{Measued value}|}{\text{Measured value}} \times 100\%$.

CHAPTER 7 SIMULATION ON T-JOINTS BETWEEN HIGH STRENGTH S690 STEEL CIRCULAR HOLLOW SECTIONS

7.1 Introduction

This Chapter describes an extension of the finite element modelling technique presented in Chapter 6 for simulation of the cyclic responses of the funnel-shaped coupons of S690 steel to simulate the cyclic responses of the T-joints between cold-formed circular hollow sections of the S690 steel. The constitutive models for the S690 steel under cyclic actions established in Chapter 6 is adopted in the present simulation, and three dimensional finite element models with solid elements are established with properly defined boundary and loading conditions according to the experiments of the T-joints reported in Chapter 5. After careful calibration of these test data, the cyclic responses of these T-joints are thoroughly examined.

7.2 Finite element modelling technique for T-joints

Many researchers developed advanced finite element models of S690 T-joints between cold-formed circular hollow sections with brace in-plane bending using the commercial finite element programme Abaqus (2020). It should be noted that many of them have employed shell elements to model T-joints between circular hollow sections, and the weld between the brace and the chord members are typically simulated also with shell elements so that their effects on strengths and stiffness of T-joints are considered in a simple and approximate manner (van der Vegte and Makino, 2010).

However, in the recent years, a number of numerical investigations have been reported in the literature, and solid elements are employed to model both the brace and the chord members together with the weld along the welded junctions (Hu et al., 2020, 2022). In the present study, the finite element modelling technique developed by Hu et al. (2022) for simulating structural responses of the S690 T-joints between cold-formed circular hollow sections under brace in-

plane bending was adopted, and welding-induced residual stresses were obtained through coupled thermal and thermomechanical analyses using Abaqus with a suitably selected model of a heat source. It was found that the presence of the welding-induced residual stresses had very minor effects on the structural behaviour of these T-joints under brace in-plane bending of i) monotonic actions, and ii) cyclic actions. Consequently, residual stresses are not included in the present study as their effects are considered to be readily neglected.

7.3 Proposed finite element models for S690 T-joints

7.3.1 Establishment of finite element models

In the present study, solid elements C3D8R are employed for modelling the T-joints between circular hollow sections, and an overall view of the finite element mesh of a typical T-joint is shown in Figure 7.1. A total of three layers of solid elements are employed through the thickness of the CFCHS in order to capture local bending behaviour. It should be noted that a general mesh size of 6 mm is determined through a mesh sensitivity study, after considering both computational efficiency and accuracy of the numerical results. A local view of the welded junction between the brace and the chord members of the T-joint is also shown together with a detailed mesh of the weld. Partial penetration butt-welds are also modelled as deep penetration fillet welds in accordance with EN 1993-1-8 (2005). The weld size between the brace and the chord member of each joint is determined as the average measured weld sizes obtained from the experiments.

The stress-strain curves of the S690 steel plates of 6 and 10 mm thickness, obtained from standard tensile tests, are converted to true stress-strain curves, as illustrated in Figure 7.2. The stress-strain curve of S690 weld metal can be simplified using an elastic-perfect plastic model, with the initial elastic modulus set at 210 kN/mm^2. Furthermore, both the isotropic hardening rule and the von Mises yield criterion are adopted for the S690 steel plates and the S690 weld

metal, with their Poisson's ratio taken as 0.3.

7.3.2 Mesh convergence study

The optimum mesh size for the numerical simulation of the proposed model of Joint MT1a has been determined by conducting a convergence study on the mesh configurations by Hu (2019). Three distinct mesh sizes were adopted for comparison purposes as illustrated in Figure 7.3. As shown in Table 7.1, the axial resistances of the "fine" and the "very fine" meshes are almost the same, with only a 0.35% difference, which is considered good enough. To achieve numerical accuracy and computational efficiency, the mesh size for subsequent analyses is set to 5 mm.

7.3.3 Boundary and loading conditions

Figure 7.4 illustrates the boundary and loading conditions of the proposed finite element model. Three reference points are set, and they are coupled with the nodes on the upper surface of the brace (i.e. Reference Point A) and both surfaces of the chord endings (i.e. Reference Points B and C), with all six degrees of freedom. The lateral load is applied onto Reference Point A through a static general method in Abaqus/Standard.

7.4 Numerical analyses and validation of finite element models

It is necessary to validate structural adequacy of the proposed finite element models through a calibration against test results of the T-joints under brace in-plane bending of monotonic actions. The finite element models are then employed to simulate the structural behaviour of the T-joints under brace in-plane bending of cyclic actions.

7.4.1 Calibration of the models under monotonic actions

A total of 4 T-joints under brace in-plane action of monotonic actions were tested, and the

configurations of these T-joints are shown in Table 7.2. Full details of the test programme and test results are presented in Section 5.3. Measured geometrical and material properties of these T-joints were adopted in the finite element models.

Geometrical and material non-linear analyses of these 4 T-joints were successfully performed. It should be noted that:

- Joints MT1a & MT1b

  The predicted applied load-lateral displacement curve of Joint MT1 is plotted in Figure 7.5a) together with the measured curves of Joints MT1a and MT1b. Typical deformed shape of Joint MT1 is also presented for easy reference. It is evident that the predicted curve follows closely to those of the measured curves along the entire deformation ranges of the tests.

- Joints MT2a & MT2b

  Similarly, the predicted applied load-lateral displacement curve of Joint MT2 is plotted in Figure 7.5b) together with the measured curves of Joints MT2a and MT2b. Typical deformed shape of Joint MT2 is also presented for easy reference. It is also evident that the predicted curve follows closely to those of the measured curves along the entire deformation ranges of the tests.

Table 7.3 summarizes key predicted and measured results of the T-joints. The ratios of the predicted and the measured moment results of both Joints MT1 and MT2 are shown to be very close to 1.0, indicating accuracy and efficiency of the proposed finite element models. Consequently, it is demonstrated that the proposed finite element models are able to predict the structural responses of these T-joints with a high level of accuracy throughout the entire deformation ranges.

7.4.2 Calibration of the models under cyclic actions

A total of 6 T-joints under brace in-plane action of monotonic actions were tested, and the configurations of these T-joints are shown in Table 7.4. Full details of the test programme and test results are presented in Section 5.4. Measured geometrical and material properties of these T-joints were adopted in the finite element models, and the constitutive models of the S690 steel presented in Section 6.3 are directly employed.

Geometrical and material non-linear analyses of these 6 T-joints were successfully performed. Figure 7.6 plots typical deformed shapes of the model of the T-joints under cyclic actions, i.e. under applied loads along both the positive and the negative x-axis while Figure 7.7 plots the applied load-lateral displacement curves of Joint CT1 under cyclic actions throughout the entire test. It should be noted that the predicted curves follow closely with the measured ones in the initial stage of deformation while they exhibit limited strength degradation in the final stage of deformation. There are kinks in the measured curves over the range of small applied loads because of bolt slippages at the supports to the T-joint. This is found to be typical in all T-joints. It should be noted that:

- Joints CT1 & CT2

  The predicted applied load-lateral displacement curve of Joints CT1 and CT2 are plotted in Figure 7.8 together with their corresponding measured curves. It is evident that the predicted curves follow closely to those of the measured curves along the entire deformation ranges of the tests, in particular, in both the first and the last cycles (i.e. at least 80% of the original applied load) of the tests.

- Joints CT3 & CT4

  Similarly, the predicted applied load-lateral displacement curves of Joints CT3 and CT4 are plotted in Figure 7.9 together with their corresponding measured curves. It is also evident

that the predicted curves follow closely to those of the measured curves along the entire deformation ranges of the tests, in particular, in both the first and the last cycles (i.e. at least 80% of the original applied load) of the tests.

- Joints CT5 & CT6

  Similarly, the predicted applied load-lateral displacement curves of Joints CT5 and CT6 are plotted in Figure 7.10 together with their corresponding measured curves. It is also evident that the predicted curves follow closely to those of the measured curves along the entire deformation ranges of the tests, in particular, in both the first and the last cycles (i.e. at least 80% of the original applied load) of the tests.

Table 7.5 summarizes key predicted and measured results of the T-joints in the first cycle. The ratios of the predicted and the measured moment results of each of these T-joints are shown to range from 0.94 to 1.19 with an average at 1.05, indicating accuracy and efficiency of the proposed finite element models. Consequently, it is demonstrated that the proposed finite element models are able to predict the structural responses of these T-joints with a high level of accuracy throughout the entire deformation ranges.

7.4.3 Total energy dissipation

An effective means to assess cyclic deformation characteristics of a structural member or joint is its energy dissipation, i.e. the energy absorbed in the member or the joint under each cycle of applied load. It should be noted that the energy dissipation of a T-joint under consideration is readily determined as the area under the applied load-lateral deformation curve. Hence, adding up the energy dissipation absorbed by the T-joint in each cycle gives the total energy dissipation, and comparison on this quantity of various T-joints gives a good picture on their relative performance under cyclic actions. Table 7.6 presents both the predicted and the measured total

energy dissipation, and it is evident that:

- Joints CT1 and CT2

  Owing to their different target displacements, the total energy dissipations of these two tests are expected to be very different. It should be noted that as the target displacements of Joints CT1 and CT2 are 19.0 and 38.0 mm, fracture takes place after 388 and 1 cycles respectively. Hence, the total energy dissipations of these two joints are very different.

- Joints CT3 and CT4

  Owing to their different target displacements, the total energy dissipations of these two tests are expected to be very different. It should be noted that as the target displacements of Joints CT3 and CT4 are 20.3 and 30.3 mm, fracture takes place after 237 and 18 cycles respectively.

- Joints CT5 and CT6

  Similarly, the total energy dissipations of these two tests are expected to be very different. Similar to those in Joints CT3and CT4, the target displacements of Joints CT5 and CT6 are 20.3 and 30.3 mm, and fracture takes place after 207 and 26 cycles respectively.

The differences between the predicted and the measured total energy dissipation among all these 6 T-joints are found to range from 0.7 to 18.2 %. In general, the comparison is considered to be acceptable.

7.5 Conclusion

The finite element modelling technique presented in Chapter 6 for simulation of the cyclic responses of the funnel-shaped coupons of S690 steel is extended to simulate the cyclic responses of the T-joints between cold-formed circular hollow sections of the S690 steel. The constitutive models for the S690 steel under cyclic actions established in Chapter 6 is adopted,

and three dimensional finite element models with solid elements are established with properly defined boundary and loading conditions according to the experiments of the T-joints reported in Chapter 5. After careful calibration of these test data, it is shown:

- Advanced finite element models for the T-joints between circular hollow sections of the S690 steel under brace in-plane bending of monotonic actions have been successfully established after calibration against test data of 4 T-joints. The applied load-lateral displacement curves of these T-joints under monotonic actions are readily predicted along the entire deformation ranges in the tests.
- Moreover, advanced finite element models for these T-joints under brace in-plane bending of cyclic actions have been successfully established after calibration against test data of 6 T-joints. Based on the constitutive models for cyclic actions, the applied load-lateral displacement curves of these T-joints under cyclic actions are readily predicted along the entire deformation ranges in the tests over the numbers of cycles completed before fracture.
- The total energy dissipations of these T-joints are shown to be satisfactorily predicted, when compared with those of the measured values, based on the predicted and the measured deformation characteristics. Hence, the finite element models are readily employed to simulate cyclic deformation characteristics of these T-joints under brace in-plane bending of both monotonic and cyclic actions.

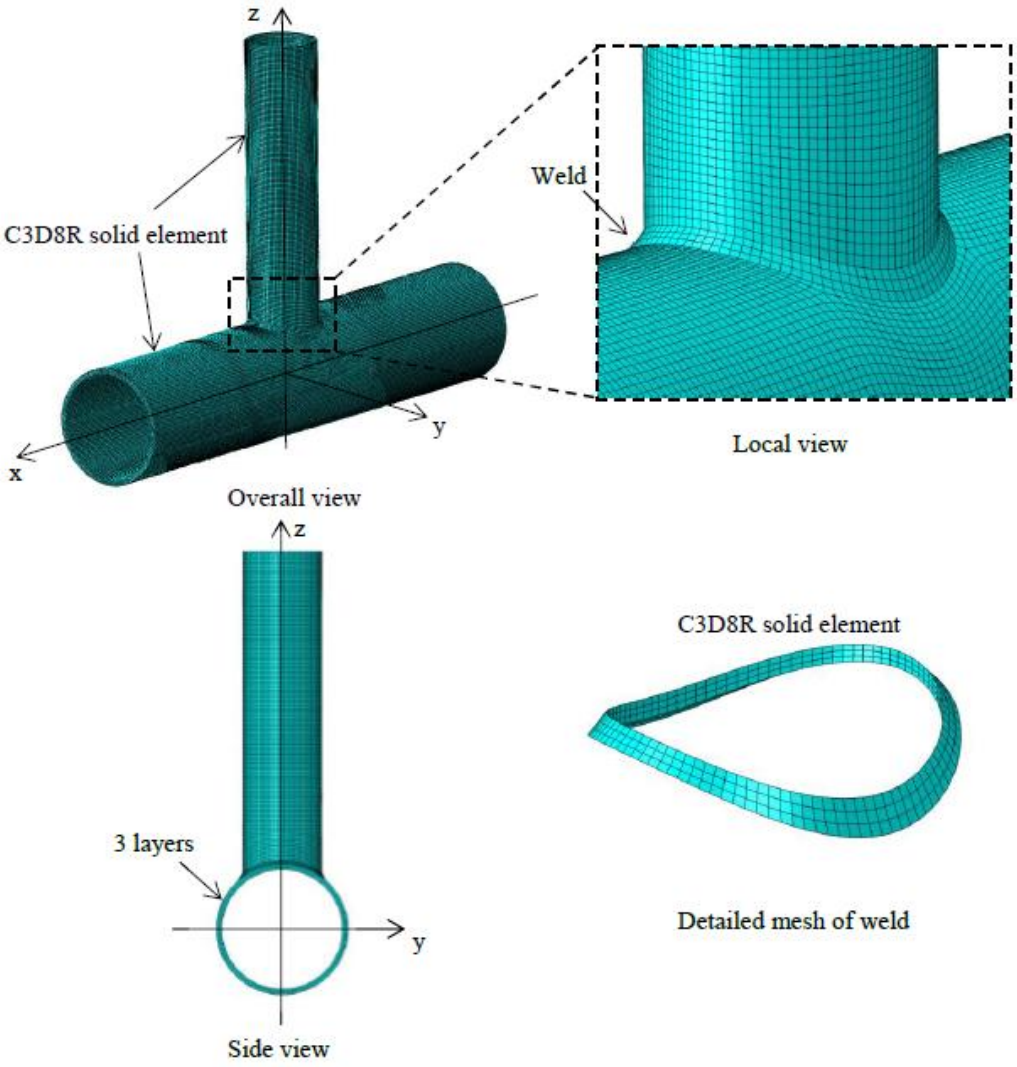

Figure 7.1 Overview of finite element model of T-joint

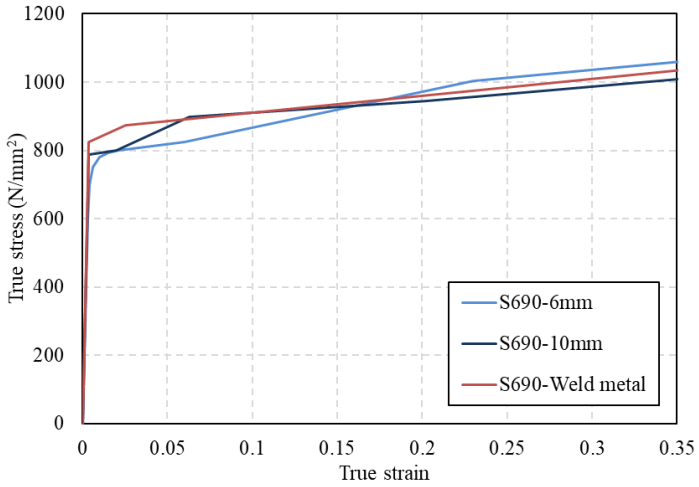

Figure 7.2 True stress-strain curves of the model of T-joint

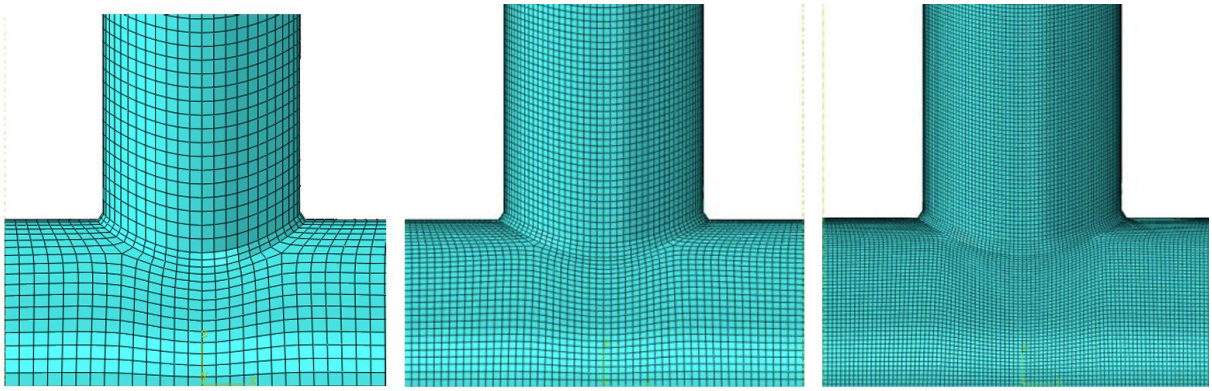

a) Coarse mesh b) Fine mesh c) Very fine mesh

Figure 7.3 Different meshing method of finite element models of T-joint

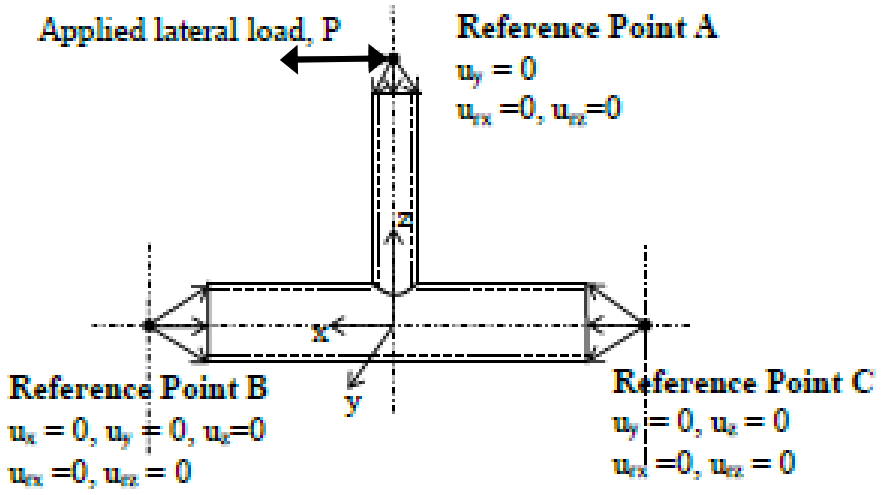

Figure 7.4 Boundary and loading conditions of the model of T-joints under monotonic and cyclic tests

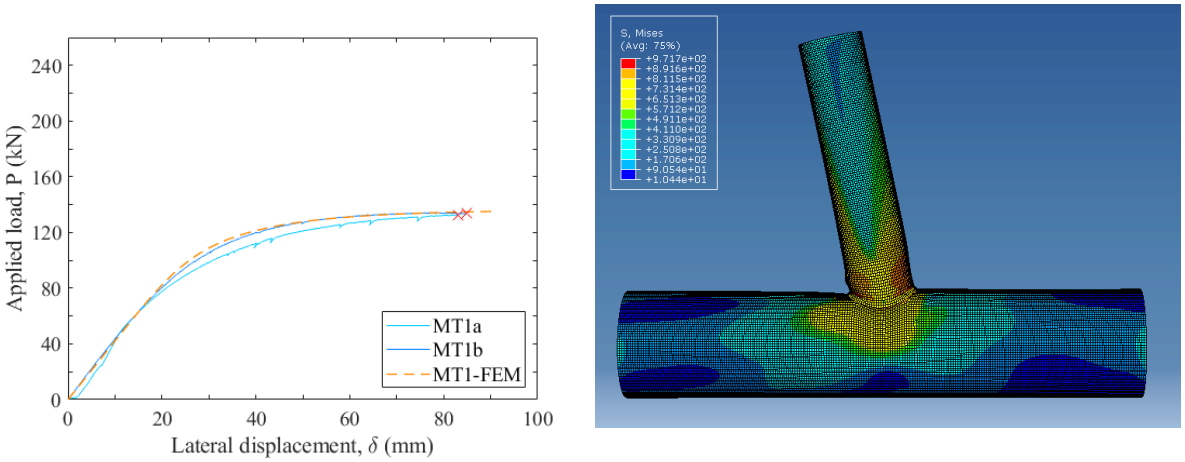

a) Joints MT1a & MT1b

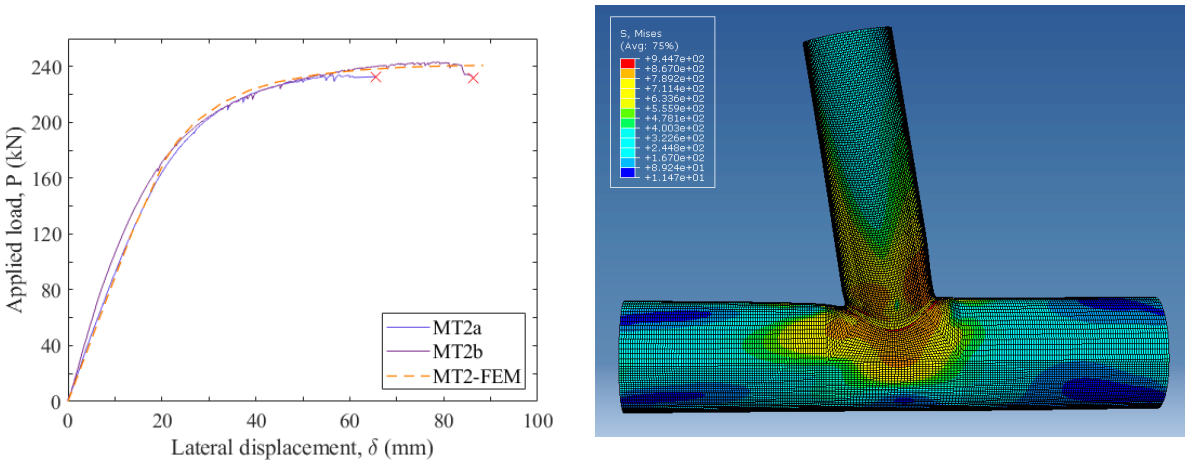

b) Joints MT2a & MT2b

Figure 7.5 Typical deformed shapes of the models of T-joints under monotonic actions

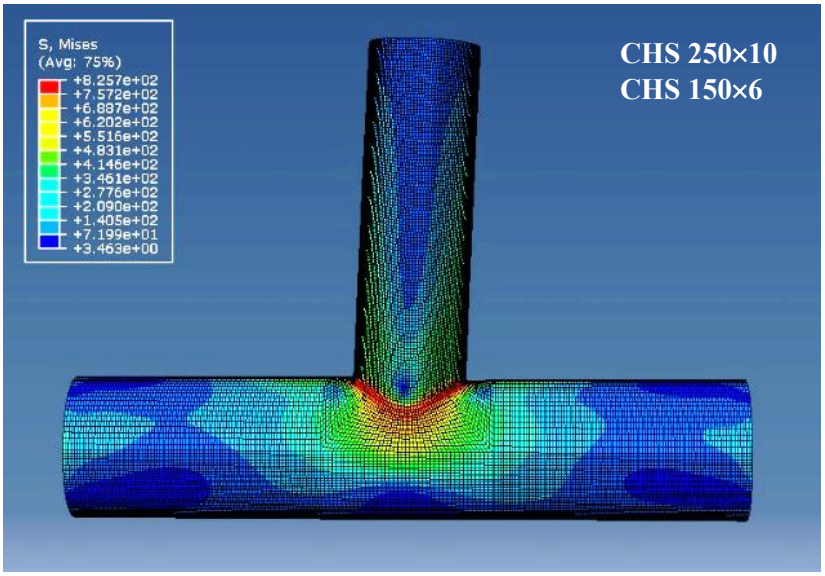

a) Joint CT6 – applied load along positive x-axis

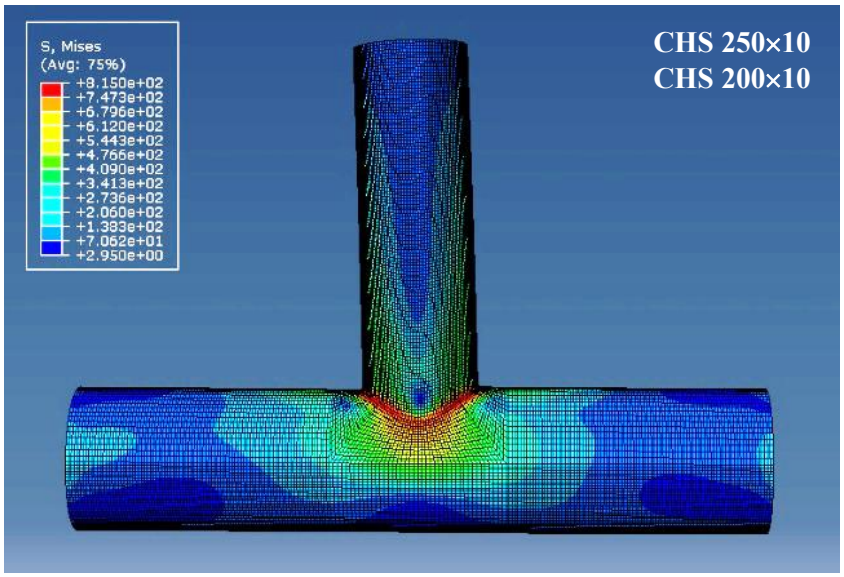

b) Joint CT6 – applied load along negative x-axis

Figure 7.6 Typical deformed shapes of the model of T-joints under cyclic actions

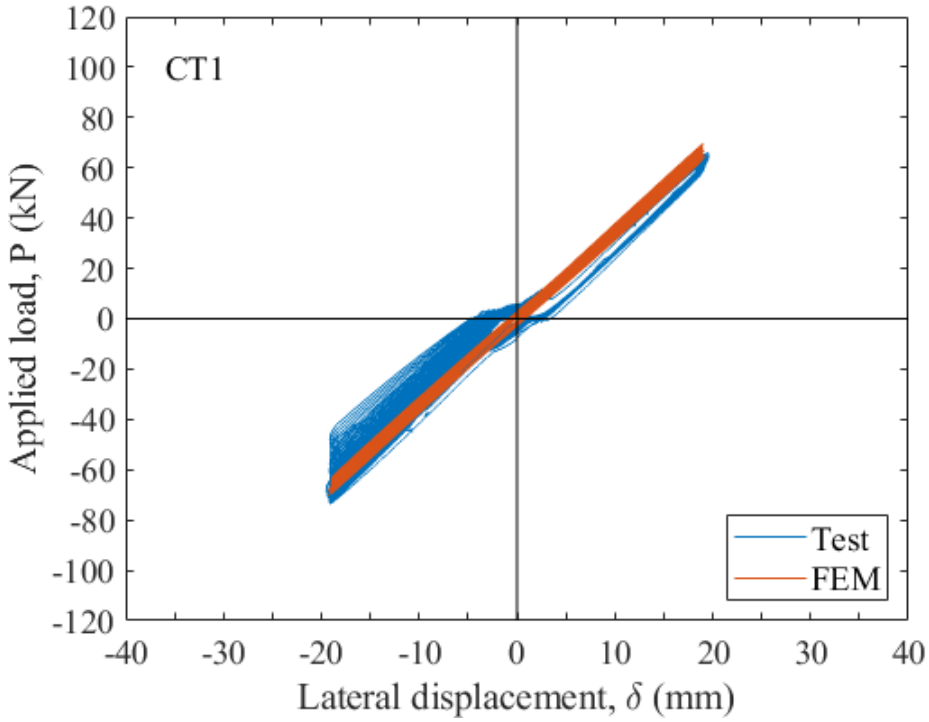

Figure 7.7 Applied load-lateral displacement curves of Joint CT1 under cyclic actions

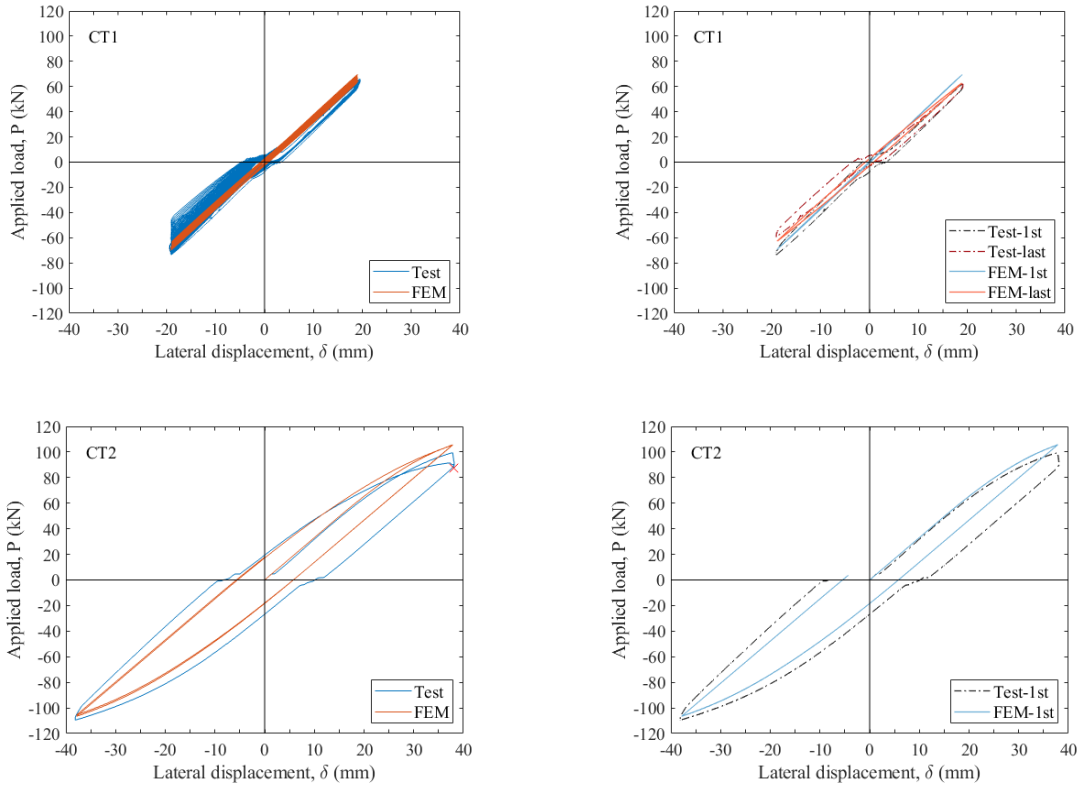

Figure 7.8 Comparison on applied load-lateral displacement curves of Joints CT1 and CT2

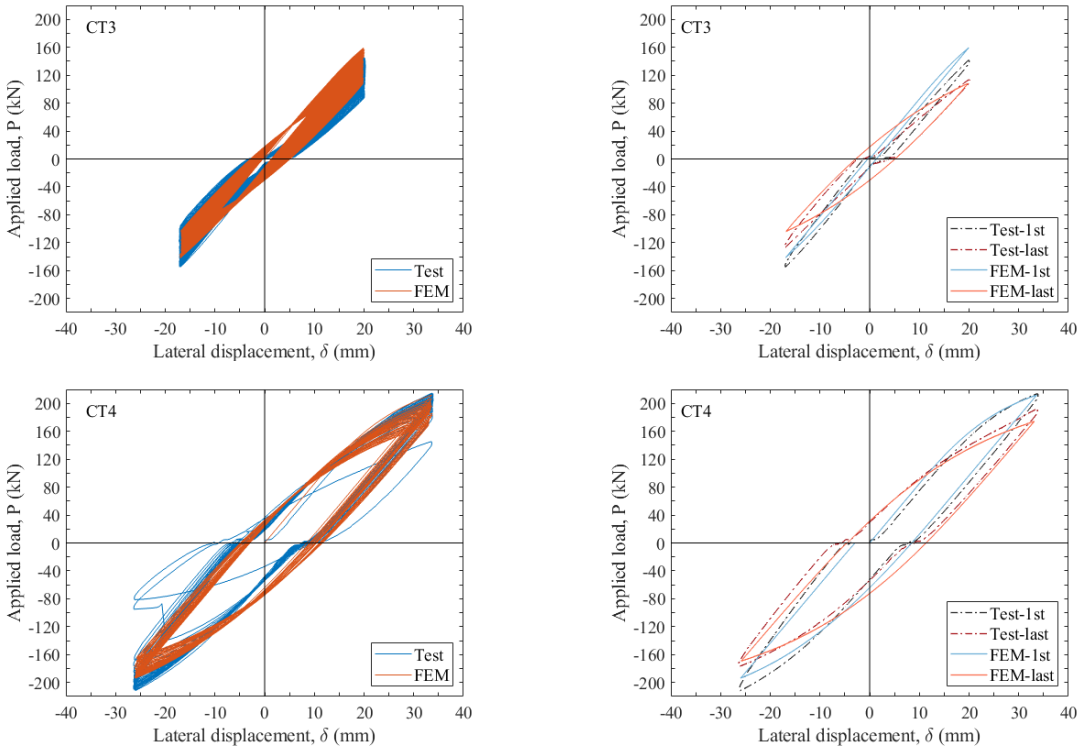

Figure 7.9 Comparison on applied load-lateral displacement curves of Joints CT3 and CT4

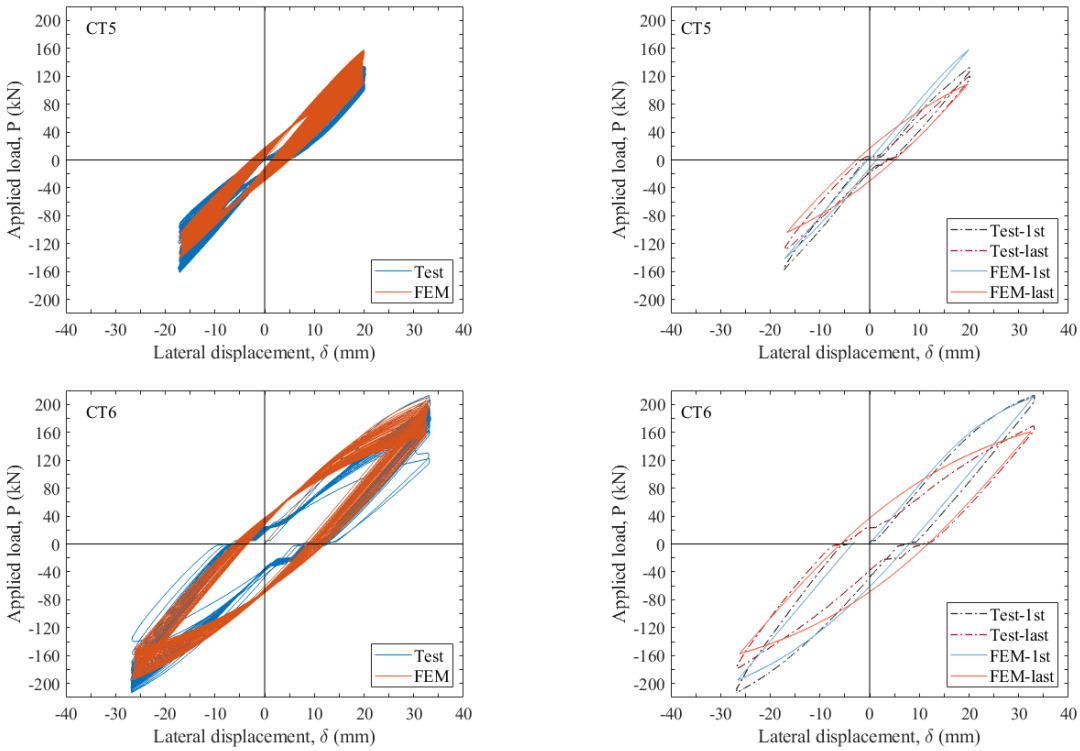

Figure 7.10 Comparison on applied load-lateral displacement curves of Joints CT5 and CT6

Table 7.1 Mesh convergence study on T-joints

Mesh	Mesh size (mm)	Number of elements	Model running time (mins)	Simulated axial resistance (kN)	Difference in simulated axial resistance (%)
Coarse	10	36,960	10	878	1.27
Fine	5	138,864	60	864	-0.35
Very fine	3	355,932	240	867	0

Table 7.2 Configuration of S690 T-joints under monotonic actions

Joint	Steel grade	Heat energy input (kJ/mm)	Chord member $d_0 \times t_0$	Brace member $d_1 \times t_1$	α	β	2γ	τ
MT1a	690	1.2~1.5	250×10	150×6	9.6	0.60	25.0	0.6
MT1b	690	1.2~1.5	250×10	150×6	9.6	0.60	25.0	0.6
MT2a	690	1.2~1.5	250×10	200×10	9.6	0.80	25.0	1.0
MT2b	690	1.2~1.5	250×10	200×10	9.6	0.80	25.0	1.0

Table 7.3 Comparison of measured and predicted moment resistances of T-joints under brace in-plane bending of monotonic actions

Joint	Steel grade	P_{Test} (kN)	M_{Test} (kN·m)	P_{FEM} (kN)	M_{FEM} (kN·m)	Moment resistance ration M_{FEM} / M_{Test}
MT1a	690	132.7	100.9	135.1	102.7	1.02
MT1b	690	134.2	102.0			1.01
MT2a	690	234.2	178.0	240.8	183.0	1.03
MT2b	690	243.3	184.9			0.99

Table 7.4 Configuration of S690 T-joint for cyclic tests

Joint	Steel grade	Heat energy input (kJ/mm)	Chord member $d_0 \times t_0$	Brace member $d_1 \times t_1$	α	β	2γ	τ
CT1	690	1.0	250×10	150×6	9.6	0.60	25.0	0.6
CT2	690	2.0	250×10	150×6	9.6	0.60	25.0	0.6
CT3	690	1.0	250×10	200×10	9.6	0.80	25.0	1.0
CT4	690	1.0	250×10	200×10	9.6	0.80	25.0	1.0
CT5	690	2.0	250×10	200×10	9.6	0.80	25.0	1.0
CT6	690	2.0	250×10	200×10	9.6	0.80	25.0	1.0

Table 7.5 Comparison of measured and predicted moment resistances of T-joints under brace in-plane bending of cyclic actions – positive x-direction in the first cycle

Joint	Steel grade	P_{Test} (kN)	M_{Test} (kN·m)	P_{FEM} (kN)	M_{FEM} (kN·m)	Moment resistance ration M_{FEM} / M_{Test}
CT1	690	73.7	56.0	69.5	52.8	0.94
CT2	690	99.4	75.6	105.7	80.3	1.06
CT3	690	141.4	107.4	159.2	121.0	1.13
CT4	690	213.6	162.3	212.0	161.1	0.99
CT5	690	132.5	100.7	157.9	120.0	1.19
CT6	690	212.8	161.7	210.2	159.7	0.99

Table 7.6 Comparison on predicted and measured total energy dissipation

Model	Target displacement δ (mm)	No. of cycles completed before fracture	Predicted total energy dissipation J_{FEM} (J)	Measured total energy dissipation J_{Test} (J)	Percentage error between J_{FEM} and J_{Test} (%)
CT1	19.0	388	9,717	11,326	14.2
CT2	38.0	1	82	84	0.7
CT3	20.3	237	11,136	13,607	18.2
CT4	30.3	18	2,211	2,253	1.9
CT5	20.3	207	9,816	11,721	16.3
CT6	30.3	26	3,058	3,296	7.2

Note: Percentage error (%) = $\frac{|\text{Simulated value} - \text{Measued value}|}{\text{Measured value}} \times 100\%$.

CHAPTER 8 CONCLUSIONS AND FUTURE WORK

8.1 Introduction

This thesis presents a comprehensive examination into deformation characteristics of the high strength S690 and S960 steel under axial cyclic actions loads, and both experimental and numerical investigations have been conducted to provide scientific understanding and engineering data to assess their suitability in seismic resistant structures. It should be noted that the effects of welding onto the deformation characteristics of these S690 and S960 steel have also been studied systematically.

8.2 Key activities

Key activities of the present study are summarized as follows:

8.2.1 Part I Experimental investigations

iv) Deformation characteristics of the S355, the S690 and the S960 steel plates and their welded sections *under monotonic actions* were obtained from standard tensile tests on cylindrical coupons. These provide essential reference data on both strength and ductility of the steel.

v) *Cyclic deformation characteristics* of the S355, the S690 and the S960 steel plates and their welded sections were also obtained, and funnel-shaped coupons were subjected to cyclic actions with 4 different target strains, i.e. $\varepsilon_m = \pm 1.0\%, \pm 2.5\%, \pm 5.0\%, \pm 7.5\%$ and $\pm 10.0\%$, and 2 loading frequency, f, i.e. f = 0.1 Hz and 1.0 Hz. It should be noted that 3 different heat input energy, i.e. q = 1.0, 1.5 and 2.0 kJ/mm, are adopted during welding.

vi) Deformation characteristics of T-joints between cold-formed circular hollow sections of S690 steel under in-plane bending of *monotonic and cyclic actions* were attained, and different heat input energy, i.e. q = 1.0 to 2.0 kJ/mm, are adopted during welding of the T-

joints.

8.2.2 Part II Numerical investigations

i) Advanced finite element models on cylindrical coupons of S355, S690 and S960 steel and their welded sections *under monotonic actions* have been established, and these models have been calibrated carefully against test data.

ii) Advanced finite element models have also been established to simulate deformation characteristics of funnel-shaped coupons of S355, S690 and S960 steel *under cyclic actions* of various target strains ε_m and loading frequencies f, and these models have been calibrated successfully against test data.

v) All these structural models are established with solid elements using the general finite element package **Abaqus**, and all structural analyses are performed to determine *structural responses* of these sections, i.e. deformations, and stresses and strains.

vi) Based on the modelling technique acquired from the two sets of models mentioned above, advanced finite element models on T-joints of S690 CFCHS under *monotonic and cyclic actions* of various target displacements have also been established, and these models have been calibrated against test data.

8.3 Key research findings

Key research findings of the present study are summarized as follows:

e) Axial cyclic actions in coupons of base plates and welded sections

According to the observed hysteretic curves of the coupons with various steel grades, it is found that both the numbers of cycles completed before fracture for the S690 and the S960 steel coupons are about 70% of those of the S355 steel. However, the total energy dissipation of both the S690 and the S960 steel coupons are found to be similar to those of

the S355 steel. Hence, despite the number of cycles completed of the S690 and the S960 steel coupons are smaller than those of the S355 steel, *all of these steel possess the same amount of dissipation energy*. In addition, similar results have also been obtained for all these welded sections. ***These contradict to the common understanding on the high strength S690 and S960 steel held by many researchers***.

f) Simple and effective constitutive models for the S355, the S690 and the S960 steel and their welded sections under cyclic actions have been developed, and ***specific values of various parameters of the constitutive models are established after careful calibration against test data***. It is noteworthy that these proposed models are demonstrated to be capable of predicting both the hysteretic curves and the total strain energy dissipation of both the coupons and the T-joints of these high strength steel with a high level of accuracy.

g) According to the measured deformation characteristics of the T-joints between cold-formed circular hollow sections of the S690 steel under brace in-plane bending of cyclic actions, it is found that ***these T-joints exhibit a high level of cyclic ductility with large dissipation energy***. Moreover, there is a strong relation between the cyclic deformation characteristic of the coupons and those of the T-joints. ***In general, the numbers of cycles completed before fracture of the T-joints are related inversely to the values of the target lateral displacements through a highly non-linear manner.***

Consequently, it is demonstrated that the S690 and the S960 steel exhibit good cyclic deformation characteristics in both welded sections and T-joints under a wide range of cyclic actions with different magnitudes of target strains. Hence, these steel are considered to possess good cyclic deformation characteristics under large cyclic deformations, and they are readily adopted for seismic resistant structures.

8.4 Limitations and future work

After a rigorous experimental investigation into the cyclic deformation characteristics of the high strength S690 and S960 steel through axial cyclic tests on their coupons, an investigation onto the S690 T-joints between circular hollow sections was carried out. After data analysis, it is found that the numbers of cycles completed before fracture of these T-joints are related inversely to the values of the target lateral displacements through a highly non-linear manner. Numerical investigations have also been performed, and good modelling results have been obtained. However, only S690 QT and S960 QT steel were considered in this study, while different heat treatments and chemical compositions may result in different HAZ. Furthermore, only limited joint types and plate thicknesses are considered. Consequently, it is proposed to carry out the following investigations in the future:

i) *Cyclic deformation characteristics of the high strength S690 and S960 TMCP steel with different plate thicknesses through axial cyclic tests on their coupons.*

   These axial cycle tests should be carried out with target strains designated to range from 1.0 to 10.0%.

ii) *Advanced finite element modelling of these coupons under different cyclic actions.*

   The constitutive models for different steel should be developed and calibrated carefully against test data. The predicted cyclic deformation characteristics and their total energy dissipation will be examined and compared carefully with the measured data.

iii) *Cyclic responses of different joint types under brace in-plane bending for S355, S690 and S960 steel of cyclic actions.*

   These cycle tests should be carried out under different loading protocols, i.e. under i) various constant target strains, and ii) varying target strains while the target strains are designated to range from 1.0 to 5.0%.

iv) *Advanced finite element modelling of these T-joints of different steel and under different*

cyclic actions.

The constitutive models for different steel should be developed and calibrated carefully against test data. The predicted cyclic deformation characteristics of these T-joints, in particular, their total energy dissipation, will be examined and compared carefully with the measured data.

v) *A systematic parametric study to generate structural insights and engineering data on the structural performance of different joint types of different steel over a practical range of cyclic actions.*

A wide range of geometrical and material data of T-joints will be covered. The knowledge is essential for adoption of the high strength S690 and S960 steel sections and their T-joints in seismic resistant structures.

REFERENCES

AISC (2016). ANSI/AISC 360-16: Specification for Structural Steel Buildings. American Institute of Steel Construction, Chicago, U.S.A.

Armstrong, P. J., & Frederick, C. O. (1966). A mathematical representation of the multiaxial Bauschinger effect (Vol. 731). Berkeley, CA: Berkeley Nuclear Laboratories.

AWS. (2005), Specification for Low-Alloy Steel Electrodes and Rods for Gas Shielded Arc Welding. Structural Welding Code – Steel, American Welding Society, Miami, United States.

Azhari, F., Al-Amin Hossain, A., Heidarpour, A, Zhao, X. L., & Hutchinson, C. R. (2018). Mechanical response of ultra-high strength (Grade 1200) steel under extreme cooling conditions. Constructional Building Materials; 175:790–803.

BD. Code of Practice for the Structural Use of Steel 2011 (2023 Edition), Buildings Department (BD), Hong Kong SAR, China.

Bridgman, P. W. (1952). Studies in Large Plastic Flow and Fracture. Mc Grraw Hill, New York.

CEN. (2004). Hot rolled products of structural steels – Part 1: General technical delivery conditions. British Standards Institution. BS EN 10025-1: 2004, European Committee for Standardization (CEN), Brussels, Belgium.

CEN. (2004). Hot rolled products of structural steels – Part 1: Technical delivery conditions for non-alloy structural steels. British Standards Institution. BS EN 10025-2: 2004, European Committee for Standardization (CEN), Brussels, Belgium.

CEN. (2004). Hot rolled products of structural steels – Part 1: Technical delivery conditions for normalized/normalized rolled weldable fine grain structural steels. British Standards Institution. BS EN 10025-3: 2004. European Committee for Standardization (CEN), Brussels, Belgium.

CEN. (2005). BS EN 1993-1-8, Eurocode 3: Design of steel structures Part 1-8: Design of joints. European Committee for Standardization.

CEN. (2005). Eurocode 3 - Design of steel structures - Part 1-9: Fatigue. BS EN 1993-1-9:2005, European Committee for Standardization (CEN), Brussels, Belgium.

CEN. (2007). Eurocode 3 - Design of steel structures - Part 1-12: Additional rules for the extension of EN 1993 up to steel grades S 700. BS EN 1993-1-12:2007, European Committee for Standardization (CEN), Brussels, Belgium.

CEN. (2013). Eurocode 8 - Design of structures for earthquake resistance - Part 1: General rules, seismic actions and rules for buildings. BS EN 1998-1:2004+A1:2013, European Committee for Standardization (CEN), Brussels, Belgium.

CEN. (2014). Eurocode 3 - Design of steel structures - Part 1-1: General rules and rules for buildings. BS EN 1993-1-1:2005+A1:2014, European Committee for Standardization (CEN), Brussels, Belgium.

CEN. (2019). Metallic materials - Tensile testing - Part 1: Method of test at room temperature. BS EN ISO 6892-1:2019, European Committee for Standardization (CEN), Brussels, Belgium.

CEN. (2022). Hot rolled products of structural steels – Part 1: Technical delivery conditions for thermomechanical rolled weldable fine grain structural steels. British Standards Institution. BS EN 10025-4:2019+A1:2022. European Committee for Standardization (CEN), Brussels, Belgium.

CEN. (2022). Hot rolled products of structural steels - Part 6: Technical delivery conditions for flat products of high yield strength structural steels in the quenched and tempered condition. BS EN 10025-6:2019+A1:2022, European Committee for Standardization (CEN), Brussels, Belgium.

CEN. (2022). Eurocode 3 - Design of steel structures - Part 1-1: General rules and rules for buildings. BS EN 1993-1-1:2022, European Committee for Standardization (CEN), Brussels, Belgium.

Chaboche, J. L., Van, K. D., & Cordier, G. (1979). Modelization of the strain memory effect on the cyclic hardening of 316 stainless steel.

Chaboche, J. L. (1986). Time-independent constitutive theories for cyclic plasticity. International Journal of plasticity, 2(2), 149-188.

Chaboche, J. L. (1989). Constitutive equations for cyclic plasticity and cyclic viscoplasticity. International journal of plasticity, 5(3), 247-302.

Chaboche, J. L. (2008). A review of some plasticity and viscoplasticity constitutive theories. International journal of plasticity, 24(10), 1642-1693.

Chen, Y., Sun, W. & Chan, T. M. (2013). Effect of loading protocols on the hysteresis behaviour of hot-rolled structural steel with yield strength up to 420 MPa. Advanced Structural Engineering, 16 (4): 707-719.

Dafalias, Y. F., & Popov, E. P. (1975). A model of nonlinearly hardening materials for complex loading. Acta Mechanica, 21, 173-192.

Dafalias, Y. F., & Popov, E. P. (1976). Plastic internal variables formalism of cyclic plasticity. Journal of Applied Mechanics, 43, 645-651.

Dassault Systemes Simulia Corp. (2020). SIMULIA Abaqus FEA (Abaqus/CAE 2020). [Computer software]. https://www.3ds.com/products/simulia

Ding, Q., Wang, T., Shi, Z., Wang, Q., Wang, Q., & Zhang, F. (2017). Effect of welding heat input on the microstructure and toughness in simulated CGHAZ of 800 MPa Grade steel for hydropower penstocks. Metals; 7(4):115.

ECCS. (1986). Recommended testing procedure for assessing the behaviour of structural steel elements under cyclic loads. Tech Comm 1 – Structural safety and loadings. TWG 1.3 Rep. No. 45; 1986.

FEMA 461. (2007). Interim testing protocols for determining the seismic performance characteristics of structural and non-structural components. Washington, D.C., U.S.A: Federal Emergency Management Agency, Department of Homeland Security; 2007.

Fournier, B., Sauzay, M., Caës, C., Noblecourt, M. & Mottot, M. (2006). Analysis of the hysteresis loops of a martensitic steel – Part I: Study of the influence of strain amplitude and temperature under pure fatigue loadings using an enhanced stress partitioning method. Material Science and

Engineering: A, 437: 183-196.

Fournier, B., Sauzay, M., Caës, C., Noblecourt, M., Mottot, M. & Pineau, A. (2006). Analysis of the hysteresis loops of a martensitic steel – Part II: Study of the influence of creep and stress relaxation holding times on cyclic behaviour. Mater Sci Eng, A;437:197–211.

Guo, Y. B., Ho, H. C., Chung, K. F., & Elghazouli, A. Y. (2020). Cyclic deformation characteristics of S355 and S690 steels under different loading protocols. Engineering Structures, 221, 111093.

Havula, J., Garifullin, M., Heinisuo, M., Mela, K. & Pajunen, S. (2018). Moment-rotation behaviour of welded tubular high strength steel T joint. Eng Struct, 172:523–37.

He, Q., Yam, M. C., Xie, Z., Ho, H. C., & Chung, K. F. (2022). Experimental and modelling study of cyclic plasticity of high strength steel Q690. Journal of Constructional Steel Research, 196, 107433.

Ho, H. C., Liu, X., Chan, T. M. & Chung, K. F. (2016). Hysteretic behavior of Q275 and Q690 structural steel materials. In: Proceedings of the 14th East Asia-pacific conference on structural engineering and construction (EASEC-14), Ho Chi Minh City, Vietnam, 6–8 January 2016.

Ho, H. C., Liu, X., Chung, K. F., Elghazouli, A. Y., & Xiao, M. (2018). Hysteretic behaviour of high strength S690 steel materials under low cycle high strain tests. Engineering Structures, 165, 222-236.

Ho, H. C., Chung, K. F., Huang, M. X., Nethercot, D. A., Liu, X, Jin, H, Wang, G. D. & Tian, Z. H. (2020). Mechanical properties of high strength S690 steel welded sections through tensile tests on heat-treated coupons. Journal of Construction Steel Research, 166: 105922.

Ho, H. C., Guo, Y. B., Xiao, M., Xiao, T. Y., Jin, H., Yam, M. C. H., Chung, K. F. & Elghazouli, A. Y. (2021). Structural response of high strength S690 welded sections under cyclic loading conditions. Journal of Constructional Steel Research, 182, 106696.

Hu, F. & Shi, G. (2018). Constitutive model for full-range cyclic behaviour of high strength steel without yield plateau. Constructional Building Materials, 162: 596-607.

Hu, Y. F. (2019). Structural behaviour of high strength S690 steel cold-formed circular hollow sections (Ph.D. dissertation). The Hong Kong Polytechnic University.

Hu, Y. F., Chung, K. F., Ban, H., & Nethercot, D. A. (2020). Investigations into residual stresses in S690 cold-formed circular hollow sections due to transverse bending and longitudinal welding. Engineering Structures, 219, 110911.

Hu, Y. F., Chung, K. F., Ban, H., & Nethercot, D. A. (2022). Structural testing and numerical modelling of T-joints between cold-formed S690 circular hollow sections under brace in-plane bending. Engineering Structures, 250, 113317.

JSCE. (2000). Hagane Kouzoubutu no Taisin Kentou Syouiinkai Houkokusyo (Gaiyou syuu), 2000 Nen [Report of the Sub-Committee on Seismic Review of Steel Structures (Summary), Year of 2000]. Committee on Steel Structures, Japan Society of Civil Engineers, Japan.

KE. (1992). Introduction to Physical Metallurgy of Welding, Butterworth -Heinemann.

Khan, S., Wilde, F., Beckmann, F. & Mosler, J. (2012). Low cycle fatigue mechanism of the lightweight alloy Al2024. International Journal of Fatigue, 38: 92-99.

Kim, J. W., Kim, S. S., Lee, M. J. & Yang, J. G. (2012). Vierendeel joints in the circular hollow sections of high strength steel subjected to brace moment and chord compressive loadings. Int J Steel Struct, 12(4):579–87.

Krieg, R. D. (1975). A practical two surface plasticity theory. Journal of Applied Mechanics, 42, 641-646.

Lemaitre, J., & Chaboche, J. L. (1994). Mechanics of solid materials. Cambridge university press.

Li, Y., Pan, X. & Wang, G. (2013). Low cycle fatigue and ratcheting properties of steel 40Cr under stress controlled tests. Int J Fatigue, 55:74–80.

Ling, Y. (1996). Uniaxial true stress-strain after necking. AMP Journal of technology, 5(1), 37-48.

Liu, X. & Chung, K.-F. (2018). Experimental and numerical investigation into temperature histories and residual stress distributions of high strength steel S690 welded H-sections. Eng Struct, 165:396–411.

MathWorks. (2021). MATLAB (Version R2021b). [Computer software]. https://www.mathworks.com/products/matlab.html

Mayr, P. (2007). Evolution of microstructure and mechanical properties of the heat affected zone in B-containing 9% chromium steels. Ph.D. Thesis. Faculty of Mechanical Engineering, Graz University of Technology, Austria.

MOHURD, AQSIQ. (2016). Code for seismic design of buildings. GB 50011-2010 (2016 Edition), Ministry of Housing and Urban-Rural Development (MOHURD) & The General Administration of Quality Supervision, Inspection and Quarantine of the People's Republic of China (AQSIQ), China.

MOHURD, AQSIQ. (2017). Standard for design of steel structures. GB 50017-2017, Ministry of Housing and Urban-Rural Development (MOHURD) & The General Administration of Quality Supervision, Inspection and Quarantine of the People's Republic of China (AQSIQ), China.

Ohno, N. (1982). A constitutive model of cyclic plasticity with a nonhardening strain region, 721-727.

SAMR, SAC. (2018). High strength low alloy structural steels. GB/T 1591-2018, The State Administration for Market Regulation (SAMR) & Standardization Administration of China (SAC), China.

Śloderbach Z. & Pająk J. (2015). Determination of ranges of components of heat affected zone including changes of structures. Archives of metallurgy and materials, 60(4): 2607-2612.

Tian, Y., Wang, H. T., Li, Y., Wang, Z. D. & Wang, G. D. (2017). The analysis of the microstructure and mechanical properties of low carbon micro-alloyed steels after ultra-fast cooling. Materials Research, 20(3): 853-589.

Van der Vegte, G. J., & Makino, Y. (2005). Ultimate strength formulation for axially loaded CHS uniplanar T-joints. In The Fifteenth International Offshore and Polar Engineering Conference.

International Society of Offshore and Polar Engineers.

Wang, W. & Chen, Y. Y. (2007). Hysteretic behaviour of tubular joints under cyclic loading. J Constr Steel Res, 63(10):1384–95.

Wang, Y. B., Li, G Q., Cui, W., Chen, S. W. & Sun, F. F. (2015). Experimental investigation and modelling of cyclic behaviour of high strength steel. Journal of Constructional Steel Research, 104: 37-48.

Wang, Y. B., Li, G. Q., Sun, X., Chen, S. W., & Hai, L. T. (2017). Evaluation and prediction of cyclic response of Q690D steel. Proceedings of the Institution of Civil Engineers - Structures and Buildings, 170.11: 788-803.

Wardenier, J., Kurobane, Y., Packer, J. A., Van der Vegte, G. J. & Zhao, X. L. (2008). Design guide for circular hollow section (CHS) joints under predominantly static loading. CIDECT.

Willms R. (2009). High strength steel for steel construction. Proceedings of Nordic Steel Construction Conference, 597-604.

Xie, Z., & Chen, Y. (2021). Experimental and modeling study of uniaxial cyclic behaviors of structural steel under ascending/descending strain amplitude-controlled loading. Construction and Building Materials, 278, 122276.

Xu, L. Y.; Nie, X.; Fan, J. S.; Tao, M. X.; Ding, R. (2016) Cyclic hardening and softening behavior of the low yield point steel BLY160: Experimental response and constitutive modeling. International journal of plasticity, Vol.78, p.44-63.

Yura, J. A., Zettlemoyer, N., Edwards, I. F. (1981) Ultimate capacity of circular tubular joints.J Struct Eng,107(10):1965–84.

Zhou, F., Chen, Y. & Wu, Q. (2015). Dependence of the cyclic response of structural steel on loading history under large inelastic strains. Journal of Constructional Steel Research, 104: 64-73.